

Universiteit
Leiden
The Netherlands

Systematic investigations into the role of ceramide subclass composition on lipid organization and skin barrier

Nadaban, A.

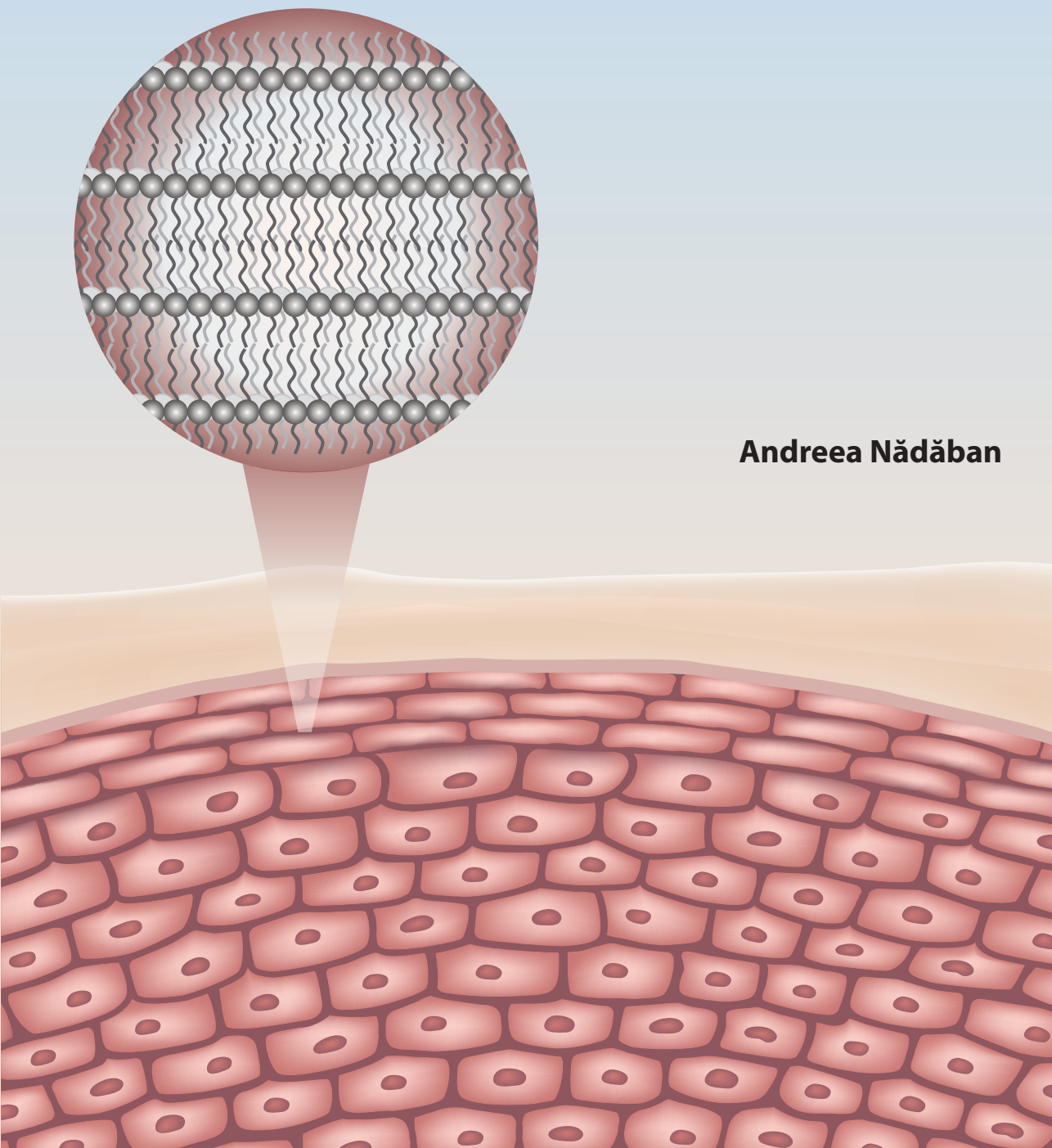
Citation

Nadaban, A. (2024, May 16). *Systematic investigations into the role of ceramide subclass composition on lipid organization and skin barrier*. Retrieved from https://hdl.handle.net/1887/3754008

Version:	Publisher's Version
License:	Licence agreement concerning inclusion of doctoral thesis in the Institutional Repository of the University of Leiden
Downloaded from:	https://hdl.handle.net/1887/3754008

Note: To cite this publication please use the final published version (if applicable).

Systematic investigations into the role of ceramide subclass composition on lipid organization and skin barrier



Andreea Nădăban

Systematic investigations into the role of ceramide subclass composition on lipid organization and skin barrier

Andreea Nădăban

Systematic investigations into the role of ceramide subclass composition on lipid organization and skin barrier

PhD thesis with summary in Dutch

The research described in this thesis was performed at the division of BioTherapeutics of the Leiden Academic Centre for Drug Research (LACDR), Leiden University (Leiden, The Netherlands). The research was financially supported by the National Institutes of Health (National Institute of Arthritis and Muscoskeletal and Skin Diseases, U.S.A.), grant number R01AR072679.

Cover image: A schematic representation of the epidermis, the upper layer of the skin. Stratum corneum (SC) is the top layer of the epidermis and it consists of corneocytes embedded in a lipid matrix. The zoomed in section shows an illustration of the SC lipids, which represent the main focus of this thesis. Some elements of the cover image were obtained from iStock photo.

Cover design: Andreea Nădăban
Layout: Andreea Nădăban
Printed by: Ipskamp Printing

ISBN: 978-94-6473-439-3

© Copyright, Andreea Nădăban, 2024. All rights reserved. No part of this thesis may be reproduced or transmitted in any form or by any means without the permission of the author.

Systematic investigations into the role of ceramide subclass composition on lipid organization and skin barrier

Proefschrift

ter verkrijging van de graad van doctor aan de Universiteit Leiden,
op gezag van rector magnificus prof.dr.ir. H. Bijl,
volgens besluit van het college voor promoties
te verdedigen op donderdag 16 mei 2024
klokke 15.00 uur

door

Andreea Nădăban
geboren te Arad, Roemenië
in 1993

Promotores:

Prof. dr. J.A. Bouwstra

Prof. dr. R. Rissmann

Promotiecommissie:

Prof. dr. H. Irth

Prof. dr. E.C.M. de Lange

Prof. dr. D.J. Moore (University of Edinburgh)

Prof. dr. E. Sparr (Lund University)

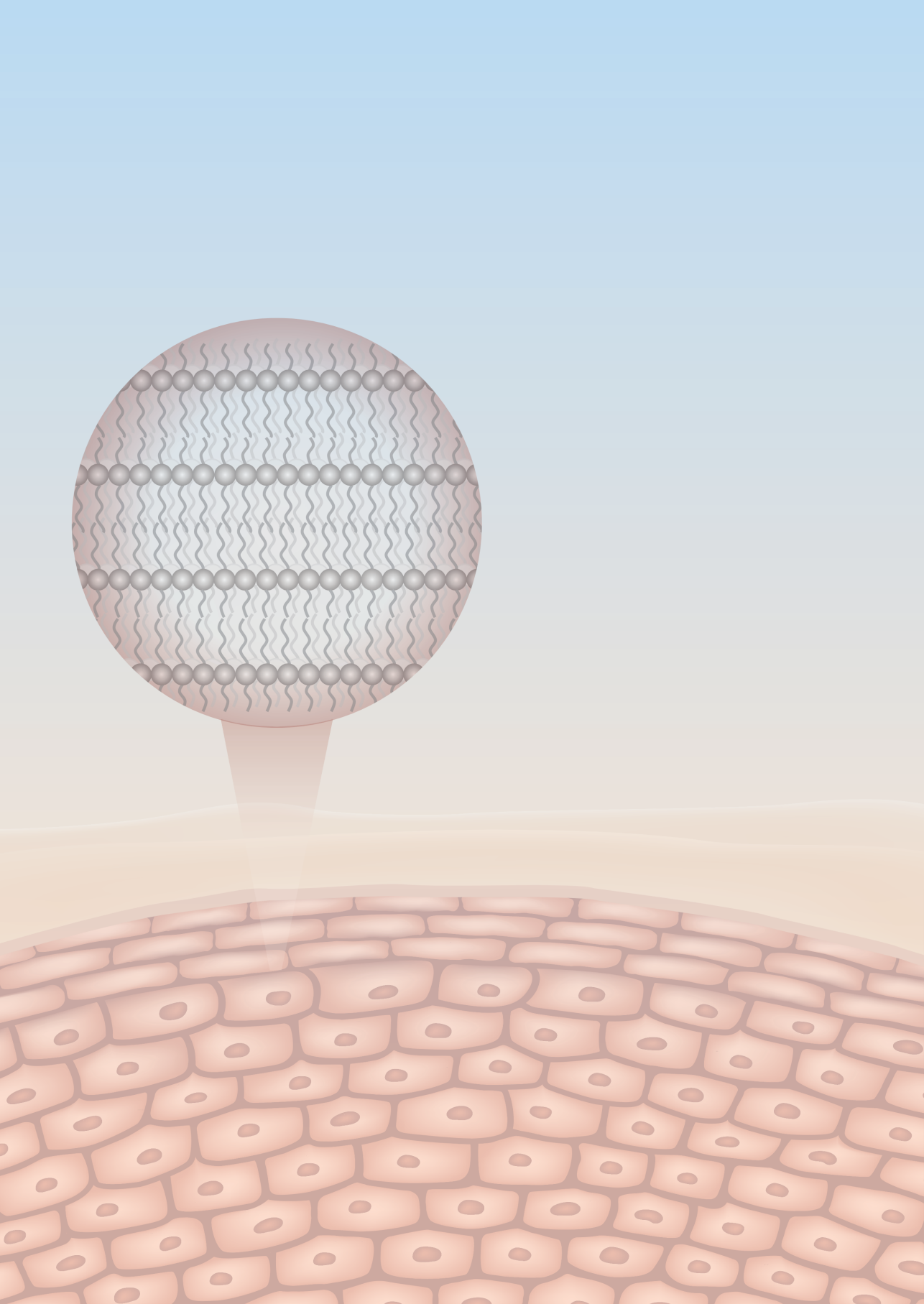
Prof. dr. A. Kros

Dr. J. van Smeden

To my parents

TABLE OF CONTENTS

Chapter 1	Introduction, aim and outline of the thesis	9
Chapter 2	Lesional skin of Seborrheic Dermatitis patients is characterized by skin barrier dysfunction and correlating alterations in the stratum corneum ceramide composition	29
Chapter 3	Phytosphingosine ceramide mainly localizes in the central layer of the unique lamellar phase of skin lipid model systems	63
Chapter 4	Effect of sphingosine and phytosphingosine ceramide ratio on lipid arrangement and barrier function in skin lipid models	93
Chapter 5	Influence of the sphingosine and phytosphingosine ceramide ratio on the lipid organization in the short periodicity phase	125
Chapter 6	The molecular arrangement of ceramides in the unit cell of the long periodicity phase of stratum corneum models shows a high adaptability to different ceramide head group structures	151
Chapter 7	Summary and perspectives	183
Appendices	Nederlandse samenvatting, Curriculum Vitae, List of publications	195



CHAPTER 1

Introduction, aim and outline of the thesis

INTRODUCTION

The structure of human skin and its barrier function

The skin, the largest organ of the body, is the main barrier against unwanted environmental factors. The essential biological functions of the skin also encompass thermoregulation, sensing external environmental stimuli, like pain and heat, synthesizing vitamin D and excreting urea and salts (1). The human skin consists of an epidermis, dermis and subcutaneous tissue (2). The epidermis, the superficial layer of the skin, continuously renews itself and it is composed of four different layers, depicted schematically in Figure 1. Keratinocytes, the most abundant cell type in the epidermis, proliferate in the stratum basale (SB) and subsequently reach the stratum spinosum (SS), where the differentiation of the keratinocytes is initiated. As the keratinocytes gradually move towards the skin surface, their function and content changes. The biosynthesis of the precursors of barrier lipids starts in the SS and is further intensified in the next layer of the epidermis, the stratum granulosum (SG). The phospholipids (precursors of free fatty acids, FFAs) and the precursors of the ceramides (CERs), the glucosylceramides and sphingomyelin, are synthesized and stored in lamellar bodies (3-6).

During the formation of the stratum corneum (SC), the final differentiation product, the keratinocytes, transform into keratin-containing corneocytes and a layer of non-polar lipids (bound lipids) is esterified to the cornified envelope, the outermost layer of these cells. Simultaneously, the formation of the intracellular SC lipid matrix is initiated. The SC lipid matrix consists of non-polar free lipids, formed by extruding lamellar bodies containing precursor lipids, together with lipid enzymes (7, 8) from the keratinocytes into the extracellular space. The monolayer of bound lipids represents a template for the free lipids to form lipid lamellae, which are oriented approximately parallel to the corneocytes (9).

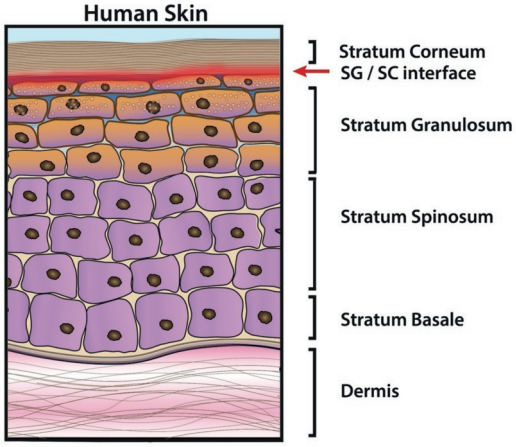


Figure 1. Schematic overview of the skin's epidermis with its four layers: stratum basale, stratum spinosum, stratum granulosum and stratum corneum (SC). Adapted from (10).

The barrier function of the skin is provided mainly by the SC, its uppermost layer (11). The only continuous pathway through the skin is the SC lipid matrix, thus any chemicals, drugs or pathogens have to pass through the intercellular lipid matrix in order to penetrate in the deeper layers. The SC has an important role to prevent unwanted environmental compounds from entering the body and prevents the excess water loss.

Lipid composition in the SC

The SC lipids consist mainly of three lipid classes: CERs, FFAs and cholesterol (CHOL), which are present approximately in an equimolar ratio in human SC (12). The CER: CHOL: FFA molar ratio varies to some extent and a comprehensive overview of the ratios obtained in previous studies is presented by Bouwstra et al. (13), also based on an earlier report of Weerheim et al. (12).

CERs are part of the sphingolipids family and besides their main function in the formation of the skin barrier, CERs are also regulators of cellular processes, such as apoptosis, proliferation and differentiation of skin cells (14, 15). CERs are composed of a sphingolipid base linked by an amide bond to an acyl chain and nowadays, there are 25 CER subclasses identified in human SC (16). In this thesis, CER subclasses are denoted according to the nomenclature introduced by Motta et al., with the first one (or two) letters representing the type of acyl chain and the last one (or two) letters indicating the type of sphingoid base (17). This is referred to as CER XY and the structures of most of the CERs subclasses present in human SC are presented in Figure 2.

A special group of CERs are the CER EO subclass (also referred to in literature as acylCERs), which have a very long ω-hydroxy acyl chain linked with an ester bond to a fatty acid chain of 18 carbon atoms (primarily a linoleate chain, but oleate or saturated chains have also been reported) (18). The CER EO subclass is very important as it is only found in the epidermis and it mostly consists of CER EOdS, CER EOS, CER EOP, CER EOH, with the exceptional structures shown in Figure 2.

Apart from the variation in the CER subclasses, in each subclass the total chain length (acyl chain + sphingoid base) varies. In this thesis, the acyl chain length of synthetic CERs is denoted as CXX. For example, CER NP C24 indicates the phytosphingosine-based CER with a non-hydroxy fatty acid chain of 24 carbon atoms. If not specified, the chain length of the sphingoid base of synthetic CERs is 18 carbon atoms in length. The total chain length of CERs is usually between 32 and 72 carbon atoms, with the variation of the acyl chain length larger than the variation in sphingoid base chain length (16, 19, 20).

The FFAs also have a large variation in the chain length (between 16 and 36 carbon atoms), with C24 and C26 representing the most abundant in human SC (21). In SC, saturated FFAs are predominantly found, with only a minor amount of monounsaturated FFAs (muFFAs) or FFAs with an extra hydroxyl group present (22).

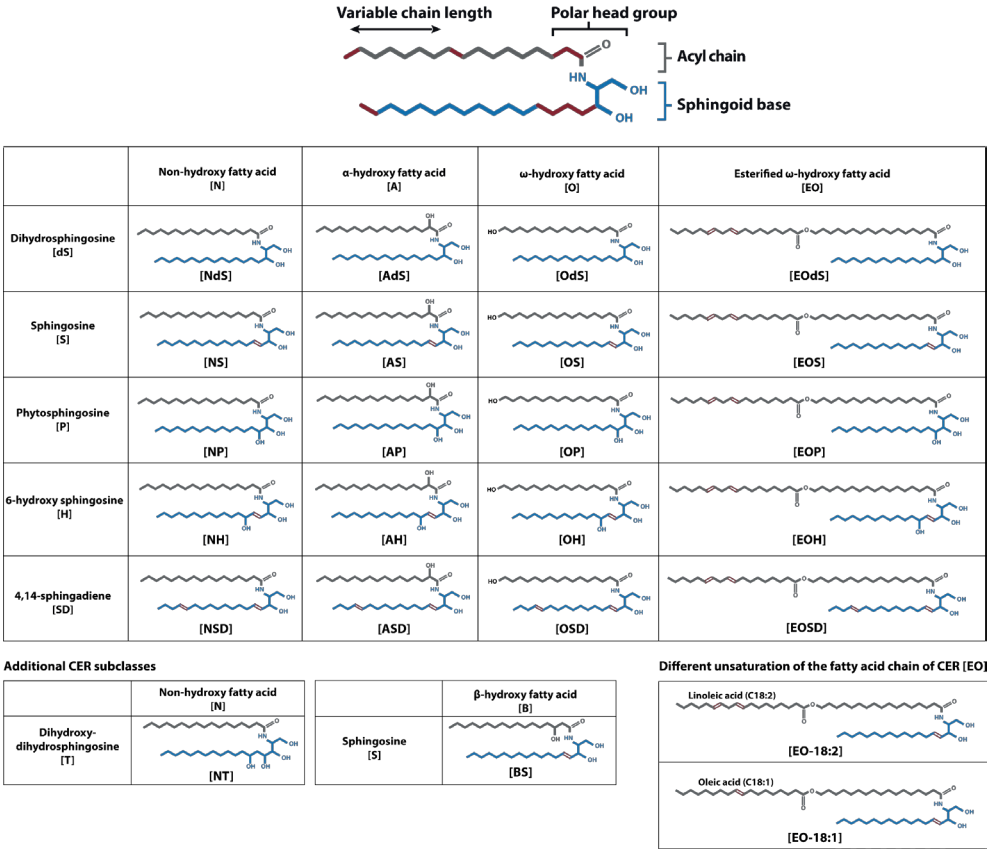


Figure 2. The structure of the SC CER subclasses and their nomenclature according to Motta et al. (17). CERs consist of an acyl chain linked with an amide bond to a sphingoid base. The CER acyl chains are non-hydroxy (N), α-hydroxy (A), ω-hydroxy (O), esterfied-ω-hydroxy (EO) or β-hydroxy acyl (B), while the sphingoid bases are dihydrosphingosine (dS), sphingosine (S), phytosphingosine (P), 6-hydroxy-sphingosine (H), 4,14-sphingadiene (SD) and dihydroxy-dihydrosphingosine (T). Figure reprinted from (13).

Lipid organization in the SC

The SC intercellular lipid matrix is organized in crystalline lamellae, arranged approximately parallel to the corneocyte surface, thus to the SC surface (9). The first studies that observed the presence of the lamellar layers in SC used freeze-fracture electron microscopy (23). Then, using ruthenium tetroxide (RuO_4) fixation of the SC the lipid lamellae were characterized by a repeating broad-narrow-broad sequence of the electron translucent bands (9, 24, 25). RuO_4 reacts with saturated SC lipid chains and the distance of this repeating pattern (referred to as the repeat distance of the unit cell) was around 12-13 nm (9). The existence of this specific repeating pattern suggests a unique molecular arrangement of the lipids in the lamellar repeating pattern. More details about the lipid organization were obtained using X-ray and neutron diffraction and Fourier

transform infrared spectroscopy (FTIR). While electron microscopy provides information in a nm-range of the field of view, X-ray diffraction and FTIR obtain average structural information.

The human SC lamellar phases were reported in 1991 using small angle X-ray diffraction, with the measurements performed at synchrotron radiation facilities. This has the advantage of a highly intense primary beam, which makes it possible to obtain structural information using a very small amount of material (26). This is important for SC as only around 15 w/w% of the material is lipids. The X-ray beam interacts with the electrons in the atoms of the lipids and the obtained data using two-dimensional detection of the X-rays can be converted to a one-dimensional plot, where equidistant peaks can be attributed to a single lamellar phase (Figure 3). X-ray studies of human SC identified two coexisting lamellar phases with repeating distances of approximately 13 nm and 6 nm, referred to as the long periodicity phase (LPP) and short periodicity phase (SPP) (26, 27). A schematic representation of these phases is presented in Figure 4.

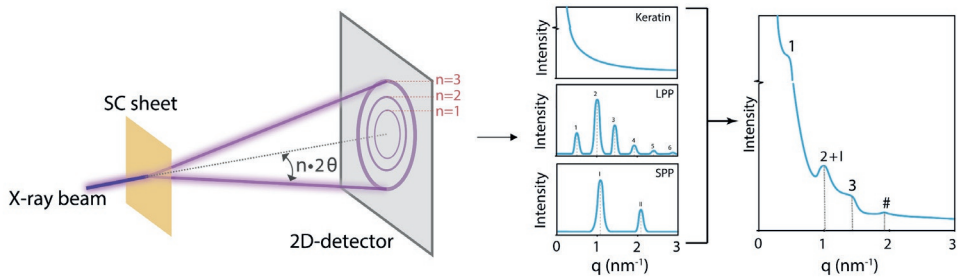


Figure 3. The lamellar organization of SC measured by X-ray diffraction. Adapted from (34).

Within the lamellar phases in the SC, the lipid chains can adopt different packing densities, referred to as the lateral organization: orthorhombic (ordered phase, very dense packing), hexagonal (an ordered phase, but the lipid chains are less densely packed) or liquid phase (highly disordered phase) (Figure 4) (28-30). In human SC, the lipids are predominantly organized in a dense crystalline orthorhombic packing, however a small fraction of lipids also adopts hexagonal packing and a minor part even a liquid phase (31, 32). The lipid packing can be analyzed using FTIR; Figure 5 provides a brief overview of the technique (13). The conformational ordering of the lipids is examined using the symmetric and asymmetric stretching frequencies of the CH_2 bond. The orthorhombic to hexagonal phase transition can be detected by measuring the FTIR spectra as a function of temperature. When the lipids adopt an orthorhombic packing, the hydrocarbon chains are very close and there is a short-range coupling of the CH_2 scissoring vibrations, resulting in two peaks at ~1463 cm^{-1} and ~1473 cm^{-1}. In case of a hexagonal packing, the hydrocarbon chains are still ordered but the distance between them causes the loss of the CH_2 frequency short-range coupling and a single peak is present in the CH_2 scissoring vibrations at ~1468 cm^{-1}. The lipid composition together with environmental factors determine the

lipid organization and thus has a great impact on the permeability of SC and skin barrier function (33, 34).

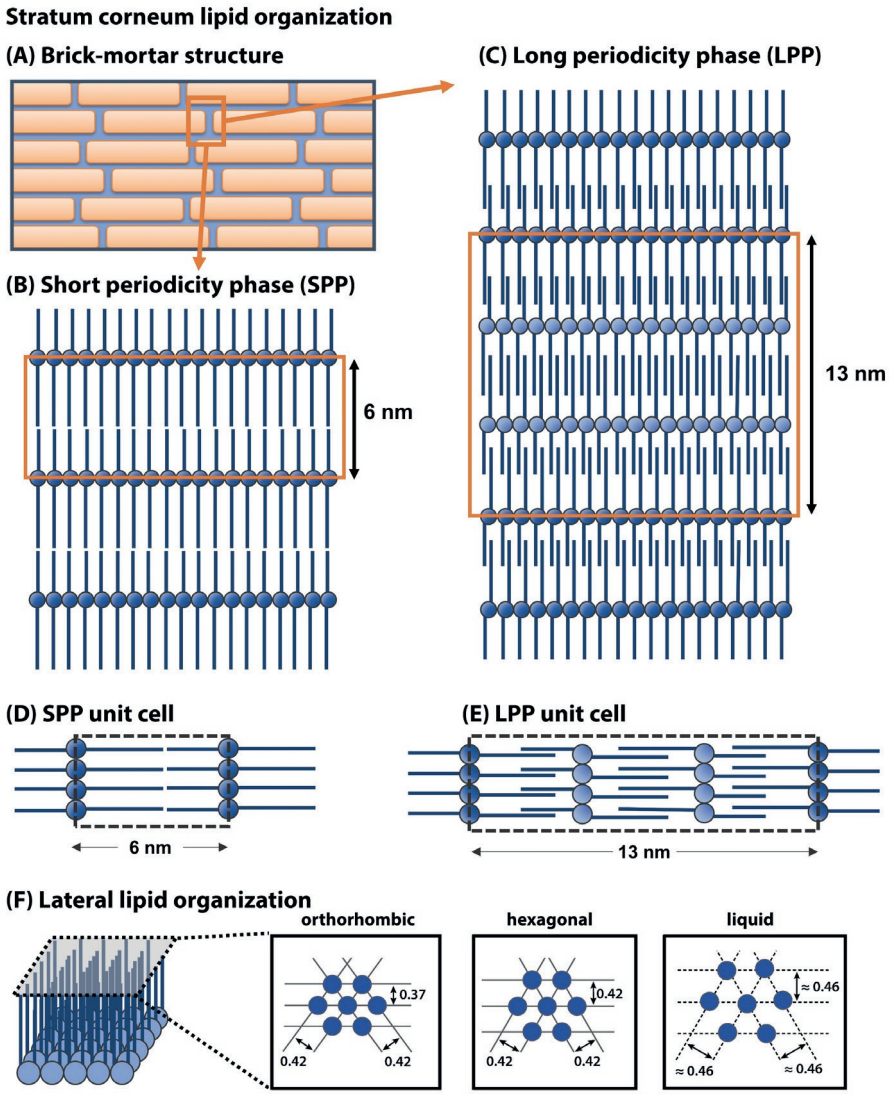


Figure 4. Schematic representation of the lamellar and lateral organization of SC lipids. The LPP and SPP with the repeat unit cells are schematically shown (B-E), along the three different packing densities of the lipids (F). Reprinted from (13).

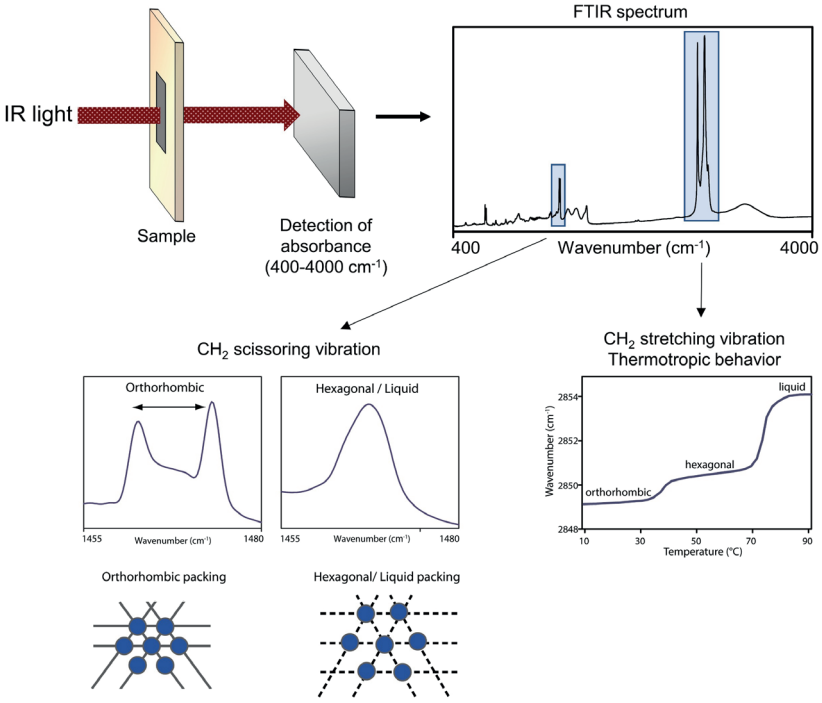


Figure 5. Brief overview of FTIR spectroscopy and the two types of vibrations mostly discussed in this thesis: the scissoring and stretching vibrations of the CH_2 and CD_2 bonds. Reprinted from (13).

Impaired barrier function and changes in barrier lipid properties in skin diseases

Inflammatory skin diseases have an important impact on our society, because of the increased patient population and the significant physical and psychological consequences of these skin disorders. Numerous patients with inflammatory skin diseases experience constant itches that cause sleep disturbances, diminished self-esteem and impacting significantly their social engagement. Due to these problems, the quality of life of the inflammatory skin disease patients is severely affected (35, 36). Psoriasis, atopic dermatitis and Netherton syndrome are some examples of inflammatory skin diseases that exhibit an impaired barrier function. Besides changes in protein composition, the SC lipid composition is also altered in these diseases. Therefore, it is important to determine whether the changes in lipid composition results in changes in lipid organization, thereby changing the skin barrier. Furthermore, it is important to determine whether there are similarities in these lipid compositional changes in the SC of these diseases.

Psoriasis is a chronic inflammatory skin disease which affects ~2% of Western countries (37). Motta et al. first reported the CER composition of lesional psoriatic SC and a reduced barrier function in lesional skin, as measured by trans epidermal water loss (TEWL) (17). A relative decrease of CER EOS, CER NP and CER AP was reported in lesional

SC, while CER NS and CER AS were increased. A clinical study by Yokose et al. reported that the ratios of CER NP and CER NH subclasses relative to CER NS and CER AS were reduced, both in lesional skin, as well as non-lesional skin (38). Moreover, the increased CER NS / CER NP molar ratio correlated positively with the TEWL values. An altered lipid composition was also observed by Uchino et al. that reported increased levels of CER NS and CER AS and reduced levels of CER NP and CER AP subclasses in psoriatic SC compared to healthy skin (39). The same study concluded that lipid composition of psoriatic SC was also characterized by shorter total chain lengths of CERs and FFAs compared to healthy SC.

Atopic dermatitis is the most frequently studied skin disease with a perturbed skin barrier. It is a chronic inflammatory skin disease that affects 2-10% of adults and over 15% of children, with an increasing prevalence in developed countries (36, 40). The barrier function of AD skin is decreased in lesional SC (34, 41-43). The major lipid compositional changes reported for atopic dermatitis SC comprise of: i) decreased total amount of CERs (44-46) and FFAs (46) in non-lesional and lesional skin, ii) reduced relative abundances of CER EOS (34, 41, 47, 48) and CER NP (47, 48), iii) increased abundance of CER NS and CER AS (45), as well as iv) short chain CER NS (34, 45). Yokose et al. showed the strong correlation of the TEWL values with the ratio of CER NS/CER NP, which was increased in lesional skin (38), in agreement with previous studies that reported separate correlations between increased TEWL values and the increased concentration of CER NS and decreased amount of CER NP in the diseased SC, respectively (34, 45, 49).

Netherton syndrome is a rare genetic skin disorder with a SPINK5 (serine protease inhibitor Kazal-type 5 gene) mutation, which is characterized by severe atopic manifestations and erythroderma (50). Similar to atopic dermatitis and psoriasis, an altered lipid composition and organization is reported in the SC of this disease. In comparison with control skin, there is a significant decrease in the FFA chain lengths and an increase in the FFAs unsaturation (51). The CER subclasses are also affected, as the concentration of CER EOS and CER NP is decreased, while the concentrations of CER NS and CER AS are elevated (51, 52). This lipid compositional change has an effect on the lipid organization as well, with a higher degree of disordering of lipid chains reported for SC of Netherton syndrome. A summary of the lipid compositional changes in atopic dermatitis, psoriasis and Netherton syndrome is presented in Table 1. As seen in the table, there are a series of lipid compositional changes occurring in all three inflammatory skin diseases.

Lipid compositional changes have an effect on the lipid organization in all three skin diseases described above: the position of the diffraction peaks (of the LPP and SPP) is shifted compared to healthy skin (34, 51, 53) and a lower fraction of lipids adopts the orthorhombic phase, as the fraction of lipids forming a less dense hexagonal organization is higher (21, 34, 51). The changes in lateral organization of the lipids in diseased SC correlated with impaired barrier function (measured by TEWL) (21, 34).

Table 1. Summary of lipid composition and organization changes observed in psoriasis, atopic dermatitis and Netherton syndrome, compared to control. Adapted from Bouwstra et al. (13).

Skin disease	Lipid composition change	Lipid organization change	References
Psoriasis	CER chain length ↓ CER EOS, EOP, EOH, NP, AP, AH ↓ CER NS, AS ↑ FFAs chain length ↓ Unsaturated FFAs ↑	Changes in lamellar phases Changes in lateral packing	(17, 38, 39, 54)
Atopic dermatitis	CER chain length ↓ CER EOS, EOP, EOH, NP, NH, AH, NdS ↓ CER NS, AS ↑ FFAs chain length ↓ Unsaturated FFAs ↑	Changes in lamellar phases Orthorhombic packing ↓ Conformational disordering of the chains ↑	(21, 34, 38, 41, 44-47)
Netherton syndrome	CER chain length ↓ CER EOS, EOP, EOH, EOdS, NP ↓ CER NS, AS ↑ FFAs chain length ↓ Unsaturated FFAs ↑	Changes in lamellar phases Conformational disordering of the chains ↑	(51, 52)

Lipid models as a tool for studying the lipid composition and organization changes

When the diseased SC is compared with healthy SC in clinical studies, the various lipid compositional changes occur simultaneously and therefore the contribution of each of the underlying factors cannot be unraveled. To understand the relationship between different lipid (sub)classes, lipid models that mimic the organization in the SC lipid matrix can be used. These models offer the possibility to systematically study the effect of compositional changes of individual components on the lipid organization and lipid barrier. In this way more detailed insights can be obtained about the main underlying factors that cause barrier impairment (55-57).

Lipid compositions

Previous studies reported that lipid model systems prepared with isolated pig (58, 59) or human CERs (60) mixed with synthetic CHOL and FFAs mimicked the unique lamellar structure observed in SC (LPP and SPP). When the various synthetic CER subclasses became available commercially, isolated pig and isolated human CERs were replaced by their synthetic counterparts. Unlike the isolated CERs, the synthetic CER mixtures have an almost uniform chain length, but this hardly influences the lamellar phase behavior: the lamellar phases of the lipid mixtures containing CERs, CHOL and FFAs, were similar to that of the mixtures prepared with isolated CER and thus also closely mimicking the native SC lipid organization (61-64). Further reducing the CER subclass composition to four, three or even two subclasses in the mixture demonstrated that selecting the proper CER

subclasses, together with CER EOS, CHOL and FFAs, it is possible to form the same lamellar phases still resembling the SC (62, 63, 65, 66). This finding is important as simple model systems with a limited number of lipid components are mandatory to obtain detailed information about the molecular arrangement of the lipids, as in such studies the protiated lipids are replaced with their deuterated counterparts.

The lipid composition of the models has an important role for the lipid organization. The presence of CERs and CHOL in lipid models is important for the formation of the lamellar phases (58, 59). Studies report the essential role of the FFAs for the lateral packing of the lipids. Short chain FFAs (C14-C18) did not influence the formation of the lamellar phases, however an additional phase was detected using X-ray diffraction. The additional phase was not formed when the FFA mix was replaced with the long-chain FFAs (with the most abundant chain lengths C22 and C24) in lipid models prepared with isolated porcine CERs (58). This was further investigated in models with synthetic CERs mimicking porcine CER composition and it was reported that short chain FFAs (C16 and C18) determine a lower conformational ordering of the lipid system, phase-separated domains, as well as a higher fraction of lipids adopting a hexagonal packing, in comparison with long-chain FFAs (C22, C24) or a FFA mix (with the most abundant chain lengths C22 and C24) (67, 68).

The presence of CER EOS in the CER composition is vital for the formation of the LPP (59, 61, 69). Increasing the CER EOS concentration from 15 mol% (mimicking the natural CER EOS concentration) to 40 mol% (of total CER fraction) results in the exclusive formation of the LPP, while the intensity distribution of the LPP diffraction orders is not changed compared to mixtures with 15 mol% CER EOS (70, 71). In the latter CER composition, the LPP and SPP are both formed. No differences in the flux of a model drug across lipid membranes of the lipid models were reported when comparing a 10 mol% and 30 mol% CER EOS fraction in the CER composition, with a significant permeability increase only present above 70 mol% CER EOS level and when no CER EOS is present (61, 72). Thus, the concentration of CER EOS can be increased or decreased to affect the fraction of lipids forming the LPP and SPP for the study of the lipid models.

Comprehensive studies were previously performed on lipid models forming only the SPP, by excluding the CER EO subclass from the lipid composition. Most frequently lipid compositions with only one or a few CER subclasses were mostly used. The most frequently investigated composition is CER NS: CHOL: FFAs. The phase behavior of these models depends on various factors (such as CER head group structure and the lipid chain length of CERs and FFAs). While CER NS C24 mixed with CHOL and FFA (C24 or the FFA_{mix} consisting primarily of C22 and C24) in equimolar ratio results in a single lamellar phase (SPP) and phase separated crystalline CHOL, using other CER subclasses in the absence of CER EOS (such as CER NP, CER AP, CER AS, CER NdS or CER NH) results in phase-separated crystalline domains, next to crystalline CHOL. This highlights the importance of the head group structure for the mixing of the lipids in the SPP (73-77). The studies using SPP

models show that CHOL improves the mixing of FFAs and CERs, and the FFAs interdigitate with the other lipid chains (78, 79).

The localization of the lipid subclasses in the LPP model

To unravel in more details the role played by the lipid (sub)classes in the lipid organization, it is important to determine the localization of the lipids in the unit cell of the lamellar phases. The unit cell represents the repeating pattern of the lamellar structure, as explained in Figure 4. Information on the lipid arrangement can be obtained using neutron diffraction, a technique that allows the identification of the exact location of the lipid chains in the unit cell. The neutron scattering of protiated and deuterated compounds is different (deuterium atoms have a higher scattering intensity than hydrogen atoms). By replacing protiated lipids by (partly) deuterated counterparts, the deuterated moiety of the lipid can be located in the structure.

The location of the water molecules can be determined by varying the D_2O/H_2O ratio in the buffer used to hydrate the samples. The water molecules are localized next to the lipid head groups, rather than the hydrophobic lipid chains. Their location indicates the four lipid head group regions in the LPP and the LPP trilayer structure comprised of a central layer with two similar outer layers (70, 80). The location of deuterated lipid chains in a lipid model can be identified by measuring the diffraction pattern of the protiated sample and its deuterated counterpart (sample with the deuterated lipid chain of interest). The scattering length density (SLD) profile of the deuterated lipid moiety is obtained by the subtraction of the SLD profiles of the protiated sample from the deuterated sample. This provides the location of the deuterated moiety in the unit cell.

The location of some lipid (sub)classes was previously examined in the LPP unit cell (Figure 6). In a lipid model with the CER subclasses mimicking the porcine CER composition, CHOL was localized in the outer layers of the LPP, with its hydroxyl group close to the inner lipid head group region (80). The position of the esterified linoleate chain of CER EOS was determined using CER EOS with a deuterated linoleate chain. The SLD profiles obtained indicate that in the LPP unit cell, the linoleate is in an isotropic phase, positioned close to the inner layer of lipid head groups (80). The proposed location of the linoleate chain of CER EOS is in agreement with previous reports of liquid droplets of esterified linoleate or oleate chains of CER EOS (81, 82). The positions of the FFA C24 and of the acyl chain of CER NS were identified in the inner layer of the LPP, with the chains interdigitating in this layer (70). Beddoes et al. determined the location of the sphingosine chain of CER NS and therefore could determine the CER NS conformation (66, 83). CER NS with the head group in the inner region of the LPP is arranged in an linear (extended) conformation: the acyl chain is mainly located in the inner layer (in agreement with the previous study of Mojumdar et al. (70)) and the sphingosine chain is positioned in the two outer layers (either side of the CER NS head group). The linear arrangement of CERs could allow a strong connection between the lipid layers and prevent the swelling

upon hydration of the LPP (81). Moreover, in this CER conformation the cross section of the polar lipid head group is reduced, allowing a higher lipid packing density (83). The localization of the two chains of CER NS is the same when comparing a complex lipid system that mimics the porcine CER composition and a lipid model with a simple composition (CER EOS, CER NS, CHOL, FFA_{mix}). Figure 6 represents a schematic arrangement of the LPP unit, according to the previously reported studies.

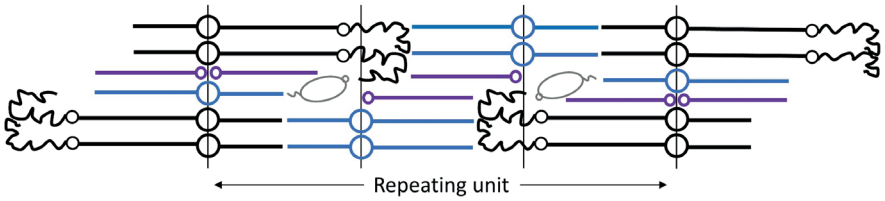


Figure 6. The lipid arrangement in the LPP unit cell (repeating unit) obtained by neutron diffraction. CER EOS is represented in black, CER NS in blue, FFAs are shown in purple and the CHOL molecules in grey. Adapted from Mojumdar et al. (80).

Lipid models for studying the lipid composition changes in skin diseases

As reported in Table 1, several changes in lipid composition have been identified in SC of inflammatory skin diseases. In order to determine the effect of each of these changes on the lipid barrier, these alterations can be systematically implemented in the lipid model systems. The influence of some lipid compositional changes on lipid barrier and phase behavior have already been studied (Table 2).

1. *Chain length of FFA and CERs*

In previous studies the effect of the lipid chain length on the conformational ordering of the lipid chains and the lateral packing was investigated. Shorter lipid chains result in a more prominent presence of lipids forming the hexagonal phase, reduce the lipid ordering and determine a difference in the lamellar organization, with a slightly altered LPP repeat distance and co-existing phases (63, 68, 84-86). This lipid compositional change also caused an impaired barrier in the lipid model membranes, as monitored by TEWL and the fluxes of model drugs, such as ethyl-p-aminobenzoic acid (E-PABA), indomethacin or theophylline.

2. *Increase in degree of unsaturation*

The degree unsaturation, that is an increase in muFFAs, influences the lateral organization resulting in a decrease of the orthorhombic packing and elevated conformational disordering of the lipid chains (87), but no change in the lamellar organization. The barrier function is also affected as monitored by TEWL and the hydrocortisone flux.

3. Variation in the fraction of CER EO subclass

Decreasing the concentration of CER EO subclass (CER EOS or a mix of CER EOS, CER EOP and CER EOdS) in lipid models has the main effect on the lamellar organization, as the LPP cannot be formed in the absence of CER EO subclass (55, 62, 64). The lateral organization is also affected, as a less dense lipid packing was predominant in the models. When the concentration of CER EO subclass in the lipid models is reduced, the lipid fraction forming the LPP is also decreased. This has a significant effect on the flux of the model drugs.

Table 2. The lipid compositional changes reported in skin diseases previously studied using lipid models.

Change in lipid composition	Barrier function	Lipid organization and molecular arrangement	References
Unsaturated FFAs ↑	TEWL and diffusion (hydrocortisone flux) ↑	Orthorhombic packing ↓ Conformational disordering ↑ No effect on lamellar phases	(87)
FFA chain length ↓	TEWL and diffusion (E-PABA, indomethacin, theophylline) ↑	Orthorhombic packing ↓	(63, 68, 84, 85)
CER chain length ↓	Diffusion (E-PABA flux) ↑	Conformational disordering ↑ No effect on lamellar phases	(63, 86)
CER EO subclass ↓	TEWL not changed Diffusion (flux of E-PABA and indomethacin) ↑	Orthorhombic packing ↓ LPP not formed when CER EO subclass is 0%	(55, 62, 64)

AIM OF THIS THESIS

The studies presented in this thesis focused on the effect of the CER subclass composition on the lipid organization, molecular arrangement and barrier function of the skin. First, the CER compositional changes were examined in human SC of seborrheic dermatitis patients by means of a clinical trial. A particular emphasis was paid to the CER NS:CER NP ratio and its correlation to the skin barrier. In the subsequent chapters lipid model systems with a simple CER subclass composition were used to study the influence of the CER NS:CER NP ratio on the barrier function, lipid organization and CER arrangement.

OUTLINE OF THIS THESIS

Chapter 2 describes a clinical study investigating the CER composition and barrier function of seborrheic dermatitis patients, an inflammatory skin disease characterized by erythema and scaling on seborrheic areas of the face and scalp. In this study, the CER composition, the severity of the disease and the skin barrier function are characterized. The CER

composition (including CER NS:CER NP ratio) was correlated with the impaired skin barrier monitored by TEWL.

In subsequent studies, lipid models with a simple lipid composition were used for a more detailed study on the influence of CER subclass composition on the lipid organization, CER arrangement and barrier function. One of the key findings regarding the CER compositional changes in SD, the CER NS:CER NP subclass ratio, was investigated using the lipid models.

Chapter 3 represents the first step in understanding the effect of changing the CER NS:CER NP molar ratio on the lipid organization, using a CER composition comprising of CER EOS, CER NS and CER NP. The location of CER NP and CER NS (ratio 1:1) in the LPP unit cell was determined.

In **Chapter 4**, the CER NS:CER NP molar ratio was changed from 1:2 (mimicking a healthy SC ratio) to 2:1 (mimicking the ratio found in severe skin conditions) in lipid models forming exclusively the LPP. The lipid organization was investigated, as well as the location of CER NS and CER NP in the LPP unit cell and the barrier function of these lipid models.

Chapter 5 continued the topic of the CER NS:CER NP molar ratio change (from 1:2 to 2:1), focusing on lipid models forming exclusively the SPP. The lipid organization of these models was investigated and compared to that of the LPP models.

In **Chapter 6**, the effect of the CER subclass composition on the arrangement of CER NP and CER NS is examined, including in a composition mimicking human CER composition. The lipid organization, molecular arrangement of CER NS and CER NP and the permeability of the lipid models with different CER head group structures were investigated.

Finally, **Chapter 7** summarizes the results of this thesis and provides an overall conclusion and some remarks on perspectives.

REFERENCES

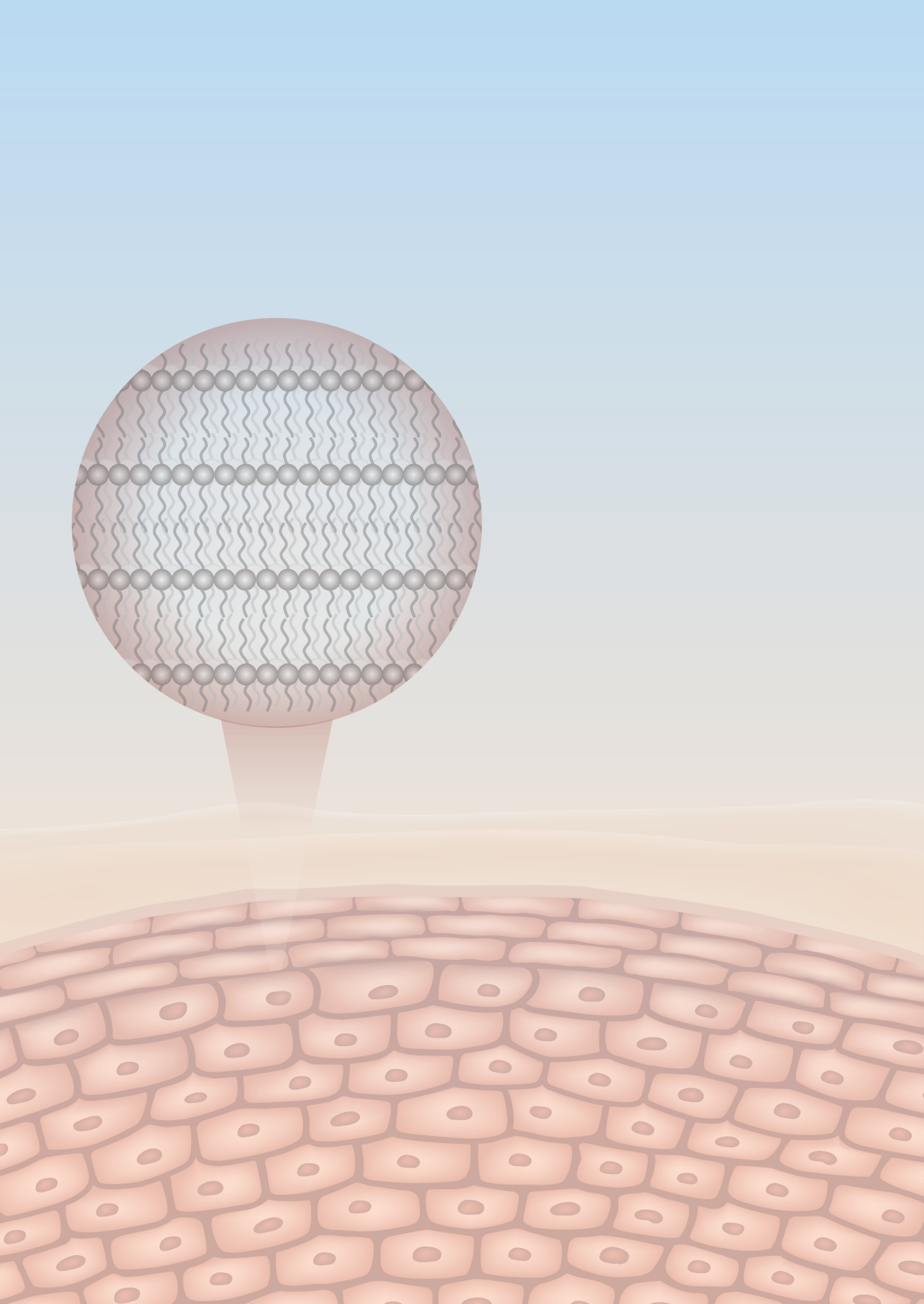
1. Chuong, C. M., Nickoloff, B. J., Elias, P. M., Goldsmith, L. A., Macher, E., Maderson, P. A., et al. (2002). What is the 'true' function of skin? *Experimental Dermatology*. 11(2), 159-87.
2. Proksch, E., Brandner, J. M., Jensen, J.-M. (2008). The skin: an indispensable barrier. *Experimental Dermatology*. 17(12), 1063-72.
3. Mao-Qiang, M., Feingold, K. R., Jain, M., Elias, P. M. (1995). Extracellular processing of phospholipids is required for permeability barrier homeostasis. *J Lipid Res*. 36(9), 1925-35.
4. Wertz, P. W., Downing, D. T., Freinkel, R. K., Traczyk, T. N. (1984). Sphingolipids of the stratum corneum and lamellar granules of fetal rat epidermis. *J Invest Dermatol*. 83(3), 193-5.
5. Holleran, W. M., Takagi, Y., Menon, G. K., Legler, G., Feingold, K. R., Elias, P. M. (1993). Processing of epidermal glucosylceramides is required for optimal mammalian cutaneous permeability barrier function. *J Clin Invest*. 91(4), 1656-64.
6. Holleran, W. M., Takagi, Y., Uchida, Y. (2006). Epidermal sphingolipids: metabolism, function, and roles in skin disorders. *FEBS Lett*. 580(23), 5456-66.
7. Ishida-Yamamoto, A., Igawa, S., Kishibe, M. (2018). Molecular basis of the skin barrier structures revealed by electron microscopy. *Experimental Dermatology*. 27(8), 841-6.
8. Menon, G. K., Ghadially, R., Williams, M. L., Elias, P. M. (1992). Lamellar bodies as delivery systems of hydrolytic enzymes: Implications for normal and abnormal desquamation. *British Journal of Dermatology*. 126(4), 337-45.
9. Madison, K. C., Swartzendruber, D. C., Wertz, P. W., Downing, D. T. (1987). Presence of intact intercellular lipid lamellae in the upper layers of the stratum corneum. *J Invest Dermatol*. 88(6), 714-8.
10. Bouwstra, J. A., Helder, R. W. J., El Ghalbzouri, A. (2021). Human skin equivalents: Impaired barrier function in relation to the lipid and protein properties of the stratum corneum. *Adv Drug Deliv Rev*. 175, 113802.
11. Menon, G. K., Cleary, G. W., Lane, M. E. (2012). The structure and function of the stratum corneum. *Int J Pharm*. 435(1), 3-9.
12. Weerheim, A., Ponec, M. (2001). Determination of stratum corneum lipid profile by tape stripping in combination with high-performance thin-layer chromatography. *Arch Dermatol Res*. 293, 191-9.
13. Bouwstra, J. A., Nadaban, A., Bras, W., McCabe, C., Bunge, A., Gooris, G. S. (2023). The skin barrier: An extraordinary interface with an exceptional lipid organization. *Prog Lipid Res*. 101252.
14. Hannun, Y. A., Obeid, L. M. (2008). Principles of bioactive lipid signalling: lessons from sphingolipids. *Nat Rev Mol Cell Biol*. 9(2), 139-50.
15. Cha, H. J., He, C., Zhao, H., Dong, Y., An, I. S., An, S. (2016). Intercellular and intracellular functions of ceramides and their metabolites in skin (Review). *Int J Mol Med*. 38(1), 16-22.
16. Kawana, M., Miyamoto, M., Ohno, Y., Kihara, A. (2020). Comparative profiling and comprehensive quantification of stratum corneum ceramides in humans and mice by LC/MS/MS. *J Lipid Res*. 61(6), 884-95.
17. Motta, S., Monti, M., Sesana, S., Caputo, R., Carelli, S., Ghidoni, R. (1993). Ceramide composition of the psoriatic scale. *Biochim Biophys Acta*. 1182, 147-51.
18. Wertz, P. W., Miethke, M. C., Long, S. A., Strauss, J. S., Downing, D. T. (1985). The composition of the ceramides from human stratum corneum and from comedones. *J Invest Dermatol*. 84(5), 410-2.
19. Ohnari, H., Naru, E., Sakata, O., Obata, Y. (2023). Distribution of Domains Formed by Lateral Packing of Intercellular Lipid in the Stratum Corneum. *Chem Pharm Bull*. 71, 31-40.
20. Masukawa, Y., Narita, H., Sato, H., Naoe, A., Kondo, N., Sugai, Y., et al. (2009). Comprehensive quantification of ceramide species in human stratum corneum. *J Lipid Res*. 50(8), 1708-19.
21. van Smeden, J., Janssens, M., Kaye, E. C., Caspers, P. J., Lavrijsen, A. P., Vreeken, R. J., et al. (2014). The importance of free fatty acid chain length for the skin barrier function in atopic eczema patients. *Experimental Dermatology*. 23(1), 45-52.
22. van Smeden, J., Boiten, W. A., Hankemeier, T., Rissmann, R., Bouwstra, J. A., Vreeken, R. J. (2014). Combined LC/MS-platform for analysis of all major stratum corneum lipids, and the profiling of skin substitutes. *Biochim Biophys Acta*. 1841(1), 70-9.

23. Breathnach, A. S., Goodman, T., Stolinski, C., Gross, M. (1973). Freeze-fracture replication of cells of stratum corneum of human epidermis. *J Anat*. 114(1), 65-81.
24. Elias, P. M., Friend, D. S. (1975). The permeability barrier in mammalian epidermis. *Journal of Cell Biology*. 65, 180-91.
25. Swartzendruber, D. C., Wertz, P. W., Kitko, D. J., Madison, K. C., Downing, D. T. (1989). Molecular models of the intercellular lipid lamellae in mammalian stratum corneum. *J Invest Dermatol*. 92(2), 251-7.
26. Bouwstra, J. A., Gooris, G. S., van der Spek, J. A., Bras, W. (1991). Structural investigations of human stratum corneum by small-angle X-ray scattering. *J Invest Dermatol*. 97(6), 1005-12.
27. Garson, J. C., Doucet, J., Leveque, J. L., Tsoucaris, G. (1991). Oriented structure in human stratum corneum revealed by X-ray diffraction. *J Invest Dermatol*. 96(1), 43-9.
28. Mendelsohn, R., Rerek, M. E., Moore, D. J. (2000). Infrared spectroscopy and microscopic imaging of stratum corneum models and skin. *Physical Chemistry Chemical Physics*. 2(20), 4651-7.
29. Boncheva, M., Damien, F., Normand, V. (2008). Molecular organization of the lipid matrix in intact Stratum corneum using ATR-FTIR spectroscopy. *Biochim Biophys Acta*. 1778(5), 1344-55.
30. Damien, F., Boncheva, M. (2010). The extent of orthorhombic lipid phases in the stratum corneum determines the barrier efficiency of human skin in vivo. *J Invest Dermatol*. 130(2), 611-4.
31. Bouwstra, J. A., Gooris, G. S., Salomons-de Vries, M. A., van der Spek, J. A., Bras, W. (1992). Structure of human stratum corneum as a function of temperature and hydration: A wide-angle X-ray diffraction study. *Int J Pharm*. 84, 205-16.
32. Björklund, S., Nowacka, A., Bouwstra, J. A., Sparr, E., Topgaard, D. (2013). Characterization of Stratum Corneum Molecular Dynamics by Natural-Abundance 13C Solid-State NMR. *PLoS One*. 8(4), e61889.
33. Elias, P. M., Bonar, L., Grayson, S., Baden, H. P. (1983). X-ray diffraction analysis of stratum corneum membrane couplets. *J Invest Dermatol*. 80(3), 213-4.
34. Janssens, M., van Smeden, J., Gooris, G. S., Bras, W., Portale, G., Caspers, P. J., et al. (2012). Increase in short-chain ceramides correlates with an altered lipid organization and decreased barrier function in atopic eczema patients. *J Lipid Res*. 53(12), 2755-66.
35. Bhosle, M. J., Kulkarni, A., Feldman, S. R., Balkrishnan, R. (2006). Quality of life in patients with psoriasis. *Health Qual Life Outcomes*. 4, 35.
36. Blome, C., Radtke, M. A., Eissing, L., Augustin, M. (2016). Quality of Life in Patients with Atopic Dermatitis: Disease Burden, Measurement, and Treatment Benefit. *Am J Clin Dermatol*. 17(2), 163-9.
37. Raychaudhuri, S. P., Farber, E. M. (2001). The prevalence of psoriasis in the world. *J Eur Acad Dermatol Venereol*. 15(1), 16-7.
38. Yokose, U., Ishikawa, J., Morokuma, Y., Naoe, A., Inoue, Y., Yasuda, Y., et al. (2020). The ceramide [NP]/[NS] ratio in the stratum corneum is a potential marker for skin properties and epidermal differentiation. *BMC Dermatology*. 20(1).
39. Uchino, T., Kamiya, D., Yagi, H., Fujino-Shimaya, H., Hatta, I., Fujimori, S., et al. (2023). Comparative analysis of intercellular lipid organization and composition between psoriatic and healthy stratum corneum. *Chem Phys Lipids*. 254, 105305.
40. Ražnatović Djurović, M., Janković, J., Cirkovic, A., Tomic Spiric, V., Maksimovic, N., Sojevic Timotijevic, Z., et al. (2020). Quality of life in infants with atopic dermatitis and their families. *Advances in Dermatology and Allergology*. 37(1), 66-72.
41. Di Nardo, A., Wertz, P. W., Giannetti, A., Seidenari, S. (1998). Ceramide and Cholesterol Composition of the Skin of Patients with Atopic Dermatitis. *Acta Derm Venereol* 78, 27-30.
42. Elias, P. M., Steinhoff, M. (2008). "Outside-to-inside" (and now back to "outside") pathogenic mechanisms in atopic dermatitis. *J Invest Dermatol*. 128(5), 1067-70.
43. Werner, Y., Lindberg, M. (1985). Transepidermal Water Loss in Dry and Clinically Normal Skin in Patients with Atopic Dermatitis *Acta Derm Venereol*. 65, 102-5.
44. Imokawa, G., Abe, A., Jin, K., Higaki, Y., Kawashima, M., Hidano, A. (1991). Decreased level of ceramides in stratum corneum of atopic dermatitis: an etiologic factor in atopic dry skin? *J Invest Dermatol*. 96(4), 523-6.
45. Ishikawa, J., Narita, H., Kondo, N., Hotta, M., Takagi, Y., Masukawa, Y., et al. (2010). Changes in the Ceramide Profile of Atopic Dermatitis Patients. *J Invest Dermatol*. 130(10), 2511-4.

46. Boer, D. E. C., van Smeden, J., Al-Khakany, H., Melnik, E., van Dijk, R., Absalah, S., et al. (2020). Skin of atopic dermatitis patients shows disturbed beta-glucocerebrosidase and acid sphingomyelinase activity that relates to changes in stratum corneum lipid composition. *Biochim Biophys Acta Mol Cell Biol Lipids*. 1865(6), 158673.
47. Yamamoto, A., Serizawa, S., Ito, M., Sato, Y. (1991). Stratum corneum lipid abnormalities in atopic dermatitis. *Arch Dermatol Res*. 283, 219-23.
48. Bleck, O., Abeck, D., Ring, J., Hoppe, U., Vietzke, J. P., Wolber, R., et al. (1999). Two ceramide subfractions detectable in Cer(AS) position by HPTLC in skin surface lipids of non-lesional skin of atopic eczema. *J Invest Dermatol*. 113(6), 894-900.
49. van Smeden, J., Janssens, M., Gooris, G. S., Bouwstra, J. A. (2014). The important role of stratum corneum lipids for the cutaneous barrier function. *Biochim Biophys Acta*. 1841(3), 295-313.
50. Greene, S. L., Muller, S. A. (1985). Netherton's syndrome. Report of a case and review of the literature. *Journal of the American Academy of Dermatology*. 13(2), 329-37.
51. van Smeden, J., Janssens, M., Boiten, W. A., van Drongelen, V., Furio, L., Vreeken, R. J., et al. (2014). Intercellular skin barrier lipid composition and organization in Netherton syndrome patients. *J Invest Dermatol*. 134(5), 1238-45.
52. van Smeden, J., Al-Khakany, H., Wang, Y., Visscher, D., Stephens, N., Absalah, S., et al. (2020). Skin barrier lipid enzyme activity in Netherton patients is associated with protease activity and ceramide abnormalities. *J Lipid Res*. 61(6), 859-69.
53. Janssens, M., van Smeden, J., Gooris, G. S., Bras, W., Portale, G., Caspers, P. J., et al. (2011). Lamellar lipid organization and ceramide composition in the stratum corneum of patients with atopic eczema. *J Invest Dermatol*. 131(10), 2136-8.
54. Tawada, C., Kanoh, H., Nakamura, M., Mizutani, Y., Fujisawa, T., Banno, Y., et al. (2014). Interferon-γ Decreases Ceramides with Long-Chain Fatty Acids: Possible Involvement in Atopic Dermatitis and Psoriasis. *J Invest Dermatol*. 134(3), 712-8.
55. de Jager, M., Groenink, W., Bielsa i Guivernau, R., Andersson, E., Angelova, N., Ponec, M., et al. (2006). A novel in vitro percutaneous penetration model: evaluation of barrier properties with p-aminobenzoic acid and two of its derivatives. *Pharm Res*. 23(5), 951-60.
56. Groen, D., Gooris, G. S., Ponec, M., Bouwstra, J. A. (2008). Two new methods for preparing a unique stratum corneum substitute. *Biochim Biophys Acta*. 1778(10), 2421-9.
57. Basse, L. H., Groen, D., Bouwstra, J. A. (2013). Permeability and lipid organization of a novel psoriasis stratum corneum substitute. *Int J Pharm*. 457(1), 275-82.
58. Bouwstra, J., Gooris, G., Cheng, K., A., W., Bras, W., Ponec, M. (1996). Phase behavior of isolated skin lipids. *J Lipid Res*. 37, 999 - 1011.
59. McIntosh, T. J., Stewart, M. E., Downing, D. T. (1996). X-ray Diffraction Analysis of Isolated Skin Lipids: Reconstitution of Intercellular Lipid Domains. *Biochemistry*. 35(12), 3649-53.
60. Bouwstra, J. A., Gooris, G. S., Dubbelaar, F. E. R., Ponec, M. (2001). Phase behavior of lipid mixtures based on human ceramides: coexistence of crystalline and liquid phases. *J Lipid Res*. 42(11), 1759-70.
61. de Jager, M. W., Gooris, G. S., Ponec, M., Bouwstra, J. A. (2005). Lipid mixtures prepared with well-defined synthetic ceramides closely mimic the unique stratum corneum lipid phase behavior. *J Lipid Res*. 46(12), 2649-56.
62. Opalka, L., Kovacik, A., Maixner, J., Vavrova, K. (2016). Omega-O-Acylceramides in Skin Lipid Membranes: Effects of Concentration, Sphingoid Base, and Model Complexity on Microstructure and Permeability. *Langmuir*. 32(48), 12894-904.
63. Uche, L. E., Gooris, G. S., Bouwstra, J. A., Beddoes, C. M. (2019). Barrier Capability of Skin Lipid Models: Effect of Ceramides and Free Fatty Acid Composition. *Langmuir*. 35(47), 15376-88.
64. Opálka, L., Kováčik, A., Pullmannová, P., Maixner, J., Vávrová, K. (2020). Effects of omega-O-acylceramide structures and concentrations in healthy and diseased skin barrier lipid membrane models. *J Lipid Res*. 61(2), 219-28.
65. Janssens, M., Gooris, G. S., Bouwstra, J. A. (2009). Infrared spectroscopy studies of mixtures prepared with synthetic ceramides varying in head group architecture: coexistence of liquid and crystalline phases. *Biochim Biophys Acta*. 1788(3), 732-42.
66. Beddoes, C. M., Gooris, G. S., Bouwstra, J. A. (2018). Preferential arrangement of lipids in the long-periodicity phase of a stratum corneum matrix model. *J Lipid Res*. 59(12), 2329-38.

67. Oguri, M., Gooris, G. S., Bito, K., Bouwstra, J. A. (2014). The effect of the chain length distribution of free fatty acids on the mixing properties of stratum corneum model membranes. *Biochim Biophys Acta*. 1838(7), 1851-61.
68. Beddoes, C. M., Rensen, D. E., Gooris, G. S., Malfois, M., Bouwstra, J. A. (2021). The Importance of Free Fatty Chain Length on the Lipid Organization in the Long Periodicity Phase. *Int J Mol Sci*. 22(7).
69. Bouwstra, J. A., Gooris, G. S., Dubbelaar, F. E., Weerheim, A., IJzerman, A. P., Ponec, M. (1998). Role of ceramide 1 in the molecular organization of the stratum corneum lipids. *J Lipid Res*. 39, 186-96.
70. Mojumdar, E. H., Gooris, G. S., Barlow, D. J., Lawrence, M. J., Deme, B., Bouwstra, J. A. (2015). Skin lipids: localization of ceramide and fatty acid in the unit cell of the long periodicity phase. *Biophys J*. 108(11), 2670-9.
71. Gooris, G. S., Kamran, M., Kros, A., Moore, D. J., Bouwstra, J. A. (2018). Interactions of dipalmitoylphosphatidylcholine with ceramide-based mixtures. *Biochim Biophys Acta Biomembr*. 1860(6), 1272-81.
72. Uche, L. E., Gooris, G. S., Bouwstra, J. A., Beddoes, C. M. (2021). High concentration of the ester-linked omega-hydroxy ceramide increases the permeability in skin lipid model membranes. *Biochim Biophys Acta Biomembr*. 1863(1), 183487.
73. Skolova, B., Hudska, K., Pullmannova, P., Kovacik, A., Palat, K., Roh, J., et al. (2014). Different phase behavior and packing of ceramides with long (C16) and very long (C24) acyls in model membranes: infrared spectroscopy using deuterated lipids. *J Phys Chem B*. 118(35), 10460-70.
74. Skolova, B., Jandovska, K., Pullmannova, P., Tesar, O., Roh, J., Hrabalek, A., et al. (2014). The role of the trans double bond in skin barrier sphingolipids: permeability and infrared spectroscopic study of model ceramide and dihydroceramide membranes. *Langmuir*. 30(19), 5527-35.
75. Schroeter, A., Stahlberg, S., Skolova, B., Sonnenberger, S., Eichner, A., Huster, D., et al. (2017). Phase separation in ceramide[NP] containing lipid model membranes: neutron diffraction and solid-state NMR. *Soft Matter*. 13(10), 2107-19.
76. Skolova, B., Kovacik, A., Tesar, O., Opalka, L., Vavrova, K. (2017). Phytosphingosine, sphingosine and dihydrosphingosine ceramides in model skin lipid membranes: permeability and biophysics. *Biochim Biophys Acta Biomembr*. 1859(5), 824-34.
77. Kovacik, A., Pullmannova, P., Opalka, L., Silarova, M., Maixner, J., Vavrova, K. (2021). Effects of (R)- and (S)-alpha-Hydroxylation of Acyl Chains in Sphingosine, Dihydrosphingosine, and Phytosphingosine Ceramides on Phase Behavior and Permeability of Skin Lipid Models. *Int J Mol Sci*. 22(14).
78. Chen, H., Mendelsohn, R., Rerek, M. E., Moore, D. J. (2001). Effect of cholesterol on miscibility and phase behavior in binary mixtures with synthetic ceramide 2 and octadecanoic acid. Infrared studies. *Biochim Biophys Acta*. 1512, 345-56.
79. Schroeter, A., Kiselev, M. A., Hauss, T., Dante, S., Neubert, R. H. (2009). Evidence of free fatty acid interdigitation in stratum corneum model membranes based on ceramide [AP] by deuterium labelling. *Biochim Biophys Acta*. 1788(10), 2194-203.
80. Mojumdar, E. H., Gooris, G. S., Groen, D., Barlow, D. J., Lawrence, M. J., Deme, B., et al. (2016). Stratum corneum lipid matrix: Location of acyl ceramide and cholesterol in the unit cell of the long periodicity phase. *Biochim Biophys Acta*. 1858(8), 1926-34.
81. Paz Ramos, A., Gooris, G., Bouwstra, J., Lafleur, M. (2018). Evidence of hydrocarbon nanodrops in highly ordered stratum corneum model membranes. *J Lipid Res*. 59(1), 137-43.
82. Pham, Q. D., Mojumdar, E. H., Gooris, G. S., Bouwstra, J. A., Sparr, E., Topgaard, D. (2018). Solid and fluid segments within the same molecule of stratum corneum ceramide lipid. *Q Rev Biophys*. 51, e7.
83. Beddoes, C. M., Gooris, G. S., Foglia, F., Ahmadi, D., Barlow, D. J., Lawrence, M. J., et al. (2020). Arrangement of Ceramides in the Skin: Sphingosine Chains Localize at a Single Position in Stratum Corneum Lipid Matrix Models. *Langmuir*. 36(34), 10270-8.
84. Uchiyama, M., Oguri, M., Mojumdar, E. H., Gooris, G. S., Bouwstra, J. A. (2016). Free fatty acids chain length distribution affects the permeability of skin lipid model membranes. *Biochim Biophys Acta*. 1858(9), 2050-9.
85. Pullmannova, P., Pavlikova, L., Kovacik, A., Sochorova, M., Skolova, B., Slepicka, P., et al. (2017). Permeability and microstructure of model stratum corneum lipid membranes containing ceramides with long (C16) and very long (C24) acyl chains. *Biophys Chem*. 224, 20-31.

86. Uche, L. E., Gooris, G. S., Bouwstra, J. A., Beddoes, C. M. (2021). Increased Levels of Short-Chain Ceramides Modify the Lipid Organization and Reduce the Lipid Barrier of Skin Model Membranes. *Langmuir*. 37(31), 9478-89.
87. Mojumdar, E. H., Helder, R. W., Gooris, G. S., Bouwstra, J. A. (2014). Monounsaturated fatty acids reduce the barrier of stratum corneum lipid membranes by enhancing the formation of a hexagonal lateral packing. *Langmuir*. 30(22), 6534-43.



CHAPTER 2

Lesional skin of Seborrheic Dermatitis patients is characterized by skin barrier dysfunction and correlating alterations in the stratum corneum ceramide composition

Authors and affiliations:
Jannik Rousel[1,2], Andreea Nădăban[2], Mahdi Saghari[1,3], Lisa Pagan[1,3], Ahnjili Zhuparris[1,3,4], Bart Theelen[5], Tom Gambrah[1], Hein E.C. van der Wall[1], Rob J. Vreeken[6], Gary L. Feiss[7], Tessa Niemeyer-van der Kolk[1,3], Jacobus Burggraaf[1,2,3], Martijn B.A. van Doorn[1,8], Joke A. Bouwstra[2], Robert Rissmann[1,2,3]

[1]Centre for Human Drug Research, Leiden, The Netherlands
[2]Leiden Academic Centre for Drug Research, Leiden University, Leiden, The Netherlands
[3]Leiden University Medical Center, Leiden, The Netherlands
[4]Leiden Institute of Advanced Computer Science, Leiden University, Leiden, Netherlands
[5]Westerdijk Fungal Biodiversity Institute, Utrecht, The Netherlands
[6]Maastricht Multimodal Molecular Imaging Institute, Maastricht University, Maastricht, The Netherlands
[7]Cutanea Life Sciences, Wayne, Pennsylvania, USA
[8]Department of Dermatology, Erasmus Medical Centre, Rotterdam, The Netherlands

Adapted from: **Experimental Dermatology** (2024). 33(1): e14952

ABSTRACT

Background: Seborrheic dermatitis (SD) is a chronic inflammatory skin disease characterized by erythematous papulosquamous lesions in sebum rich areas such as the face and scalp. Its pathogenesis appears multifactorial with a disbalanced immune system, *Malassezia* driven microbial involvement and skin barrier perturbations. Microbial involvement has been well described in SD, but skin barrier involvement remains to be properly elucidated.

Objective: To establish whether barrier impairment is a critical factor of inflammation in SD alongside microbial dysbiosis.

Methods: A cross-sectional study was performed in 37 patients with mild-to-moderate facial SD. Their lesional and non-lesional skin was comprehensively and non-invasively assessed with standardized 2D-photography, optical coherence tomography (OCT), microbial profiling including *Malassezia* species identification, functional skin barrier assessments and ceramide profiling.

Results: Inflammation was established through significant increases in erythema, epidermal thickness, vascularization and superficial roughness in lesional skin compared to non-lesional skin. Lesional skin showed a perturbed skin barrier with an underlying skewed ceramide subclass composition, impaired chain elongation and increased chain unsaturation. Changes in ceramide composition correlated with barrier impairment indicating interdependency of the functional barrier and ceramide composition. Lesional skin showed significantly increased *Staphylococcus* and decreased *Cutibacterium* abundances but similar *Malassezia* abundances and mycobial composition compared to non-lesional skin. Principal component analysis highlighted barrier properties as main discriminating features.

Conclusions: SD is associated with skin barrier dysfunction and changes in the ceramide composition. No significant differences in the abundance of *Malassezia* were observed. Restoring the cutaneous barrier might be a valid therapeutic approach in the treatment of facial SD.

INTRODUCTION

Seborrheic dermatitis (SD) is an inflammatory, eczematous skin disease of the face and scalp with a multifactorial underlying pathophysiology. SD is characterized by the development of erythematous, scaly and itchy skin on seborrheic areas with high sebaceous gland activity such as the nasolabial folds, eyebrows and upper chest (supplemental Fig. S1) (1). The exact pathophysiology of SD remains unclear due to its multifactorial and complex aetiology. Three major interdependent driving factors of the aberrant immunological responses behind SD are I) individual susceptibility due to an imbalanced immune system leading to inflammation, II) cutaneous microbial dysbiosis with pronounced colonization by *Malassezia* species and III) a perturbed epidermal barrier(1,2).

While these three hallmarks all contribute towards the development of SD, much emphasis has been on the microbiome and especially the involvement of *Malassezia*. *Malassezia* is a commensal yeast which is regarded as a key pathogen due to its concurrence with lesional skin and the clinical response of SD to antifungals(3). It is hypothesized that the predilection of *Malassezia* for sebum-rich skin sites is due to its inability to perform *de novo* fatty acid synthesis, necessitating the processing of exogenous lipids which disturbs the epidermal barrier integrity and enables inflammation (4,5). While this provides rationale for why inflammation is limited to these areas, it has been shown that neither the amount of *Malassezia* (5,6) nor an increased level of sebum production (1,2,6) are strictly tied to the development of SD.

Due to the implication that external triggers such as *Malassezia* and its metabolites can penetrate the skin (7), the cutaneous barrier function itself has been proposed to be involved in SD pathogenesis (6). The epidermal barrier function is located in the stratum corneum which consists of layers of cornified cells embedded in a lipid matrix mainly composed of cholesterol, fatty acids and ceramides (8). Changes in the composition and consequently the lipid organization of this matrix directly impacts skin permeability (9,10). Barrier perturbations and simultaneous alterations of the lipid matrix composition, such as reduced chain length and changes in ceramide subclass composition, have been observed in other inflammatory skin diseases such as atopic dermatitis and psoriasis (11,12). This raised the question whether barrier repair can be exploited as a treatment option (13).

The apparent contribution of host immunity, the microbiome and cutaneous barrier to the development of SD warrants a multimodal assessment for phenotyping SD. In this study, we established cutaneous inflammation by clinical scoring complemented with imaging. We elucidated the bacterial and fungal composition as both are implicated in SD (14), with additional species-level profiling of *Malassezia*. Lastly, the cutaneous barrier function was characterized in-depth by trans-epidermal water loss (TEWL) measurements complemented with ceramide profiling using lipidomic analysis. This might yield new insights into how these modalities are implicated in disease.

METHODS

An extended version of the methods can be found in the supporting information.

Study design and population

The study was conducted at the Centre for Human Drug Research (Leiden, the Netherlands) from November 2018 to January 2020 following the Declaration of Helsinki principles after approval by the medical ethics committee Stichting Beoordeling Ethiek Biomedisch Onderzoek (Assen, the Netherlands). Patients gave written informed consent prior to participation in the study. The use of SD medication was prohibited prior to enrolment for a period of two weeks for topical treatments, including dandruff shampoos, three weeks for phototherapy and four weeks for systemic treatments. In total, 37 patient exhibiting mild-to-moderate SD defined by an Investigator's Global Assessment (IGA) score of 2 to 3 after verification by a dermatologist were included and assessments performed during a single visit. Due to the heterogeneous presentation of SD and the invasiveness of assessments, assessments are performed on different sites of the face as listed in supplemental table S1-3. See Supplementary Material for further details.

Clinical characteristics

Disease severity was scored using the Seborrheic Dermatitis and Severity Index (SDASI) adapted from Baysal, *et al.* (2004) (15), 5-point IGA and percentage affected body surface area (%BSA). Patient reported outcomes included the 0 – 100 Numeric Rating Scale (NRS) itch, 5-Domain Itch Questionnaire(16) and Dermatology Life Quality Index (DLQI) (17,18). See Supplementary Material for further details.

Standardized photography

Standardized two dimensional cross-polarized images of the face were taken using a VISIA-CR (Canfield Scientific, New Jersey, United States). Erythema Index calculations were performed based on a method by Yamamoto, *et al.* (2008) (19). See Supplementary Material for further details.

Optical Coherence Tomography

Lesional and non-lesional skin was imaged by Vivosight Dx optical coherence tomography (OCT) (Michelson Diagnostics, Kent, United Kingdom) and epidermal thickness, superficial roughness and average epidermal vascularization were determined. See Supplementary Material for further details.

Microbiome composition

Skin swabs were collected by rubbing the skin for 10 seconds. Swabs were extracted and 16s rRNA and internal transcribed spacer (ITS) sequencing was performed to determine the bacterial and fungal composition, respectively. After genus level classification,

microbes contributing <1% of the total were excluded and relative abundances determined. See Supplementary Material for further details.

Malassezia culturing

Agar plates with modified Dixon medium were pressed against the skin for 20 seconds and cultured for *Malassezia*. *Malassezia* species determination by matrix-assisted laser desorption ionization-time of flight mass spectrometry (MALDI-TOF MS) was performed on mycological isolates as described by Kolecka *et al.* (2014) (20). See Supplementary Material for further details.

Skin barrier integrity by trans-epidermal water loss

Subjects were allowed to acclimatize to controlled environmental conditions (humidity <60%, temperature 22±2 °C) in rested state for at least 15 minutes prior to measurements. TEWL was measured using an AquaFlux AF200 (Biox Systems Ltd., London, United Kingdom). See Supplementary Material for further details.

Skin barrier lipidomics

Stratum corneum was harvested with 4 polyphenylene sulfide tape (Nichiban, Tokyo, Japan) after applying pressure using a D500 D-squame Pressure Instrument (CuDerm Corporation, Dallas, TX, United States). Tapes were extracted and the ceramide fraction analyzed through a validated Liquid Chromatography-Mass Spectrometry (LC-MS) setup as described by Boiten *et al.* (2016) (21). Supplemental figure S2 lists the 12 most prevalent ceramide classes included in the analysis using the nomenclature by Motta *et al.* (1993) (22). Sebum levels were determined using a Sebumeter SM815 (Courage+Khazaka, Köln, Germany). See Supplementary Material for further details.

Statistical analysis

Data visualization and statistical testing was performed using Prism 9 (Graphpad Software, San Diego, California, United States). 2-way ANOVA, or a mixed effects model in the case of missing data points, was performed using Bonferroni's multiple comparison test in the case of multiple variables and paired t-test in the case of two variables. P-values are denoted as ns: $P>0.05$, *: $P\leq0.05$, **: $P\leq0.01$, ***: $P\leq0.001$. Integrative data graphing by principal component analysis (PCA) and min-max radar plotting has been performed through Python version 3.8.0 (Python Software Foundation, Wilmington, Delaware, United States). See Supplementary Material for further details.

RESULTS

In total, 37 patients were enrolled into the study. The patient population exhibited mild-to-moderate SD as shown by a SDASI score of 7.0 ± 4.3 and IGA score of ≤ 3 for 97% of all patients (Table 1). Patient reported disease burden was rated mild-to-moderate as evident from the DLQI (7.2±5.5/30; "moderate effect on patient's life"), average itch rating scale (23.6± 22.5/100) and 5-Domain itch scale rating (11.6± 3.2/25).

Table 1. Baseline demographics including clinical scoring and patient reported outcomes from the study population. The minimal and maximal values are indicated among their respective scores. BMI; Body Mass Index, SD; standard deviation.

Subjects (n)		37
Age (years)		37.8 ± 15.6
BMI (kg/m^2)		25.4 ± 3.4
Sex	Female	5 (13.5%)
	Male	32 (86.5%)
Race	Asian	1 (2.7%)
	Mixed (White, African)	1 (2.7%)
	Latino	1 (2.7%)
	White	34 (91.9%)
Fitzpatrick skin type	1	4 (10.8%)
	2	19 (51.4%)
	3	13 (35.1%)
	4	1 (2.7%)
	5	0 (0.0%)
	6	0 (0.0%)
Seborrheic Dermatitis Area and Severity index (0 – 45) (Mean ±SD)		7.0 ± 4.3
Investigator's Global Assessment	1 (almost clear)	4 (10.8%)
	2 (mild)	19 (51.4%)
	3 (moderate)	13 (35.1%)
	4 (severe)	1 (2.7%)
Affected body surface area (%) (Mean ±SD)		1.3 ± 0.7
Dermatology Life Quality Index (0 – 30) (Mean ±SD)		7.2 ± 5.5
Average Itch Numeric Rating scale (0 - 100) (Mean ±SD)		23.6 ± 22.5
5-Domain Itch Scale (5 - 25) (Mean ±SD)		11.6 ± 3.2

Inflammation

Apart from clinical scoring, hallmarks of inflammation were assessed using standardized 2D-photography and OCT. Lesional skin had a significantly higher erythema index compared to non-lesional skin (67.62 AU vs. 49.19 AU, P≤0.001, Fig. 1A). Despite high epidermal disorganization hampering the localization of the dermal-epidermal junction in multiple measurements, the epidermis of lesional skin was significantly thicker compared to non-lesional skin (0.15 mm vs. 0.10 mm, P≤0.001, Fig. 1B). Superficial roughness of the skin was significantly increased in lesional skin (0.013 AU vs 0.009 AU, P≤0.001, Fig. 1C). Higher superficial vascularization was observed in lesional skin compared to non-lesional skin at a shallow skin depth of 0.1 to 0.25 mm (P≤0.05-0.001, Fig. 1D) with no significant differences at greater depths. This culminates to an increased average vascularization between 0.1 to 0.25 mm of 0.079 in lesional skin compared to 0.058 in non-lesional skin (P≤0.001, supplemental Fig. S3).

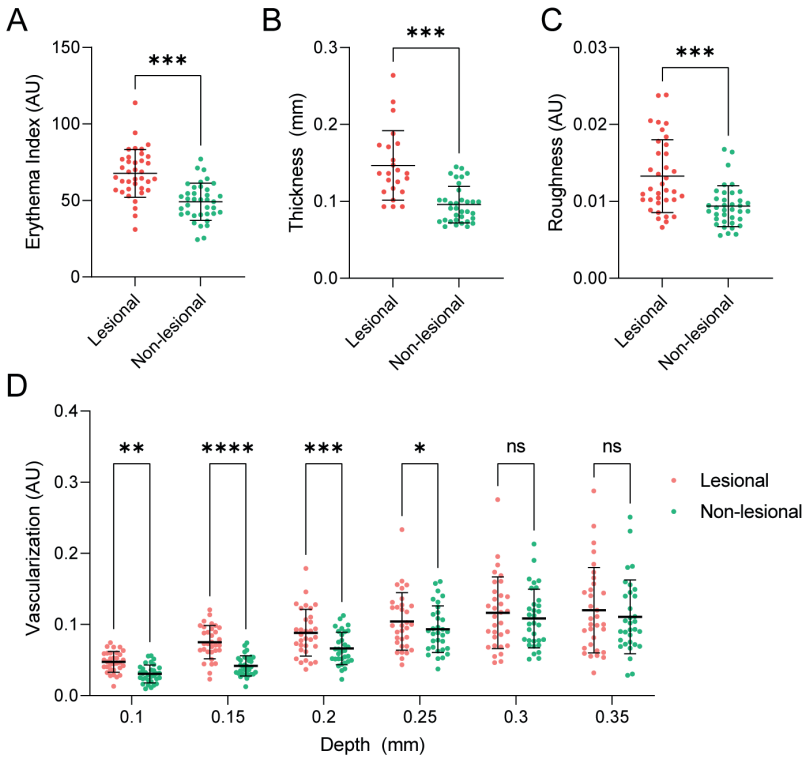


Figure 1. Erythema index as determined by standardized photography (A) and the epidermal thickness (B), superficial roughness (C) and the degree of vascularization at different depths in the epidermis (D) as determined by optical coherence tomography of lesional and non-lesional skin. Epidermal thickness could only be determined in 23 of 37 lesional and 34 of 37 non-lesional measurements. AU; Arbitrary Units, NS; not significant.

Microbiome

After establishing the presence of inflammation, the facial microbial composition was investigated using 16s rRNA and ITS sequencing for the bacterial and fungal microbiome, respectively.

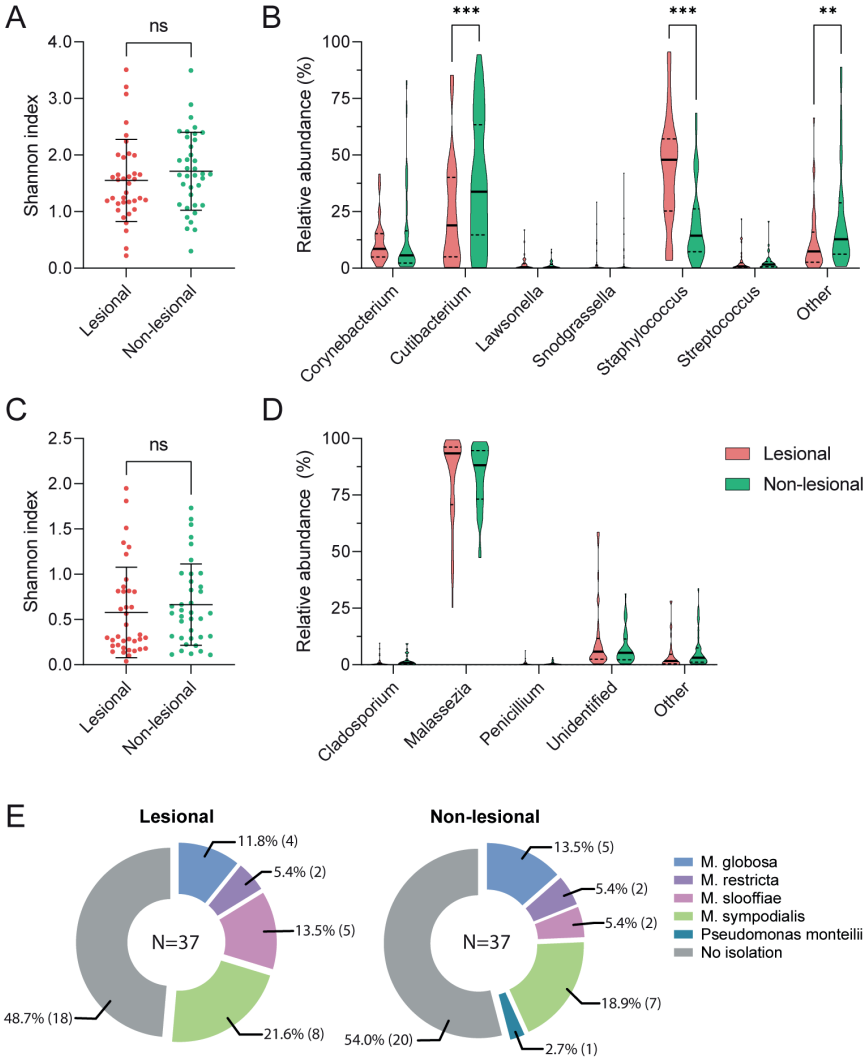


Figure 2. Bacterial Shannon diversity index (A) and composition of the bacterial microbiome (B) by 16s rRNA sequencing along with the fungal Shannon diversity index (C) and composition of the fungal microbiome (D) by ITS sequencing. The presented genera are filtered for minimal prevalence of 1% over all samples and presented relative to the total amount of microbes detected per analysis. Presence of different *Malassezia* species per site after isolation with contact plates and subsequent MALDI-TOF analysis (E). None of the samples yielded two or more different isolates.

Neither Shannon indexes showed a significant difference between lesional and non-lesional skin sites (1.55 vs 1.71, P>0.24 and 0.58 vs 0.66, P>0.23, for bacteria and fungi respectively, Fig. 2A, 2C), indicating biodiversity on average did not differ between skin sites. However, *Staphylococcus* was significantly overrepresented and *Cutibacterium* significantly underrepresented in lesional skin compared to non-lesional skin (44.05% vs 19.50% and 23.04% vs 38.20%, respectively, P≤0.001, Fig. 2B). The mycobiome proved small with only 3 genera present over the detection thresholds used (Fig. 2D), of which over 80% comprised of *Malassezia* hits in both lesional and non-lesional skin without any significant differences (82.20% vs. 83,52%, P>0.05). Due to the limitations associated with reliable identification of *Malassezia* at the species-level using ITS-sequencing, axenic culture plates were taken and subsequent MALDI-TOF MS was performed as a more specific qualitative alternative. Using *Malassezia* specific protocols successful isolation and identification of 16 from 37 lesional and 18 from 37 non-lesional samples was possible. No clear differences were observed between skin sites with *M. sympodialis* being the most prevalent at both sites (21.6% and 18.9% on lesional and non-lesional skin, respectively), followed by *M. slooffiae* (13.5%) on lesional and *M. globosa* (13.5%) on non-lesional skin (Fig. 2E).

Skin barrier

Finally, the skin barrier was studied as it represents the interface between external pathogens and the established epidermal inflammation. TEWL was used as an endpoint for skin barrier integrity and was significantly higher in lesional skin compared to non-lesional skin indicating an impaired barrier function (35.89 g/m^2/hr vs 21.27 g/m^2/hr, p>0.001, Fig. 3A). Sebum levels were not significantly different between lesional and non-lesional skin (90.70±54.93 vs 82.78±53.29, p=0.521, supplemental Fig. S4). The relative abundance was determined of all twelve major ceramide classes. The lesional ceramide profile showed a significant increase in Cer[NS] and Cer[AS] (17.25% vs 11.86% and 16.99% vs 10.61%, respectively, P≤0.001) and significantly decreased abundance of Cer[NdS], Cer[EOS] (7.15% vs 8.06% and 2.52% vs 3.51%, respectively, P≤0.01) and Cer[NP], Cer[NH], Cer[AP] (10.58% vs 14.29%, 10.87% vs 12.23%, 13.22% vs 16.03%, respectively, P≤0.001, Fig. 3B) compared to non-lesional skin. The abundance of other classes was not significantly different.

The skewing of ceramide subclass synthesis can be easily interpreted by comparing the abundance of Cer[NS] and Cer[NP]. Indeed, alterations in lipid processing were evident from a significant increase of the Cer[NS]:Cer[NP] ratio in lesional compared to non-lesional skin (1.68 vs 0.87, P≤0.001, Fig. 3C). Additionally, the presence of Cer[NSc34], a Cer[NS] species with a total chain length of 34 carbons, was significantly elevated in lesional compared to non-lesional skin (8.19% vs 5.10%, P≤0.001, Fig. 3D). Using the monounsaturation in Cer[NS] as an indicator for the overall monounsaturation, ceramides at lesional skin sites were further impacted by a higher degree of unsaturation compared

to non-lesional skin (7.32% vs 3.71%, P≤0.001, Fig. 3E). Lastly, lipid elongation was impaired in lesional skin as evident from a decreased average total carbon chain length of the ceramides compared to non-lesional skin (42.64 carbons vs 43.85 carbons, P≤0.001, Fig. 3F).

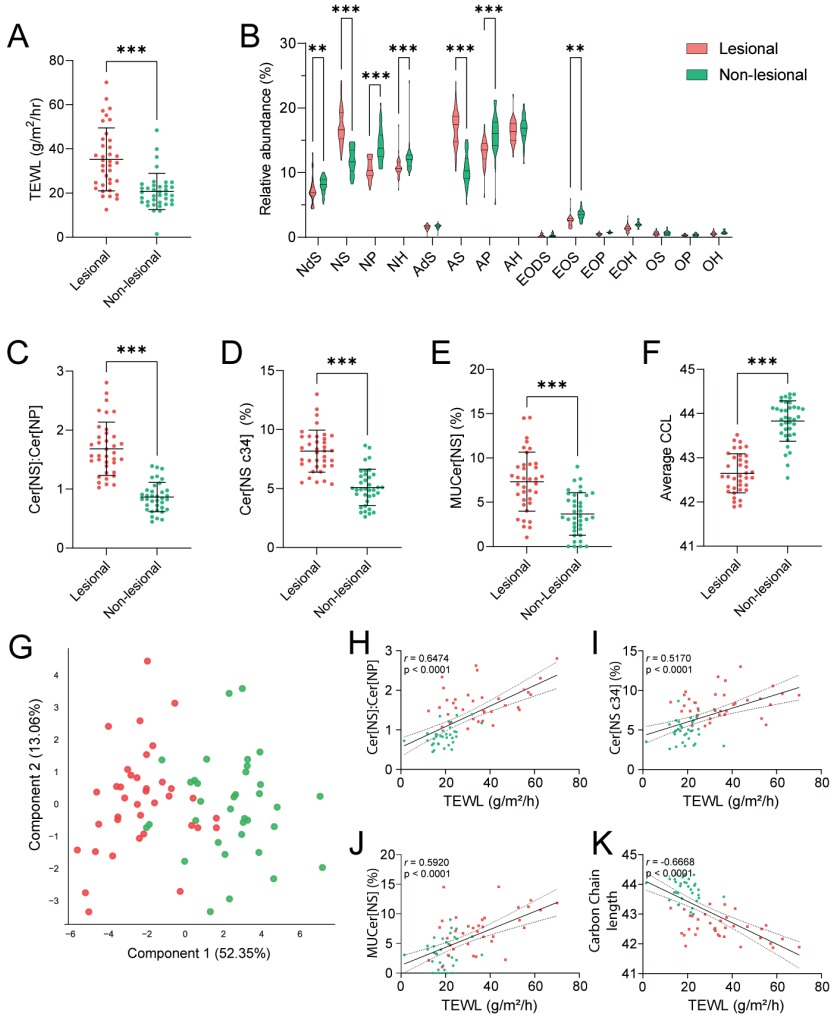


Figure 3. Barrier parameters of lesional compared to non-lesional skin demonstrate impaired barrier function in lesional skin. Functional barrier integrity is measured by trans-epidermal water loss (A). The ceramide profile is depicted after grouping individual ceramides per subclass (B), with the ratio between the abundance of Cer[NS] and Cer[NP] highlighted (C). The abundance of short ceramide species Cer[NSc34] (D) and degree of unsaturation (E) within Cer[NS] is shown. The average carbon chain length (CCL) of the combined sphingosine base and fatty acid tail within the non-Cer[EO] moiety is depicted (F). PCA analysis using all individual detected saturated ceramides yields two distinct population (G). Axes list the percentage of variance explained by the first two principal

components, with the proximity of datapoints indicating similarity between samples. Correlations between TEWL and Cer[NS]:Cer[NP] (H), percentage Cer[NSc34] (I), percentage of unsaturation (J) and CCL (K) are shown with a line representing the optimal fit from linear regression analysis and 95% confident interval and Pearson's correlation coefficient. TEWL; Trans-Epidermal Water Loss, MUCer; monounsaturated ceramide, CCL; carbon chain length, hr: hour.

Visualization of the roughly 300 individual ceramide responses using dimension reduction analysis by PCA showed two distinguishable populations when stratifying for skin site (Fig. 3G). This indicates the ceramide profile of lesional skin is alike between subjects, but differs from non-lesional skin. Plotting the TEWL values against ceramide parameters revealed a positive correlation for ceramide Cer[NS]:Cer[NP] ratio (*r*=0.6474), amount of Cer[NSc34] (*r*=0.5170) and degree of unsaturation (*r*=0.5920) and a negative correlation against the ceramide chain length (*r*=-0.6668) (Fig. 3H-K).

Integration of results

Integration of quantitative clinical characteristics (Fig. 1A, C, D), microbial properties (Fig. 2A-D) and barrier parameters (Fig. 3A-F) was performed using the entire dataset. The resulting PCA shows two distinguishable sets of data points with minimal overlap when stratifying for site (Fig. 4A). The abundance of Cer[NS], the carbon chain length and the Cer[NS]:Cer[NP] ratio contribute most to the overall differential analysis (supplemental table S4). Min-max normalized visualisation of the most significant findings in a radar chart underline that the biggest differences are observed in the barrier compartment followed by inflammation (Fig. 4B). Small differences between lesional and non-lesional skin were observed in the microbial parameters, with only the abundance of *Staphylococcus* being markedly different.

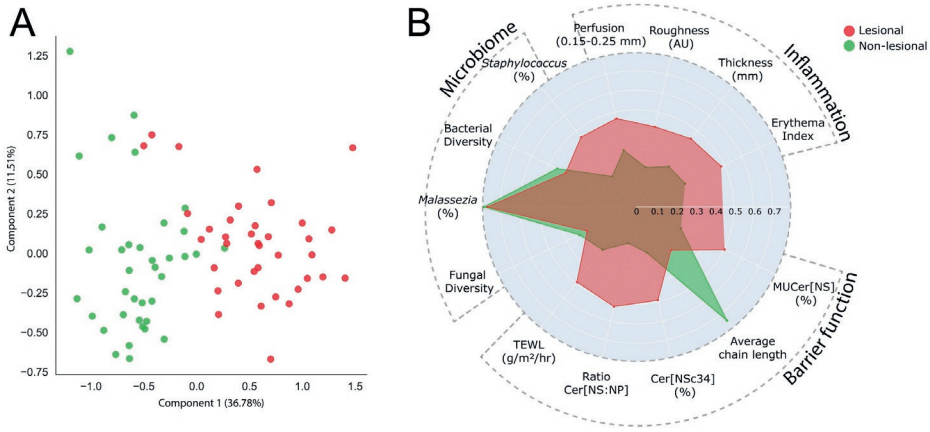


Figure 4. Principal component analysis (PCA) of lesional and non-lesional skin using all individual datapoints (A). Axes list the percentage of variance explained by the first two principal components. Integrative visualization of major contributors within the three different axes by radar chart (B). The

distance of a datapoint from the center represent the average value per parameter per site compared to the average value per parameter of both sites. AU; arbitrary units, TEWL; Trans-Epidermal Water Loss, MUCer; monounsaturated ceramide, CCL; carbon chain length, hr: hour

DISCUSSION

SD is a multifactorial disease in which the interplay between the cutaneous microbiome, especially the presence of *Malassezia*, impaired skin barrier function and abnormal immunological responses seem integral to its pathogenesis (1). In this study we comprehensively and non-invasively characterized the clinical representation of mild-to-moderate SD. We demonstrated a profound involvement of cutaneous barrier dysfunction with only small alterations in the microbiome, including the abundance of *Malassezia*, based on differences between lesional and non-lesional skin. This trial was performed in a sizeable number of 37 patients with similar disease burden after appropriate wash-outs and screening.

Inflammation objectively quantified by OCT and standardized imaging

Visual assessment of SD, which includes the evaluation of erythema, is frequently used in daily clinical practice for disease monitoring. However, visual examination of the skin can be hampered by limited sensitivity, observer bias and overall intra- and inter-rater variability (23,24). Therefore, we selected an objective approach to quantify cutaneous inflammation. Digitalized erythema assessments have been reported but not applied to SD (25–28). Here, standardized cross-polarized light photography is used to capture consistent images and enhanced erythema (29), resulting in a clear differentiation between lesional and non-lesional skin. Optical biopsies by OCT enabled the determination of additional (sub)cutaneous parameters. Inflammatory characteristics such as increased perfusion (30) and epidermal thickness, corresponding to acanthosis(31,32), were observed in lesional skin. Furthermore, a rougher lesional skin surface corresponds to the scaly phenotype of the disease (1). Increased blood flow and epidermal thickness have been observed by OCT in the involved skin of psoriasis and atopic dermatitis patients compared to uninvolved skin and healthy controls (33,34). Stand-alone, but also combined, standardized photography and OCT qualify as valuable non-invasive tools which enable sensitive and selective endpoints for disease monitoring and detection of treatment responses in clinical trials (35).

Malassezia and Staphylococcus dominate the lesional microbiome

Bacterial analysis of the skin surface showed an increased abundance of *Staphylococcus* and decreased abundance of *Cutibacterium* on lesional skin which concurs with previous SD profiling studies (14,36). *Staphylococcus*, and especially *S. aureus*, is considered to be a

pro-inflammatory mediator in atopic dermatitis(37). While limited phylogenetic resolution prevents the identification of *S. aureus* in this study, the observed increase of *Staphylococcus* combined with reports that *S. aureus* is more abundant in SD patients compared to healthy controls might indicate bacterial involvement in SD pathogenesis (38). Despite reports of bacterial involvement in SD, microbial involvement remains primarily focused on *Malassezia* as a key pathogen. However, no differences were observed between the abundance of *Malassezia* on lesional and non-lesional skin. This is in accordance with findings showing the presence of *Malassezia* is neither limited to lesional skin nor SD patients (3,6,14). Additionally, facial skin of healthy volunteers also showed a seemingly small and *Malassezia* dominated mycobiome (39,40). Although it is hypothesized that specific *Malassezia* species might be responsible for instigating inflammation as virulence factors differ between *Malassezia* species (41–43), no significant differences on species level were observed in this study. Culturing led to successful isolation of *Malassezia* species in approximately half of the subjects, illustrating the known challenges of isolating *Malassezia* from clinical samples (44). Except for *M. slooffiae*, all species are relatively frequently isolated from healthy and SD skin (45). Remarkably, *M. slooffiae* has been reported to have little virulence when directly compared to *M. globosa* and *M. sympodialis* (42). However, intra-species variation in virulence has been reported indicating that microbial activity rather than abundance is an important factor for the association of specific species to lesional skin (46,47). Based on these results, it seems too straightforward to attribute SD pathogenesis to the presence of *Malassezia* alone.

Substantial functional and compositional barrier alterations

Until now, the limited studies that have demonstrated functional barrier impairment in SD have neglected the lipid compartment as barrier component (48,49). In this study, we show a substantially impacted barrier in lesional skin on functional grounds by TEWL and demonstrate concomitant changes in the ceramide profile. These compositional changes correlated with the degree of barrier impairment as judged by TEWL. In line with our study in SD, changes in the Cer[NS]:Cer[NP] ratio(50), degree of unsaturation (51), ceramide chain length (12,52) and presence of extremely short chain Cer[NSc34] (12,51,53,54) in lesional skin have been observed in atopic dermatitis where barrier involvement is firmly established. These changes to the lipid profile appear to be induced by inflammation as lipid alterations can be evoked by atopic dermatitis and psoriasis associated pro-inflammatory cytokines *in vitro* (55–57) and normalize in response to anti-inflammatory treatment in atopic dermatitis patients (58). Whether these alterations are therefore primarily linked to inflammation and only coincide with barrier dysfunction has been investigated in mechanistic studies using lipid model systems. Lacking an inflammatory component, these models have shown that increased Cer[NS] (59,60), increased

unsaturation (61) and decreased lipid chain length (62) directly increase permeability. Additionally, studies in healthy volunteers have shown Cer[NS]:Cer[NP] ratios in the face comparable to non-lesional skin without a location-dependent effect on Cer[NSc34] abundances (63,64). It is of note that total ceramide levels can change with age and seasons as demonstrated in healthy skin and acne, but without much effect on the relative ceramide subclass composition as reported on in the current study (63,65,66). Additionally, the impact of these factors might be limited as patients serve as their own control. The predilection of SD lesions with areas known for increased water loss such as the mouth, eyelids and nasolabial folds might be confounding for the increased TEWL (49,67). Indeed, healthy volunteers have shown TEWL values at the nasolabial fold that approach the lesional values observed in this study with comparable TEWL values at the cheek or forehead, sites where non-lesional measurements were often conducted(68,69). Therefore, increased TEWL values in lesional skin may not reflect barrier impairment but rather indicate differences in normal physiological functioning between skin sites. However, the concurrent correlations between the TEWL values and ceramide composition reaffirm the interdependence of SD functional barrier impairment and ceramide-compositional alterations.

Integrative data analysis emphasizes importance of barrier dysfunction

An integrative approach was taken to visualize the data after investigating the three hallmarks of SD separately. Using PCA, we elucidated which parameters of our dataset predominantly contribute to the SD phenotype. The abundance of Cer[NS] and ceramide chain length showed to be the most important discriminating features. Indeed, the radar plot directs emphasis towards barrier function with little differences in the micro- and mycobiome. While the contribution of *Malassezia* seems to be negligible when only considering relative abundances, it should be re-emphasized that SD appears to be neither caused solely by barrier dysfunction nor microbial involvement but rather by the interplay between factors. This finding correlates with the shifting belief in literature that *Malassezia* might not be solely responsible for causing SD (5,6). This highlights the added value of a multimodal and integrative approach to disease profiling which enables in-depth characterization with the possibility to unravel part of pathogenesis (35).

CONCLUSION

In conclusion, this study demonstrates the importance of the barrier-inflammation axis in mild-to-moderate SD which seems to be more prominently involved compared to the microbiome. While not incorporating an internal healthy control group, our results are compared thoroughly with prior research in healthy volunteers through literature. Moreover, the results agree with and support existing literature regarding inflammation and microbial involvement in SD while complementing the current understanding of

barrier dysfunction in SD. Barrier impairment parallels that of atopic dermatitis where emollients are used effectively(70). Treating SD by improving the skin barrier function has been proposed as a potential adjuvant therapy(71), but the management of SD remains focused on anti-inflammatory and anti-fungal treatments(72). Taken together, the incorporation of emollients, humectants or other barrier repair agents should not be neglected in the management of SD and might support current treatment modalities.

REFERENCES

1. Borda, L.J., Wikramanayake, T.C. (2015). Seborrheic Dermatitis and Dandruff: A Comprehensive Review. *J Clin Investig Dermatol*. 3(2).
2. Goldenberg, G. (2013). Optimizing Treatment Approaches in Seborrheic Dermatitis. *J Clin Aesthet Dermatol*. 6(2):44.
3. del Rosso, J.Q., Kim, G.K. (2009). Seborrheic Dermatitis and Malassezia species: How Are They Related? *J Clin Aesthet Dermatol*. 2(11):14.
4. Juntachai, W., Oura, T., Murayama, S.Y., Kajiwara, S. (2009). The lipolytic enzymes activities of Malassezia species. *Med Mycol*. 47(5):477–84.
5. Adalsteinsson, J.A., Kaushik, S., Muzumdar, S., Guttman, E., Ungar, J. (2020). An update on the microbiology, immunology and genetics of seborrheic dermatitis. *Exp Dermatol*. 29(5):481–9.
6. Wikramanayake, T.C., Borda, L.J., Miteva, M., Paus, R. (2019). Seborrheic dermatitis—Looking beyond Malassezia. *Exp Dermatol*. 28(9):991–1001.
7. Goh, J.P.Z., Ruchti, F., Poh, S.E., Koh, W.L.C., Tan, K.Y., Lim, Y.T., et al. (2022). The human pathobiont Malassezia furfur secreted protease Mfsap1 regulates cell dispersal and exacerbates skin inflammation. *Proc. Natl. Acad. Sci.* 119(49):e2212533119.
8. Proksch, E., Brandner, J.M., Jensen, J.M. (2008). The skin: an indispensable barrier. *Exp Dermatol*. 17(12):1063–72.
9. Uche, L.E., Gooris, G.S., Bouwstra, J.A., Beddoes, C.M. (2021). High concentration of the ester-linked ω-hydroxy ceramide increases the permeability in skin lipid model membranes. *Biochimica et Biophysica Acta (BBA) – Biomembranes*. 1863(1):183487.
10. Beddoes, C.M., Gooris, G.S., Barlow, D.J., Lawrence, M.J., Dalgliesh, R.M., Malfois, M., et al. (2022). The importance of ceramide headgroup for lipid localisation in skin lipid models. *Biochimica et Biophysica Acta (BBA) - Biomembranes*. 1864(6):183886.
11. Ishikawa, J., Narita, H., Kondo, N., Hotta, M., Takagi, Y., Masukawa, Y., et al. (2010). Changes in the Ceramide Profile of Atopic Dermatitis Patients. *J. Invest. Dermatol*. 130(10):2511–4.
12. Janssens, M., van Smeden, J., Gooris, G.S., Bras, W., Portale, G., Caspers, P.J., et al. (2012). Increase in short-chain ceramides correlates with an altered lipid organization and decreased barrier function in atopic eczema patients. *J Lipid Res*. 53(12):2755–66.
13. Elias, P.M. (2022). Optimizing emollient therapy for skin barrier repair in atopic dermatitis.*Annals of Allergy, Asthma & Immunology*. 128(5):505–11.
14. Tao, R., Li, R., Wang, R. (2021). Skin microbiome alterations in seborrheic dermatitis and dandruff: A systematic review. *Exp Dermatol*. 30(10):1546–53.
15. Baysal, V., Yildirim, M., Ozcanli, C., Ceyhan, A.M. (2004). Itraconazole in the treatment of seborrheic dermatitis: a new treatment modality. *Int J Dermatol*. 43(1):63–6.
16. Elman, S., Hynan, L.S., Gabriel, V., Mayo, M.J. (2010). The 5-D itch scale: a new measure of pruritus. *Br J Dermatol*. 162(3):587–93.
17. Finlay, A.Y., Khan, G.K. (1994). Dermatology Life Quality Index (DLQI)—a simple practical measure for routine clinical use. *Clin Exp Dermatol*. 19(3):210–6.
18. Basra, M.K.A., Fenech, R., Gatt, R.M., Salek, M.S., Finlay, A.Y. (2008). The Dermatology Life Quality Index 1994–2007: a comprehensive review of validation data and clinical results. *Br J Dermatol*. 159(5):997–1035.
19. Yamamoto, T., Takiwaki, H., Arase, S., Ohshima, H. (2008). Derivation and clinical application of special imaging by means of digital cameras and Image J freeware for quantification of erythema and pigmentation. *Skin Res Technol*. 14(1):26–34.
20. Kolecka, A., Khayhan, K., Arabatzis, M., Velegraki, A., Kostrzewa, M., Andersson, A., et al. (2014). Efficient identification of Malassezia yeasts by matrix-assisted laser desorption ionization-time of flight mass spectrometry (MALDI-TOF MS). *Br J Dermatol*. 170(2):332–41.
21. Boiten, W., Absalah, S., Vreeken, R., Bouwstra, J., van Smeden, J. (2016). Quantitative analysis of ceramides using a novel lipidomics approach with three dimensional response modelling. *Biochimica et Biophysica Acta (BBA) - Molecular and Cell Biology of Lipids*. 1861(11):1652–61.
22. Motta, S., Monti, M., Sesana, S., Caputo, R., Carelli, S., Ghidoni, R. (1993). Ceramide composition of the psoriatic scale. *Biochim Biophys Acta*. 1182(2):147–51.

23. Poon, T.S.C., Kuchel, J.M., Badruddin, A., Halliday, G.M., Barnetson, R.StC., Iwaki, H., et al. (2003). Objective Measurement of Minimal Erythema and Melanogenic Doses Using Natural and Solar-simulated Light. *Photochem Photobiol*. 78(4):331–6.
24. Ten Voorde, W., Saghari, M., Boltjes, J., Marieke, |, De Kam, L., Zhuparris, A., et al. (2023). A multimodal, comprehensive characterization of a cutaneous wound model in healthy volunteers. *Exp Dermatol*. 00:1–14.
25. Logger, J.G.M., de Jong, E.M.G.J., Driessen, R.J.B., van Erp, P.E.J. (2020). Evaluation of a simple image-based tool to quantify facial erythema in rosacea during treatment. *Skin Res Technol*. 26(6):804–12.
26. Ohshima, H., Takiwaki, H., Washizaki, K., Ishiko, A., Itoh, M., Kanto, H. (2011). Quantitative evaluation of patch test reactions: a comparison between visual grading and erythema index image analysis. *Skin Res Technol*. 17(2):220–5.
27. Tao, M., Li, M., Zhang, Y., Liu, Y., Jiang, P., Liu, Y., et al. (2023). Objectively quantifying facial erythema in rosacea aided by the ImageJ analysis of VISIA red images. *Skin Res Technol*. 29(1):e13241.
28. Frew, J., Penzi, L., Suarez-Farinas, M., Garcet, S., Brunner, P.M., Czarnowicki, T., et al. (2021). The erythema Q-score, an imaging biomarker for redness in skin inflammation. *Exp Dermatol*. 30(3):377.
29. Oh, Y., Markova, A., Noor, S.J., Rotemberg, V. (2022). Standardized clinical photography considerations in patients across skin tones. *Br J Dermatol*.. 186(2):352–4.
30. Rajabi-Estarabadi, A., Tsang, D.C., Nouri, K., Tosti, A. (2019). Evaluation of positive patch test reactions using optical coherence tomography: A pilot study. *Skin Res Technol*. 25(5):625–30.
31. Odorici, G., Losi, A., Ciardo, S., Pellacani, G., Conti, A. (2018). Non-invasive evaluation of Secukinumab efficacy in severe plaque psoriasis with confocal microscopy and optical coherence tomography: A case report. *Skin Res Technol*. 24(1):160–2.
32. Yélamos, O., Alejo, B., Ertekin, S.S., Villa-Crespo, L., Zamora-Barquero, S., Martinez, N., et al. (2021). Non-invasive clinical and microscopic evaluation of the response to treatment with clobetasol cream vs. calcipotriol/betamethasone dipropionate foam in mild to moderate plaque psoriasis: an investigator-initiated, phase IV, unicentric, open, randomized clinical trial. *J. Eur. Acad. Dermatol. Venereol.*. 35(1):143.
33. Byers, R.A., Maiti, R., Danby, S.G., Pang, E.J., Mitchell, B., Carré, M.J., et al. (2018). Sub-clinical assessment of atopic dermatitis severity using angiographic optical coherence tomography. *Biomed Opt Express*. 9(4):2001.
34. Ha-Wissel, L., Yasak, H., Huber, R., Zillikens, D., Ludwig, R.J., Thaçi, D., et al. (2022). Case report: Optical coherence tomography for monitoring biologic therapy in psoriasis and atopic dermatitis. *Front Med (Lausanne)*. 9:2932.
35. Rissmann, R., Moerland, M., van Doorn, M.B.A. (2020). Blueprint for mechanistic, data-rich early phase clinical pharmacology studies in dermatology. *Br J Clin Pharmacol*. 86(6):1011.
36. Sanders, M.G.H., Nijsten, T., Verlouw, J., Kraaij, R., Pardo, L.M. (2021). Composition of cutaneous bacterial microbiome in seborrheic dermatitis patients: A cross-sectional study. *PLoS One*. 16(5):e0251136.
37. Geoghegan, J.A., Irvine, A.D., Foster, T.J. (2018). Staphylococcus aureus and Atopic Dermatitis: A Complex and Evolving Relationship. *Trends Microbiol*. 26(6):484–97.
38. Tamer, F., Yuksel, M., Sarifakioglu, E., Karabag, Y. (2018). Staphylococcus aureus is the most common bacterial agent of the skin flora of patients with seborrheic dermatitis. *Dermatol Pract Concept*. 8(2):80–4.
39. Findley, K., Oh, J., Yang, J., Conlan, S., Deming, C., Meyer, J.A., et al. (2013). Topographic diversity of fungal and bacterial communities in human skin. *Nature.* 498(7454):367–70.
40. Tao, R., Li, R., Wang, R., Tao, R., Li, R., Wang, R. (2023). Comparative analysis of the facial microbiome between rosacea and seborrheic dermatitis. *Indian J Dermatol Venereol Leprol*. 0(0):1–3.
41. Grice, E.A., Dawson, T.L. (2017). Host–microbe interactions: Malassezia and human skin. *Curr Opin Microbiol*. 40:81–7.
42. Angiolella, L., Rojas, F., Mussin, J., Greco, R., Sosa, M.D.L.A., Zalazar, L., et al. (2020). Biofilm formation, adherence, and hydrophobicity of M. sympodialis, M. globosa, and M. slooffiae from

clinical isolates and normal skin virulence factors of M. sympodialis, M. globosa and M. slooffiae. *Med Mycol*. 58(8):1162–8.
43. Theelen, B., Cafarchia, C., Gaitanis, G., Bassukas, I.D., Boekhout, T., Dawson, T.L. (2018). Malassezia ecology, pathophysiology, and treatment. *Med Mycol*. 56(suppl_1):S10–25.
44. Abdillah, A., Ranque, S. (2021). MalaSelect: A Selective Culture Medium for Malassezia Species. *Journal of Fungi*. 7(10).
45. Prohic, A., Jovovic Sadikovic, T., Krupalija-Fazlic, M., Kuskunovic-Vlahovljak, S. (2016). Malassezia species in healthy skin and in dermatological conditions. *Int J Dermatol*. 55(5):494–504.
46. Angiolella, L., Leone, C., Rojas, F., Mussin, J., Angeles Sosa, M. de los, Giusiano, G. (2018). Biofilm, adherence, and hydrophobicity as virulence factors in Malassezia furfur. *Med Mycol*. 56(1):110–6.
47. Chebil, W., Rhimi, W., Haouas, N., Romano, V., Belgacem, S., Belhadj Ali, H., et al. (2022). Virulence factors of Malassezia strains isolated from pityriasis versicolor patients and healthy individuals. *Med Mycol*. 60(8):60.
48. Tollesson, A., Frithz, A. (1993). Transepidermal water loss and water content in the stratum corneum in infantile seborrhoeic dermatitis. *Acta Derm Venereol*. 73(1):18–20.
49. Suchonwanit, P., Triyangkulsri, K., Ploydaeng, M., Leerunyakul, K. (2019). Assessing Biophysical and Physiological Profiles of Scalp Seborrheic Dermatitis in the Thai Population. *Biomed Res Int*. .
50. Yokose, U., Ishikawa, J., Morokuma, Y., Naoe, A., Inoue, Y., Yasuda, Y., et al. (2020). The ceramide [NP]/[NS] ratio in the stratum corneum is a potential marker for skin properties and epidermal differentiation. *BMC Dermatol*. 20(1).
51. Danso, M., Boiten, W., van Drongelen, V., Gmelig Meijling, K., Gooris, G., el Ghalbzouri, A., et al. (2017). Altered expression of epidermal lipid bio-synthesis enzymes in atopic dermatitis skin is accompanied by changes in stratum corneum lipid composition. *J Dermatol Sci*. 88(1):57–66.
52. Berdyshev, E., Goleva, E., Bissonnette, R., Bronova, I., Bronoff, A.S., Richers, B.N., et al. (2022). Dupilumab significantly improves skin barrier function in patients with moderate-to-severe atopic dermatitis. *Allergy*. 77(11):3388–97.
53. Ito, S., Ishikawa, J., Naoe, A., Yoshida, H., Hachiya, A., Fujimura, T., et al. (2017). Ceramide synthase 4 is highly expressed in involved skin of patients with atopic dermatitis. *J Eur Acad Dermatol Venereol*. 31(1):135–41.
54. Kim, B.K., Shon, J.C., Seo, H.S., Liu, K.H., Lee, J.W., Ahn, S.K., et al. (2022). Decrease of ceramides with long-chain fatty acids in psoriasis: Possible inhibitory effect of interferon gamma on chain elongation. *Exp Dermatol*. 31(2):122–32.
55. Danso, M.O., van Drongelen, V., Mulder, A., van Esch, J., Scott, H., van Smeden, J., et al. (2014). TNF-α and Th2 cytokines induce atopic dermatitis-like features on epidermal differentiation proteins and stratum corneum lipids in human skin equivalents. *J Invest Dermatol*. 134(7):1941–50.
56. Tawada, C., Kanoh, H., Nakamura, M., Mizutani, Y., Fujisawa, T., Banno, Y., et al. (2014). Interferon-γ Decreases Ceramides with Long-Chain Fatty Acids: Possible Involvement in Atopic Dermatitis and Psoriasis. *J Invest Dermatol*.. 134(3):712–8.
57. Berdyshev, E., Goleva, E., Bronova, I., Dyjack, N., Rios, C., Jung, J., et al. (2018). Lipid abnormalities in atopic skin are driven by type 2 cytokines. *JCI Insight*. 3(4).
58. Berdyshev, E., Goleva, E., Bissonnette, R., Bronova, I., Bronoff, A.S., Richers, B.N., et al. (2022). Dupilumab significantly improves skin barrier function in patients with moderate-to-severe atopic dermatitis. *Allergy*. 77(11):3388–97.
59. Uche, L.E., Gooris, G.S., Bouwstra, J.A., Beddoes, C.M. (2019). Barrier Capability of Skin Lipid Models: Effect of Ceramides and Free Fatty Acid Composition. *Langmuir*. 35(47):15376–88.
60. Nădăban, A., Rousel, J., El Yachioui, D., Gooris, G.S., Beddoes, C.M., Dalgliesh, R.M., et al. (2023). The effect of sphingosine and phytosphingosine ceramide ratio on lipid arrangement and barrier functionality in skin lipid models. *J Lipid Res*. 64(8):100400
61. Mojumdar, E.H., Helder, R.W.J., Gooris, G.S., Bouwstra, J.A. (2014). Monounsaturated fatty acids reduce the barrier of stratum corneum lipid membranes by enhancing the formation of a hexagonal lateral packing. *Langmuir*. 30(22):6534–43.
62. Uche, L.E., Gooris, G.S., Bouwstra, J.A., Beddoes, C.M. (2021). Increased Levels of Short-Chain Ceramides Modify the Lipid Organization and Reduce the Lipid Barrier of Skin Model Membranes. *Langmuir*. 37(31):9478–89.

63. Ishikawa, J., Shimotoyodome, Y., Ito, S., Miyauchi, Y., Fujimura, T., Kitahara, T., et al. (2013). Variations in the ceramide profile in different seasons and regions of the body contribute to stratum corneum functions. *Arch Dermatol Res*. 305(2):151–62.
64. Mori, S., Shiraishi, A., Epplen, K., Butcher, D., Murase, D., Yasuda, Y., et al. (2017). Characterization of skin function associated with obesity and specific correlation to local/systemic parameters in American women. *Lipids Health Dis*. 16(1).
65. Rogers, J., Harding, C., Mayo, A., Banks, J., Rawlings, A. (1996). Stratum corneum lipids: the effect of ageing and the seasons. *Arch Dermatol Res*. 288(12):765–70.
66. Pappas, A., Kendall, A.C., Brownbridge, L.C., Batchvarova, N., Nicolaou, A. (2018). Seasonal changes in epidermal ceramides are linked to impaired barrier function in acne patients. *Exp Dermatol*. 27(8):833–6.
67. Voegeli, R., Gierschendorf, J., Summers, B., Rawlings, A. v. (2019). Facial skin mapping: from single point bio-instrumental evaluation to continuous visualization of skin hydration, barrier function, skin surface pH, and sebum in different ethnic skin types. *Int J Cosmet Sci*. 41(5):411–24.
68. Kobayashi, H., Tagami, H. (2004). Distinct locational differences observable in biophysical functions of the facial skin: with special emphasis on the poor functional properties of the stratum corneum of the perioral region. *Int J Cosmet Sci*. 26(2):91–101.
69. Voegeli, R., Rawlings, A. V., Seroul, P., Summers, B. (2015). A novel continuous colour mapping approach for visualization of facial skin hydration and transepidermal water loss for four ethnic groups. *Int J Cosmet Sci*. 37(6):595–605.
70. van Zuuren, E.J., Fedorowicz, Z., Christensen, R., Lavrijsen, A., Arents, B.W.M. (2017). Emollients and moisturisers for eczema. *Cochrane Database Syst Rev*. 2017(2).
71. Mangion, S.E., Mackenzie, L., Roberts, M.S., Holmes, A.M. (2023). Seborrheic dermatitis: topical therapeutics and formulation design. *Eur. J. Pharm. Biopharm.* 185:148–64.
72. Desai, S., McCormick, E., Friedman, A. (2022). An Up-to-Date Approach to the Management of Seborrheic Dermatitis. *J Drugs Dermatol*. 21(12):1373–4.

SUPPLEMENTAL INFORMATION

EXTENDED MATERIAL AND METHODS

Study design and population

This was a cross-sectional study which consisted of one screening and one visit. The study was conducted at the facilities of the Centre for Human Drug Research (Leiden, the Netherlands). Between November 2018 and December 2019, a total of 115 persons were screened for eligibility with the study in- and exclusion criteria. Inclusion criteria included being 18 years or older, SD scored with an Investigators Global Assessment of 2 or 3 with sufficient surface area for all assessments, confirmation of SD by a dermatologist and willingness to refrain from any SD treatments during study participation. Exclusion criteria included the presence of any current or recurrent clinically significant (skin) condition other than SD, recent excessive sun exposure, adapting a different washing routing 1 week prior to screening and the use of SD topical treatments and dandruff shampoo 2 weeks, phototherapy 3 weeks and systemic treatments 4 weeks prior to enrolment. In total, 37 patients were included after successfully passing the screening. All 37 included subjects underwent the visit as planned within 28 days of screening. No formal power calculations were performed to determine group size because of the exploratory nature of the study. Patients were instructed not to wash their face 12 hours preceding the study visit. Non-lesional was defined as an area of skin without any clinical characteristics of SD and was similarly located on the face. Different areas for measurements were chosen on a per-subject basis depending on the availability of sufficient lesional skin and the disqualification of areas due to invasive measurements. These areas have been listed in the supplementary table 2 and 3.

Clinical characteristics

Clinical assessments were performed by trained physicians. The Seborrheic Dermatitis and Severity Index (SDASI) was adapted from Baysal, et al. (2004) (1) to include only the facial extent of SD. Additionally, a 5-point IGA and an estimation of the percentage of affected body surface area (%BSA) were performed. Patient reported outcomes included the average amount of itch experienced by a 0 – 100 Numeric Rating Scale (NRS) itch, the 5-Domain Itch Questionnaire (2) as well as impact of SD on general life by the Dermatology Life Quality Index (DLQI) (3,4). Facial Seborrheic Dermatitis Area and Severity Index (SDASI): Erythema, scaling and papules are scores 0 – 4 with; 0 = none, 1 = mild, 2 = moderate, 3 = severe. The area of involvement is estimated as the fraction of the face with lesional skin and is scored by: 1 = less than 10%, 2 = 11 – 30%, 3 = 31 – 50%, 4 = 51 – 70 and 5 = more than 70%. Erythema, scaling and papule scores are then summed and multiplied by the area score. The scoring is based on the SDASI by Baysal et al. (2004) (1).

Investigator's Global Assessment (IGA): The IGA is a general 5-point scale in which the severity of disease is scored with 0 = clear, 1 = almost clear, 2 = mild, 3 = moderate and 4 = severe. Percentage body surface area affected (%BSA): The area of involvement is estimated using the hand palm method where the surface of a patient's hand equals 1% of the total body surface area.

Standardized photography

Standardized 2D cross-polarized images of the face were taken using a VISIA-CR (Canfield Scientific, New Jersey, United States). Erythema Index calculations were performed based on a method by Yamamoto, et al. (2008) (5). In short, obtained Red Green Blue (RGB) images were split and the R and G channels log transformed using ImageJ (version 1.51h) (6). After subtraction of the R channel with the G channel, brightness was increased by 3 and the mean grey value within a predefined region of interest of 500000 pixels was determined for a lesional and non-lesional area.

Optical Coherence Tomography

Lesional and non-lesional skin was imaged with a Vivosight Dx OCT (Michelson Diagnostics, Kent, United Kingdom). The epidermal thickness, superficial roughness and average epidermal perfusion depth was determined from the resulting scans using the proprietary VivoTools 4.12 software. Individual perfusion-over-depth curves were reviewed and excluded if high superficial levels of perfusion were observed, indicating an invalid measurement in 4 lesional and 4 non-lesional measurements. Epidermal thickness could only be determined in 23 of 37 lesional and 34 of 37 non-lesional measurements because of pronounced epidermal disorganization resulting in troublesome localization of the dermal-epidermal junction.

Microbial analysis by sequencing

Sterile 0.9% NaCl soaked skin swabs (Puritan Sterile Polyester Tipped Applicators, Puritan, Guilford, Maine, United States) were collected by rubbing over a lesional or non-lesional site for 10 seconds while rotating the swab and subsequently stored in DNA/RNA shield lysis buffer and beat beads (Zymo Research, Irvine, California, Unites States) at -80 °C. Swabs were transferred to Baseclear B.V. (Leiden, the Netherlands) for extraction and subsequent sequencing. DNA was extracted using a ZymoBIOMICS DNA Miniprep Kit (Zymo Research) according to manufacturer's instructions. Next-Generation Sequencing for the bacterial and fungal composition was performed using amplification of 16S rRNA region V3-V4 and Internal transcribed spacer region 2 (ITS2), respectively. An Illumina NovaSeq 6000 or MiSeq system was used to generate single- or pair-end sequence reads. FASTQ read sequence files were generated using bcl2fastq2 version 2.18. Primary quality was assessed using the Illumina Chastity filtering and reads containing a PhiX control

signal removed. Quality was finally assessed using the FASTQC quality control tool version 0.11.5. USEARCH version 9.2(7) was used to create pseudoreads and classification of these reads performed based on the alignment with SNAP version 1.0.23 (8) against the RDP database for bacterial (9) and UNITE ITS gene database for fungal classification (10). The resulting list of Operational Taxonomic Units per sample was filtered to genus level and the detected genera included in analysis if it exceeded 1% of the total composition within a sample. Data was presented in the Genome Explorer database (Baseclear B.V., Leiden, the Netherlands) and further processed in Python version 3.8.0 (Python Software Foundation, Wilmington, Delaware, United States) in which microbes contributing <1% of the total were excluded after which their relative abundance at the genus level was determined.

Malassezia culturing

9 cm diameter Agar plates with modified Dixon medium (Mediaproducts B.V., Groningen, the Netherlands) were pressed against a lesional and non-lesional site for 20 seconds. Plates were cultured at 33 °C for up to 21 days at the Microbiology department of the Alrijne Hospital (Leiden, the Netherlands). A sample from each colony forming unit was isolated after positive identification for bacterial or fungal growth through light microscopy. Mycological isolates were transported to the Westerdijk Fungal Biodiversity Institute (Utrecht, the Netherlands) for Malassezia species determination by matrix-assisted laser desorption ionization-time of flight mass spectrometry (MALDI-TOF MS) as described by Kolecka et al. (2014) (11).

Skin barrier integrity by trans-epidermal water loss

Subjects were allowed to acclimatize to controlled environmental conditions (humidity <60%, temperature 22±2 °C) in rested state for at least 15 minutes prior to measurements. An AquaFlux AF200 (Biox Systems Ltd., London, United Kingdom) was used to measure the TEWL of lesional and non-lesional skin. Baseline calibration was performed and TEWL was measured for up to 200 seconds or until a steady state was reached.

Tape stripping procedure

Stratum corneum was harvested by pressing polyphenylene sulfide tape (Nichiban, Tokyo, Japan) to the skin with a D500 D-squame Pressure Instrument (CuDerm Corporation, Dallas, TX, United States) and exerting pressure 5 times. Tapes were transferred to a cutting board with the glue side up. 16 mm diameter holes were punched within the region that was pressed against the skin. The individual punched out tape samples were stored in 20 ml vials with 1.5 ml of chloroform:methanol (2:1) at -20 °C before extraction.

Ceramide analysis by liquid chromatography-mass spectrometry

HPLC grade chloroform (Honeywell, Charlotte, North Carolina, United States), UPLC grade Methanol (Biosolve, Valkenswaard, the Netherlands), UPLC grade heptane (LiChorSolv, Merck, Darmstadt, Germany), UPLC grade isopropyl alcohol (Biosolve, Valkenswaard, the Netherlands), UPLC grade ethanol (Biosolve, Valkenswaard, the Netherlands), reagent grade potassium chloride (Sigma Aldrich, Saint-Louis, Missouri, USA) and ultrapure water from a Milli-Q Advantage A10 system (Merck, Darmstadt, Germany) were used. Synthetic ceramides and deuterated standards were purchased from Avanti Polar Lipids (Alabaster, Alabama, United States) or kindly provided by Evonik (Essen, Germany).

Extraction of tape strips and analysis of the ceramide profile was performed as described Boiten et al. (2016) (12). In short, individual tape samples were stored in 1.5 ml of chloroform:methanol (2:1) in a 20 ml glass vial and stored at -20 °C before analysis. Tapes were extracted by shaking the tape samples in an IKA S4000 rotary shaker at 120 rounds per minute at 40 °C for one hour. Solvent was isolated and shaking repeated three times with 1 ml of different solvent mixtures; chloroform:methanol:water (1:2:0.5), chloroform:methanol (1:1) and heptane:isopropylalcohol (1:1). Solvent was isolated each time and pooled with the previous collected organic solvent. 4 ml of 0.25M KCl was added to the pooled solvent and phase separation achieved overnight. The organic layer was isolated and washed with the addition of 4 ml chloroform. The isolated organic layer was combined with the washing solvent and filtered through 0.45 µm PVDF syringe filters (Grace, Deerfield IL, USA). Samples were transferred to 1.5 ml HPLC vials and reconstituted in 750 µl chloroform:methanol (2:1). 225 µl of this stock was transferred to a separate HPLC vial, dried, and reconstituted in 60 µl heptane:chloroform:methanol (95:2.5:2.5) containing 10 µM CER[N(24deu)S(18)] for analysis by UPLC-MS. Separation was achieved by a 5 µl injection using an Acquity UPLC H-class (Waters, Milford, MA, USA) and a normal phase PVA-silica column (5 µm particles, 100 × 2.1 mm i.d.) (YMC, Kyoto, Japan) over a gradient from 98% heptane and 2% heptene:isopropylalcohol:ethanol (2:1:1) to 50% heptane and 50% heptene:isopropylalcohol:ethanol (2:1:1) at a flow rate of 0.8 ml/min. Detection was performed using atmospheric pressure chemical ionization (APCI) on a XEVO TQ-S mass spectrometer (Waters, Milford, MA, USA) in positive ion mode scanning from 350 to 1200 m/z. Quality control samples from combined stratum corneum extracts and standard calibration curves containing 50, 20, 10, 5, 2, 1, 0.5, 0 µM of several ceramides (Cer[NS, NdS, NP, AS, EOS and EOP] in triplicate were added to the run. Responses of 2 out of 64 samples were below the limit of detection and therefore excluded from analysis.

Peaks at the ceramides monoisotopic mass were integrated using TargetLynx V4.1 (Waters, Milford, MA, USA) and Area Under the Curve (AUC) responses corrected for the internal standard in Excel (Microsoft 365, Redmond, Washington, United States). The monoisotopic AUC was further corrected by the degree of water loss as determined from quality control samples. AUC were further corrected by the ceramides theoretic 13C

isotope distribution. Using the calibration curves, correction for increased responses at higher masses was performed. This corrected response per ceramide was converted to relative data using the total corrected AUC and calculations were made after grouping individual ceramides by class or chain lengths for further graphing.

Sebum measurements

Lesional and non-lesional skin was measured using a Sebumeter SM815 (Courage+Khazaka, Köln, Germany). The Sebumeter was calibrated before a patient was measured. Three measurements were performed next to each other on the same predefined lesional or non-lesional site. The average of this triplicate measurement was used for graphing.

Statistical analysis

Data visualization and statistical testing was performed using Prism 9 (Graphpad Software, San Diego, California, United States). 2-way ANOVA, or a mixed effects model in the case of missing data points, was performed using Bonferroni's multiple comparison test in the case of multiple variables and paired t-test in the case of two variables. P-values are denoted as *: P≤0.05, **: P≤0.01, ***: P≤0.001. Integrative data graphing by principal component analysis (PCA) and radar plot has been performed through Python version 3.8.0 (Python Software Foundation, Wilmington, Delaware, United States). PCA analysis of the ceramides composition was performed using relative individual ceramide abundance as percentage of all detected saturated ceramides, with values below the limit of quantification set to 0 in order to prevent missing datapoints and allow for PCA analysis. Multimodal integration through PCA was performed on all the data presented in the figures of this paper with mean imputation in the case of missing data, but without epidermal thickness data due to a high amount of data not missing at random in this set as higher epidermal disorganization was more evident in lesional skin. Radar charts using min-max scaling were used to visualize differences between lesional and non-lesional skin in an integrative and descriptive manner. Data used in generation of the ceramide PCA, integrative PCA and integrative radar plot is added as supplemental information.

SUPPLEMENTAL FIGURES

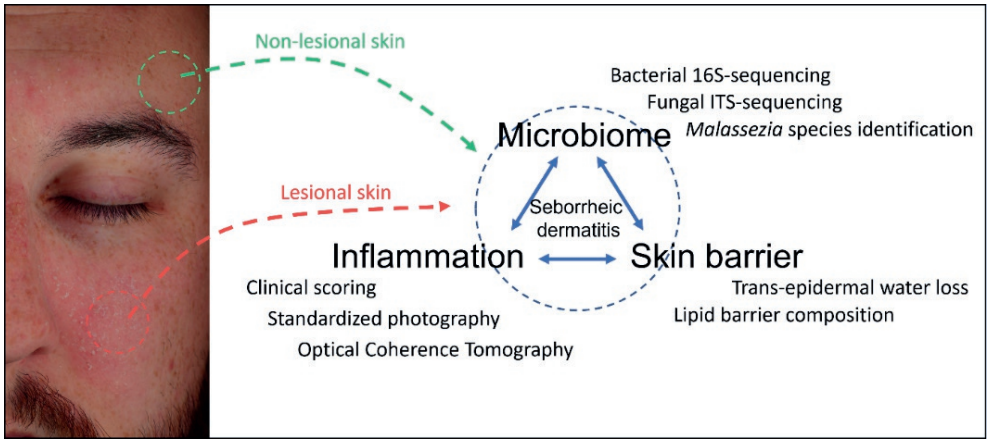


Figure S1. Clinical presentation of a seborrheic dermatitis patient and overview of the study setup showing the assessments performed on lesional and non-lesional skin and the interdependency of inflammation, microbiome and barrier function. Note that the locations indicated are examples of lesional and non-lesional skin and can differ between subjects based on the availability of affected skin as listed in the supplemental data.

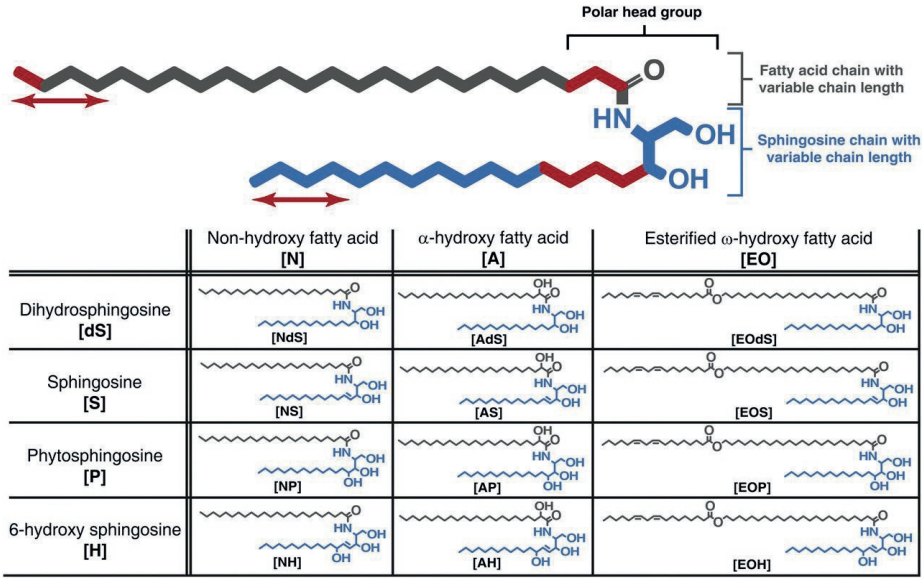


Figure S2. General structure of a ceramide composed of a sphingoid base coupled to a fatty acid chain. The carbon chains attached to the polar head group can vary in length. Differences in the ceramide headgroup architecture is indicated using the naming convention conceived by Motta *et al.* (1993). This image was adapted from Janssens *et al.* (2012) (13).

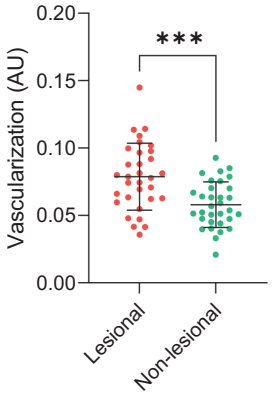


Figure S3. Average vascularization between 0.15 mm up to and including 0.25 mm of lesional and non-lesional skin as determined by optical coherence tomography.

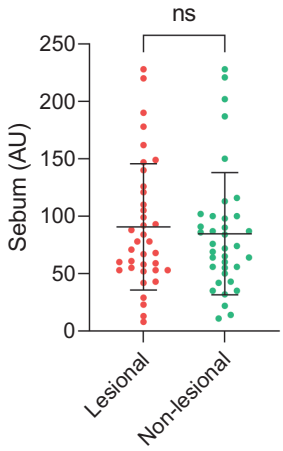


Figure S4. Sebum levels on lesional and non-lesional skin. Datapoints represent the average value of a triplicate measurement.

Table S1. Overview of the location that assessments were performed. Imaging includes both the Erythema Index as determined through standardized 2D-photograpy with VISIA and Optical Coherence Tomography. Lesional and non-lesional sites are indicated with the suffix "*_L*" and "*_NL*", respectively. The table is continued in supplemental table 2.

Subject	Lesional Erythema and OCT	Non-lesional Erythema and OCT	Lesional TEWL	Non-lesional TEWL
1	Nosebridge	Left forehead	Nosebridge	Right forehead
2	Right nosefold	Right forehead	Right nosefold	Right forehead
3	Right nosefold	Right cheek	Right nosefold	Right cheek
4	Left nosefold	Right forehead	Left nosefold	Right forehead
5	Right nosefold	Right cheek	Left nosefold	Right cheek
6	Right nosefold	Left forehead	Right nosefold	Left forehead
7	Left forehead	Right cheek	Left forehead	Right cheek
8	Right nosefold	Right forehead	Right nosefold	Right forehead
9	Right nosefold	Right forehead	Right nosefold	Right forehead
10	Right nosefold	Right lower eyelid	Right nosefold	Right lower eyelid
11	Chin	Right forehead	Right nosefold	Right forehead
12	Right nosefold	Right forehead	Right nosefold	Right forehead
13	Right nosefold	Right forehead	Right nosefold	Right forehead
14	Right upper lip	Right forehead	Right upper lip	Right forehead
15	Right eyebrow, upper	Right cheek	Right eyebrow, upper	Right cheek
16	Nosebridge	Right cheek	Nosebridge	Right cheek
17	Right nosefold	Left forehead	Right nosefold	Left forehead
18	Left nosefold	Right forehead	Left nosefold	Right forehead
19	Right nosefold	Right forehead	Right nosefold	Right forehead
20	Right nosefold	Right cheek	Right nosefold	Right cheek
21	Left upper lip	Left forehead	Left upper lip	Left forehead
22	Right nosefold	Right forehead	Right nosefold	Right forehead
23	Right nosefold	Left forehead	Right nosefold	Left forehead
24	Right nosefold	Right forehead	Right nosefold	Right forehead
25	Right nosefold	Right forehead	Right nosefold	Right forehead
26	Right nosefold	Left forehead	Right nosefold	Left forehead
27	Right forehead	Left Cheek	Right forehead	Left Cheek
28	Left nosefold	Right cheek	Left nosefold	Right cheek
29	Right nosefold	Right forehead	Right nosefold	Right forehead
30	Nosebridge	Right cheek	Nosebridge	Right cheek
31	Left forehead	Left Cheek	Left forehead	Left Cheek

32	Left nosefold	Left Cheek	Left nosefold	Left Cheek
33	Right nosefold	Right cheek	Right nosefold	Right cheek
34	Left nosefold	Left Cheek	Left nosefold	Left Cheek
35	Left nosefold	Left forehead	Left nosefold	Left forehead
36	Left nosefold	Right forehead	Left nosefold	Right forehead
37	Right nosefold	Right forehead	Right nosefold	Right forehead

Table S2. Overview of the location that assessments were performed. Imaging includes both the Erythema Index as determined through standardized 2D-photograpy with VISIA and Optical Coherence Tomography. Lesional and non-lesional sites are indicated with the suffix "*_L*" and "*_NL*", respectively. This is a continuation of supplemental table 1.

Subject	Lesional Swab location	Non-lesional Swab location	Lesional agar plates	Non-lesional agar plates
1	Nosebridge	Right forehead	Nosebridge	Left Cheek
2	Right nosefold	Right cheek	Nosebridge	Right forehead
3	Right nosefold	Right cheek	Left nosefold	Left Cheek
4	Left nosefold	Nosebridge	Left nosefold	Right forehead
5	Right nosefold	Left lower lip	Central forehead	Left lower eyelid
6	Right cheekbone	Left Cheekbone	Left nosefold	Right forehead
7	Right nosefold	Right cheek	Left forehead	Right cheek
8	Right nosefold	Right cheek	Nosebridge	Right forehead
9	Left nosefold	Left forehead	Left nosefold	Right forehead
10	Right upper lip	Right cheek	Left nosefold	Left Cheek
11	Left nosefold	Right forehead	Left Cheek	Left forehead
12	Right lower lip	Right forehead	Left lower lip	Left forehead
13	Right nosefold	Right forehead	Left nosefold	Left forehead
14	Left upper lip	Left forehead	Left eyebrow, upper	Right forehead
15	Left nosefold	Right cheek	Nosebridge	Left Cheek
16	Left Cheek	Right cheek	Nosebridge	Chin
17	Nosebridge	Left Cheek	Left nosefold	Right forehead
18	Right nosefold	Left Cheekbone	Left nosefold	Right forehead
19	Left nosefold	Right forehead	Right cheek	Left forehead
20	Left nosefold	Left forehead	Nosebridge	Left Cheek
21	Nosebridge	Left Cheek	Right upper lip	Right forehead
22	Left nosefold	Left forehead	Right lower lip	Left Cheek
23	Nosebridge	Left Cheek	Left nosefold	Right forehead
24	Left nosefold	Left forehead	Right cheek	Left Cheek

25	Left nosefold	Left forehead	Left nosefold	Left Cheek
26	Right nosefold	Left forehead	Nosebridge	Right cheekbone
27	Left Cheekbone	Left Cheek	Nosebridge	Left Cheek
28	Left nosefold	Right cheek	Nosebridge	Right cheekbone
29	Right nosefold	Left forehead	Right lower lip	Left forehead
30	Left nosefold	Left Cheek	Nosebridge	Left Cheek
31	Right forehead	Left Cheek	Left forehead	Right cheek
32	Nosebridge	Right cheek	Left nosefold	Left Cheek
33	Left nosefold	Left Cheek	Nosebridge	Right cheek
34	Nosebridge	Right cheekbone	Right nosefold	Left Cheek
35	Nosebridge	Right forehead	Right nosefold	Right cheek
36	Left upper lip	Right forehead	Left nosefold	Left Cheek
37	Chin	Right forehead	Left nosefold	Right forehead

Table S3. Overview of the location that assessments were performed. Imaging includes both the Erythema Index as determined through standardized 2D-photograpy with VISIA and Optical Coherence Tomography. Lesional and non-lesional sites are indicated with the suffix "*_L*" and "*_NL*", respectively. This is a continuation of supplemental table 1 and 2.

Subject	Lesional tape stripping	Non-lesional tape stripping	Lesional sebum measurement	Non-lesional sebum measurement
1	Right nosefold	Right cheek	Nosebridge	Right forehead
2	Right nosefold	Left forehead	Left nosefold	Right forehead
3	Right nosefold	Left forehead	Right nosefold	Right cheekbone
4	Right nosefold	Left forehead	Left nosefold	Right forehead
5	Left nosefold	Right cheek	Left nosefold	Right cheekbone
6	Right nosefold	Left forehead	Right nosefold	Left forehead
7	Left forehead	Right forehead	Left forehead	Right cheekbone
8	Right nosefold	Left forehead	Right nosefold	Right forehead
9	Right nosefold	Right cheek	Right nosefold	Right forehead
10	Left upper lip	Left forehead	Right nosefold	Left forehead
11	Right nosefold	Right cheek	Right nosefold	Right forehead
12	Left eyebrow, upper	Right cheekbone	Right nosefold	Right forehead
13	Nosebridge	Left forehead	Right nosefold	Right forehead
14	Right upper lip	Right cheekbone	Right lip, upper	Right eyebrow, upper
15	Left eyebrow, upper	Left Cheek	Right eyebrow, upper	Right cheekbone
16	Right forehead	Left Cheek	Nosebridge	Right cheekbone

17	Right nosefold	Left forehead	Right nosefold	Left forehead
18	Nosebridge	Left forehead	Left forehead	Right forehead
19	Left nosefold	Left Cheekbone	Right cheekbone	Right forehead
20	Right nosefold	Right cheek	Right nosefold	Right cheek
21	Left upper lip	Left forehead	Left forehead	Left forehead
22	Left lower lip	Right cheekbone	Right nosefold	Right forehead
23	Left nosefold	Right forehead	Right nosefold	Left forehead
24	Left nosefold	Left forehead	Right nosefold	Left nosefold
25	Nosebridge	Left forehead	Right nosefold	Right forehead
26	Right nosefold	Right forehead	Right nosefold	Left forehead
27	Right cheekbone	Right cheek	Left cheek	Right forehead
28	Right nosefold	Right cheek	Left forehead	Right cheekbone
29	Left lower lip	Left Cheek	Right nosefold	Right forehead
30	Right nosefold	Right cheek	Nosebridge	Right cheek
31	Right forehead	Left Cheek	Left forehead	Left cheekbone
32	Right nosefold	Right forehead	Left nosefold	Left cheek
33	Right nosefold	Right cheekbone	Right nosefold	Left cheek
34	Left nosefold	Right cheek	Left forehead	Left cheek
35	Left nosefold	Left forehead	Left forehead	Left forehead
36	Right nosefold	Right cheek	Left nosefold	Right forehead
37	Right nosefold	Right cheekbone	Right nosefold	Right forehead

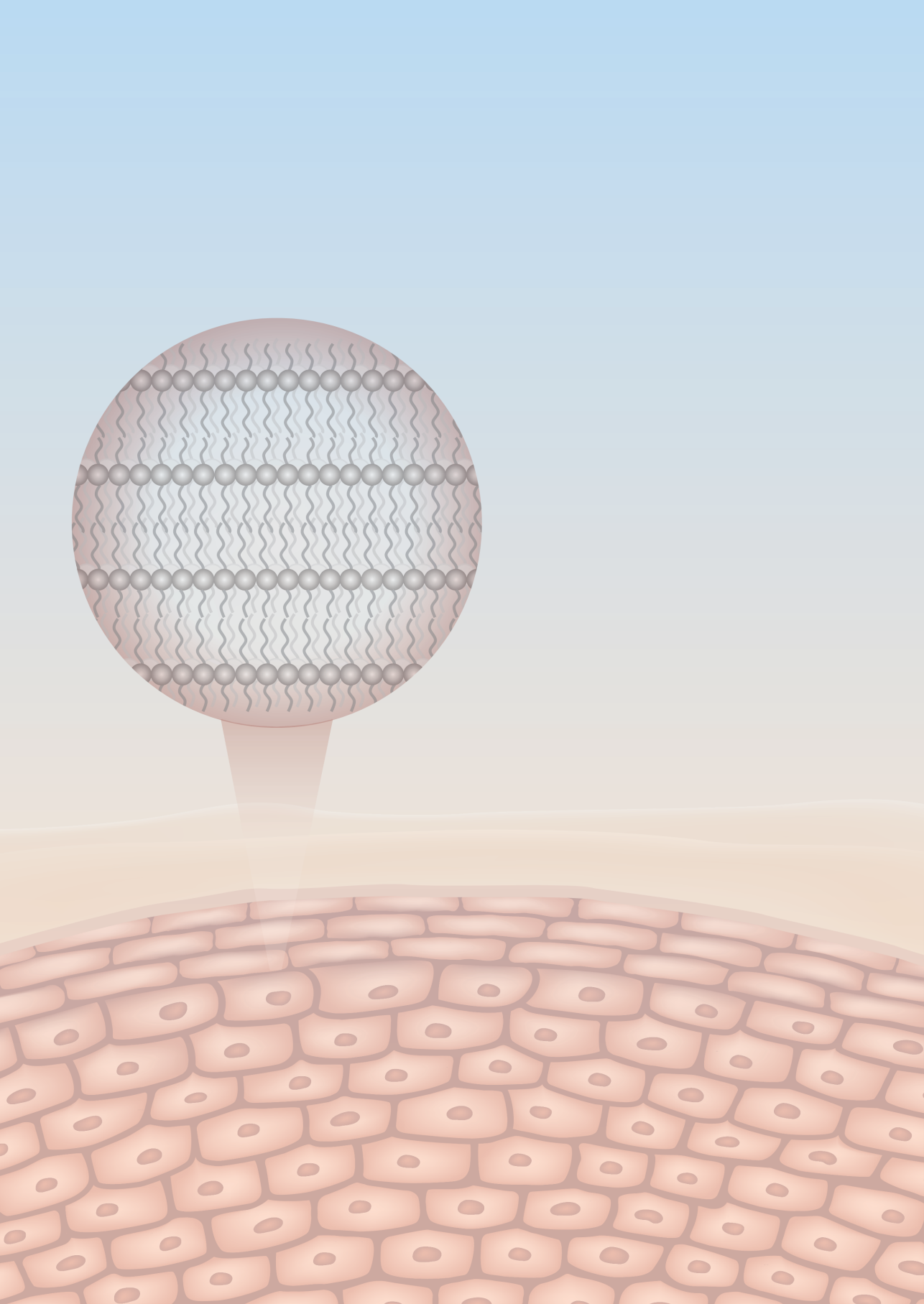
PCA loadings

Table S4. The loadings per parameter used in the generation of the Principal Component Analysis in figure 4A.

	Principal component 1 (36.78%)			Principal component 2 (11.51%)	
	Parameter	**Loading**		**Parameter**	**Loading**
1	Cer[NS]	0.304353	**1**	Cer[OS]	0.377582
2	Ratio Cer[NS:NP]	0.291921	**2**	Cer[OP]	0.337539
3	Cer[AS]	0.291615	**3**	Cer[OH]	0.329363
4	Cer[NSc34]	0.251295	**4**	Cer[EOdS]	0.242378
5	*Staphylococcus* (%)	0.207942	**5**	Fungal Diversity	0.214079
6	Trans-epidermal water loss	0.186069	**6**	Bloodflow at 0.2 mm	0.170678
7	Roughness	0.183875	**7**	Erythema	0.170665
8	MUCer[NS]	0.182895	**8**	Ratio Cer[NS:NP]	0.168114
9	Erythema	0.143098	**9**	Bloodflow at 0.25 mm	0.16635
10	*Malassezia* (%)	0.028224	**10**	Cer[EOH]	0.162232
11	Bloodflow at 0.15 mm	0.004897	**11**	Cer[EOS]	0.161557
12	Bloodflow at 0.35 mm	0.003023	**12**	Bloodflow at 0.15 mm	0.158108
13	Bloodflow at 0.3 mm	-0.00488	**13**	Bloodflow at 0.3 mm	0.156788
14	Bloodflow at 0.2 mm	-0.0056	**14**	Bloodflow at 0.35 mm	0.145911
15	Cer[AdS]	-0.00785	**15**	Bloodflow at 0.1 mm	0.130806
16	Bloodflow at 0.25 mm	-0.01004	**16**	Cer[AH]	0.128493
17	Bloodflow at 0.1 mm	-0.01428	**17**	Trans-epidermal water loss	0.116807
18	Cer[AH]	-0.02809	**18**	Cer[AS]	0.116675
19	Bacterial Diversity	-0.02977	**19**	MUCer[NS]	0.109013
20	Fungal Diversity	-0.06081	**20**	Cer[NS]	0.088148
21	Cer[NdS]	-0.07766	**21**	Cer[EOP]	0.039438
22	Cer[NH]	-0.08445	**22**	Cer[NH]	0.019096
23	Cer[OS]	-0.11084	**23**	Roughness	-0.00196
24	Cer[EOdS]	-0.11781	**24**	Cer[AdS]	-0.02022
25	Cer[AP]	-0.12997	**25**	Cer[NSc34]	-0.05328
26	Cer[OP]	-0.14308	**26**	*Staphylococcus* (%)	-0.07786
27	Cer[OH]	-0.18532	**27**	Bacterial Diversity	-0.09176
28	Cer[EOS]	-0.22501	**28**	Carbon chain length	-0.13019
29	Cer[NP]	-0.22817	**29**	Cer[AP]	-0.15411
30	Cer[EOH]	-0.24775	**30**	*Malassezia* (%)	-0.18649
31	Cer[EOP]	-0.26718	**31**	Cer[NdS]	-0.24213
32	Carbon chain length	-0.39401	**32**	Cer[NP]	-0.24222

SUPPLEMENTARY REFERENCES

1. Baysal, V., Yildirim, M., Ozcanli, C., Ceyhan, A.M. (2004). Itraconazole in the treatment of seborrheic dermatitis: a new treatment modality. *Int J Dermatol*. 43(1):63–6.
2. Elman, S., Hynan, L.S., Gabriel, V., Mayo, M.J. (2010). The 5-D itch scale: a new measure of pruritus. *Br J Dermatol*. 162(3):587–93.
3. Finlay, A.Y., Khan, G.K. (1994). Dermatology Life Quality Index (DLQI)—a simple practical measure for routine clinical use. *Clin Exp Dermatol*. 19(3):210–6.
4. Basra, M.K.A., Fenech, R., Gatt, R.M., Salek, M.S., Finlay, A.Y. (2008). The Dermatology Life Quality Index 1994–2007: a comprehensive review of validation data and clinical results. *British Journal of Dermatology*. 159(5):997–1035.
5. Yamamoto, T., Takiwaki, H., Arase, S., Ohshima, H. (2008). Derivation and clinical application of special imaging by means of digital cameras and Image J freeware for quantification of erythema and pigmentation. *Skin Res Technol*. 14(1):26–34.
6. Rasband, W.S. ImageJ. Bethesda, Maryland, USA: U.S. National Institutes of Health;
7. Edgar, R.C. (2010). Search and clustering orders of magnitude faster than BLAST. *Bioinformatics*. 26(19):2460–1.
8. Zaharia, M., Bolosky, W.J., Curtis, K., Fox, A., Patterson, D., Shenker, S., et al. (2011). Faster and More Accurate Sequence Alignment with SNAP.
9. Cole, J.R., Wang, Q., Fish, J.A., Chai, B., McGarrell, D.M., Sun, Y., et al. (2014). Ribosomal Database Project: data and tools for high throughput rRNA analysis. *Nucleic Acids Res*. 42(Database issue).
10. Abarenkov, K., Nilsson, R.H., Larsson, K.H., Alexander, I.J., Eberhardt, U., Erland, S., et al. (2010). The UNITE database for molecular identification of fungi – recent updates and future perspectives. *New Phytologist*. 186(2):281–5.
11. Kolecka, A., Khayhan, K., Arabatzis, M., Velegraki, A., Kostrzewa, M., Andersson, A., et al. (2014). Efficient identification of Malassezia yeasts by matrix-assisted laser desorption ionization-time of flight mass spectrometry (MALDI-TOF MS). *British Journal of Dermatology*. 170(2):332–41.
12. Boiten, W., Absalah, S., Vreeken, R., Bouwstra, J., van Smeden, J. (2016). Quantitative analysis of ceramides using a novel lipidomics approach with three dimensional response modelling. *Biochimica et Biophysica Acta (BBA) - Molecular and Cell Biology of Lipids*. 1861(11):1652–61.
13. Janssens, M., van Smeden, J., Gooris, G.S., Bras, W., Portale, G., Caspers, P.J., et al. (2012). Increase in short-chain ceramides correlates with an altered lipid organization and decreased barrier function in atopic eczema patients. *J Lipid Res*. 53(12):2755–66.



CHAPTER 3

Phytosphingosine ceramide mainly localizes in the central layer of the unique lamellar phase of skin lipid model systems

Authors and affiliations:
Andreea Nădăban[1], Gerrit S. Gooris[1], Charlotte M. Beddoes[1], Robert M. Dalgliesh[2], Joke A. Bouwstra[1*]

[1]Division of BioTherapeutics, Leiden Academic Centre for Drug Research, Leiden University, Leiden, The Netherlands
[2]ISIS Neutron and Muon Source, Science and Technology Facilities Council, Rutherford Appleton Laboratory, Didcot, United Kingdom

Adapted from: **Journal of Lipid Research** (2022). 63(9): 100258

ABSTRACT

Understanding the arrangement of the lipids within the skin's outermost layer, the stratum corneum (SC), is important for advancing the knowledge on the skin barrier function. The SC lipid matrix consists of ceramides (CER), cholesterol and free fatty acids, which form unique crystalline lamellar phases, referred to as the long periodicity (LPP) and short periodicity phase. As the SC lipid composition is complex, lipid model systems that mimic the properties of native SC are used to study the SC lipid organization and the molecular arrangement. In previous studies such lipid models were used to determine the molecular organization in the trilayer structure of the LPP unit cell. The aim of this study was to examine the location of CER *N*-(tetracosanoyl)-phytosphingosine (CER NP) in the unit cell of this lamellar phase and compare its position with CER *N*-(tetracosanoyl)-sphingosine (CER NS)**.** CER NP was selected as it is the most prevalent CER subclass in the human SC and its location in the LPP is not known. The neutron diffraction results demonstrate that the acyl chain of CER NP was positioned in the central part of the trilayer structure, with a fraction also present in the outer layers, the same location as determined for the acyl chain of CER NS. FTIR results are in agreement with this molecular arrangement suggesting a linear arrangement for the CER NS and CER NP. These findings provide a more detailed insight in the lipid organization in the SC lipid matrix.

INTRODUCTION

The skin acts as a barrier to protect the body against the environment (1). The skin barrier function is primarily located in the outermost layer of the skin, the stratum corneum (SC), which consists of corneocytes (dead keratin containing cells) embedded in a lipid matrix. The SC lipid matrix provides the only continuous pathway for substances through the SC. This lipid matrix is therefore considered a crucial element in the barrier function (2). The three main SC lipid subclasses are ceramides (CER), free fatty acids (FFA) and cholesterol (CHOL), in an approximately equimolar ratio (3-5). The CER subclasses differ by their molecular structure, as they consist of a long acyl chain linked through an amide bond to a sphingoid base (6-8). The CER nomenclature used is according to Motta et al (9). Nowadays at least 21 different CER subclasses have been identified in human SC (8, 10, 11).

X-ray diffraction studies revealed that the SC lipids simultaneously form two unique crystalline lamellar phases referred to as the short periodicity phase (SPP) and long periodicity phase (LPP), with a repeat distance of approximatively 6 and 13 nm, respectively (12, 13). Apart from this lamellar organization, the lateral organization of the lipids is also important for barrier functionality (14). The lateral packing represents the arrangement of the lipids within the lamellae. The lipids are packed in either an orthorhombic (densely packed lipids), a hexagonal (less dense packing, but still an ordered organization) or a liquid (fluid) (disordered lipids) phase. In human SC, the lipids primarily adopt an orthorhombic packing at physiological temperature, while a small portion of the lipids adopt a hexagonal packing (14-16). In lipid model membranes, besides the hexagonal and orthorhombic packing, a liquid or isotropic phase has also been encountered (17-19).

When focusing on CER composition, changes in CER subclass composition have been reported in several inflammatory skin diseases, such as atopic dermatitis, psoriasis or Netherton syndrome, which correlated with an impaired skin barrier function, demonstrating that the lipid composition is important for the skin barrier (9, 10, 20-24). Clinical studies revealed that especially the concentration of CER *N*-(tetracosanoyl)-sphingosine (CER NS) was increased, while the concentration of CER *N*-(tetracosanoyl)-phytosphingosine (CER NP) was reduced (Figure 1) (9, 24-26). Furthermore, another interesting observation can be made when comparing the CER subclass composition in porcine, dog, mice and human SC. In dog, mice and porcine SC, CER NS is by far the most abundant CER subclass (11, 27-29), while in healthy human SC, CER NP is one of the most abundant CER subclasses (6, 8, 30). Therefore, a comparison of the role of CER NP and CER NS in the lipid organization will result in a more thorough understanding of the lipid arrangement and the barrier function. In native SC it is not possible to study selectively the role of these CER subclasses, thus, for such studies lipid model systems are an attractive tool.

Lipid model membranes can be used as an alternative to investigate the relationship between lipid composition, lipid organization and lipid barrier functionality. These systems are prepared with SC lipids, using selected CER subclasses, CHOL and a suitable FFA chain length composition, creating a model that resembles the lipid composition and organization in healthy SC lipid matrix (17, 21, 29, 31-34).

Previous studies have shown the importance of the lamellar lipid organization for maintaining the skin barrier functionality, in which the presence of the LPP plays an important role (23, 35). Using lipid models, it was identified that CER *N*-(30-linoleoyloxy-triacontanoyl)-sphingosine (CER EOS) is required for the formation of the LPP (36), therefore including CER EOS in the lipid composition is essential for the SC lipid matrix (34, 37-39) . The unit cell of the LPP consists of three stacked lipid layers, as illustrated by the electron density profile and water profiles determined by analyzing the X-ray diffraction pattern (including that of human SC) and neutron scattering profiles, respectively (32, 40). Investigating the molecular organization of the lipids within the LPP trilayer unit is important for understanding the role of the different lipid subclasses in the formation of this phase. To achieve this, it is important that the lipid mixture only forms the LPP. This can be obtained by increasing the CER EOS level to at least 30mol% of the total amount of CERs without changing the unit cell structure (41, 42).

Small-angle neutron scattering (SANS) is an excellent tool that can be used to investigate the localization of lipid subclasses (40, 43-46). Previous studies focused on the localization of CER NS, CER EOS, CHOL and FFA in the LPP and based on these results a trilayer unit molecular arrangement was proposed (44). However, to our knowledge the location of CER NP, the most abundant CER in the human SC in the LPP is not yet determined. Therefore, the localization and arrangement of CER NP in the LPP is the aim of the present study.

We have investigated the position of the acyl chain of CER NP in the LPP unit cell using SANS and compared it with the acyl and sphingosine chains of CER NS. The lipid model consisted of only five lipids, CER EOS, CER NS, CER NP, CHOL and FFA C24 (chain length 24 carbon atoms). This allows a more detailed analysis especially as Fourier transform infrared (FTIR) spectroscopy is used to assess the lateral organization and the lipid chain interactions. As we are primarily interested whether the head group architecture affects the position and arrangement of the CERs, we chose an equal fraction of CER NP and CER NS. The location of CER NP was determined and compared with that of CER NS, using CER NP and CER NS with deuterated acyl chains. First, we showed that this composition indeed formed the LPP, as observed in more complex lipid model systems and intact SC. Within the LPP, CER NP adopts a similar localization as CER NS, with the acyl chains of CER NP being localized predominantly in the inner layer of the LPP unit. Furthermore, we demonstrate that the acyl chains of CER NP and CER NS and the FFA C24 chains are neighbors in the central layer of the LPP unit cell and that CER NP adopts a linear conformation, similar to that of CER NS.

MATERIALS AND METHODS

Materials

The synthetic CER mixture used for the LPP model consists of CER EOS, CER NS and CER NP, whose molecular structures are presented in Figure 1. The sphingoid chains of CER NS and CER NP have a chain length of 18 carbons (C18), while the acyl chain length is 24 carbons (C24). These protiated CERs, alongside the deuterated CER NS and CER NP with a perdeuterated acyl chain (d47), referred to as NSd47 and NPd47 respectively, were kindly provided by Evonik (Essen, Germany). CER NS with the sphingosine chain terminally deuterated, referred to as NSd7, was purchased from Avanti Polar Lipids (Alabama, USA). Lignoceric acid (FFA24), CHOL, acetate buffer salts and D_2O were supplied by Sigma-Aldrich Chemie GmbH (Schnelldorf, Germany). Deuterated lignoceric acid (DFFA24) was obtained from Arc Laboratories BV (Apeldoorn, The Netherlands). All organic solvents were HPLC grade or higher and were purchased from Biosolve BV (Valkenswaard, The Netherlands). The Millipore quality water was produced by a Milli-Q water filtration system. The silicon substrates (wafers) were purchased from Okmetic (Vantaa, Finland).

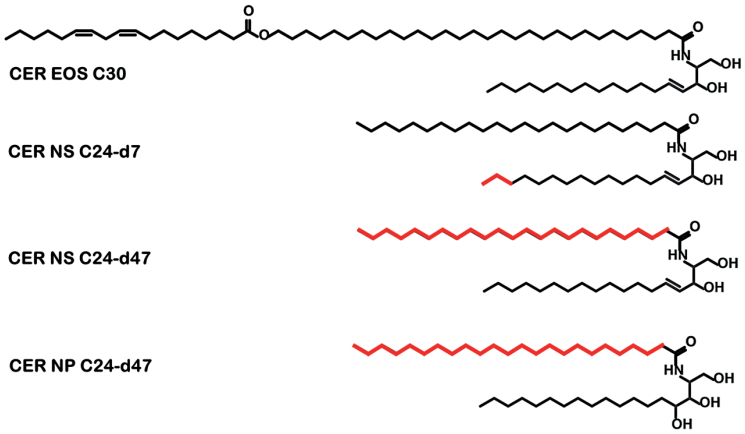


Figure 1. The molecular structure of the CERs used in this study. The deuterated chains are highlighted in red: the d7 sphingosine chain of CER NS and the acyl chains d47 of CER NS and CER NP.

Composition of the lipid models

The lipid models were prepared from the synthetic CERs, CHOL and FFA in a 1:1:1 molar ratio. In order to form exclusively the LPP, the ratio of CER EOS was set to 40 mol% of the total CER concentration (41). The concentrations of CER NS and CER NP were equal, each 30 mol% of the total CERs. In this study the FFA included was only FFA24, in order to limit the total number of components in the model. The composition of the lipid models with their molar ratios and the abbreviations are provided in Table 1.

Table 1. The composition of the lipid model membranes and the molar ratios. The deuterated lipids and their molar ratios are highlighted in bold.

Model abbreviation	Lipid composition	Molar ratio
LPP:prot	CER EOS: CER NS: CER NP: CHOL: FFA C24	0.4:0.3:0.3:1:1
LPP:NPd47	CER EOS: CER NS: **CER NPd47**: CHOL: FFA C24	0.4:0.3:**0.3**:1:1
LPP:NSd47	CER EOS: **CER NSd47**: CER NP: CHOL: FFA C24	0.4:**0.3**:0.3:1:1
LPP:NSd7	CER EOS: **CER NSd7**: CER NP: CHOL: FFA C24	0.4:**0.3**:0.3:1:1
LPP:NSd47:DFFA24	CER EOS: **CER NSd47**: CER NP: CHOL: **DFFA C24**	0.4:**0.3**:0.3:1:**1**
LPP:NPd47:DFFA24	CER EOS: CER NS: **CER NPd47**: CHOL: **DFFA C24**	0.4:0.3:**0.3**:1:**1**
LPP:NSd47:NPd47:DFFA24	CER EOS: **CER NSd47**: **CER NPd47**: CHOL: **DFFA C24**	0.4:**0.3:0.3**:1:**1**

Sample preparation of the lipid models

To prepare the samples, the required amount of lipids was dissolved in a chloroform/methanol solution (2:1; v/v) at a concentration of 5 mg/mL. The samples were sprayed using a Camag Linomat IV device (Muttenz, Switzerland) at a rate of 14 s/µL, under a gentle stream of nitrogen. For the FTIR measurements, 1 mg of the lipid mixture was sprayed on AgBr windows over an area of 1 x 1 cm^2. The lipids were then equilibrated by increasing the temperature to 85°C (using a constant rate of 4°C/min), and it was maintained at this temperature for 50 min to ensure the lipids melted. This was followed by a slow cooling to room temperature. For the neutron diffraction experiments, 10 mg of lipids were sprayed on a silicon substrate in an area of 1.2 x 3.8 cm^2 using the sample preparation method described above. To avoid contraction of the lipid layers during the melting process, the sample equilibration temperature was 81-82°C. Prior to the measurements, the samples were hydrated either with deuterated acetate buffer (pH 5.0) (for FTIR studies) or a D_2O/H_2O buffer (for neutron experiments) at 37°C for ≥12 h. For contrast variation in the neutron experiments, the samples were hydrated at three different D_2O/H_2O buffer levels (100%, 50% and 8%).

Neutron diffraction measurements

The neutron diffraction data was collected at the ISIS Neutron and Muon Source (Rutherford Appleton Laboratory, United Kingdom), on the LARMOR instrument, set in small angle neutron scattering (SANS) mode. The wavelength range of the neutron beam was 1-12.5 Å and its diameter was 1x30 mm. The distance from the sample to the detector was 4.4 m. The ^{3}He tube detector angle was set at a 2θ angle of 5° to the direct neutron beam and covered approximately 4° in both directions. The incident flux shape and detector efficiency were accounted for by using the direct beam measurement, thus all the different curves measured at the different wavelengths would overlap. Each sample sprayed on the silicon substrate was placed in a custom-made aluminum humidity chamber maintained at a constant temperature of 25°C and measured for 4 h (40 µA/h accelerator proton charge). The windows of the aluminum chambers were maintained at

42°C to prevent condensation. The sample angle to the neutron beam was set to 2.5° and kinematic mounts ensured reproducible positions. An empty aluminum chamber was measured as background and was subtracted from each scattering curve.

Neutron data analysis

The MANTID software framework was used for the SANS data analysis (47). First, the detector readout was reduced to one-dimensional plots and the background (empty chamber measurement) was subtracted. The data was then analyzed following the steps described previously (40). Briefly, a one-dimensional diffraction pattern of the scattering intensity as a function of the scattering angle (2θ) was obtained. The 2θ scattering angle was converted to the scattering vector *q* using the following equation:

$$q = \frac{4\pi sin\theta}{\lambda} \quad (1)$$

where λ is the wavelength of the neutron beam and θ is the Bragg angle. The repeat distance of the LPP unit cell (*d*) was calculated from the position of a series of equidistant diffraction peaks attributed to the lamellar phase (Bragg peaks):

$$d = \frac{2\pi n}{q_n} \quad (2)$$

where n is the order of the diffraction peak. To obtain the intensity (I_n) of each peak, the Bragg peaks were fitted using a Pearson VII function (using Fityk software). From these peak intensities the absolute structure factor amplitude for each diffraction order ($|F_n|$) was calculated:

$$\left| F_n \right| = A_n \sqrt{LI_n} \quad (3)$$

In this formula, *L* refers to the Lorentz correction and it can be assumed *L = q* because of the high degree of orientation of the lipid lamellae in the samples. A_n represents the correction factor for the sample absorption, which can be calculated using the following equation (48):

$$A_n = \frac{1}{\sqrt{\frac{sin\theta}{2\mu l}\left(1 - e^{\frac{-2\mu l}{sin\theta}}\right)}} \quad (4)$$

where μ is the linear attenuation coefficient and *l* represents the lipid film thickness. The latter was calculated to be ~0.03 mm, knowing the lipid density and surface area of the sample, as described previously (49).

The D_2O/H_2O contrast variation method was used to determine the water phase signs of the amplitudes of the different diffraction orders. The lipid head groups are located at the boundary of the lamellar phases (40, 49, 50). In a hydrated lipid model, most of the water molecules are located close to the hydrophilic lipid head groups, rather than the hydrophobic tails. With this assumption, the phase signs of the water profile were selected, which can be either positive (+) or negative (-). The phase signs of the water profile are obtained from the positive or negative signs of the slope of the difference between the absolute structure factors $|F_n|$ of the sample hydrated at 100% and 8%

D_2O/H_2O. The combination of phase signs for the water profiles in this study is - + - + - +. Using these phase signs, four regions are observed in the LPP unit cell, corresponding to the lipid head group locations at the boundary of the unit cell and in the inner layer. Other phase sign combinations resulted in unrealistic water profiles and were thus discarded. The phase signs of the water profile used in this study are in agreement with previously reported structure factor phase signs for the LPP (32, 40, 44, 46).

Next, the structure factors (calculated with Eq. 3) with the corresponding phase signs are plotted as a function of the D_2O/H_2O buffer ratio (Figure 2). There is a linear correlation of the relative structure factor amplitudes as a function of the D_2O/H_2O buffer ratio, thus demonstrating the centrosymmetric structure of the LPP unit cell. This is in agreement with previous studies (40, 44). The phase signs of the protiated and deuterated samples were individually determined based on the positive or negative sign of the structure factors at 8% D_2O/H_2O hydration (Figure 2). For the LPP:prot, and LPP:NSd7 lipid models, the same combination of phase signs was obtained (- + - + - +). The phase signs of the samples match those obtained for the water profile if the linear regression of the structure factors plotted as a function of the buffer level does not intersect the x-axis. The phase sign is switched for the respective diffraction order if the line crosses the x-axis. This can be seen in the LPP:NPd47 and LPP:NSd47 models (Figure 2) for the first diffraction order, when the slope of the regression line is negative but the F_n at 8% D_2O/H_2O has a positive value, determining the phase signs combination + + - + - +.

Using the phase signs and the values of the structure factors, the scattering length density (SLD) profile of the unit cell was calculated by Fourier reconstructions:

$$\rho(x) = F_0 + 2\sum_{n=1}^{n_{max}} F_h \cos\left(\frac{2\pi n x}{d}\right) \quad (5)$$

where x is the distance in the unit cell, with x=0 center of the unit cell (40). F_0, the scattering density per unit volume, was calculated using the chemical composition of the lipid sample (which included one water molecule per lipid molecule from the hydration of the samples) and its density (51, 52).

The SLD profiles of each deuterated lipid moiety were calculated by subtracting the protiated profiles from the deuterated profiles of each sample hydrated at 8% D_2O/H_2O buffer. At this exact buffer ratio, the scattering contribution of the buffer is zero and the SLD profiles show only the scattering of the lipid chains.

A scaling factor was calculated to place the SLD data on a 'relative absolute' scale, as previously described (36, 44, 53). First, the SLD peak height (SLD_h) and peak area (SLD_a) were fitted for the sample with NSd7. The peak area obtained from the difference in SLD profile (SLD_{dif}) of the LPP:NSd7 and LPP:prot lipid models represents the deuterium atoms on the CER sphingosine chain. The relative absolute SLD value ($SLD_{correct}$) was determined using the following equation:

$$SLD_{correct} = \frac{SLD_h * SLD_{dif}}{SLD_a} \quad (6)$$

Finally, the scaling factor was calculated as the ratio between $SLD_{correct}$ and SLD_h and it was then applied to the F_n values to obtain the results on the relative absolute scale.

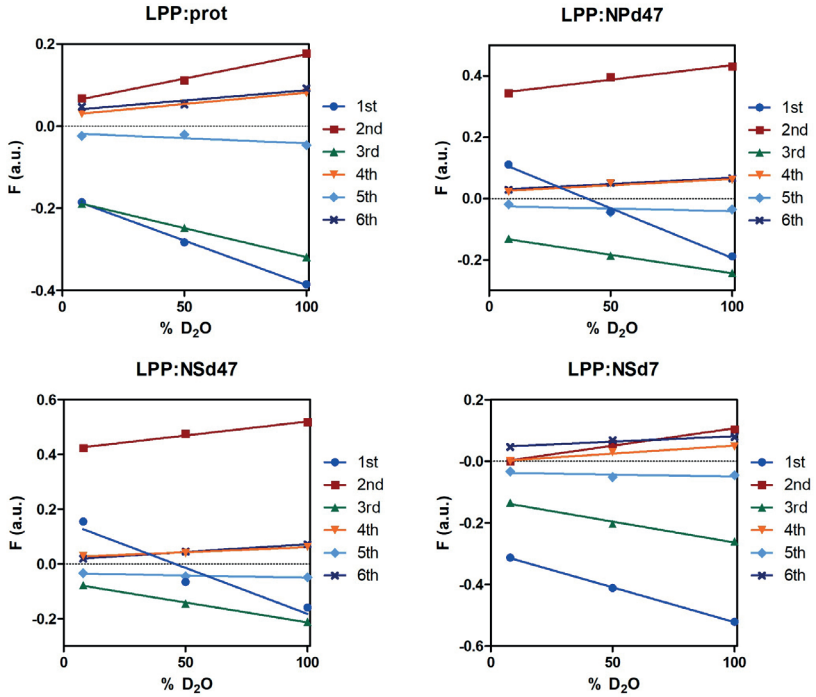


Figure 2. Linear fitting of the relative structure factors (F) as a function of the percentage of D_2O in the D_2O/H_2O buffer for the six diffraction orders of the LPP:prot, LPP:NPd47, LPP:NSd47 and LPP:NSd7 models. The diffraction orders are each represented by different colors and symbols: 1st (dot, dark blue), 2nd (square, red), 3rd (triangle, green), 4th (triangle, orange), 5th (diamond, light blue), 6th (cross, purple).

FTIR measurements

The FTIR measurements were performed on a Varian 670-IR spectrometer (Agilent Technologies, Santa Clara, USA) using a broad-band mercury cadmium telluride detector, cooled by liquid nitrogen. The FTIR spectra were acquired by the co-addition of 256 scans, with a resolution of 1 cm^{-1}, collected over 4 min in transmission mode. Starting 30 min prior to the measurement, the samples were purged continuously under dry air. In order to examine the thermotropic phase behavior, the lipid models were measured between 10 - 90°C at a heating rate of 0.25°C/min (resulting in a 1°C temperature rise per recorded spectrum). The measurement was performed in the wavenumber range of 600–4000 cm^{-1}. The software Resolution Pro (Agilent Technologies, Palo Alto, USA) was used for data collection and analysis. During data analysis, the spectra were deconvoluted using a half-

width of 4 cm^{-1} and an enhancement factor of 1.4. At least three samples were prepared and measured for each experimental condition.

The conformational ordering determined at 10°C and phase transitions of the lipid chains were examined using the CH_2 symmetric stretching vibration (ν_sCH_2, wavenumber range: 2845-2855 cm^{-1}) and CD_2 symmetric stretching vibration (ν_sCD_2, 2080-2100 cm^{-1}). The lateral packing of the lipids was analyzed using the CH_2 scissoring vibration (δCH_2, 1462-1473 cm^{-1}), while the mixing properties of the lipid chains was determined using the CD_2 and CH_2 scissoring vibration (δCD_2, 1085-1095 cm^{-1}). The accurate peak position determination of the δCH_2 and δCD_2 vibrations was performed in the Enthought Canopy software, using in-house developed Python scripts. The three scissoring peaks were fitted using a Lorentzian function.

Statistical analysis was performed using GraphPad Prism (v.8). An unpaired t-test was conducted to determine the significance of the peak height ratio values of the two orthorhombic δCD_2 modes (at 1086 and 1091 cm^{-1}) and the central δCD_2 peak (at 1088.5 cm^{-1}). Differences in mean values of the different models ($n \geq 3$) are considered statistically significant when $P < 0.05$.

The mid-point temperature of the ordered-disordered phase transition (T_M) was determined by fitting a linear regression curve, as described before (54).

RESULTS

Localization of CER NP and CER NS in the LPP lipid model system

Neutron diffraction studies were performed to examine the molecular arrangement of CER NP and CER NS in the LPP trilayer unit. In Figure 3 the neutron patterns of the lipid samples are depicted and they showed six equidistant peaks that all could be attributed to the LPP. A small peak appeared at q=1.2 nm^{-1}, which did not overlap the Bragg peaks corresponding to the LPP, indicating that a very small portion of the lipids formed another phase. The reflection attributed to crystalline phase separated CHOL was observed at q=1.8 nm^{-1} and it did not interfere with the diffraction orders of the LPP. The repeat distance of the LPP unit was calculated from the series of equidistant Bragg peaks with Eq. 2. The d-spacing values obtained for the four samples were very similar: 12.6 ± 0.1 nm (LPP:prot), 12.5 ± 0.05 nm (LPP:NSd7), 12.5 ± 0.1 nm (LPP:NSd47) and 12.6 ± 0.1 nm (LPP:NPd47).

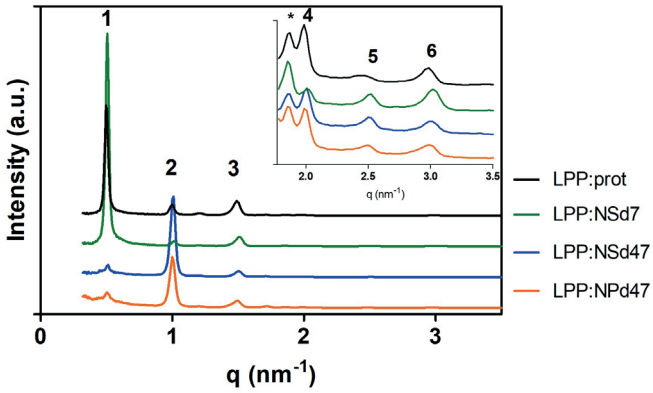


Figure 3. The one-dimensional neutron diffraction patterns of the four samples hydrated at 100% D_2O/H_2O (LPP:prot, LPP:NPd47, LPP:NSd47 and LPP:NSd7), the intensity plotted as a function of the scattering vector (q). The insert represents the zoomed-in region q=1.7-3.5 nm^{-1}. The first six diffraction orders are indicated by numbers and the crystalline CHOL peak is indicated by an asterisk.

Data analysis based on the calculated structure factors and phase signs led to the construction of the SLD profiles, using Eq. 5. Figure 4A displays the SLD profile of the LPP:prot sample hydrated at 100% and 8% D_2O/H_2O. The intensity of the SLD profiles is directly proportional with the percentage of D_2O in the hydration buffer, thus the highest intensity was noticed after hydration with 100% D_2O/H_2O, while the SLD profile of the sample after 8% D_2O/H_2O hydration has no contribution of the water (Supplemental Figure S1A). Therefore, by subtracting the profile of the 8% D_2O/H_2O from the 100% D_2O/H_2O buffer, the water profile for this sample is obtained. This SLD water profile is shown in Figure 4B and it indicates that the water molecules were present at the outer regions of the centrosymmetric LPP unit cell (at 6.3 ± 0.1 nm from the center) and at two distinct regions inside the unit cell (2.2 ± 0.1 nm from the unit cell center). The positions of the water profile correspond to the locations of the hydrophilic head groups of the lipids. Therefore, the SLD water profile is in agreement with the trilayer structure of the LPP (40, 44). The water profile followed the same pattern in all four compositions analyzed in this study.

Using the phase signs for the deuterated samples, the next step was to calculate the SLD profiles for the LPP:NPd47, LPP:NSd47 and LPP:NSd7 compositions from the structure factors for each of the three D_2O/H_2O buffer hydration levels (Supplemental Figure S1). Then the 8% D_2O/H_2O hydrated samples were selected for calculating the localization of the deuterated samples, as at this ratio there is no contribution of water to the SLD profile. The SLD profiles are provided in Figure 4C-E. To identify the localization for the deuterated lipid chains in these systems, the difference between the SLD profile of the deuterated and the protiated model was determined. The difference of the SLD profiles indicate the location of the deuterated moiety in the LPP trilayer unit. Figure 4F clearly

shows that the maximum of the SLD profile was obtained in the inner layer of the LPP unit, however there is a SLD elevation at the unit cell border. This indicates that the perdeuterated acyl chain of CER NP is primarily located in this inner layer of the LPP unit, with a small fraction of the chains positioned in the outer layers.

Similarly, the SLD profiles of the deuterated chains of CER NS were calculated in the LPP:NSd47 and LPP:NSd7 models and are both shown in Figure 4G. The SLD profile indicates that the maximum intensity of the d47 acyl chain of CER NS was located in the central layer of the LPP trilayer unit cell but an increase in SLD profile was also observed near the LPP unit cell border (Figure 4G, red curve). Therefore, the deuterated acyl chains of CER NS were localized predominantly in the inner layer of the LPP, but a fraction of the CER NS acyl chains is also positioned in the outer layers. This indicates that both the CER NS and CER NP head groups are not only located at the inner water layer region, but also at the unit cell border, although clearly less abundant.

CERs can adopt two conformational arrangements: in an extended (linear) conformation the lipid tails are located on either side of the lipid headgroup, while in a hairpin conformation the two lipid chains are located on the same side of the headgroup. In this study, the conformation of the CER NS was examined by determining the localization of the terminally deuterated sphingosine chain of CER NSd7. The SLD profile of the d7-deuterated sphingosine chain of CER NS (LPP:NSd7) presented in Figure 4G (green curve) clearly revealed that the maximum scattering intensity was located at 4.2 nm from the center of the LPP unit cell (respectively 2 nm outer unit cell boundary in the two outer lipid layers). No maximum was observed in the inner layer. This demonstrates that the CER NS with the head groups in the inner head group regions have their acyl chain in the central lipid layer and the sphingosine tail in the outer lipid layers. Therefore, these lipids are in a linear arrangement. When CER NS is either in a linear or hairpin conformation in the outer layers, the deuterated sphingosine moiety will be located at a very similar position coinciding to that of the CER NS located in the inner layers of the LPP. Therefore, we were unable to determine the conformation of the CER NS with the head group located at the unit cell boundaries of the LPP.

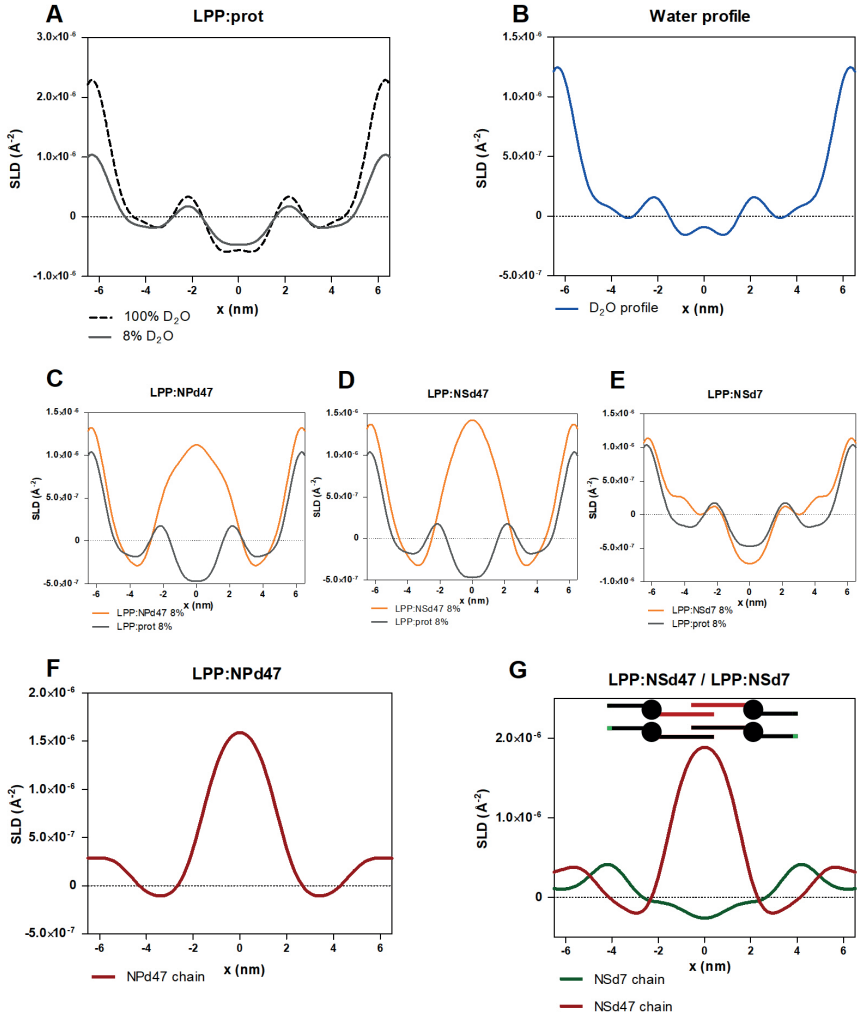


Figure 4. Neutron SLD profiles of: (A) LPP:prot, measured at 100% (top dashed line) and 8% (bottom solid line) D_2O/H_2O hydration; (B) The D_2O (water) profile determined from the difference between the 100% and 8% SLD profiles of the LPP:prot model; (C) LPP:prot (grey line) and LPP:NPd47 (orange) overlapped, both measured at 8% D_2O/H_2O buffer ratio – the difference between these represents the net SLD profile of the deuterated moiety; (D) LPP:prot (grey) and LPP:NSd47 (orange) samples, at 8% D_2O/H_2O hydration; (E) LPP:prot (grey) and LPP:NSd7 (orange) models, measured at 8% D_2O/H_2O; (F) The net SLD profile of the perdeuterated CER NPd47 chain (red line), determined from the SLD profile of LPP:prot subtracted from the LPP:NPd47 model; (G) The net SLD profile of the deuterated acyl chain of CER NSd47 (red line) and sphingosine chain of CER NSd7 (green line) obtained from the two models: LPP:NSd47 and LPP:NSd7. The maximum SLD intensity for the NSd47 chain was predominantly localized in the inner layer of the LPP unit, but with a small part also in the outer layers, while NSd7 was located in the outer layers of the LPP.

$\nu_s CH_2$ frequencies indicate mixing of the lipids

Information about the thermotropic behavior and the lipid packing is obtained from the $\nu_s CH_2$ peak position in the FTIR spectra. The $\nu_s CH_2$ vibrations are a measure for the conformational disordering of the hydrocarbon chains. Based on the $\nu_s CH_2$ wavenumber, the transitions from an ordered to a disordered lipid model can be monitored. Figure 5A depicts the thermotropic behavior of the LPP:prot sample. The $\nu_s CH_2$ vibrations indicate that between 10°C and 35°C the lipid chains of the LPP:prot model were organized in an ordered phase ($\nu_s CH_2$ peak position at 10°C: 2849 cm^{-1}). Between 35-40°C a transition from the orthorhombic to the hexagonal phase occurred. This is monitored by an increase of the $\nu_s CH_2$ peak wavenumber with ~1 cm^{-1}. A further increase of the temperature of the sample resulted in a gradual increase of the wavenumber and at around 69°C the phase transition from the ordered to the disordered fluid phase started. During this transition the $\nu_s CH_2$ wavenumber increased from 2850.5 cm^{-1} to 2854 cm^{-1}.

The presence of phase separation in the lipid samples was examined by systematically replacing protiated lipids by their deuterated counterparts (CER NSd47, CER NPd47 and DFFA24). The $\nu_s CH_2$ and $\nu_s CD_2$ thermotropic responses of the single replacements of the CERs are provided in Figure 5 B, C. The shifts in the wavenumber of the $\nu_s CD_2$ and the $\nu_s CH_2$ vibrations indicate an hexagonal to liquid phase transition in a similar temperature range in the LPP:NSd47 and LPP:NPd47 samples, between 65-70°C. A similar temperature range for the phase transitions is a first indication that the deuterated and protiated lipids mixed in the same lattice. In the $\nu_s CD_2$ vibrations, the orthorhombic to hexagonal transition is hardly visible due to the shift in the $\nu_s CD_2$ frequency being less sensitive to this phase transition (55).

When including deuterated DFFA24 alongside either NSd47 or NPd47 in the LPP model, the wavenumber $\nu_s CH_2$ peak at 10°C was increased to ~2850.5 cm^{-1} for both compositions (Supplemental Figure S2), indicating a higher conformational disordering of the remaining protiated lipids. A similar effect was also observed when FFA and both the CER NS and CER NP were replaced by their deuterated counterparts (LPP:NSd47:NPd47:DFFA24, Figure 5D) with a further increase to ~2850.8 cm^{-1}. This wavenumber increase of the $\nu_s CH_2$ peak position indicates that the acyl chain of CER EOS with the protiated sphingoid base of CER NS and CER NP had a higher mobility than the acyl chains of CER NS, CER NP and the DFFA24. Moreover, the shift of the $\nu_s CH_2$ wavenumber at 32-34°C indicates an orthorhombic to hexagonal phase transition, which means that a part of the remaining protiated lipids are in an orthorhombic packing, despite the higher wavenumber. This increase in wavenumber is caused by the linoleate chain of CER EOS that represents approximately 19% of the total protiated fraction of hydrocarbon chains and it was previously reported to be in a liquid phase (19). Table 2 displays the $\nu_s CH_2$ and $\nu_s CD_2$ peak wavenumber at 10°C and the mid-transition temperatures from an ordered to a disordered phase.

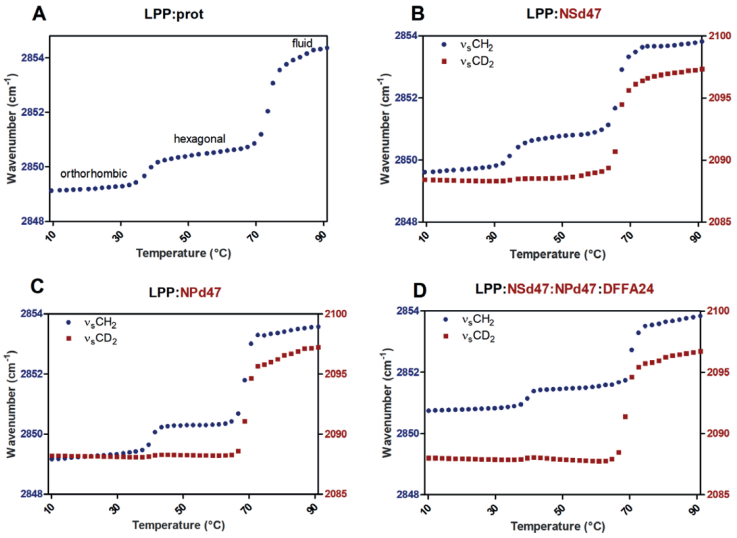


Figure 5. Thermotropic curves of the stretching vibrations for the LPP:prot lipid model (A) and deuterated models with CER NSd47(B) and CER NPd47(C) and the LPP model with CER NSd47, CER NPd47 and DFFA24 (D). The phase transitions temperatures of the lipids are plotted as a function of the ν_sCH_2 and ν_sCD_2 peak position, on the left and right y-axis, respectively. Both the protiated (blue circle) and deuterated (red square) lipids melted over the same temperature range, indicating that the deuterated lipids were integrated with the protiated lipids in the model membrane.

Table 2. The wavenumber corresponding to the ν_sCH_2 and ν_sCD_2 peak positions at 10°C, while the lipids were organized in an orthorhombic packing (shown as the mean value of n≥3 measurements, SD of ± 0.1 cm^{-1}) and the mid-point transition temperatures (T_M) for the ordered-disordered (hexagonal – liquid) phase transitions (average ± SD, n≥3).

Lipid model	ν_sCH_2 wavenumber (cm^{-1})	ν_sCD_2 wavenumber (cm^{-1})	T_M ordered-disordered phase transition (°C)
LPP:prot	2849.0	-	71.2 ± 1.2
LPP:NSd47	2849.4	2088.3	71.4 ± 1.0
LPP:NPd47	2849.1	2088.3	68.0 ± 1.5
LPP:NSd47:DFFA24	2850.4	2088.1	66.9 ± 1.5
LPP:NPd47:DFFA24	2850.5	2088.1	68.5 ± 1.7
LPP:NSd47:NPd47:DFFA24	2850.8	2088.0	69.2 ± 3.3

CD_2-CD_2 chain interactions provide information about the CER arrangement

To investigate the packing and mixing of the lipid chains in more details, the shape and splitting of the δCH_2 and δCD_2 frequencies were examined. The δCH_2 vibrations of the LPP:prot sample at 10°C is presented in Figure 6A (black line). Two peaks were observed at 1463 and 1473 cm^{-1} with a deep minimum in between, an indication that most of the lipid chains were densely organized in an orthorhombic packing, while the small peak at 1467 cm^{-1} represented the hexagonal packing adopted by a fraction of the lipids. The splitting

distance between the two δCH_2 peaks was calculated and for the LPP:prot model this distance was 10.3 ± 0.1 cm^{-1}. Comparing this with pure FFA C24, with a maximum δCH_2 peak splitting of 10.7 cm^{-1} (not shown), provides an indication that the size of the domains forming an orthorhombic phase are close to 100 lipid molecules (56, 57).

In partially deuterated lipid samples, the δCH_2 and δCD_2 vibrations of the hydrocarbon chains cannot directly interact due to the large vibrational energy difference (CH_2: ~1470 cm^{-1}; CD_2: ~1090 cm^{-1}). If the deuterated lipid chains are neighboring one another in large domains, the minima between the two δCD_2 peaks would be very deep due to the large number of CD_2-CD_2 interactions (pure DFFA24 has the maximum splitting distance of 7.3 ± 0.1 cm^{-1}, representing a deuterated chain domain size of at least 100 lipid molecules). A decrease in the δCD_2 splitting distance represents a smaller deuterated domain size. However, if the protiated and deuterated lipid chains are fully integrated and participate in the same orthorhombic lattice, the interaction will be lost and only one peak will be observed. The δCH_2 and δCD_2 vibrations in the infrared spectrum of the lipid membranes with deuterated CER NSd47, CER NPd47 and/or DFFA24 were examined. In Figure 6A and 6B the δCH_2 and δCD_2 vibrations are provided measured at 10°C. Substituting either CER NS or CER NP with its deuterated counterpart (LPP:NSd47 and LPP:NPd47, respectively) resulted in a splitting distance of the δCH_2 peaks of 9.3±0.1 cm^{-1} (LPP:NSd47 model) and 9.5±0.1 cm^{-1} (LPP:NPd47 model) (Table 3). A peak height ratio was calculated for the δCH_2 peaks, to evaluate the difference of the average height of the two orthorhombic peaks (at 1473 and 1463 cm^{-1}) and the peak height of the central peak (1467 cm^{-1}). Fitting these peaks and calculating their ratio allows a quantitative assessment of the chain interactions present in the model. The peak height ratio of the LPP:NPd47 composition is also different compared to the ratio in the spectrum of the protiated sample (Table 3) suggesting that protiated and deuterated chains are neighboring. However, the fittings did not lead to a statistically significant difference. A single peak is observed for the δCD_2 vibrations at 1088 cm^{-1} demonstrating that the deuterated lipids did not form separate lipid domains.

Next, FFA24 was replaced by DFFA24 alongside either CER NSd47 or CER NPd47 (Figure 6A and B: LPP:NSd47:DFFA24 and LPP:NPd47:DFFA24 models respectively). These two compositions displayed very different splitting of the scissoring vibrations in the spectra than observed for the LPP:NSd47 and LPP:NPd47 samples and both compositions showed a similar trend. The δCH_2 vibrations were characterized by a single peak at ~1468 cm^{-1} indicating that protiated hydrocarbon chains in orthorhombic packing are not neighboring. Two separated scissoring modes were observed in the δCD_2 vibrations at 1086 and 1091 cm^{-1}. The δCD_2 peak to peak distance was 5.2 ± 0.0 cm^{-1} (LPP:NSd47:DFFA24 model) and 5.4 ± 0.1 cm^{-1} (LPP:NPd47:DFFA24 model) (Table 3). These results demonstrate that the deuterated acyl chains of the CER NSd47 or CER NPd47 were frequently neighboring the DFFA24 chains, as the introduction of DFFA24 allowed the coupling of the CD_2-CD_2 vibrations. To obtain quantitative information, the peak height

ratio between the two orthorhombic scissoring modes (at 1086 and 1091 cm^{-1}) and the central scissoring mode (at 1088.5 cm^{-1}) was calculated by peak fitting (Table 3). The statistical analysis results (t-test with P <0.05) show that the peak height ratio for the LPP:NPd47:DFFA24 model is significantly higher than for the LPP:NSd47:DFFA24, illustrating that the CH_2-CD_2 chain interactions were less pronounced for the LPP:NPd47:DFFA24 than for the LPP:NSd47:DFFA24 model. Thus, in the LPP:NSd47:DFFA24 model the protiated and deuterated chains were more frequently neighboring compared to the LPP:NPd47:DFFA24 model.

Finally, when the majority of lipids were deuterated creating a model with DFFA24, NSd47 and NPd47, the FTIR spectrum displayed an increased δCD_2 vibration peak splitting of 6.4 ± 0.1 cm^{-1}, indicating a larger mean domain size of the deuterated chains in an orthorhombic packing (Table 3). The δCD_2 vibration of the LPP:NSd47:NPd47:DFFA24 lipid sample had a deeper minima between the two peaks than in the δCD_2 vibrations of the LPP:NSd47:DFFA24 and LPP:NPd47:DFFA24 models (Table 3). This suggests that the deuterated acyl chains of CER NS and CER NP were located in the same regions of the LPP unit demonstrating less CH_2-CD_2 interactions. The single peak observed in the δCH_2 vibrations of this model indicates that the protiated lipid chains did not form phase separated domains and they were well mixed with the deuterated lipids or the remaining protiated lipids are partly in a hexagonal phase.

The neutron diffraction measurements were performed at 25°C, however the lipid organization of these models is similar to that at 10°C and this data for the δCH_2 and δCD_2 vibrations is shown in the Supplemental Figure S3.

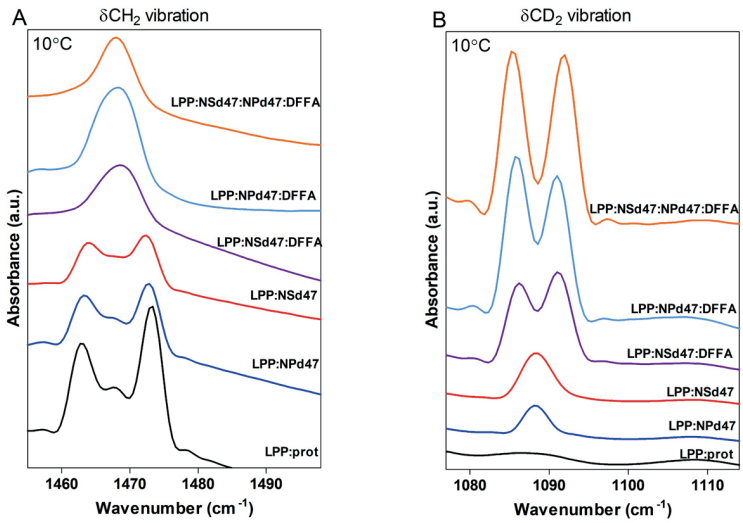


Figure 6. The FTIR peak splitting of the (A) δCH_2 and (B) δCD_2 vibrations for the six LPP model membranes, measured at 10°C, when the lipids were packed in the orthorhombic phase. Each curve has an annotation with the lipid model it represents.

Table 3. Peak splitting values of the δCH_2 and δCD_2 vibrations the for the six models, at 10°C, the peak height ratio of the δCH_2 peaks (average of the peak height of the orthorhombic peaks at 1473 and 1463 cm^{-1} compared to the middle peak at 1467 cm^{-1}) and peak height ratio of the δCD_2 (average peak height of the orthorhombic peaks at 1086 and 1091 cm^{-1} divided by the peak height of the middle peak at ~1088.5 cm^{-1}). The values are shown as average ± SD of n≥3 measurements.

Lipid model	δCH_2 peak split (cm^{-1})	δCD_2 peak split (cm^{-1})	δCH_2 peak height ratio (OR/MID)	δCD_2 peak height ratio (OR/MID)
LPP:prot	10.3 ± 0.1	-	3.1 ± 0.2	-
LPP:NSd47	9.3 ± 0.1	-	2.5 ± 0.1	-
LPP:NPd47	9.5 ± 0.1	-	2.4 ± 0.1	-
LPP:NSd47:DFFA24	-	5.2 ± 0.0	-	3.1 ± 0.2
LPP:NPd47:DFFA24	-	5.4 ± 0.1	-	3.5 ± 0.1
LPP:NSd47:NPd47:DFFA24	-	6.4 ± 0.1	-	5.0 ± 0.1

DISCUSSION

In the present study a lipid model membrane consisting of CER EOS, CER NS, CER NP, CHOL and FFA C24 forming the LPP was investigated. Previous studies revealed that the unit cell of the LPP has a three-layer structure (32, 40). In this study we were particularly interested in the location of CER NP in the LPP, as CER NP is the most abundant CER subclass in human SC (6-8, 10, 11, 30). This was compared to the position of CER NS, which is the most abundant CER subclass in mice, dog and porcine SC (11, 27-29). Our results show both the acyl chains of CER NP and of CER NS are not only positioned in the central layer, but a minor part of the chains is also located in the outer layers of the LPP. Furthermore, the arrangement of the CER NP and CER NS positioned in the central layer is for both CERs primarily linear. Based on these results, we proposed the molecular arrangement of the lipids in the LPP unit, depicted in Figure 7, adapted from the structure proposed by Mojumdar et al (44).

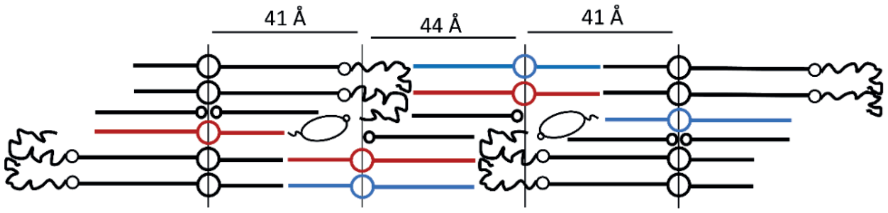


Figure 7. The molecular arrangement of the trilayer structure of the LPP unit according to the locations of CER NP and CER NS determined in this study and the positions of CER EOS, CHOL and FFA C24 determined previously (40, 44). CER NS is depicted in red, CER NP in blue, while CER EOS, CHOL and FFA C24 are drawn in black. The figure is adapted with permission from Mojumdar et al (44).

Arrangement of CER NP in unit cell of the LPP

Using neutron diffraction, six diffraction orders of the LPP could be detected and we demonstrate a symmetric arrangement of the LPP unit cell, in agreement with previous studies which elucidated the electron density profile of the LPP trilayer using X-ray diffraction (32). The SLD profile of the LPP:NPd47 model revealed that most of the deuterated acyl chains of CER NP are located in the central layer, but a minor fraction is also positioned in the outer layers of the unit cell of the LPP (Figure 7). The FTIR results for the LPP:NPd47:DFFA24 model demonstrate that the acyl chains of CER NPd47 and the DFFA24 chains are neighboring, as shown by the interactions of the deuterated chains and the δCD_2 peak height ratio (OR/MID) for this composition. Thus, these chains are located in close proximity in the central layer of the unit cell.

The conformation of CER NP in a LPP model membrane has also not been examined before. Information on whether this lipid adopts a hairpin or an extended conformation can be obtained from the FTIR measurements. Focusing on the splitting of the δCD_2 vibrations for the LPP:NPd47:DFFA24 and LPP:NSd47:NPd47:DFFA24 models, the inner layer of the LPP is characterized by large size domains of deuterated chains. In a hairpin structure, the protiated CER NP phytosphingosine chains are neighboring the deuterated acyl chains and this would strongly disturb the CD_2-CD_2 interactions in this layer and thus precludes a large splitting as encountered in the δCD_2 vibrations. However, the opposite occurs, as when deuterated CER NP is used, the deuterated domain sizes increase. Therefore, it is very likely that CER NP adopts primarily an extended conformation with the phytosphingosine and acyl chains on either side of the headgroup.

Arrangement of CER NP in comparison with CER NS in the LPP models

The SLD profile of the unit cell of the model membrane that includes CER NPd47 is similar to the model with CER NSd47, thus the deuterated acyl chain of CER NS is not only located in the center of the LPP unit, but a minor fraction is also located in the two boundary lipid layers. Assuming a C-C bond length of 0.125 nm, the length of the C24 acyl chain is approximately 2.9 nm (46). As the inner layer of the LPP has a total length of approximatively 4.4 nm, the acyl chains are interdigitated, as illustrated in the schematic arrangement proposed in Figure 7. Interdigitating chains are quite often encountered in SC lipid organization and it has been previously reported in SPP models (36, 49, 58-60) and LPP models (40, 44), as well as in computational models of the SC lipid models (61). All these studies support the interdigitated acyl chains and FFA chains in SC lamellar structures. In one of these papers, it has been discussed why interdigitation is more likely to occur to fit the chain length with the width of the central lipid layer than the alternative, namely a large angle of the acyl and FFA chain with the basal plain of the lipid membrane (46). The results of this study are in agreement with the molecular organization proposed in earlier studies, which examined the localization of the acyl chain

of CER NS both in a simple model, comprising of only CER EOS and CER NS, and a complex lipid model mimicking the lipid composition of porcine SC (40, 46).

The difference between the structure of CER NP and CER NS is the C4-hydroxyl group located on the phytosphingosine chain, instead of the double bond of CER NS. This extra hydroxyl group can cause different lipid head group interactions. It was previously shown that the additional OH group of CER NP was very important in the formation of hydrogen bonds with surrounding hydrogen donors/acceptors (62), and CER NP caused 25% more H-bonds in a lipid bilayer, compared to CER NS (63). Moreover, it was hypothesized that the H-bonding could be participating in the connection of the ordered lipid domains in SC and decreasing the permeability of the SC, thus highlighting the importance of the CER NP subclass for the SC lipid matrix (62).

When comparing the δCD_2 vibrations of the LPP:NPd47:DFFA24 and LPP:NSd47:DFFA24 models an interesting difference is noticed. The δCD_2 peak height ratio (the two orthorhombic peaks resulting from the CD_2-CD_2 interactions) compared to the central peak (resulting from the CD_2-CH_2 interaction) for the LPP:NSd47:DFFA24 model is significantly lower than for the LPP:NPd47:DFFA24. This difference suggests that more CD_2-CH_2 interactions are encountered in the LPP:NSd47:DFFA24 model, compared to the LPP:NPd47:DFFA24 model. This likely occurs in the outer layers of the LPP, where the protiated CER EOS and sphingoid chains are located and can interact with the deuterated acyl chains of the CERs. However, the neutron diffraction data indicates that the location of the two CERs is the same in the LPP trilayer. It might be that the δCD_2 vibrations in the FTIR spectra are more sensitive to small differences in the localization of CER NS and CER NP.

The arrangement of CER NS is not changed in lipid models of different complexity

CER NS is the most frequently investigated CER subclass with regard to its properties and molecular arrangement in model membranes mimicking the SC lipid composition. The arrangement of CER NS was also examined in our study, when analyzing the SLD profile of the LPP:NSd7 system. These results demonstrate the extended conformation of CER NS that is located in the inner layer of the LPP unit, as the acyl and sphingosine chains of CER NS are positioned on either side of the head group, as shown in Figure 7. Based on the length of the sphingosine C18 chain, which extends over 15 C-C bonds from the head group, and assuming the length of the C-C bond of 0.125 nm, the total length of the sphingosine chain is approximatively 1.9 nm. Taking into account the location of the inner lipid head groups, the position of the terminally deuterated sphingosine chain of CER NS is calculated to be at 4.1 nm from the center, being close to the experimentally observed location.

Recent studies by Beddoes et al. provided insights into the conformation of CER NS both in a membrane prepared with a complex synthetic porcine CER mixture and a simple LPP lipid model system prepared with only two CER subclasses, CER EOS and NS (46, 64).

In these studies, it was also concluded that CER NS with the head group in the inner head group layers adopts an extended conformation. Furthermore, in this paper it was thoroughly discussed why interdigitation occurs in the central layer of the LPP. An extended conformation of CER NS was also proposed in a SPP model composed of CER NS C24: CHOL: FFAC24, with an equimolar ratio of the lipids (65). This system was studied with ^{2}H NMR and FTIR and it was concluded that the acyl chain of CER NS was neighboring the FFAC24 chain and thus CER NS is present in a linear conformation in the SPP, similarly as observed in the LPP (46, 64).

Lipid ordering in the outer layers of the LPP

When comparing the $\nu_s CH_2$ peak positions of the LPP:prot and the LPP NSd47:NP47:DFFA24, the corresponding $\nu_s CH_2$ frequencies indicate that the outer layers of the unit cell of the LPP, where CHOL, CER EOS and the sphingoid chains of CER NS and CER NP are located, have a higher conformational disordering than the central region, where the acyl chains of CER NS and CER NP are primarily positioned. Furthermore, in the LPP:NSd47:NPd47:DFFA24 model the protonated lipid chains adopt at least partially an orthorhombic organization at 10°C, even though there is an increased $\nu_s CH_2$ frequency. This can be concluded from the orthorhombic to hexagonal packing observed in the thermotropic behavior of $\nu_s CH_2$ frequencies, indicating the phase transition occurs at 32-34°C. However, the single peak observed in the δCH_2 vibrations of this model, attributed primarily to the protiated chains in the outer layers, indicates that a part of the protiated lipid chains may adopt a hexagonal packing. The presence of a hexagonal phase is also observed in the δCH_2 vibrations of the LPP:prot model, which are characterized by two separated peaks and a small central peak, the latter indicating that at 10°C not all lipid chains are organized in an orthorhombic packing. Considering the proposed molecular organization of the LPP unit and the observations mentioned above, the sphingoid bases could be contributing to the formation of the hexagonal (less densely packed) phase, as it was suggested for a SPP model with CER NS (65).

Extrapolation of the results to the lipid matrix in SC

Understanding the arrangement of the barrier lipids within the SC is important for advancing the knowledge on the skin barrier function. The results of this study contribute to a better understanding of the SC lipid organization. First of all, CER NS and CER NP are positioned at the same location in the unit cell of the LPP and both CER subclasses are primarily aligned in a linear arrangement, in which the acyl chains are interdigitating together with the FFA chains. This linear arrangement has various advantages for the SC to provide an excellent barrier. Due to the reduced cross section per lipid molecule in a linear arrangement compared to the hairpin structure, the linear arrangement accommodates a

tighter packing of the hydrocarbon chains in the structure, which is favorable for the barrier functionality (66).

Furthermore, a linear arrangement makes the structure more flexible as the interdigitating chain length can be adapted to the requirements to obtain a dense and thermodynamically stable structure**.** A linear conformation of CER NS and CER NP also provides a tight connection of the adjacent lipid layers, so it reduces the permeability through the SC lipid matrix (66) and it discourages swelling of the lipid lamellae during hydration (19). In this respect it is important to mention that a linear arrangement has been proposed not only in the LPP, but also in the SPP unit cell with CER NS (65). Interestingly in both the LPP and SPP unit structure, the CHOL is at a similar position as the sphingoid base of the CERs, while the FFA chains and acyl chains are neighboring. A linear arrangement has also been proposed for the molecular models proposed by Norlén et al (67).

Another important message is the similar position of the acyl chains of both CER NP and CER NS in the LPP unit as it indicates the adaptability of the lamellar phase to differences in the lipid head group architecture**.** This observation is a possible explanation that while in human SC CER NP is one of the most prevalent CER subclasses, in mice, porcine and dog SC CER NS is the most abundant one, the SC lipid organization is very similar in all species. However, the effect of changing the concentration of CER NS and CER NP on their position and alignment in the unit cell of the LPP has not yet been investigated and may affect the outcome.

Using Ruthenium tetroxide (RuO_4) staining the lamellar organization in SC was for the first time reported by Madison et al. (68). These studies showed broad-narrow-broad sequence of lucent bands in one repeating unit. RuO_4 is a strong oxidizer that reacts with the double bonds of the lipid chains and the hydroxyl groups of the CERs (69). Thus, both the head groups and the linoleate position will turn into dark regions in the electron micrographs. As the CER EOS linoleate chains are present in the inner part of the central region close to the inner head group region, this inner region represents the narrow lucent band, while the two broad lucent bands represent the two outer regions. Therefore, our proposed molecular arrangement is in agreement with the RuO_4 pattern reported.

Selection of the CER composition in the lipid systems

As the composition of the human SC lipid matrix is too complex to selectively analyze the localization of individual CER subclasses in the LPP structure, model systems composed of selected lipids can be used. Previous studies show that lipid models provide reproducible structures mimicking those found in SC of native skin. These lipid models consisted of CERs extracted from native porcine or human SC (29, 32), or a synthetic CER composition that mimicked the CER composition of the porcine SC (31, 32, 70). However, to obtain more detailed information about the molecular arrangement, a simple model with a limited number of lipids is required. The advantage of a simple model is the possibility to

incorporate sufficient deuterated CERs of interest to provide information about the interactions between different lipid subclasses, thus we chose such a model for studying the localization of CER NP and CER NS in the LPP unit.

An important difference between the native SC lipid composition and the synthetic lipid models is the concentration of CER EOS. This CER is crucial for the formation of the LPP and varying its concentration leads to forming simultaneous an LPP and SPP phase at 15 mol% (32, 41, 71), the approximate level in human SC, while a minimum of 30 mol% CER EOS is required for the formation of only the LPP (41, 72). Increasing the concentration of CER EOS to 40 mol% did not change the LPP structure and organization and resulted in a peak separation of crystalline CHOL and the fourth order diffraction peak of the LPP, important for analyzing neutron data (42).

CONCLUSION

In this study we determined for the first time the position of the acyl chain of CER NP in the LPP unit cell of a simple lipid model membrane. Our studies revealed that in the 12.6 nm repeating unit of the LPP, the acyl chain of CER NP is predominantly located in the central part of the trilayer structure, with a minor fraction present at the unit cell boundary. The location and the arrangement of CER NP was similar to that of CER NS and both CERs adopt a linear arrangement, indicating that even though there is a difference in the headgroup structure of CER NS and CER NP, they adopt a similar molecular arrangement in the LPP unit. This study expands the current knowledge of the molecular arrangement of lipids in the LPP, a very important structure present in the native SC.

ACKNOWLEDGEMENTS

The project was supported by the National Institute of Arthritis and Muscoskeletal and Skin Diseases, grant number R01AR072679. We thank Evonik (Essen, Germany) for their kind donation of the CERs. We are grateful to the personnel at ISIS Neutron and Muon Source (Didcot, United Kingdom) for awarding us experimental beamtime and their assistance during the neutron scattering measurements. ISIS raw neutron data DOI: 10.5286/ISIS.E.RB1969000 (73).

REFERENCES

1. Proksch, E., Brandner, J. M., Jensen, J.-M. (2008). The skin: an indispensable barrier. *Experimental Dermatology*. 17(12), 1063-72.
2. Wertz, P. W., van den Bergh, B. (1998). The physical, chemical and functional properties of lipids in theskin and other biological barriers. *Chem Phys Lipids*. 91, 85-96.
3. Wertz, P. W., Miethke, M. C., Long, S. A., Strauss, J. S., Downing, D. T. (1985). The composition of the ceramides from human stratum corneum and from comedones. *J Invest Dermatol*. 84(5), 410-2.
4. Weerheim, A., Ponec, M. (2001). Determination of stratum corneum lipid profile by tape stripping in combination with high-performance thin-layer chromatography. *Arch Dermatol Res*. 293, 191-9.
5. Ponec, M., Weerheim, A., Lankhorst, P., Wertz, P. (2003). New Acylceramide in Native and Reconstructed Epidermis. *J Invest Dermatol*. 120(4), 581-8.
6. Masukawa, Y., Narita, H., Shimizu, E., Kondo, N., Sugai, Y., Oba, T., et al. (2008). Characterization of overall ceramide species in human stratum corneum. *J Lipid Res*. 49(7), 1466-76.
7. van Smeden, J., Hoppel, L., van der Heijden, R., Hankemeier, T., Vreeken, R. J., Bouwstra, J. A. (2011). LC/MS analysis of stratum corneum lipids: ceramide profiling and discovery. *J Lipid Res*. 52(6), 1211-21.
8. t'Kindt, R., Jorge, L., Dumont, E., Couturon, P., David, F., Sandra, P., et al. (2012). Profiling and characterizing skin ceramides using reversed-phase liquid chromatography-quadrupole time-of-flight mass spectrometry. *Anal Chem*. 84(1), 403-11.
9. Motta, S., Monti, M., Sesana, S., Caputo, R., Carelli, S., Ghidoni, R. (1993). Ceramide composition of the psoriatic scale. *Biochim Biophys Acta*. 1182, 147-51.
10. van Smeden, J., Bouwstra, J. A. (2016). Stratum Corneum Lipids: Their Role for the Skin Barrier Function in Healthy Subjects and Atopic Dermatitis Patients *Curr Probl Dermatol* 48, 8-26.
11. Kawana, M., Miyamoto, M., Ohno, Y., Kihara, A. (2020). Comparative profiling and comprehensive quantification of stratum corneum ceramides in humans and mice by LC/MS/MS. *J Lipid Res*. 61(6), 884-95.
12. Bouwstra, J. A., Gooris, G. S., van der Spek, J. A., Bras, W. (1991). Structural investigations of human stratum corneum by small-angle X-ray scattering. *J Invest Dermatol*. 97(6), 1005-12.
13. White, S. H., Mirejovsky, D., King, G. I. (1988). Structure of Lamellar Lipid Domains and Corneocyte Envelopes of Murine Stratum Corneum. An X-ray Diffraction Study. *Biochemistry*. 27, 3725-32.
14. Damien, F., Boncheva, M. (2010). The extent of orthorhombic lipid phases in the stratum corneum determines the barrier efficiency of human skin in vivo. *J Invest Dermatol*. 130(2), 611-4.
15. Boncheva, M., Damien, F., Normand, V. (2008). Molecular organization of the lipid matrix in intact Stratum corneum using ATR-FTIR spectroscopy. *Biochim Biophys Acta*. 1778(5), 1344-55.
16. Mendelsohn, R., Rerek, M. E., Moore, D. J. (2000). Infrared spectroscopy and microscopic imaging of stratum corneum models and skin. *Physical Chemistry Chemical Physics*. 2(20), 4651-7.
17. Bouwstra, J. A., Gooris, G. S., Dubbelaar, F. E., Ponec, M. (2002). Phase behavior of stratum corneum lipid mixtures based on human ceramides: the role of natural and synthetic ceramide 1. *J Invest Dermatol*. 118(4), 606-17.
18. Bouwstra, J., Gooris, G., Ponec, M. (2002). The Lipid Organisation of the Skin Barrier: Liquid and Crystalline Domains Coexist in Lamellar Phases. *Journal of Biological Physics*. 28, 211-23.
19. Paz Ramos, A., Gooris, G., Bouwstra, J., Lafleur, M. (2018). Evidence of hydrocarbon nanodrops in highly ordered stratum corneum model membranes. *J Lipid Res*. 59(1), 137-43.
20. Janssens, M., van Smeden, J., Gooris, G. S., Bras, W., Portale, G., Caspers, P. J., et al. (2011). Lamellar lipid organization and ceramide composition in the stratum corneum of patients with atopic eczema. *J Invest Dermatol*. 131(10), 2136-8.
21. Sahle, F. F., Gebre-Mariam, T., Dobner, B., Wohlrab, J., Neubert, R. H. (2015). Skin diseases associated with the depletion of stratum corneum lipids and stratum corneum lipid substitution therapy. *Skin Pharmacol Physiol*. 28(1), 42-55.
22. Di Nardo, A., Wertz, P. W., Giannetti, A., Seidenari, S. (1998). Ceramide and Cholesterol Composition of the Skin of Patients with Atopic Dermatitis. *Acta Derm Venereol* 78, 27-30.

23. Janssens, M., van Smeden, J., Gooris, G. S., Bras, W., Portale, G., Caspers, P. J., et al. (2012). Increase in short-chain ceramides correlates with an altered lipid organization and decreased barrier function in atopic eczema patients. *J Lipid Res*. 53(12), 2755-66.
24. van Smeden, J., Al-Khakany, H., Wang, Y., Visscher, D., Stephens, N., Absalah, S., et al. (2020). Skin barrier lipid enzyme activity in Netherton patients is associated with protease activity and ceramide abnormalities. *J Lipid Res*. 61(6), 859-69.
25. Imokawa, G., Abe, A., Jin, K., Higaki, Y., Kawashima, M., Hidano, A. (1991). Decreased level of ceramides in stratum corneum of atopic dermatitis: an etiologic factor in atopic dry skin? *J Invest Dermatol*. 96(4), 523-6.
26. Yokose, U., Ishikawa, J., Morokuma, Y., Naoe, A., Inoue, Y., Yasuda, Y., et al. (2020). The ceramide [NP]/[NS] ratio in the stratum corneum is a potential marker for skin properties and epidermal differentiation. *BMC Dermatology*. 20(1).
27. Chermprapai, S., Broere, F., Gooris, G., Schlotter, Y. M., Rutten, V., Bouwstra, J. A. (2018). Altered lipid properties of the stratum corneum in Canine Atopic Dermatitis. *Biochim Biophys Acta Biomembr*. 1860(2), 526-33.
28. Wertz, P. W., Downing, D. T. (1983). Ceramides of pig epidermis: structure determination. *J Lipid Res*. 24(6), 759-65.
29. Bouwstra, J., Gooris, G., Cheng, K., A., W., Bras, W., Ponec, M. (1996). Phase behavior of isolated skin lipids. *J Lipid Res*. 37, 999 - 1011.
30. Masukawa, Y., Narita, H., Sato, H., Naoe, A., Kondo, N., Sugai, Y., et al. (2009). Comprehensive quantification of ceramide species in human stratum corneum. *J Lipid Res*. 50(8), 1708-19.
31. de Jager, M. W., Gooris, G. S., Dolbnya, I. P., Ponec, M., Bouwstra, J. A. (2004). Modelling the stratum corneum lipid organisation with synthetic lipid mixtures: the importance of synthetic ceramide composition. *Biochim Biophys Acta*. 1664(2), 132-40.
32. Groen, D., Gooris, G. S., Bouwstra, J. A. (2009). New insights into the stratum corneum lipid organization by X-ray diffraction analysis. *Biophys J*. 97(8), 2242-9.
33. Janssens, M., Gooris, G. S., Bouwstra, J. A. (2009). Infrared spectroscopy studies of mixtures prepared with synthetic ceramides varying in head group architecture: coexistence of liquid and crystalline phases. *Biochim Biophys Acta*. 1788(3), 732-42.
34. Uche, L. E., Gooris, G. S., Bouwstra, J. A., Beddoes, C. M. (2019). Barrier Capability of Skin Lipid Models: Effect of Ceramides and Free Fatty Acid Composition. *Langmuir*. 35(47), 15376-88.
35. van Smeden, J., Janssens, M., Gooris, G. S., Bouwstra, J. A. (2014). The important role of stratum corneum lipids for the cutaneous barrier function. *Biochim Biophys Acta*. 1841(3), 295-313.
36. Mojumdar, E. H., Groen, D., Gooris, G. S., Barlow, D. J., Lawrence, M. J., Deme, B., et al. (2013). Localization of cholesterol and fatty acid in a model lipid membrane: a neutron diffraction approach. *Biophys J*. 105(4), 911-8.
37. Bouwstra, J. A., Gooris, G. S., Dubbelaar, F. E., Weerheim, A., IJzerman, A. P., Ponec, M. (1998). Role of ceramide 1 in the molecular organization of the stratum corneum lipids. *J Lipid Res*. 39, 186-96.
38. Groen, D., Gooris, G. S., Bouwstra, J. A. (2010). Model membranes prepared with ceramide EOS, cholesterol and free fatty acids form a unique lamellar phase. *Langmuir*. 26(6), 4168-75.
39. Opálka, L., Kováčik, A., Pullmannová, P., Maixner, J., Vávrová, K. (2020). Effects of omega-O-acylceramide structures and concentrations in healthy and diseased skin barrier lipid membrane models. *J Lipid Res*. 61(2), 219-28.
40. Mojumdar, E. H., Gooris, G. S., Barlow, D. J., Lawrence, M. J., Deme, B., Bouwstra, J. A. (2015). Skin lipids: localization of ceramide and fatty acid in the unit cell of the long periodicity phase. *Biophys J*. 108(11), 2670-9.
41. Uche, L. E., Gooris, G. S., Bouwstra, J. A., Beddoes, C. M. (2021). High concentration of the ester-linked omega-hydroxy ceramide increases the permeability in skin lipid model membranes. *Biochim Biophys Acta Biomembr*. 1863(1), 183487.
42. Gooris, G. S., Kamran, M., Kros, A., Moore, D. J., Bouwstra, J. A. (2018). Interactions of dipalmitoylphosphatidylcholine with ceramide-based mixtures. *Biochim Biophys Acta Biomembr*. 1860(6), 1272-81.

43. Kessner, D., Kiselev, M., Dante, S., Hauss, T., Lersch, P., Wartewig, S., et al. (2008). Arrangement of ceramide [EOS] in a stratum corneum lipid model matrix: new aspects revealed by neutron diffraction studies. *Eur Biophys J*. 37(6), 989-99.
44. Mojumdar, E. H., Gooris, G. S., Groen, D., Barlow, D. J., Lawrence, M. J., Deme, B., et al. (2016). Stratum corneum lipid matrix: Location of acyl ceramide and cholesterol in the unit cell of the long periodicity phase. *Biochim Biophys Acta*. 1858(8), 1926-34.
45. Eichner, A., Sonnenberger, S., Dobner, B., Hauss, T., Schroeter, A., Neubert, R. H. H. (2016). Localization of methyl-branched ceramide [EOS] species within the long-periodicity phase in stratum corneum lipid model membranes: A neutron diffraction study. *Biochim Biophys Acta*. 1858(11), 2911-22.
46. Beddoes, C. M., Gooris, G. S., Foglia, F., Ahmadi, D., Barlow, D. J., Lawrence, M. J., et al. (2020). Arrangement of Ceramides in the Skin: Sphingosine Chains Localize at a Single Position in Stratum Corneum Lipid Matrix Models. *Langmuir*. 36(34), 10270-8.
47. Arnold, O., Bilheux, J. C., Borreguero, J. M., Buts, A., Campbell, S. I., Chapon, L., et al. (2014). Mantid—Data analysis and visualization package for neutron scattering andμSR experiments. *Nuclear Instruments and Methods in Physics Research Section A: Accelerators, Spectrometers, Detectors and Associated Equipment*. 764, 156-66.
48. Franks, N. P., Lieb, W.R. (1979). The Structure of Lipid Bilayers and the Effects of General Anaesthetics: An X-ray and Neutron Diffraction Study. *J Mol Biol*. 133, 469-500.
49. Groen, D., Gooris, G. S., Barlow, D. J., Lawrence, M. J., van Mechelen, J. B., Deme, B., et al. (2011). Disposition of ceramide in model lipid membranes determined by neutron diffraction. *Biophys J*. 100(6), 1481-9.
50. Kiselev, M. A., Ryabova, N. Y., Balagurov, A. M., Dante, S., Hauss, T., Zbytovska, J., et al. (2005). New insights into the structure and hydration of a stratum corneum lipid model membrane by neutron diffraction. *Eur Biophys J*. 34(8), 1030-40.
51. Harroun, T. A., Katsaras, J., Wassall, S. R. (2006). Cholesterol Hydroxyl Group Is Found To Reside in the Center of a Polyunsaturated Lipid Membrane. *Biochemistry*. 45, 1227-33.
52. NIST Center of Neutron Research, https://www.ncnr.nist.gov/resources/activation/ (Accessed: 2021).
53. Wiener, M. K., G.; White, S. (1991). Structure of a fluid dioleoylphosphatidylcholine bilayer determined by joint refinement of x-ray and neutron diffraction data 1. Scaling of neutron data and the distributions of double bonds and water. *Biophys J*. 60, 568-76.
54. Oguri, M., Gooris, G. S., Bito, K., Bouwstra, J. A. (2014). The effect of the chain length distribution of free fatty acids on the mixing properties of stratum corneum model membranes. *Biochim Biophys Acta*. 1838(7), 1851-61.
55. Kodati, V. R., El-Jastimi, R., Lafleur, M. (1994). Contribution of the Intermolecular Coupling and Librotorsional Mobility in the Methylene Stretching Modes in the Infrared Spectra of Acyl Chains. *J Phys Chem*. 98, 12191 - 7.
56. Mendelsohn, R., Moore, D. J. (1998). Vibrational spectroscopic studies of lipid domains in biomembranes and model systems. *Chem Phys Lipids*. 96, 141-57.
57. Moore, D. J., Rerek, M. E., Mendelsohn, R. (1997). Lipid Domains and Orthorhombic Phases in Model Stratum Corneum: Evidence from Fourier Transform Infrared Spectroscopy Studies. *Biochemical and Biophysical Research Communications*. 231, 797 - 801.
58. Schroeter, A., Kiselev, M. A., Hauss, T., Dante, S., Neubert, R. H. (2009). Evidence of free fatty acid interdigitation in stratum corneum model membranes based on ceramide [AP] by deuterium labelling. *Biochim Biophys Acta*. 1788(10), 2194-203.
59. Schmitt, T., Neubert, R. H. H. (2018). State of the art in Stratum Corneum research: The biophysical properties of ceramides. *Chem Phys Lipids*. 216, 91-103.
60. Schmitt, T., Lange, S., Dobner, B., Sonnenberger, S., Hauss, T., Neubert, R. H. H. (2018). Investigation of a CER[NP]- and [AP]-Based Stratum Corneum Modeling Membrane System: Using Specifically Deuterated CER Together with a Neutron Diffraction Approach. *Langmuir*. 34(4), 1742-9.
61. Podewitz, M., Wang, Y., Gkeka, P., von Grafenstein, S., Liedl, K. R., Cournia, Z. (2018). Phase Diagram of a Stratum Corneum Lipid Mixture. *J Phys Chem B*. 122(46), 10505-21.

62. Rerek, M. E., Chen, H., Markovic, B., Van Wyck, D., Garidel, P., Mendelsohn, R., et al. (2001). Phytosphingosine and Sphingosine Ceramide Headgroup Hydrogen Bonding: Structural Insights through Thermotropic Hydrogen/Deuterium Exchange. *J Phys Chem B*. 105, 9355 - 62.
63. Guo, S., Moore, T. C., Iacovella, C. R., Strickland, L. A., McCabe, C. (2013). Simulation study of the structure and phase behavior of ceramide bilayers and the role of lipid head group chemistry. *J Chem Theory Comput*. 9(11), 5116-26.
64. Beddoes, C. M., Gooris, G. S., Bouwstra, J. A. (2018). Preferential arrangement of lipids in the long-periodicity phase of a stratum corneum matrix model. *J Lipid Res*. 59(12), 2329-38.
65. Engberg, O., Kovacik, A., Pullmannova, P., Juhascik, M., Opalka, L., Huster, D., et al. (2020). The Sphingosine and Acyl Chains of Ceramide [NS] Show Very Different Structure and Dynamics That Challenge Our Understanding of the Skin Barrier. *Angew Chem Int Ed*. 59, 17383 - 7.
66. Vávrová, K., Kováčik, A., Opálka, L. (2017). Ceramides in the skin barrier. *European Pharmaceutical Journal*. 64(2), 28-35.
67. Norlen, L., Lundborg, M., Wennberg, C., Narangifard, A., Daneholt, B. (2022). The Skin's Barrier: A Cryo-EM Based Overview of its Architecture and Stepwise Formation. *J Invest Dermatol*. 142(2), 285-92.
68. Madison, K. C., Swartzendruber, D. C., Wertz, P. W., Downing, D. T. (1987). Presence of intact intercellular lipid lamellae in the upper layers of the stratum corneum. *J Invest Dermatol*. 88(6), 714-8.
69. Hill, J. R., Wertz, P. W. (2003). Molecular models of the intercellular lipid lamellae from epidermal stratum corneum. *Biochimica et Biophysica Acta (BBA) - Biomembranes*. 1616(2), 121-6.
70. de Jager, M. W., Gooris, G. S., Ponec, M., Bouwstra, J. A. (2005). Lipid mixtures prepared with well-defined synthetic ceramides closely mimic the unique stratum corneum lipid phase behavior. *J Lipid Res*. 46(12), 2649-56.
71. Opalka, L., Kovacik, A., Pullmannova, P., Maixner, J., Vavrova, K. (2020). Effects of omega-O-acylceramide structures and concentrations in healthy and diseased skin barrier lipid membrane models. *J Lipid Res*. 61(2), 219-28.
72. Sochorova, M., Audrlicka, P., Cervena, M., Kovacik, A., Kopecna, M., Opalka, L., et al. (2019). Permeability and microstructure of cholesterol-depleted skin lipid membranes and human stratum corneum. *J Colloid Interface Sci*. 535, 227-38.
73. Bouwstra, J., Nădăban, A., Beddoes, C. M., Dalgliesh, R. M., Gooris, G. (2019) The location of an essential ceramide for skin barrier function within the long periodicity phase. STFC ISIS Facility, http://doi.org/10.5286/ISIS.E.RB1969000.

SUPPLEMENTAL INFORMATION

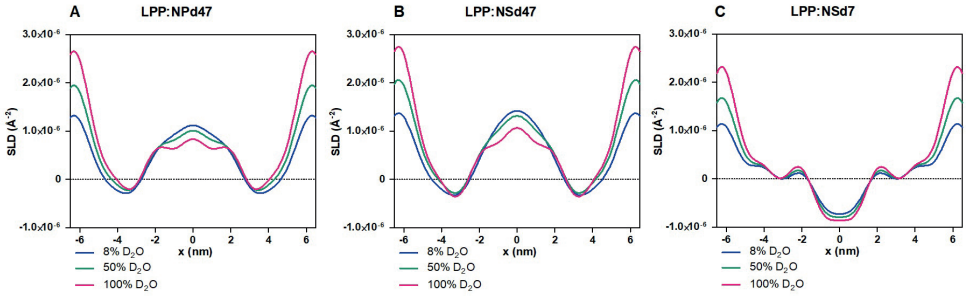


Figure S1. The SLD profiles for the LPP:NPd47 (A), LPP:NSd47 (B) and LPP:NSd7 (C) models plotted for each of the three D_2O/H_2O buffer hydration levels (8% in blue, 50% in green, 100% in magenta).

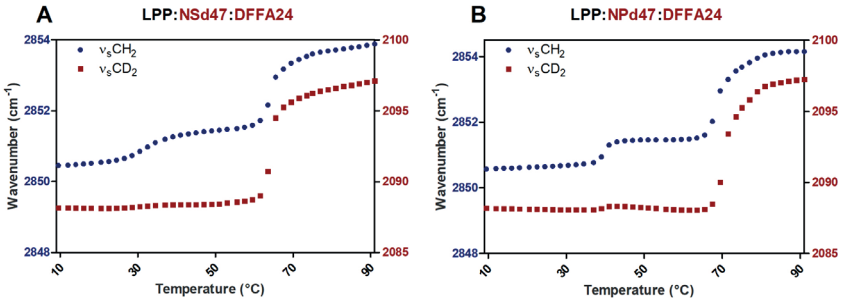


Figure S2. Thermotropic curves of the stretching vibrations for the partially deuterated systems: (A) LPP:NSd47:DFFA24 and (B) LPP:NPd47:DFFA24. The phase transitions temperatures of the lipids are plotted as a function of the $\nu_s CH_2$ and $\nu_s CD_2$ peak position, on the left and right y-axis, respectively. Both the protiated (blue circle) and deuterated (red square) lipids melted over the same temperature range, indicating that the deuterated lipids were integrated with the protiated lipids in the lipid system.

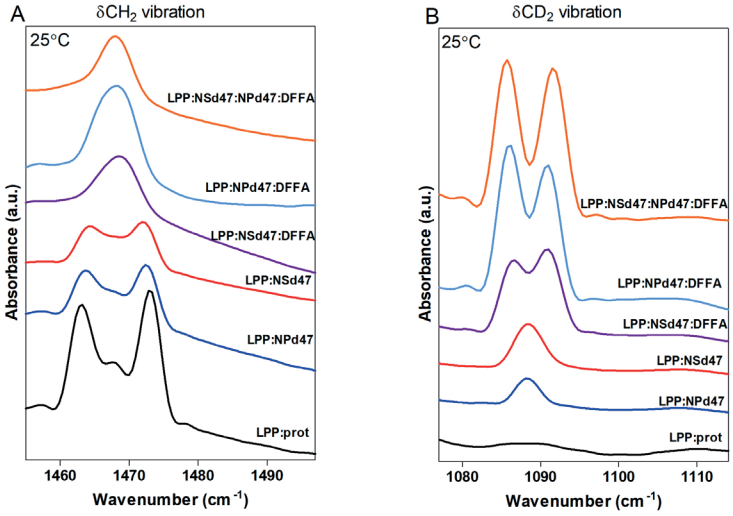
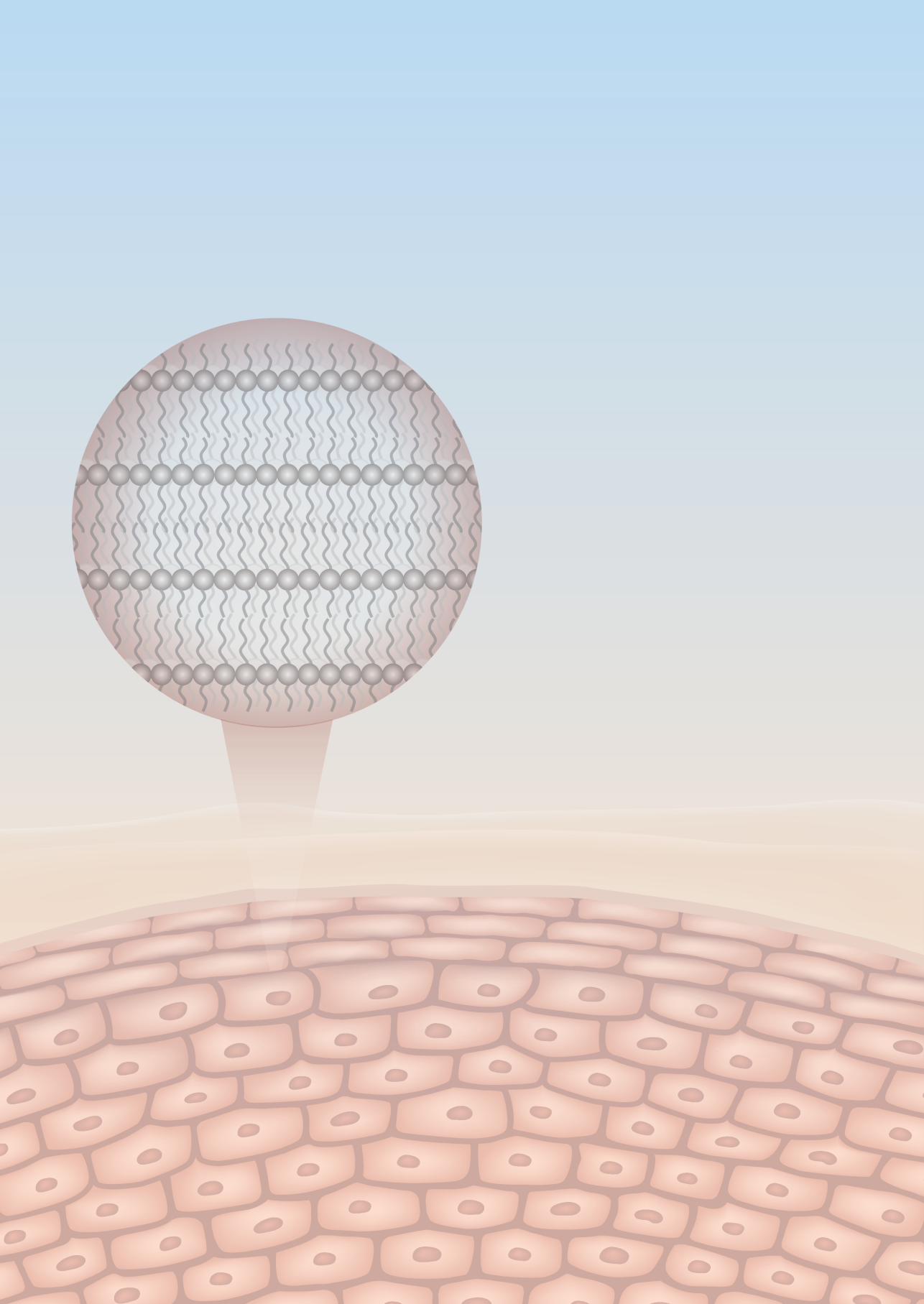


Figure S3. The δCH_2 (A) and δCD_2 (B) vibrations of the six lipid systems, determined by FTIR, at 25°C (same temperature used during the neutron diffraction measurements). Each curve has an annotation with the lipid model it represents.



CHAPTER 4

Effect of sphingosine and phytosphingosine ceramide ratio on lipid arrangement and barrier function in skin lipid models

Authors and affiliations:
Andreea Nădăban[1], Jannik Rousel[1,2], Dounia El Yachioui[1], Gerrit S. Gooris[1], Charlotte M. Beddoes[1], Robert M. Dalgliesh[3], Marc Malfois[4], Robert Rissmann[1,2,5], Joke A. Bouwstra[1*]

[1]Division of BioTherapeutics, Leiden Academic Centre for Drug Research, Leiden University, Leiden, The Netherlands
[2]Centre for Human Drug Research, Leiden, The Netherlands
[3]ISIS Neutron and Muon Source, Science and Technology Facilities Council, Rutherford Appleton Laboratory, Didcot, United Kingdom
[4]ALBA Synchrotron, Cerdanyola del Vallès, Barcelona, Spain
[5]Leiden University Medical Center, Leiden, The Netherlands

Adapted from: **Journal of Lipid Research** (2023). 64(8), 100400.

ABSTRACT

The lipids in the uppermost layer of the skin, the stratum corneum (SC), play an important role in the skin barrier function. The three main subclasses in the SC lipid matrix are ceramides (CER), cholesterol and free fatty acids. In inflammatory skin diseases, such as atopic dermatitis and psoriasis, the SC lipid composition is modulated compared to the composition in healthy SC. One of the main alterations is the molar ratio between the concentration of CER *N*-(tetracosanoyl)-sphingosine (CER NS) and CER *N*-(tetracosanoyl)-phytosphingosine (CER NP), which correlated with an impaired skin barrier function. In the present study we investigated the impact of varying the CER NS:CER NP ratios on the lipid organization, lipid arrangement and barrier functionality in SC lipid model systems. The results indicate that a higher CER NS:CER NP ratio as observed in diseased skin did not alter the lipid organization or lipid arrangement in the long periodicity phase encountered in SC. The trans-epidermal water loss, an indication of the barrier functionality, was significantly higher for the CER NS:CER NP 2:1 model (mimicking the ratio in inflammatory skin diseases) compared to the CER NS:CER NP 1:2 ratio (in healthy skin). These findings provide a more detailed insight into the lipid organization in both healthy and diseased skin and suggest that in vivo the molar ratio between CER NS:CER NP contributes to barrier impairment as well, but might not be the main factor.

INTRODUCTION

Skin, the largest organ of the human body, has the important role of protecting the body against pathogens, chemicals and radiation, while also preventing excessive water loss (1-3). The outermost layer of the skin's epidermis is the stratum corneum (SC), with a thickness varying between 10 – 20 µm. It consists of 10 – 25 layers of corneocytes, which are dead differentiated keratinocytes, embedded in a lipid matrix, forming a well-organized "brick-mortar" structure (4). The intercellular SC lipid matrix is mainly composed of three lipid classes: ceramides (CER), free fatty acids (FFA) and cholesterol (CHOL) (5, 6). These lipid classes are present at an equimolar ratio (1:1:1) in healthy human SC. Currently, at least 20 CER subclasses have been identified in human SC, which differ based on their head group structure (7-10).

CERs belong to the family of sphingolipids and are formed in the viable epidermis by three general pathways: degradation of glucosylceramides, hydrolysis of sphingomyelin or de novo synthesis in the endoplasmic reticulum (11). Sphingolipids, together with phospholipids (which are the precursors of FFAs in the epidermis) are structural components of living cell membranes (12). Sphingolipids preferentially associate with CHOL and form lipid rafts, dynamic lateral membrane inhomogeneities, which can interact with membrane proteins and modulate their activity (13). Unlike other biological membranes, the SC lipid matrix does not include phospholipids, but contains CHOL (14). Due to the altered lipid composition, the phase behavior in SC is different from the membranes of living cells. However, similar to living cell membranes, CHOL plays an important role in the lipid organization in SC (15, 16).

The intercellular SC lipids are organized as two lamellar phases: a long periodicity phase (LPP), with the repeat distance of 13 nm, and a short periodicity phase (SPP), with a repeat distance of 6 nm (17, 18). The LPP is observed exclusively in SC and is assumed to be critical for the skin barrier function (19-22). It was previously shown that for the formation of the LPP, among the various CER subclasses, the esterified ω-hydroxy sphingosine ceramide (CER EOS) and CHOL are crucial (15, 22). In the absence of CER EOS only the SPP is formed (23), while in the absence of CHOL the LPP and SPP are not formed (15). The organization of the lipid chains within this lamellar structure of the SC is referred to as the lateral organization. Based on the density of the packing, this can be orthorhombic (very dense and ordered), hexagonal (less dense, but still ordered), or liquid phase (highly disordered) (24-26). Barrier lipids in human SC are mainly organized in the orthorhombic packing, while a small part of the lipids is packed hexagonally and even small liquid domains are present (27). This is different from phospholipid membranes with high CHOL levels, where a liquid ordered phase is often encountered (28).

Lipids have been shown to play an important role in the skin barrier function (2, 4). Inflammatory skin diseases, such as atopic dermatitis, seborrheic dermatitis or psoriasis, and the rare hereditary disorder Netherton syndrome, are characterized by a deviation in

SC lipid composition, which may contribute to the impaired skin barrier function (4, 29-32). Clinical studies have revealed that among the lipid compositional alterations of diseased SC, the most prevalent changes are detected in the CER subclass and chain length composition (20, 29, 33-36). A previous study by Yokose et al. investigated potential biomarkers in the SC of barrier-disrupted skin and the ratio of CERs in diseased skin (atopic dermatitis and psoriasis) was compared to the CERs ratio in healthy individuals (36). They reported the ratio of CER *N*-(tetracosanoyl)-sphingosine (CER NS) to CER *N*-(tetracosanoyl)-phytosphingosine (CER NP) (Figure 1) as being a potential marker for impaired skin barrier function in these patients, as this ratio correlated positively with the trans-epidermal water loss (TEWL). Furthermore, apart from atopic dermatitis and psoriasis, an increased CER NS:CER NP ratio was also reported in the SC of Netherton syndrome patients (35) and recently in seborrheic dermatitis (32). Therefore, this CER subclass ratio change could be an important factor causing barrier dysfunction in diseased skin. However, the contribution of the altered CER NS:CER NP ratio to the barrier function is not known, as in clinical studies the various lipid composition changes always occur simultaneously and only correlations can be obtained.

To understand the relationship between lipid subclasses, lipid models can be used that mimic the organization in the SC lipid matrix. Previous studies showed that lipid models prepared either with isolated pig (37, 38) or human CERs (39), along with CHOL and FFAs mimicked the unique SC lipid organization; the mixtures form the crystalline LPP and SPP, as observed in SC. Furthermore, when isolated porcine or human CER subclasses were replaced by their synthetic counterparts with almost uniform chain length, the phase behavior of the lipid models was similar to the isolated CERs models, therefore also closely resembling the lipid organization of native SC (40-43). A further reduction in CER components to 4 or 3 and more recently to only 2 subclasses showed that when selecting the proper CER subclasses together with CER EOS and mix them with CHOL and FFAs, the models still formed the same lamellar phases and lateral packing (40, 42, 44, 45). This is an important finding as simple models with a limited number lipid components are compulsory to obtain detailed information about the molecular arrangement, as in these studies a replacement of protiated by deuterated lipids is required.

Lipid models offer the possibility to study changes systematically and to obtain more detailed insights into the underlying factors that cause barrier impairment (46-48). As the CER NS:CER NP ratio was identified as a possible factor for a dysfunctional barrier in inflammatory diseased skin, the aim of the current study is to investigate whether changing the CER NS:CER NP molar ratio results in an altered lipid organization and barrier function in lipid models. A CER composition that consists of CER NS, CER NP and CER EOS, when mixed with CHOL and FFA, has been identified to mimic the phase behavior in SC (49).

In this study different CER NS:CER NP molar ratios were investigated: 1:2, as observed in healthy SC, 1:1, and 2:1; the latter mimics the approximate ratio observed in

inflammatory skin diseases. We decided to use a simple SC lipid model as this allows us to obtain detailed insights about changes in lipid organization and lipid arrangement. In human SC, both the LPP and SPP are simultaneously present, however our focus was to examine the influence of the CER NS:CER NP ratio exclusively on the LPP. The lipid organization, lipid arrangement and barrier functionality were examined in our models. A change in CER NS:CER NP ratio did not induce changes in the lipid organization or the lipid arrangement of CER NS and CER NP in the LPP unit cell. TEWL was increased for the CER NS:CER NP 2:1 model, similarly as observed in clinical studies. These findings imply a contribution of the CER NS:CER NP ratio to the skin barrier impairment in vivo, but suggest that this might not be the main factor.

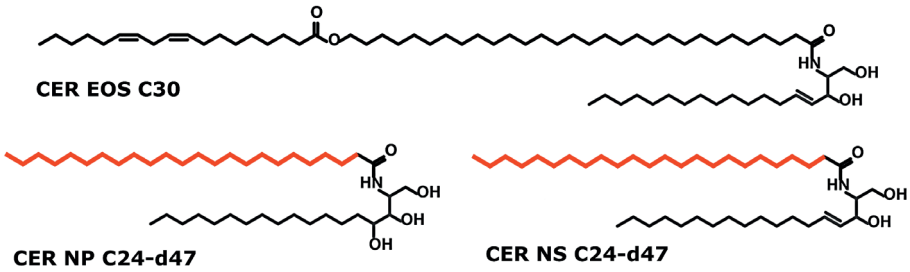


Figure 1. The molecular structure of the three CERs used in this study. The deuterated acyl chains (d47) of CER NP and CER NS are highlighted in red.

MATERIALS AND METHODS

Materials

Synthetic CER NP and CER NS with acyl chain lengths of 24 carbons (C24) and a sphingosine chain length of 18 carbon atoms (C18), along with CER NP and CER NS with a perdeuterated acyl chain (d47) (NPd47 and NSd47) and CER EOS C30 were kindly donated by Evonik (Essen, Germany). Lignoceric acid (FFA C24) was purchased from Sigma-Aldrich Chemie GmbH (Schnelldorf, Germany) and its deuterated counterpart (DFFA24) was supplied by Arc Laboratories BV (Apeldoorn, The Netherlands). CHOL, deuterium oxide (D_2O), acetate buffer salts, Na_2HPO_4, KH_2PO_4, KCl and ethyl-p-aminobenzoate (E-PABA) were supplied by Sigma-Aldrich Chemie GmbH (Schnelldorf, Germany). The organic solvents (HPLC grade or higher) were purchased from Biosolve BV (Valkenswaard, The Netherlands). Nucleopore polycarbonate filter disks with a pore size of 0.05 µm (Whatman, Kent, U.K.) were used as sample supports, as well as a silicon substrate obtained from Okmetic (Vantaa, Finland).

Lipid model compositions

An equimolar ratio of CER: CHOL: FFA was selected for the lipid models. The concentration of CER EOS was 40 mol% of the total CERs to allow an exclusive formation of the LPP structure. Furthermore, this also results in a peak separation between crystalline CHOL and the fourth-order diffraction peak of the LPP, irrespective of the CER NS:CER NP ratio. This is crucial for an accurate analysis of the neutron data. The ratio between CER NS:CER NP was changed in the different models (total 60 mol%). Different models were then prepared by substituting CER NS, CER NP or FFA C24 with their deuterated counterparts, as shown in Table 1.

Table 1. Composition of the lipid models used in this study. The deuterated lipids are indicated in bold.

Model	Lipid composition	Molar ratio
LPP NS:NP 1:2	CER EOS C30 : CER NS C24 : CER NP C24 : CHOL : FFAC24	0.4:0.2:0.4:1:1
LPP NS:NP 1:1	CER EOS C30 : CER NS C24 : CER NP C24 : CHOL : FFAC24	0.4:0.3:0.3:1:1
LPP NS:NP 2:1	CER EOS C30 : CER NS C24 : CER NP C24 : CHOL : FFAC24	0.4:0.4:0.2:1:1
LPP NSd47:NP 1:2	CER EOS C30 : **CER NS C24-d47** : CER NP C24 : CHOL : FFAC24	0.4:**0.2**:0.4:1:1
LPP NS:NPd47 1:2	CER EOS C30 : CER NS C24 : (CER NP C24 : **CER NP C24-d47**) : CHOL : FFAC24	0.4:0.2:(0.2:**0.2)**:1:1
LPP NSd47:NP 2:1	CER EOS C30 : (CER NS C24 :**CER NS C24-d47)** : CER NP C24 : CHOL : FFAC24	0.4:(0.2:**0.2)**:0.2:1:1
LPP NS:NPd47 2:1	CER EOS C30 : CER NS C24 : **CER NP C24-d47** : CHOL : FFAC24	0.4:0.4:**0.2**:1:1
LPP NSd47:NP:DFFA 1:2	CER EOS C30 : **CER NS C24-d47** : CER NP C24 : CHOL : **DFFAC24**	0.4:**0.2**:0.4:1:**1**
LPP NS:NPd47:DFFA 1:2	CER EOS C30 : CER NS C24 : **CER NP C24-d47** : CHOL : **DFFAC24**	0.4:0.2:**0.4**:1:**1**
LPP NSd47:NPd47:DFFA 1:2	CER EOS C30 : **CER NS C24-d47** : **CER NP C24-d47** : CHOL : **DFFAC24**	0.4:**0.2**:**0.4**:1:**1**
LPP NSd47:NP:DFFA 2:1	CER EOS C30 : **CER NS C24-d47** : CER NP C24 : CHOL : **DFFAC24**	0.4:**0.4**:0.2:1:**1**
LPP NS:NPd47:DFFA 2:1	CER EOS C30 : CER NS C24 : **CER NP C24-d47** : CHOL : **DFFAC24**	0.4:0.4:**0.2**:1:**1**
LPP NSd47:NPd47:DFFA 2:1	CER EOS C30 : **CER NS C24-d47** : **CER NP C24-d47** : CHOL : **DFFAC24**	0.4:**0.4**:**0.2**:1:**1**

For the neutron studies, CER NS and CER NP were substituted with their deuterated counterparts, NSd47 and NPd47 (indicated in the model's name). To allow a direct comparison of the results, the same amount of deuterated lipids should be present in the models (20% of total CERs). For this reason, the samples LPP NS:NPd47 1:2 and LPP NSd47:NP 2:1 were prepared with a mix of CER NP:NPd47 (1:1) and CER NS:NSd47 (1:1),

respectively. For the FTIR studies both CER NS and CER NP were entirely substituted in the models with their perdeuterated counterpart, alongside FFA C24 with DFFA.

Preparation of the lipid models

Approximately the same sample preparation method was used for the different analysis techniques and details are provided in Table 2. The necessary amount of lipids was dissolved in the solvent at a concentration of 5 mg/ml. The lipid samples were sprayed using a Camag Linomat IV device (Muttenz, Switzerland) under a gentle stream of nitrogen, at a spraying rate of 14 s/µl. For the samples prepared for permeability and TEWL, a ~12 µm thick lipid layer was obtained (47). All samples were equilibrated using an automatic equilibrator with a heating rate of 4°C/min until reaching 95°C, maintained at this temperature for 65 min to allow the lipid film to melt, and then slowly cooled to 25°C. Prior to the measurements, the samples were hydrated. As different analysis methods required different sample supports and nucleopore polycarbonate disks are not resistant against chloroform/methanol, in that case we used hexane/ethanol as a solvent. However, this does not affect the formation of the lipid membrane (50).

Table 2. Sample preparation details for each analytical technique used in this study.

Technique	Amount of lipids	Solvent	Spraying area	Sample support	Hydration
Permeability	1 mg	hexane/ ethanol (2:1, v/v)	1 x 1 cm^2	nucleopore polycarbonate disk	1 h, PBS in diffusion cell, at 32°C
TEWL	1 mg	hexane/ ethanol (2:1, v/v)	1 x 1 cm^2	nucleopore polycarbonate disk	30 min, water in diffusion cell, room temperature
SAXD	1 mg	hexane/ ethanol (2:1, v/v)	2 x 3 mm^2	nucleopore polycarbonate disk	24 h, 80% relative humidity, room temperature
FTIR	1 mg	chloroform/ methanol (2:1, v/v)	1 x 1 cm^2	silver bromide (AgBr) window	≥12 h, acetate buffer (pH 5) in D_2O, at 37°C
Neutron diffraction	10 mg	chloroform/ methanol (2:1, v/v)	1.2 x 3.8 cm^2	silicon substrate	≥12 h, D_2O/H_2O buffer (100%, 50%, 8%), at 37°C

Permeability

A drug permeation study was performed using Permegear in-line diffusion cells (Bethlehem, PA, USA) with a diffusion area of 0.28 cm^2. The acceptor phase was phosphate buffered saline (PBS, pH 7.4) and the donor phase consisted of a saturated ethyl-p-aminobenzoate (E-PABA) solution (0.65 mg/ml concentration, prepared in acetate buffer with pH 5). The samples were mounted in the diffusion cells and the temperature was maintained at 32°C. The acceptor solution was continuously stirred using a small

magnetic stirrer and it had a continuous flow of approximatively 2.5 ml/h. To start the experiment, E-PABA was added to the donor compartment, which was then covered with an adhesive tape. Every hour fractions of the acceptor phase were collected, over 15 h. At the end of the experiment the PBS flow was determined by weighing the collected tubes and the E-PABA concentration was determined using ultra-high performance liquid chromatography (UPLC), as described below. Each sample group consisted of at least 6 replicates. The steady-state flux of E-PABA was calculated as an average between the 10^{th} and 15^{th} hours. Statistical analysis was performed using GraphPad Prism 5 using an one-way ANOVA test.

UPLC analysis of E-PABA

UPLC analysis was performed using a validated method, described previously (51). The Acquity UPLC system (Waters, Milford, MA, USA) was connected to a UV-VIS detector. The column (1.7 µm siloxane hybrid particles) was maintained at 40°C. The mobile phase consisted of a mixture of 0.1% trifluoroacetic acid in acetonitrile : Milli-Q (40:60 ratio, v/v), with a flow rate of 1 ml/min. 10 µl of each sample and the calibration curve (described previously by Uche et al. (51)) were injected.

TEWL

Trans-epidermal water loss (TEWL) was measured using an AquaFlux AF 200 (Biox Systems Ltd., London, UK). This method was previously described by Mojumdar et al. (52). The AquaFlux device was tightly connected to the donor compartment of the diffusion cell by using a measurement cap (Biox Systems Ltd., London, UK). The TEWL flux of the lipid models was recorded for 30 min at a collection rate of 10 s. The average steady-state TEWL in the last 10 min of the measurement was calculated and statistical analysis was performed using an unpaired t-test in GraphPad Prism 5 to assess the differences between two groups ($P < 0.05$). At least 10 lipid membranes were measured for each of the two compositions.

X-ray measurements

Small-angle X-ray diffraction (SAXD) measurements were performed at the ALBA Synchrotron (Barcelona, Spain) at the NCD-SWEET beamline. The distance between the detector (Pilatus 1M detector with a pixel array of 981 × 1043, each pixel: 172 × 172 μm^2) and the sample was 2.148 m. The wavelength of the beam was 0.999 Å. The lipid samples were measured at 23°C for 20 s and the setup was calibrated with silver behenate prior to the measurements. Each composition was measured twice.

The two-dimensional scattering plot was integrated over a 90° segment from the beam center to obtain the one-dimensional X-ray intensity profiles of the scattering intensity (I) as a function of the scattering vector (q). The latter can be calculated as

$q = (4\pi \sin\theta)/\lambda$, where θ represents the scattering angle and λ is the wavelength. The peaks were fitted using the Pearson VII function in Fityk (53) to determine the peak positions (q_n). The repeat distance (d) of the lamellar phase was calculated by least square fitting using the equation $d = 2n\pi/q_n$, where n is the order number of the diffraction peak attributed to a lamellar phase.

FTIR Measurements

A Varian 670-IR spectrometer (Agilent Technologies, Santa Clara, USA) fitted with a broadband mercury cadmium telluride detector, cooled by liquid nitrogen, was used to perform the FTIR measurements. The spectra were collected at a resolution of 1 cm^{-1}, by co-addition of 256 scans over 4 min. The sample chamber was continuously purged with dry air for at least 30 min prior to the measurements. The lipid models were measured between 10-90°C, with a heating race of 0.25°C/min and the wavenumber range of the measurements was 600−4000 cm^{-1}. Data collection and analysis were performed using Resolution Pro software (Agilent Technologies, USA), and the spectra were deconvoluted using a peak half-width of 4 cm^{-1} and an enhancement factor of 1.4. Three measurements were performed for each composition.

The thermotropic behavior and conformational ordering of the samples were followed by examining the peak positions of the CH_2 and CD_2 symmetric stretching vibrations (ν_sCH_2: wavenumber range 2845-2855 cm^{-1} and ν_sCD_2: wavenumber range 2080-2100 cm^{-1}). The mid-phase transition temperatures (orthorhombic – hexagonal: T_m O-H; hexagonal – liquid: T_m H-L) were determined by linear regression fitting, as previously described (54). CH_2 and CD_2 scissoring vibrations (δCH_2, wavenumber range: 1462-1473 cm^{-1}; δCD_2, wavenumber range: 1085-1095 cm^{-1}) were examined to determine the lipid chain packing and their accurate peak positions were determined by fitting Lorentzian peaks with an in-house Python script. A peak height ratio (OR/MID) was calculated as an average of the peak heights of the two orthorhombic scissoring peaks divided by the peak height of the central scissoring peak, to quantitatively assess the chain interactions for both δCH_2 and δCD_2 vibrations. Statistical analysis was performed to determine the significance of the results obtained from the peak positions (unpaired t-test, using GraphPad Prism 5; results were statistically different when $P < 0.05$).

Neutron diffraction measurements and data analysis

The lipid arrangement of the two models with CER NS:CER NP ratios of 1:2 and 2:1 was measured using the small-angle neutron scattering (SANS) mode of the LARMOR instrument, at the ISIS Neutron and Muon Source (Rutherford Appleton Laboratory, UK). The samples were measured with a neutron beam size of 1 × 30 mm, in the wavelength range (λ) between 1 – 12.5 Å and a sample angle to the beam of 2.5°. The ^{3}He detector

was positioned at a distance of 4.4 m from the sample and was set at a 2θ angle of 5° to the direct beam, covering an area of 664 × 600 mm with a pixel size of 4 × 8 mm.

The environment of the sample was kept constant using a sealed, heated aluminum chamber and the windows of the chambers were maintained at 42°C to prevent condensation. Each sample was measured for 4 h (40 μA/h accelerator proton charge) at 25°C for each hydration level. The SANS data was normalized to the incident flux shape and detector efficiency using a direct beam measurement. An empty chamber was used as background measurement, which was subsequently subtracted from each sample.

The Mantid software framework (55) was used to reduce the neutron scattering data to monitor the normalized intensity vs. scattering vector (q), resulting in a range of q between 0.032 and 0.991 nm^{-1}. The scattering angle (2θ) was converted to q using Bragg's equation as follows:

$$q = 4\pi sin\theta \,/\, \lambda \quad (1)$$

The repeat distance (d) of the lamellar phase (LPP) was calculated based on the positions of the equidistant Bragg peaks using the following equation:

$$d = 2\pi n/q_n \quad (2)$$

where n is the diffraction order number of the peak at position q_n.

The scattering length density (SLD) profiles were calculated for each sample using the intensity vs. q data. The data analysis method has been previously described (56-58). In short, the Bragg peaks were fitted in the Fityk software (using a Pearson VII function) to obtain the intensity value of each diffraction order (53). The structure factor amplitude ($|F_n|$) for each diffraction order was calculated using the following formula:

$$\left| F_n \right| = A_n\sqrt{LI_n} \quad (3)$$

The Lorentz correction (L) can be assumed to be L=q, because of the high degree of orientation of the lipid lamellae. The correction factor for sample absorption (A_n) can be calculated:

$$A_n = \frac{1}{\sqrt{\frac{sin\theta}{2\mu l}\left(1-e^{\frac{-2\mu l}{sin\theta}}\right)}} \quad (4)$$

where *l* represents the lipid sample thickness and μ is the linear attenuation coefficient (59).

The phase signs of $|F_n|$ for the different diffraction orders were calculated using the different D_2O/H_2O hydration buffer levels (100%, 50%, and 8%), as previously described (49). First, the F_n values were plotted as a function of the D_2O amount in the hydration buffer (Figure S1). The LPP unit cell is centrosymmetric, as demonstrated by the linear correlation of the relative structure factor amplitudes as a function of the D_2O/H_2O buffer shown in Figure S1. The water molecules are located close to the hydrophilic lipid head groups, which are positioned at the boundary of the unit cell of the lamellar phases (57, 60, 61). As the structure is symmetric, the water profile phase signs can be either negative or positive. Assuming that the water is located close to the head groups at the boundary

of the unit cell, the slopes of the linear correlation of the structure factors and the buffer ratio between 100% and 8% D_2O/H_2O indicate that the phase signs of the water profile is -,+,-,+,-,+ for both CER NS:CER NP 1:2 and 2:1 models. These phase signs are in accordance with previously described LPP phase signs for the water profile (49, 56, 57, 62, 63).

Next, the phase signs of the protiated and deuterated lipid samples were individually determined based on the negative or positive sign of the F_n at 8% D_2O/H_2O hydration (Figure S1) and appeared to be -,+,-,+,-,+ for all compositions, including those with partly deuterated lipids.

Using the phase signs and the values for the structure factors, the scattering length density (SLD, *ρ(x)*) profile of the LPP unit cell was plotted using Fourier reconstructions with equation 5, where *x* represents the distance in the unit cell (center of the unit cell is *x*=0) (56):

$$\rho(x) = F_0 + 2\sum_{n=1}^{n_{max}} F_h \cos\left(\frac{2\pi n x}{d}\right) \quad (5)$$

The scattering density per unit volume (F_0) was calculated using the chemical composition and density of the lipid sample (64, 65). It included one water molecule per lipid in agreement with the obtained sample hydration (49). The SLD profiles that provide the position of the deuterated lipid chains were obtained from the difference in the SLD profiles of the deuterated and protiated samples, with the two samples hydrated at 8% D_2O/H_2O. This hydration level was chosen as the scattering contribution of the buffer at 8% D_2O is zero; therefore, the SLD profiles displayed only the scattering of the lipids.

The SLD data was calculated on a "relative absolute" scale, following the steps previously described (49, 56, 66, 67). This seemingly contradictory term was adopted to allow the detailed examination and scaling of diffraction data, as described by Wiener et al. (67). Our set of measurements did not include a sample with terminally deuterated sphingosine chain of CER NS (NSd7) that was used in previous measurements to calculate the relative absolute scale. To correct for this, a scaling factor (S_f) was introduced, which was based on previous measurements using the same settings, analysis procedure and a similar lipid model: LPP CER NS:CER NP 1:1 model (49). S_f is calculated as a ratio of the peak area of NSd7 and NPd47 chains from the CER NS:NP 1:1 model.

Next, the peak area of the NPd47 SLD profile (in the LPP NS:NPd47 2:1 model of this study) was fitted using Fityk. This peak area was then multiplied with S_f to obtain the corrected NPd47 peak area scaled to the previous measurements (SLD_{area}).

The scattering of the 47 deuterium atoms in the NPd47 acyl chain (SLD_{dif}) was calculated by subtracting the scattering of a protiated CER acyl chain ($C_{23}H_{47}$) from the scattering of a deuterated CER acyl chain ($C_{23}D_{47}$).

The factor for calculating the absolute SLD values ($SLD_{correct}$) represents the ratio between the scattering of the 47 deuterium atoms in the NPd47 chain and the corrected peak area of the NPd47 profile:

$$SLD_{correct} = \frac{SLD_{dif}}{SLD_{area}} \quad (6)$$

This $SLD_{correct}$ factor finally was applied to the F_n values, transforming the data to the 'relative absolute' scale.

This method resulted in deuterated water peaks at the border of the LPP unit cell having the same density in all samples hydrated at 100% D_2O, including the samples measured with deuterated NSd7 in our previous experiments, as expected.

RESULTS

Increasing the CER NS:CER NP ratio results in a higher TEWL, but no effect on E-PABA flux

E-PABA diffusion studies were performed to investigate the effect of increasing the CER NS:CER NP ratio on the permeability of the models (Figure 2A and B). Figure 2A shows the average E-PABA flux through the lipid model membranes of the three different CER NS:CER NP ratios (1:2, 1:1 and 2:1). The steady state was reached after 10 h and the averaged E-PABA steady-state flux calculated between 10 and 15 h is provided in Figure 2B. In the three groups (n ≥6), the E-PABA flux was very similar (LPP NS:NP 1:2: 2.0 ± 0.3 µg/cm^2/h; LPP NS:NP 1:1: 2.0 ± 0.2 µg/cm^2/h; LPP NS:NP 2:1: 2.2 ± 0.37 µg/cm^2/h) and thus no significant difference was observed between the models.

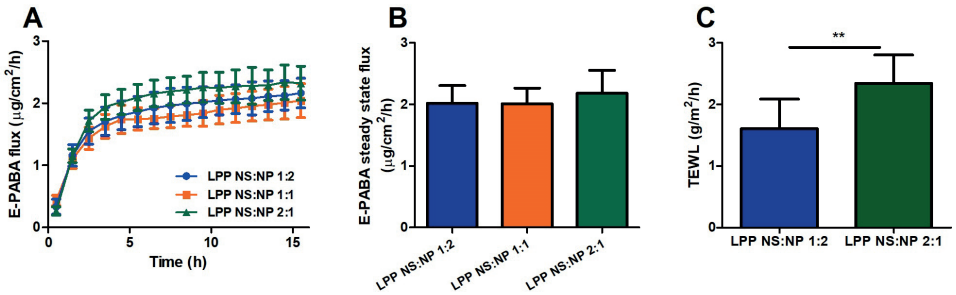


Figure 2. Permeability of the lipid models: (A) The E-PABA flux through the lipid models over 15 h. (B) The average steady-state E-PABA flux between 10-15 h (n≥6). (C) TEWL flux across the model membranes, n≥10 (**P < 0.01). All data are presented as mean ± SD.

TEWL measurements were performed on the two models with the molar ratios LPP NS:NP 1:2 and LPP NS:NP 2:1 (Figure 2C). The water loss of the LPP NS:NP 2:1 model was significantly higher than for the LPP NS:NP 1:2 model (2.34 ± 0.46 g/m^2/h compared to 1.61 ± 0.48 g/m^2/h, n≥10); P<0.01.

CER NS:CER NP ratio does not influence the lamellar or the lateral organization

SAXD studies were performed to obtain information about the lamellar organization of the lipid models and the repeat distances of the lamellar phases of the models with a changed CER NS:CER NP ratio (1:2, 1:1 and 2:1). The diffraction profiles, displayed in Figure 3A,

show a series of nine equidistant peaks, indicating a lamellar phase. The only peaks that could not be assigned to this lamellar structure correspond to the phase separated crystalline CHOL (with two orders of diffraction at q= 1.8 nm^{-1} and q= 3.6 nm^{-1}; indicated by an asterisk in Figure 3A). The repeat distance of this lamellar phase is 12.6 nm for the LPP NS:NP 2:1 model, 12.7 nm for the LPP NS:NP 1:1 model and 12.8 nm for the LPP NS:NP 1:2 model (Table 3) suggesting a slight increasing trend. The peak intensity distribution shows the following order for the first three diffraction peaks: 2^{nd} order has a higher intensity than the 1^{st} and 3^{rd} order peaks (Table 3). This intensity distribution is very characteristic for the LPP and demonstrates the formation of the LPP in all three models (62).

Table 3. The LPP repeat distance (d-spacing) of the samples shown as average (in nm). The peak height ratio is calculated as the ratio between the heights of the fitted peaks for the 1^{st}:2^{nd}:3^{rd} diffraction orders.

Lipid model	LPP d-spacing (nm)	Peak height ratio
LPP NS:NP 1:2	12.8	1: 1.8: 0.5
LPP NS:NP 1:1	12.7	1: 1.9: 0.5
LPP NS:NP 2:1	12.6	1: 2.1: 0.5

In the next step the packing of the lipids within the lamellae were examined. Figure 3B shows the δCH_2 vibrations for the protiated LPP NS:NP 1:2 and LPP NS:NP 2:1 models, with two peaks at approximately 1462 cm^{-1} and 1473 cm^{-1} and a small central peak at 1467 cm^{-1}. The exact δCH_2 peak position was determined for each sample by peak fitting using Python scripts, then the δCH_2 peak splitting (distance between the two orthorhombic peaks) and the peak height ratio of the two orthorhombic peaks and the hexagonal central peak (OR/MID) were calculated. Both models had the same δCH_2 peak splitting (10.6 ± 0.04 cm^{-1}) and OR/MID peak height ratio (3.00 ± 0.3), therefore no difference in the lateral organization was observed.

Next the symmetric stretching vibrations were examined as a function of temperature: the thermotropic curves of the $\nu_s CH_2$ stretching vibrations for the two models are provided in Figure 3C. At low temperatures the wavenumber of the stretching vibrations is <2849 cm^{-1} indicating a high conformational order. This remains constant until 34°C, then there is an increase of the $\nu_s CH_2$ wavenumber, indicating a lower conformational ordering of the chains. As the scissoring vibrations indicated the presence of an orthorhombic packing at 10°C, this transition is from an orthorhombic to hexagonal phase, which is confirmed by the scissoring vibrations (not shown). The two mixtures showed similar mid-phase transition temperature for LPP NS:NP 1:2 (T_m O-H 37.8 ± 1.2 °C, T_m H-L 68.7 ± 1.6 °C) and LPP NS:NP 2:1 (T_m O-H: 36.4 ± 0.7 °C, T_m H-L: 65.9 ± 0.3 °C) (Figure 3C). Increasing the temperature further results in a second phase transition from hexagonal to isotropic phase.

Even though 32°C is the skin temperature in vivo (also used for the permeability measurements in this study), the conformational order of the lipid models is provided at 10°C, as 32°C is close to the transition temperature from the orthorhombic – hexagonal phase.

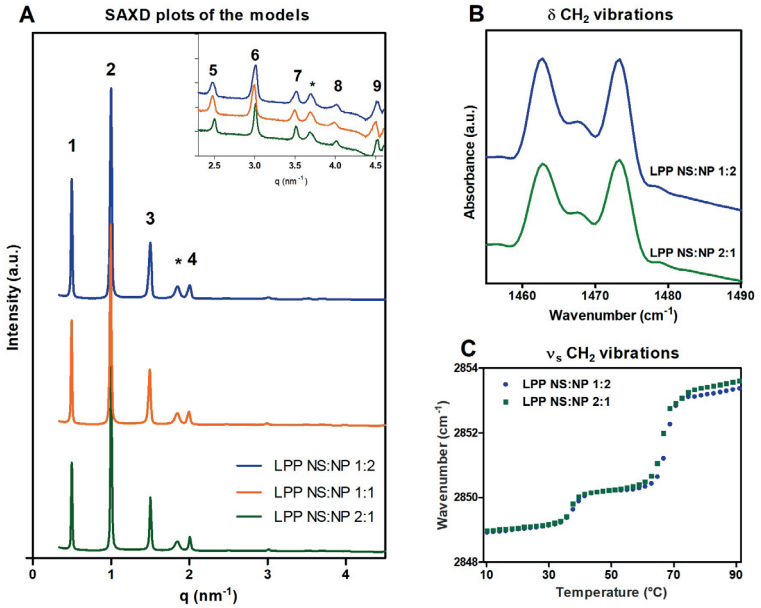


Figure 3. (A) X-ray diffraction profiles of the lipid models. The three CER NS:CER NP ratios: 1:2 (blue), 1:1 (orange) and 2:1 (green). The LPP diffraction orders are indicated with Arabic numbers and the asterisk (*) indicates the phase separated crystalline CHOL peaks. The insert represents a zoom in of the q=2.4 – 4.6 nm^{-1} range. (B) The δCH_2 vibrations of the two protiated models, measured at 10°C. (C) Thermotropic curve of the $\nu_s CH_2$ vibrations for the protiated samples, LPP NS:NP 1:2 and LPP NS:NP 2:1. The wavenumbers of the $\nu_s CH_2$ peak position are plotted as a function of temperature (10-90°C). The FTIR data is shown as an average of 3 measurements for each composition.

Stretching vibrations do not indicate phase separation in the models

The lipid mixing and homogeneity of the samples were examined by replacing protiated chains with their deuterated counterparts. Figure S2 (Supplementary Material) displays the thermotropic behavior of the lipid models with deuterated acyl chains of CER NS and CER NP and deuterated FFA (LPP NS:NPd47:DFFA 1:2, LPP:NSd47:NP:DFFA 1:2, LPP NSd47:NPd47:DFFA 1:2, LPP NS:NPd47:DFFA 2:1, LPP:NSd47:NP:DFFA 2:1 and LPP NSd47:NPd47:DFFA 2:1). This shows that for both CER NS:CER NP ratios with deuterated acyl chain of CER NP and DFFA (Figure S2 A, D) and with deuterated acyl chain of CER NS and DFFA (Figure S2 B, E) a similar thermotropic response of the $\nu_s CH_2$ and $\nu_s CD_2$ vibrations is detected. As an increase of the $\nu_s CH_2$ wavenumber is observed at ~34°C, similar to LPP NS:NP 1:2 and LPP NS:NP 2:1, indicating a shift in the conformational ordering probably caused by an orthorhombic to hexagonal phase transition, as an

orthorhombic lateral packing is present at 10°C. The samples with both the acyl chains of CER NS and CER NP and FFAC24 deuterated had a $\nu_s CH_2$ peak position at ~2850.9 cm^{-1} at 10°C, which was ~ 0.6 cm^{-1} higher than the samples with only one of the acyl chains deuterated (Figure S2 C, F). This elevated value represents an indication of a slightly higher conformational disordering of the protiated chains in these two fully deuterated models compared to the chains in the fully protiated samples.

The protiated and deuterated lipids had the same melting behavior in all six models presented in Figure S2, with a shift in $\nu_s CH_2$ and $\nu_s CD_2$ vibrations starting at ~60°C, indicating that the transition from hexagonal to liquid isotropic phase is occurring at approximately the same temperatures (Table S1). This indicates that the protiated and deuterated lipids undergo phase transitions simultaneously with increasing temperature, implying that the lipid chains mix thoroughly and there are no separated lipid domains in any of the six deuterated models. These results suggest that the altered CER NS:CER NP molar ratio, which only changes the lipid head group structure, does not influence the homogeneous mixing behavior of the compositions with CER NS:CER NP ratio of 1:2 and 2:1. The scissoring vibrations are used to obtain a more detailed insight in the mixing behavior of the lipids, as described below.

Molecular arrangement of the LPP unit is not influenced by the CER NS:CER NP ratio change

The effect of a change in CER NS:CER NP ratio on the location of the deuterated acyl chains of CER NS and CER NP in the LPP unit was examined with SANS. This was studied in models with the CER NS:CER NP ratio of 1:2 and 2:1. The one-dimensional plots of the intensity as function of the scattering vector q showed equidistant peaks attributed to the LPP (Figure 4).

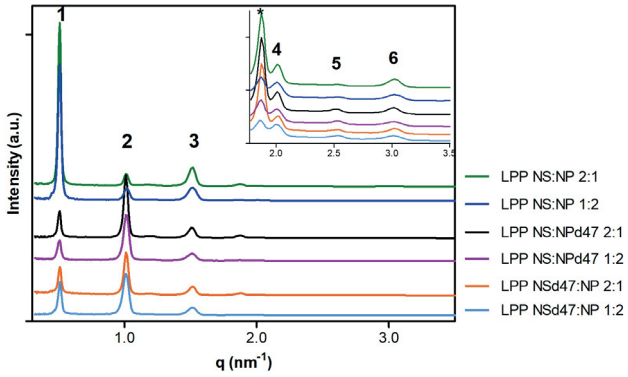


Figure 4. SANS one-dimensional plots of the six lipid models corresponding to the two CER NS:CER NP ratio systems (1:2 and 2:1), hydrated at 100% D_2O/H_2O buffer. The intensity plotted as a function of the scattering vector (q) shows the equidistant Bragg peaks corresponding to the first six diffraction peaks of the LPP and the insert displays a zoom-in of the 1.7-3.5 nm^{-1} region. The phase-separated crystalline CHOL peak is indicated by an asterisk.

The d-spacing of the unit cell was calculated and its value was 12.5 ± 0.03 nm for all samples, without a difference based on the CER NS:CER NP ratio. The phase-separated crystalline CHOL peak was observed at q=1.8 nm^{-1} and did not overlap the LPP diffraction peaks, allowing the integration of all the diffraction orders.

The SLD profiles of each model, with the three hydration levels (8%, 50% and 100% D_2O/H_2O), were determined after the calculation of the structure factors and phase signs (Eq. 5). The water SLD profiles were calculated as the difference between the SLD profile intensity of the protiated sample hydrated at 100% D_2O/H_2O and the SLD profile intensity of the same sample hydrated at 8% D_2O/H_2O buffer (Figure 5 A,C). Apart from the two regions at the unit cell border (located at 6.3 ± 0.1 nm from the center of the unit cell), the water profiles of the two protiated samples (LPP NS:NP 1:2 and LPP NS:NP 2:1) also show two inner water regions positioned at 2.2 ± 0.1 nm from the center of the unit cell (Figure 5 B,D). The location of the water molecules corresponds to the lipid head group region. This demonstrates that the LPP has a centrosymmetric trilayer structure, in agreement with previous studies (56, 57).

The SLD profiles of the deuterated samples were examined to determine if a change in the CER NS:CER NP ratio affected the lipid arrangement in the LPP unit. The positions of the deuterated acyl chains of CER NS and CER NP were determined by subtracting the SLD profile of the protiated sample from the SLD profile of the deuterated sample, both hydrated at 8% D_2O/H_2O buffer. The 8% D_2O/H_2O hydrated models were used, as there is no contribution of water to the SLD profile at this ratio. The resulting SLD profiles indicated the positions of the deuterated moieties in the LPP unit (Figure 5 E-H). The SLD profile corresponding to the LPP NS:NPd47 1:2 model displayed a high SLD intensity in the center of the unit cell; however, a slight elevation of the SLD was also observed in the outer layers of the LPP (Figure 5E). This suggests that the deuterated acyl chain of CER NP is predominantly located in the central layer of the LPP, with a small fraction located in the outer layers at the unit cell boundary. The SLD profile of the LPP NSd47:NP 1:2 model showed the same distribution, indicating that the acyl chain of CER NS has the same location as the acyl chain of CER NP (Figure 5F).

Increasing the CER NS concentration (LPP NS:NP 2:1 model) did not influence the location of the acyl chains of CER NS and CER NP in the LPP unit of this model, as the same arrangement of the lipids was observed (Figure 5 G,H). Each lipid model consisted overall of 20% NSd47 or NPd47, which represents 6.6% of total lipids, to ensure an equal number of deuterated chains to be examined by neutron diffraction and to avoid an overload of the detector. The relative absolute intensities of the SLD profiles were similar among the models indicating that the change of the CER NS:CER NP ratio did not result in any differences between the positions of the deuterated acyl chains of CER NS and CER NP in the LPP unit.

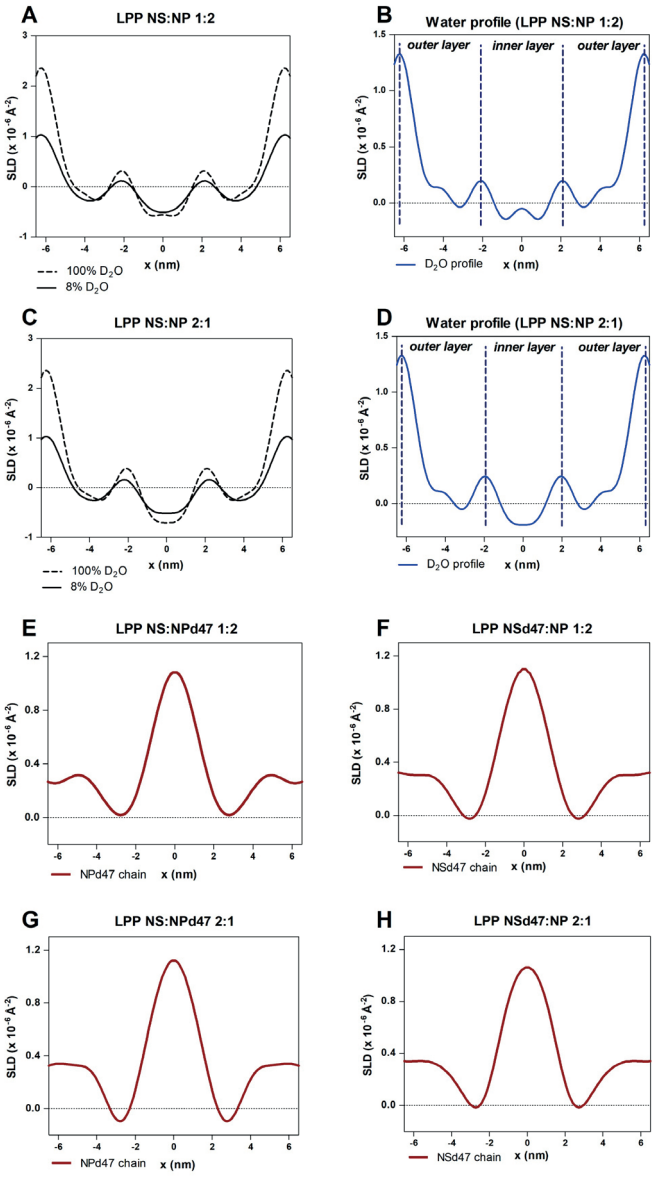


Figure 5. The neutron SLD profiles of: (A) The LPP NS:NP 1:2 protiated sample, measured at 100% D_2O/H_2O hydration and 8% D_2O/H_2O hydration; (B) The resulting water profile of the LPP NS:NP 1:2 sample; (C) LPP NS:NP 2:1 protiated sample, with the two hydration levels 100% D_2O/H_2O and 8% D_2O/H_2O; (D) Water profile of the LPP NS:NP 2:1 model; (E-H) SLD profiles of the acyl chains of CER NP and CER NS in the LPP NS:NP 1:2 models (E,F) and LPP NS:NP 2:1 models (G,H).

CER NS and CER NP both adopt the extended conformation regardless of the CER NS:CER NP ratio

The interaction of the lipid chains was further investigated by examining the shape and the splitting of the δCD_2 (Figure 6 A,B) and δCH_2 vibrations in the FTIR spectra (Figure 6 C,D). When hydrocarbon chains are packed close to each other (orthorhombic packing), the CH_2 groups interact and CH_2-CH_2 short-range coupling occurs creating two peaks in the δCH_2 vibrations. The δCH_2 peak splitting distance depends on the size of the formed orthorhombic lipid domain. A splitting of the scissoring vibrations is also noticed for deuterated samples where the CH_2 chains are replaced by CD_2 chains. The δCH_2 and δCD_2 vibrations have a large vibrational energy difference (CH_2 in the range of 1470 cm^{-1} and for CD_2 around 1090 cm^{-1}). In deuterated lipid models, if the deuterated chains are located in close proximity forming large domains, the δCD_2 peak to peak distance increases. It reaches a maximum peak to peak distance when the domains are around 100 chains (68, 69). The δCD_2 peak positions are around 1085 cm^{-1} and 1091 cm^{-1}, inducing a very deep minimum. However, when protiated and deuterated chains are neighboring and participate in the same orthorhombic lattice, CH_2-CD_2 chain interactions occur and as a consequence of the different vibrational energy, the short-range coupling of the CD_2-CD_2 chains is lost. This results in the formation of a central single peak in the δCD_2 vibration at around 1088.5 cm^{-1}, located in between the 1085 cm^{-1} and 1091 cm^{-1}, thus a shallower depth between the two orthorhombic peaks is observed.

A smaller δCD_2 splitting distance indicates a decreased deuterated lipid domain size. For pure DFFA24 the peak splitting value is 7.3 ± 0.1 cm^{-1}, which is the maximum splitting that can be obtained for large deuterated domains (not shown). In the lipid model LPP NSd47:NPd47:DFFA 1:2, where the acyl chains of both CER NS and CER NP are deuterated together with DFFA, the calculated δCD_2 peak splitting distance is 6.2 ± 0.1 cm^{-1} (Table 4). This demonstrates that large deuterated lipid domains are formed in the system. To be able to form such large domains, a majority of DFFA chains should be located in proximity of the deuterated acyl chains of CER NS and CER NP in the central layer of the LPP unit. To examine whether domains of mixed protiated and deuterated lipids occur, resulting in CD_2-CH_2 interaction, the peak height ratio between the two orthorhombic scissoring modes (OR: 1085 cm^{-1} and 1091 cm^{-1}) and the central scissoring mode (MID: 1088.5 cm^{-1}) was calculated by peak fitting, resulting in a value of 5.5 ± 0.1 (OR/MID ratio; Table 4). This value indicates a low number of CD_2-CH_2 interactions compared to the CD_2-CD_2 interactions. As sphingosine and phytosphingosine chains are protiated, this demonstrates that the sphingosine chains are hardly present in the central layer of the LPP.

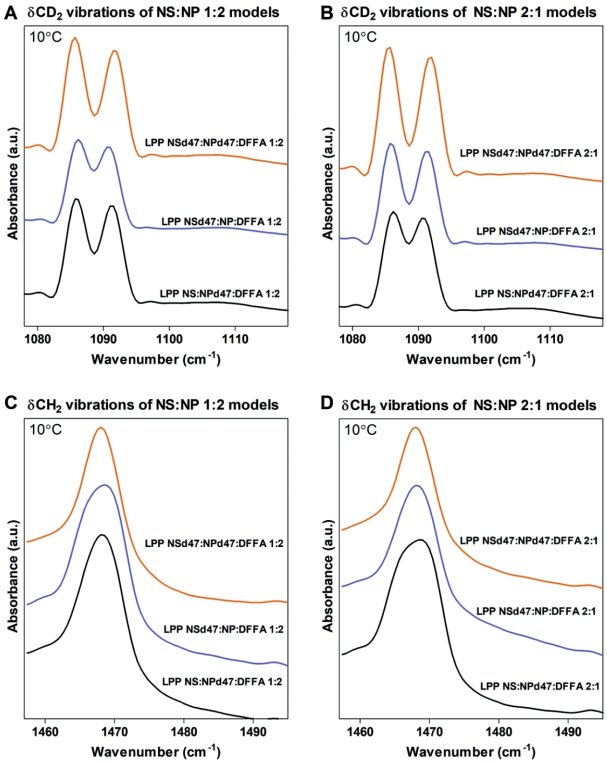


Figure 6. (A) The δCD_2 vibrations for the partially deuterated CER NS:CER NP 1:2 ratio models and (B) CER NS:CER NP 2:1 ratio models measured at 10°C. (C) The δCH_2 vibrations for the CER NS:CER NP 1:2 models and (D) CER NS:CER NP 2:1 models. Each lipid model is annotated in the graph. The δCD_2 peak splitting values were calculated as the difference between the peak positions of the two peaks and are listed in Table 4.

Table 4. δCD_2 peak splitting and the δCD_2 peak height ratio (OR/MID) of the six deuterated LPP models, at 10°C. Data is shown as an average of 3 measurements for each composition ± SD.

Lipid model	δCD_2 peak splitting (cm^{-1})	δCD_2 peak height ratio (OR/MID)
LPP NSd47:NP:DFFA 1:2	4.8 ± 0.1	3.8 ± 0.1
LPP NS:NPd47:DFFA 1:2	5.4 ± 0.1	5.0 ± 0.0
LPP NSd47:NPd47:DFFA 1:2	6.2 ± 0.0	5.4 ± 0.1
LPP NSd47:NP:DFFA 2:1	5.5 ± 0.1	5.0 ± 0.0
LPP NS:NPd47:DFFA 2:1	4.7 ± 0.1	3.9 ± 0.1
LPP NSd47:NPd47:DFFA 2:1	6.3 ± 0.0	5.5 ± 0.1

When CER NPd47 is replaced by protiated CER NP resulting in the LPP NSd47:NP:DFFA 1:2 model, the δCD_2 peak splitting reduces to 4.8 ± 0.1 cm^{-1}, indicating smaller deuterated lipid domains (Table 4). The OR/MID peak height ratio of this sample is decreased in comparison with the model with three deuterated lipids described above, resulting in a

value of 3.8 ± 0.1, indicating that in this sample there are relatively less CD_2-CD_2 chain interactions compared to the CD_2-CD_2 chain interactions in the LPP NSd47:NPd47:DFFA 1:2 model. This demonstrates that the deuterated CER NP acyl chain was a significant part of the deuterated domain formed in the LPP NSd47:NPd47:DFFA 1:2 system.

Next, CER NSd47 was exchanged for the protiated CER NS (LPP NS:NPd47:DFFA 1:2 model). The δCD_2 peak splitting distance of this model is 5.4 ± 0.1 cm^{-1}, which is also a lower value compared to the LPP NSd47:NPd47:DFFA 1:2 model, indicating that the acyl chain of CER NS was also part of the large deuterated domains. The values of the δCD_2 peak splitting distance and peak height ratio are also lower in comparison with the LPP:NS:NPd47:DFFA 1:2 model, as shown by the data in Table 4. This difference is caused by the lower concentration of CER NS compared to CER NP in the LPP NS:NP 1:2 ratio model (CER NS represents 20% of the total CERs, while the CER NP concentration is 40%).

When analyzing the lipid models with the CER NS:CER NP ratio of 2:1, a similar trend to the 1:2 models was observed (Figure 6B). The fully deuterated model (LPP NSd47:NPd47:DFFA 2:1) has a large δCD_2 peak splitting distance of 6.3 ± 0.0 cm^{-1}, comparable to the 1:2 model with the same deuterated lipids composition. This indicates that size of the deuterated domains in the two compositions is very similar. Furthermore, comparable results are obtained for the partially deuterated models LPP NSd47:NP:DFFA 2:1 and LPP NS:NPd47:DFFA 2:1, where the δCD_2 peak splitting distance is 5.5 ± 0.1 cm^{-1} and 4.7 ± 0.1 cm^{-1} and the OR/MID peak height ratios of 5 and 3.9 respectively (Table 4). This reveals that the deuterated acyl chains of CER NS and CER NP are indeed part of the large deuterated domains of the CER NS:CER NP 2:1 models. The difference in the δCD_2 peak splitting values between the LPP NSd47:NP:DFFA 2:1 and LPP NS:NPd47:DFFA 2:1 models (observed from Figure 6B and Table 4) are caused by the different concentrations of the deuterated CER NS and CER NP in the model.

When comparing the peak splitting of the LPP NSd47:NP:DFFA with the LPP NS:NPd47:DFFA models, the peak splitting distances and δCD_2 peak height ratios were similar when the same fraction of deuterated CERs was compared for both the 1:2 and 2:1 models (Table 4).

The δCH_2 vibrations of all these partially deuterated LPP models show a single peak at 1468 cm^{-1} at 10 °C (Figure 6 C,D). This indicates that the protiated lipid chains were well mixed with the deuterated lipid chains and they did not form phase separated protiated lipid domains. Possibly a fraction of the protiated chains may also be in a hexagonal packing contributing to the single peak at 1468 cm^{-1}. Figure 6C and D also indicate that the δCH_2 vibrations of the LPP NSd47:NP:DFFA 1:2 and LPP NS:NPd47:DFFA 2:1 models show a broader peak. The lower level of deuterated lipid compared to the models LPP NS:NPd47:DFFA 1:2 and LPP NSd47:NP:DFFA 2:1 may play a role here as this reduced the CD_2-CH_2 interactions and increased the CH_2-CH_2 interactions.

DISCUSSION

In living cell membranes CERs are in competition with CHOL to interact with the amide group of sphingomyelin by forming a network of hydrogen bonds. These interactions are of interest as they play a role in the formation of lipid rafts (70). In SC the situation is different as hardly no phospholipids are present. However, CHOL and CERs form stable membranes, even in the absence of FFAs, and strongly interact with each other (39). This strong interaction is important, as the SC serves as a barrier to minimize the permeation of compounds to the viable epidermis.

The present study aimed to investigate the effect of changing the CER NS:CER NP molar ratio on the composition of a simple lipid model consisting of CER EOS, CER NS, CER NP, CHOL and FFA C24. The lipid organization, lipid chain interactions, lipid arrangement and barrier functionality of these models were examined, as previous studies have shown that an altered CER NS:CER NP ratio represents one of the lipid compositional changes in the SC of inflammatory skin diseases (29, 34-36). The results of this study showed that the position of CER NS and CER NP in the unit cell is very similar and that varying the CER NS:CER NP ratio (1:2 and 2:1) did not influence the location of the acyl chains of CER NS and CER NP in the LPP unit. Both of these acyl chains were mainly positioned in the inner layer, but with a minor part located in the outer layers of the LPP, similar to a recent study on a LPP model with a CER NS:CER NP 1:1 ratio (49). A schematic drawing of the unit cell lipid arrangement is provided in Supplemental Figure S3.

Lipid models prepared either with isolated CERs (porcine or human origin) or synthetic CERs, along CHOL and FFAs have been shown to mimic the unique phase behavior of native SC (37-42). Previous studies reported the same lipid organization and molecular arrangement both in lipid models with a larger number of lipid subclasses (complex models) and in simpler compositions with only two CER subclasses (49, 56, 63). This important finding allowed the use of lipid models with limited number of components for understanding the molecular arrangement of lipids in SC models. Thus, the findings of this study using simple lipid compositions can be extrapolated both to the complex lipid models (with synthetic or isolated CERs) and to the SC lipid matrix.

The similar arrangement and location of CER NS and CER NP in the LPP unit cell regardless of the molar ratios represents an indication of the adaptability of the SC lamellar phase to changes in the lipid head group structure. This can represent a possible reason why the CER composition in murine and porcine SC (both having CER NS as the most abundant CER subclass) is very different from that in human SC (having CER NP as an abundant CER subclass), while the phase behavior in SC of these three species is very similar (10, 71). The linear conformation of the CERs in these lipid models allows a tighter packing of the lipid chains, which is favorable for the skin barrier. Overall, apart from the relevance to inflammatory skin diseases, the results of this study enhance the understanding of the lipid organization in SC of various species.

Location and conformation of CER NS and CER NP not affected by the changes in composition

Neutron diffraction was used to localize the acyl chains of CER NS and CER NP in the LPP unit of the LPP NS:NP 1:2 and LPP NS:NP 2:1 models. The SLD profiles obtained showed that the deuterated acyl chains of CER NS and CER NP had the same location in the LPP unit cell, predominantly in the central layer, with a small fraction in the outer layers of the repeating unit, for both the CER NS:CER NP 1:2 and 2:1 models. The large splitting of the δCD_2 vibrations in the FTIR spectra revealed large deuterated lipid domains in the LPP of the models LPP NSd47:NPd47:DFFA (1:2 and 2:1 ratio), suggesting that the deuterated acyl chains of CER NS, CER NP and DFFA are neighboring. Therefore, it can be concluded that the CER acyl chains and the FFA are in close proximity in the inner layer of the LPP unit cell.

Besides the large splitting, the deep minimum between the two δCD_2 peaks of the LPP NSd47:NPd47:DFFA model also indicates that the CD_2-CH_2 interactions are reduced to a minimum in the two models. Therefore, CER NS and CER NP with the headgroup located in the two central head group regions adopt primarily an extended conformation, allowing for the acyl chains and FFAs to be in close proximity in the inner layer. It is unlikely that the deuterated acyl chains of CER NS and CER NP interact with the protonated sphingoid bases of these CERs (as would be the case if the CERs adopted hairpin conformations) as this would introduce extensive CD_2-CH_2 interactions. Furthermore, our results demonstrate that the conformations of CER NS and CER NP are not influenced by the change of the CER NS:CER NP molar ratio. A similar location of the acyl chains of CER NS and CER NP and an extended conformation of these CERs were also encountered in a LPP NS:NP 1:1 model, described in a recent study (49).

The results of this study demonstrate the adaptability of the LPP unit cell organization to changes in the CER head group architecture: partial replacement of CER NS that has a double bond close to the head group region by CER NP with a C4-hydroxyl group on that position does not affect the lipid arrangement in the unit cell of the LPP.

Choice of CER NS:CER NP ratio for the models

In inflammatory skin diseases such as atopic dermatitis, psoriasis and Netherton syndrome, alongside an altered SC lipid composition and organization compared to control SC, an altered skin barrier function has been reported, often monitored by TEWL (4, 29-31). A strong correlation has been shown between an increased CER NS:CER NP molar ratio and elevated TEWL (36), which might therefore represent an important contribution to the impaired skin barrier function. In healthy SC, the approximate molar ratio of CER NS:CER NP is 1:2.3, while in diseased skin, it is increased to 1:1 or even higher, depending on the severity of the disease (4, 36). Therefore, in this study we used a CER NS:CER NP 1:2 molar ratio as a model for control (healthy) skin, while the models with a

CER NS:CER NP ratio 2:1 and CER NS:CER NP 1:1 used in our previous study mimic the variation in ratios observed in diseased skin (49). Similarly as in atopic eczema patients, we observed an elevated TEWL when increasing the CER NS:CER NP ratio, an indication that a CER head group change results in an impaired skin barrier function. However, we did not observe an increase in the flux of E-PABA through the lipid membrane. As the hydrogen bonding between the head groups is more extensive for CER NP than for CER NS (72, 73), this may cause the water molecules to interact more with the CER head groups in the LPP NS:NP 1:2 model, forming hydrogen bonds and reducing the TEWL flux. Due to its structure, E-PABA may form less hydrogen bonds with the CER headgroup and this could be a reason for the similar E-PABA flux of the two models.

In this study we varied CER NS:CER NP ratio, while keeping the CER chain lengths equal. Previous clinical studies observed that in atopic dermatitis, psoriasis and seborrheic dermatitis patients the CER NS:CER NP ratio correlates with the TEWL (32, 36, 74). However, besides the increase in the CER NS:CER NP ratio, a simultaneous reduction in chain length also occurs in vivo, as the CER NS subclass contains a higher level of CER C34 than CER NP (20, 21, 75). Since we keep the CER chain lengths the same in our models, we demonstrate that a change exclusively in the CER NS:CER NP molar ratio affects the lipid barrier. A recent study by Rousel et al. also showed a strong correlation between the CER NS:CER NP total ratio and the TEWL in SC of seborrheic dermatitis patients (32). In this study, when narrowing the chain length distribution of CER NS and CER NP between C40 and C53 (total number of carbon atoms), while excluding the influence of C34 CERs, an excellent correlation between the molar ratio CER NS:CER NP and TEWL is still observed in patients (Supplemental Figure S4), confirming that the change in CER head group ratio plays a role in the impaired skin barrier function as well. In agreement with our results, another study showed that the permeability of a LPP lipid membrane comprised of 60% CER NS C24 / 40% CER EOS was also significantly higher than that of a model with 60% CER NP / 40% CER EOS (51).

Conformational ordering of the lipid models

An increase in the $\nu_s CH_2$ wavenumber at 10°C was observed for the LPP NSd47:NPd47:DFFA (1:2 and 2:1 ratios) models in comparison with the protiated samples LPP NS:NP (1:2 and 2:1) and the LPP NSd47:NP:DFFA and LPP NS:NPd47:DFFA models. Possibly the sphingoid bases have a lower conformational ordering than the acyl chain of the CERs and FFAs and a fraction of these might be in a hexagonal packing, as also indicated by the single peak in the δCH_2 vibrations in the membranes of the LPP NSd47:NPd47:DFFA 1:2 and 2:1 ratios, as the level of deuterated chains in the outer layers is expected to be low. However, an increase can also be caused by changes in intermolecular coupling between the chains, which increases the frequency of the $\nu_s CH_2$ wavenumber in the partly deuterated samples (76). This effect is more pronounced for the $\nu_s CH_2$ vibration, as intermolecular coupling does not affect the $\nu_s CH_2$ and $\nu_s CD_2$ bands to

the same extent. The $\nu_s CH_2$ vibrations of the deuterated models (LPP NSd47:NPd47:DFFA 1:2 and 2:1 ratios) show an increase of the wavenumber between 30-40°C, characteristic for a phase transition from orthorhombic to hexagonal packing, however, there is a singlet observed in the δCH_2 vibrations. These results indicate that besides the hexagonal packing, a part of the protiated lipids is in an orthorhombic phase: sphingosine chain of CER NS, phytosphingosine chain of CER NP, alongside the CER EOS and CHOL, which are all located in the outer layers of the LPP unit cell (Supplemental Figure S3). The increased width of the singlet peak of the δCH_2 vibrations at 1468 cm^{-1} in the LPP NSd47:NP:DFFA 1:2 and LPP NS:NPd47:DFFA 2:1 compositions indicates that indeed small fractions of the acyl chains of CER NS and CER NP are present in the outer layers of the LPP, partitioning in an orthorhombic packing.

CONCLUSION

This study investigated the effect of systematically changing the molar ratio of CER NS and CER NP in lipid models that mimic the lipid organization of the SC. This is one of the lipid compositional changes previously reported in inflammatory skin diseases correlating with skin barrier impairment. Our findings show that an increased CER NS:CER NP molar ratio (mimicking the diseased SC ratio) does not alter the lipid organization and molecular arrangement of the LPP, while the TEWL was increased in the LPP NS:NP 2:1 model, suggesting an impaired barrier function for water. This indicates that the CER NS:CER NP molar ratio might impair the skin barrier function irrespective of a change in chain length observed simultaneously in clinical studies. The similar lipid organization and arrangement reported in the lipid models investigated in this study demonstrate the adaptability of the LPP to small changes in the CER head group structure.

ACKNOWLEDGEMENTS

We thank Prof. dr. A. Bunge (Colorado School of Mines, U.S.A.) and Prof. dr. C. McCabe (Heriot-Watt University, U.K.) for the critical reading of the manuscript. We thank the personnel at ISIS Neutron and Muon Source (Didcot, United Kingdom) and ALBA Synchrotron (Cerdanyola del Vallès, Spain) for awarding us experimental beam time and their kind assistance during the measurements. ISIS raw neutron data DOI: 10.5286/ISIS.E.RB1969003 (77). We are grateful to Evonik (Essen, Germany) for their donation of the CERs. This study was supported by the National Institute of Arthritis and Muscoskeletal and Skin Diseases, grant number R01AR072679.

REFERENCES

1. Proksch, E., Brandner, J. M., Jensen, J.-M. (2008) The skin: an indispensable barrier. *Experimental Dermatology*. 17(12), 1063-72.
2. Madison, K. C. (2003) Barrier function of the skin: "la raison d'etre" of the epidermis. *J Invest Dermatol*. 121(2), 231-41.
3. Wertz, P. W., van den Bergh, B. (1998) The physical, chemical and functional properties of lipids in theskin and other biological barriers. *Chem Phys Lipids*. 9185-96.
4. van Smeden, J., Janssens, M., Gooris, G. S., Bouwstra, J. A. (2014) The important role of stratum corneum lipids for the cutaneous barrier function. *Biochim Biophys Acta*. 1841(3), 295-313.
5. Wertz, P. W., Miethke, M. C., Long, S. A., Strauss, J. S., Downing, D. T. (1985) The composition of the ceramides from human stratum corneum and from comedones. *J Invest Dermatol*. 84(5), 410-2.
6. Weerheim, A., Ponec, M. (2001) Determination of stratum corneum lipid profile by tape stripping in combination with high-performance thin-layer chromatography. *Arch Dermatol Res*. 293191-9.
7. t'Kindt, R., Jorge, L., Dumont, E., Couturon, P., David, F., Sandra, P., et al. (2012) Profiling and characterizing skin ceramides using reversed-phase liquid chromatography-quadrupole time-of-flight mass spectrometry. *Anal Chem*. 84(1), 403-11.
8. Masukawa, Y., Narita, H., Shimizu, E., Kondo, N., Sugai, Y., Oba, T., et al. (2008) Characterization of overall ceramide species in human stratum corneum. *J Lipid Res*. 49(7), 1466-76.
9. van Smeden, J., Hoppel, L., van der Heijden, R., Hankemeier, T., Vreeken, R. J., Bouwstra, J. A. (2011) LC/MS analysis of stratum corneum lipids: ceramide profiling and discovery. *J Lipid Res*. 52(6), 1211-21.
10. Kawana, M., Miyamoto, M., Ohno, Y., Kihara, A. (2020) Comparative profiling and comprehensive quantification of stratum corneum ceramides in humans and mice by LC/MS/MS. *J Lipid Res*. 61(6), 884-95.
11. Mizutani, Y., Mitsutake, S., Tsuji, K., Kihara, A., Igarashi, Y. (2009) Ceramide biosynthesis in keratinocyte and its role in skin function. *Biochimie*. 91(6), 784-90.
12. Brown, R. E. (1998) Sphingolipid organization in biomembranes: what physical studies of model membranes reveal. *Journal of Cell Science*. 1111(1), 1-9.
13. Lingwood, D., Simons, K. (2010) Lipid Rafts As a Membrane-Organizing Principle. *Science*. 327(5961), 46-50.
14. Ponec, M., Weerheim, A., Lankhorst, P., Wertz, P. (2003) New Acylceramide in Native and Reconstructed Epidermis. *J Invest Dermatol*. 120(4), 581-8.
15. Mojumdar, E. H., Gooris, G. S., Bouwstra, J. A. (2015) Phase behavior of skin lipid mixtures: the effect of cholesterol on lipid organization. *Soft Matter*. 114326-36.
16. Sochorova, M., Audrlicka, P., Cervena, M., Kovacik, A., Kopecna, M., Opalka, L., et al. (2019) Permeability and microstructure of cholesterol-depleted skin lipid membranes and human stratum corneum. *J Colloid Interface Sci*. 535227-38.
17. White, S. H., Mirejovsky, D., King, G. I. (1988) Structure of Lamellar Lipid Domains and Corneocyte Envelopes of Murine Stratum Corneum. An X-ray Diffraction Study. *Biochemistry*. 273725-32.
18. Bouwstra, J. A., Gooris, G. S., van der Spek, J. A., Bras, W. (1991) Structural investigations of human stratum corneum by small-angle X-ray scattering. *J Invest Dermatol*. 97(6), 1005-12.
19. Schreiner, V., Gooris, G. S., Pfeiffer, S., Lanzendorfer, G., Wenck, H., Diembeck, W., et al. (2000) Barrier characteristics of different human skin types investigated with X-ray diffraction, lipid analysis, and electron microscopy imaging. *J Invest Dermatol*. 114(4), 654-60.
20. Janssens, M., van Smeden, J., Gooris, G. S., Bras, W., Portale, G., Caspers, P. J., et al. (2012) Increase in short-chain ceramides correlates with an altered lipid organization and decreased barrier function in atopic eczema patients. *J Lipid Res*. 53(12), 2755-66.
21. van Smeden, J., Janssens, M., Boiten, W. A., van Drongelen, V., Furio, L., Vreeken, R. J., et al. (2014) Intercellular skin barrier lipid composition and organization in Netherton syndrome patients. *J Invest Dermatol*. 134(5), 1238-45.
22. Uche, L. E., Gooris, G. S., Bouwstra, J. A., Beddoes, C. M. (2021) High concentration of the ester-linked omega-hydroxy ceramide increases the permeability in skin lipid model membranes. *Biochim Biophys Acta Biomembr*. 1863(1), 183487.

23. Bouwstra, J. A., Gooris, G. S., Dubbelaar, F. E., Weerheim, A., IJzerman, A. P., Ponec, M. (1998) Role of ceramide 1 in the molecular organization of the stratum corneum lipids. *J Lipid Res*. 39186-96.
24. Boncheva, M., Damien, F., Normand, V. (2008) Molecular organization of the lipid matrix in intact Stratum corneum using ATR-FTIR spectroscopy. *Biochim Biophys Acta*. 1778(5), 1344-55.
25. Damien, F., Boncheva, M. (2010) The extent of orthorhombic lipid phases in the stratum corneum determines the barrier efficiency of human skin in vivo. *J Invest Dermatol*. 130(2), 611-4.
26. Mendelsohn, R., Rerek, M. E., Moore, D. J. (2000) Infrared spectroscopy and microscopic imaging of stratum corneum models and skin. *Physical Chemistry Chemical Physics*. 2(20), 4651-7.
27. Björklund, S., Nowacka, A., Bouwstra, J. A., Sparr, E., Topgaard, D. (2013) Characterization of Stratum Corneum Molecular Dynamics by Natural-Abundance 13C Solid-State NMR. *PLoS One*. 8(4), e61889.
28. Demel, R. A., de Kruyff, B. (1976) The Function of Sterols in Membranes. *Biochim Biophys Acta*. 457109-32.
29. Motta, S., Monti, M., Sesana, S., Caputo, R., Carelli, S., Ghidoni, R. (1993) Ceramide composition of the psoriatic scale. *Biochim Biophys Acta*. 1182147-51.
30. Janssens, M., van Smeden, J., Gooris, G. S., Bras, W., Portale, G., Caspers, P. J., et al. (2011) Lamellar lipid organization and ceramide composition in the stratum corneum of patients with atopic eczema. *J Invest Dermatol*. 131(10), 2136-8.
31. Sahle, F. F., Gebre-Mariam, T., Dobner, B., Wohlrab, J., Neubert, R. H. (2015) Skin diseases associated with the depletion of stratum corneum lipids and stratum corneum lipid substitution therapy. *Skin Pharmacol Physiol*. 28(1), 42-55.
32. Rousel, J., Nădăban, A., Saghari, M., Pagan, L., Zhuparris, A., Theelen, B., et al. (2024) Lesional skin of seborrheic dermatitis patients is characterized by skin barrier dysfunction and correlating alterations in the stratum corneum ceramide composition. *Exp. Dermatol.* 33(1), e14952.
33. Imokawa, G., Abe, A., Jin, K., Higaki, Y., Kawashima, M., Hidano, A. (1991) Decreased level of ceramides in stratum corneum of atopic dermatitis: an etiologic factor in atopic dry skin? *J Invest Dermatol*. 96(4), 523-6.
34. Di Nardo, A., Wertz, P. W., Giannetti, A., Seidenari, S. (1998) Ceramide and Cholesterol Composition of the Skin of Patients with Atopic Dermatitis. *Acta Derm Venereol* 7827-30.
35. van Smeden, J., Al-Khakany, H., Wang, Y., Visscher, D., Stephens, N., Absalah, S., et al. (2020) Skin barrier lipid enzyme activity in Netherton patients is associated with protease activity and ceramide abnormalities. *J Lipid Res*. 61(6), 859-69.
36. Yokose, U., Ishikawa, J., Morokuma, Y., Naoe, A., Inoue, Y., Yasuda, Y., et al. (2020) The ceramide [NP]/[NS] ratio in the stratum corneum is a potential marker for skin properties and epidermal differentiation. *BMC Dermatology*. 20(1).
37. Bouwstra, J., Gooris, G., Cheng, K. A. W., Bras, W., Ponec, M. (1996) Phase behavior of isolated skin lipids. *J Lipid Res*. 37999 - 1011.
38. McIntosh, T. J., Stewart, M. E., Downing, D. T. (1996) X-ray Diffraction Analysis of Isolated Skin Lipids: Reconstitution of Intercellular Lipid Domains. *Biochemistry*. 35(12), 3649-53.
39. Bouwstra, J. A., Gooris, G. S., Dubbelaar, F. E. R., Ponec, M. (2001) Phase behavior of lipid mixtures based on human ceramides: coexistence of crystalline and liquid phases. *J Lipid Res*.42(11), 1759-70.
40. Opalka, L., Kovacik, A., Maixner, J., Vavrova, K. (2016) Omega-O-Acylceramides in Skin Lipid Membranes: Effects of Concentration, Sphingoid Base, and Model Complexity on Microstructure and Permeability. *Langmuir*. 32(48), 12894-904.
41. de Jager, M. W., Gooris, G. S., Ponec, M., Bouwstra, J. A. (2005) Lipid mixtures prepared with well-defined synthetic ceramides closely mimic the unique stratum corneum lipid phase behavior. *J Lipid Res*. 46(12), 2649-56.
42. Uche, L. E., Gooris, G. S., Bouwstra, J. A., Beddoes, C. M. (2019) Barrier Capability of Skin Lipid Models: Effect of Ceramides and Free Fatty Acid Composition. *Langmuir*. 35(47), 15376-88.
43. Opálka, L., Kováčik, A., Pullmannová, P., Maixner, J., Vávrová, K. (2020) Effects of omega-O-acylceramide structures and concentrations in healthy and diseased skin barrier lipid membrane models. *J Lipid Res*. 61(2), 219-28.

44. Janssens, M., Gooris, G. S., Bouwstra, J. A. (2009) Infrared spectroscopy studies of mixtures prepared with synthetic ceramides varying in head group architecture: coexistence of liquid and crystalline phases. *Biochim Biophys Acta*. 1788(3), 732-42.
45. Beddoes, C. M., Gooris, G. S., Bouwstra, J. A. (2018) Preferential arrangement of lipids in the long-periodicity phase of a stratum corneum matrix model. *J Lipid Res*. 59(12), 2329-38.
46. Basse, L. H., Groen, D., Bouwstra, J. A. (2013) Permeability and lipid organization of a novel psoriasis stratum corneum substitute. *Int J Pharm*. 457(1), 275-82.
47. de Jager, M., Groenink, W., Bielsa i Guivernau, R., Andersson, E., Angelova, N., Ponec, M., et al. (2006) A novel in vitro percutaneous penetration model: evaluation of barrier properties with p-aminobenzoic acid and two of its derivatives. *Pharm Res*. 23(5), 951-60.
48. Groen, D., Gooris, G. S., Ponec, M., Bouwstra, J. A. (2008) Two new methods for preparing a unique stratum corneum substitute. *Biochim Biophys Acta*. 1778(10), 2421-9.
49. Nădăban, A., Gooris, G. S., Beddoes, C. M., Dalgliesh, R. M., Bouwstra, J. A. (2022) Phytosphingosine ceramide mainly localizes in the central layer of the unique lamellar phase of skin lipid model systems. *J Lipid Res*. 63(9), 100258.
50. de Jager, M., Groenink, W., van der Spek, J., Janmaat, C., Gooris, G., Ponec, M., et al. (2006) Preparation and characterization of a stratum corneum substitute for in vitro percutaneous penetration studies. *Biochim Biophys Acta*. 1758(5), 636-44.
51. Uche, L. E., Gooris, G. S., Beddoes, C. M., Bouwstra, J. A. (2019) New insight into phase behavior and permeability of skin lipid models based on sphingosine and phytosphingosine ceramides. *Biochim Biophys Acta Biomembr*. 1861(7), 1317-28.
52. Mojumdar, E. H., Kariman, Z., van Kerckhove, L., Gooris, G. S., Bouwstra, J. A. (2014) The role of ceramide chain length distribution on the barrier properties of the skin lipid membranes. *Biochim Biophys Acta*. 1838(10), 2473-83.
53. Wojdyr, M. (2010) Fityk: a general-purpose peak fitting program. *Journal of Applied Crystallography*. 43(5), 1126-8.
54. Oguri, M., Gooris, G. S., Bito, K., Bouwstra, J. A. (2014) The effect of the chain length distribution of free fatty acids on the mixing properties of stratum corneum model membranes. *Biochim Biophys Acta*. 1838(7), 1851-61.
55. Arnold, O., Bilheux, J. C., Borreguero, J. M., Buts, A., Campbell, S. I., Chapon, L., et al. (2014) Mantid—Data analysis and visualization package for neutron scattering andμSR experiments. *Nuclear Instruments and Methods in Physics Research Section A: Accelerators, Spectrometers, Detectors and Associated Equipment*. 764156-66.
56. Mojumdar, E. H., Gooris, G. S., Barlow, D. J., Lawrence, M. J., Deme, B., Bouwstra, J. A. (2015) Skin lipids: localization of ceramide and fatty acid in the unit cell of the long periodicity phase. *Biophys J*. 108(11), 2670-9.
57. Mojumdar, E. H., Gooris, G. S., Groen, D., Barlow, D. J., Lawrence, M. J., Deme, B., et al. (2016) Stratum corneum lipid matrix: Location of acyl ceramide and cholesterol in the unit cell of the long periodicity phase. *Biochim Biophys Acta*. 1858(8), 1926-34.
58. Beddoes, C. M., Gooris, G. S., Barlow, D. J., Lawrence, M. J., Dalgliesh, R. M., Malfois, M., et al. (2022) The importance of ceramide headgroup for lipid localisation in skin lipid models. *Biochim Biophys Acta Biomembr*. 1864(6), 183886.
59. Franks, N. P., Lieb, W.R. (1979) The Structure of Lipid Bilayers and the Effects of General Anaesthetics: An X-ray and Neutron Diffraction Study. *J Mol Biol*. 133469-500.
60. Kiselev, M. A., Ryabova, N. Y., Balagurov A. M., Dante S., Hauss T., Zbytovska J., et al. (2005) New insights into the structure and hydration of a stratum corneum lipid model membrane by neutron diffraction. *Eur Biophys J*. 34(8), 1030-40.
61. Groen, D., Gooris, G. S., Barlow, D. J., Lawrence, M. J., van Mechelen, J. B., Deme, B., et al. (2011) Disposition of ceramide in model lipid membranes determined by neutron diffraction. *Biophys J*. 100(6), 1481-9.
62. Groen, D., Gooris, G. S., Bouwstra, J. A. (2009) New insights into the stratum corneum lipid organization by X-ray diffraction analysis. *Biophys J*. 97(8), 2242-9.

63. Beddoes, C. M., Gooris, G. S., Foglia, F., Ahmadi, D., Barlow, D. J., Lawrence, M. J., et al. (2020) Arrangement of Ceramides in the Skin: Sphingosine Chains Localize at a Single Position in Stratum Corneum Lipid Matrix Models. *Langmuir*. 36(34), 10270-8.
64. Harroun, T. A., Katsaras, J., Wassall, S. R. (2006) Cholesterol Hydroxyl Group Is Found To Reside in the Center of a Polyunsaturated Lipid Membrane. *Biochemistry*. 451227-33.
65. NIST Center of Neutron Research, https://www.ncnr.nist.gov/resources/activation/ (Accessed: 2021).
66. Mojumdar, E. H., Groen, D., Gooris, G. S., Barlow, D. J., Lawrence M. J., Deme B., et al. (2013) Localization of cholesterol and fatty acid in a model lipid membrane: a neutron diffraction approach. *Biophys J*. 105(4), 911-8.
67. Wiener, M. K., G.; White, S. (1991) Structure of a fluid dioleoylphosphatidylcholine bilayer determined by joint refinement of x-ray and neutron diffraction data 1. Scaling of neutron data and the distributions of double bonds and water. *Biophys J*. 60568-76.
68. Moore, D. J., Rerek, M. E., Mendelsohn, R. (1997) Lipid Domains and Orthorhombic Phases in Model Stratum Corneum: Evidence from Fourier Transform Infrared Spectroscopy Studies. *Biochemical and Biophysical Research Communications*. 231797 - 801.
69. Mendelsohn, R., Moore, D. J. (1998) Vibrational spectroscopic studies of lipid domains in biomembranes and model systems. *Chem Phys Lipids*. 96141-57.
70. Garcia-Arribas, A. B., Alonso, A., Goni, F. M. (2016) Cholesterol interactions with ceramide and sphingomyelin. *Chem Phys Lipids*. 19926-34.
71. Wertz, P. W., Downing, D. T. (1983) Ceramides of pig epidermis: structure determination. *J Lipid Res*. 24(6), 759-65.
72. Rerek, M. E., Chen, H., Markovic, B., Van Wyck, D., Garidel, P., Mendelsohn, R., et al. (2001) Phytosphingosine and Sphingosine Ceramide Headgroup Hydrogen Bonding: Structural Insights through Thermotropic Hydrogen/Deuterium Exchange. *J PHYS CHEM B*. 1059355 - 62.
73. Guo, S., Moore, T. C., Iacovella, C. R., Strickland, L. A., McCabe, C. (2013) Simulation study of the structure and phase behavior of ceramide bilayers and the role of lipid head group chemistry. *J Chem Theory Comput*. 9(11), 5116-26.
74. Ishikawa, J., Narita, H., Kondo, N., Hotta, M., Takagi, Y., Masukawa, Y., et al. (2010) Changes in the Ceramide Profile of Atopic Dermatitis Patients. *J. Invest. Dermatol*. 130(10), 2511-4.
75. Boer, D. E. C., van Smeden, J., Al-Khakany, H., Melnik, E., van Dijk, R., Absalah, S., et al. (2020) Skin of atopic dermatitis patients shows disturbed beta-glucocerebrosidase and acid sphingomyelinase activity that relates to changes in stratum corneum lipid composition. *Biochim Biophys Acta Mol Cell Biol Lipids*. 1865(6), 158673.
76. Kodati, V. R., El-Jastimi, R., Lafleur, M. (1994) Contribution of the Intermolecular Coupling and Librotorsional Mobility in the Methylene Stretching Modes in the Infrared Spectra of Acyl Chains. *J Phys Chem*. 9812191-7.
77. Bouwstra, J., Gooris, G., Dalgliesh, R.M., Beddoes, C.M., Nădăban, A. (2020) Understanding the effect of Ceramide NP concentration on the skin's long periodicity phase - relevant for atopic eczema studies. *STFC ISIS Neutron and Muon Source*.DOI: https://doi.org/10.5286/ISIS.E.RB1969003.

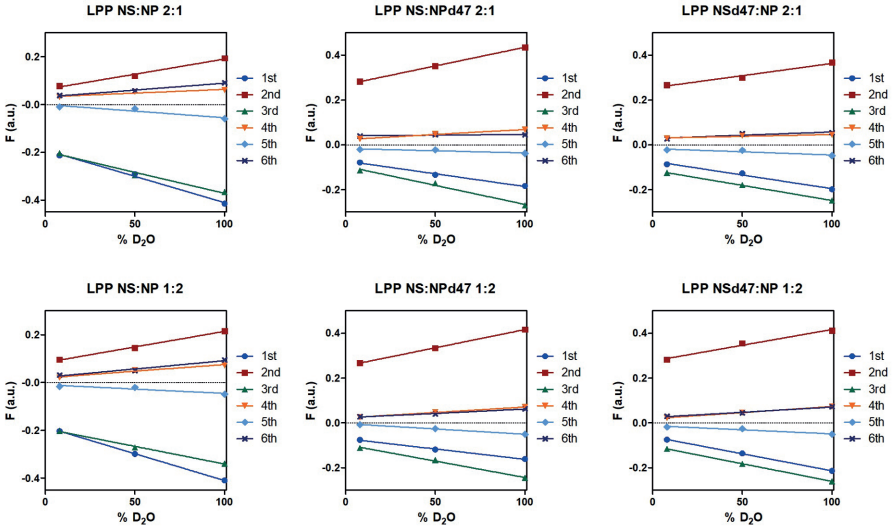


Figure S1. The relative structure factors (F) for the six diffraction orders of the LPP NS:NP, LPP NS:NPd47, LPP NSd47:NP models with the two CER NS:CER NP molar ratios. The Fs are plotted as a function of the percentage of D_2O in the D_2O/H_2O hydration buffers. The graphs were fitted using linear regression. The diffraction orders are each represented by different colors and symbols: 1st (circle, dark blue), 2nd (square, red), 3rd (triangle, green), 4th (triangle, orange), 5th (diamond, light blue), 6th (cross, purple).

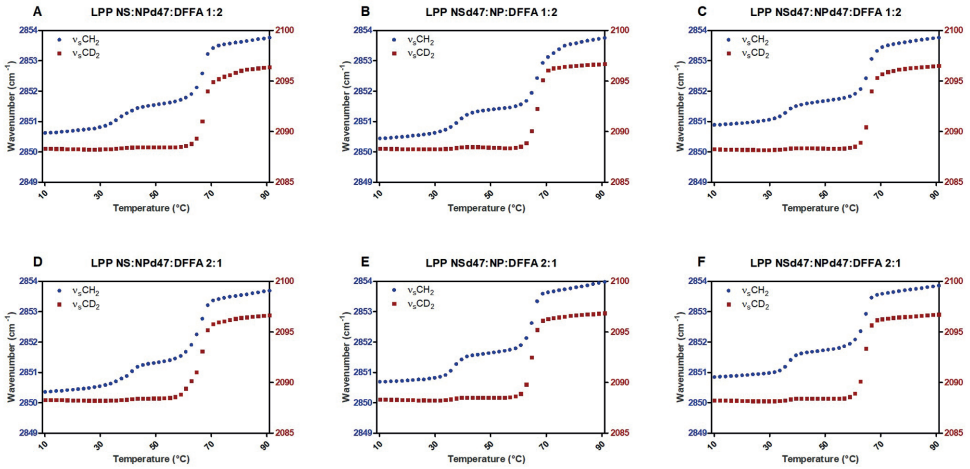


Figure S2. Thermotropic curves of the ν_sCH_2 and ν_sCD_2 vibrations for the CER NS:CER NP 1:2 and 2:1 ratio models with different deuterated chains. The wavenumbers of the ν_sCH_2 and ν_sCD_2 peak positions (left and right y-axis) are plotted in the 10-90°C temperature range. Data shown as an average of 3 measurements for each composition.

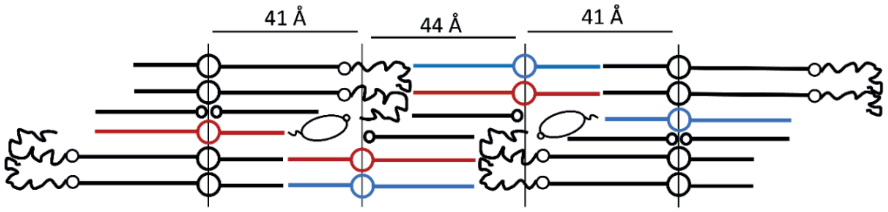


Figure S3. The molecular arrangement of the trilayer structure of the LPP unit cell in a CER EOS C30: CER NS C24: CER NP C24: CHOL: FFA C24 (0.4:0.3:0.3:1:1) model. Reprinted from Nădăban et al. (1). CER NS is depicted in red, CER NP in blue, and CER EOS, CHOL and FFA C24 are drawn in black.

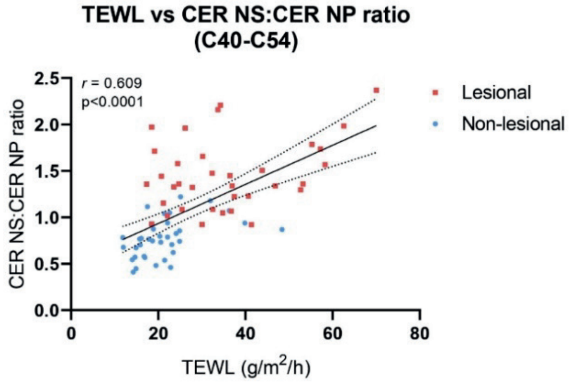


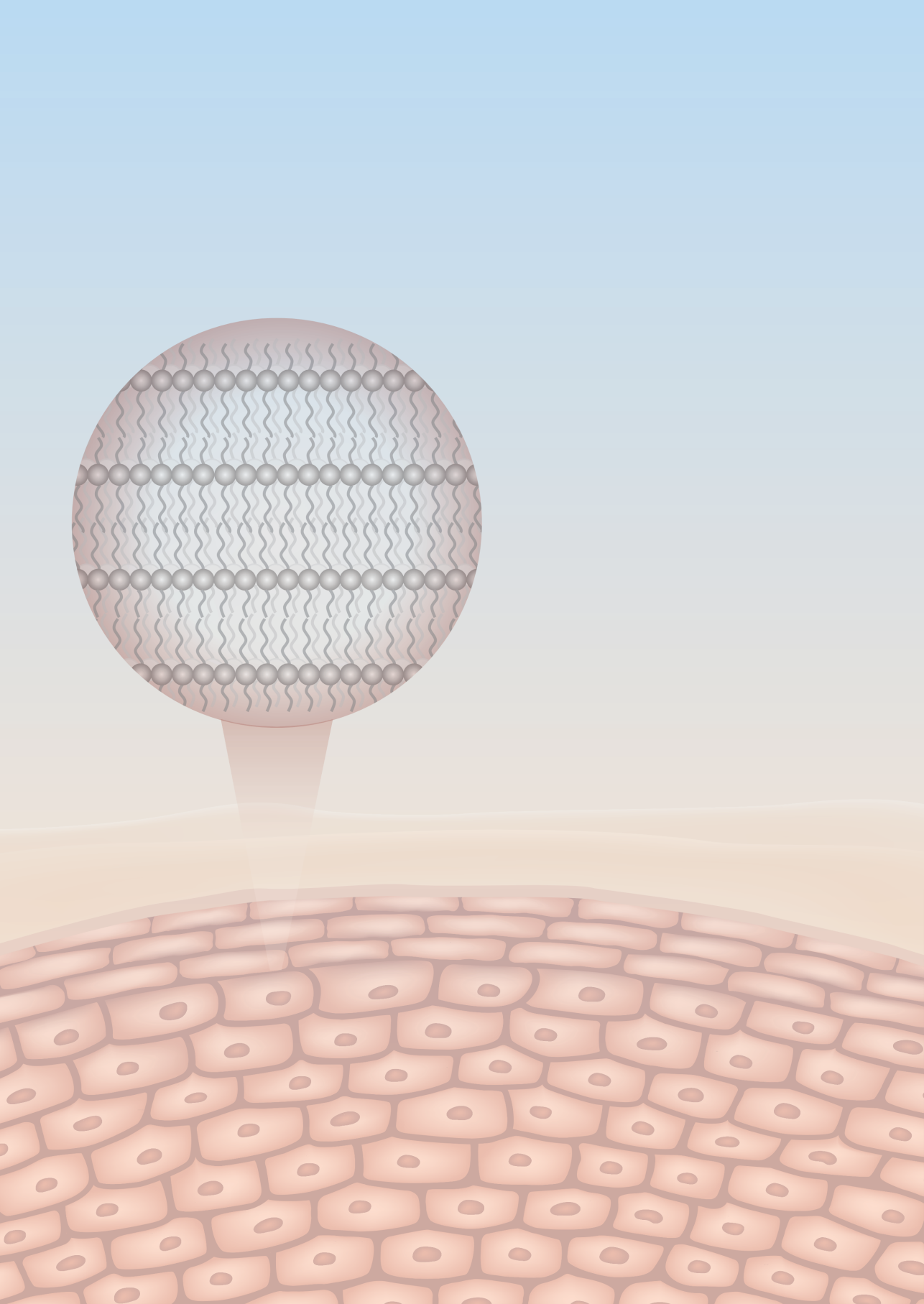
Figure S4. Correlation between the CER NS:CER NP ratio with CER chain lengths between C40 – C54 carbon atoms and TEWL from lesional and non-lesional SC of seborrheic dermatitis subjects. This data is part of the clinical study on 37 subjects described by Rousel et al. (2). The correlation is shown with the Pearson's correlation coefficient. Tape-strips were collected from subjects, the lipids were extracted and quantitatively analyzed using liquid chromatography – mass spectrometry (LC-MS). TEWL measurements were conducted on the subjects prior to the tape-stripping. The materials and methods of this study can be found in Rousel et al. (2).

Table S1. The average mid-transition temperatures (T_m) of the orthorhombic to hexagonal (O-H) phase and hexagonal to liquid (H-L) phase transitions for the six deuterated models. The data is shown as the average of 3 measurements for each composition, with the standard deviation.

Model	T_m O-H (°C)	T_m H-L (°C)
LPP NSd47:NP:DFFA 1:2	37.7 ± 1.5	66.9 ± 1.5
LPP NS:NPd47:DFFA 1:2	36.6 ± 1.1	66.3 ± 0.6
LPP NSd47:NPd47:DFFA 1:2	35.3 ± 0.4	65.5 ± 0.4
LPP NSd47:NP:DFFA 2:1	37.0 ± 0.5	64.7 ± 0.5
LPP NS:NPd47:DFFA 2:1	39.1 ± 0.9	65.8 ± 1.0
LPP NSd47:NPd47:DFFA 2:1	36.8 ± 0.7	63.7 ± 0.3

SUPPLEMENTARY REFERENCES:

1. Nădăban, A., Gooris, G. S., Beddoes, C. M., Dalgliesh, R. M., Bouwstra, J. A. (2022) Phytosphingosine ceramide mainly localizes in the central layer of the unique lamellar phase of skin lipid model systems. *J Lipid Res*. 63(9), 100258.
2. Rousel, J., Nădăban, A., Saghari, M., Pagan, L., Zhuparris, A., Theelen, B., et al. (2024) Lesional skin of seborrheic dermatitis patients is characterized by skin barrier dysfunction and correlating alterations in the stratum corneum ceramide composition. *Exp. Dermatol.* 33(1), e14952.



CHAPTER 5

Influence of the sphingosine and phytosphingosine ceramide ratio on the lipid organization in the short periodicity phase

Authors and affiliations:
Andreea Nădăban[1], Dounia El Yachioui[1], Gerrit S. Gooris[1], Robert M. Dalgliesh[2], Marc Malfois[3], Joke A. Bouwstra[1*]

[1]Division of BioTherapeutics, Leiden Academic Centre for Drug Research, Leiden University, Leiden, The Netherlands
[2]ISIS Neutron and Muon Source, Science and Technology Facilities Council, Rutherford Appleton Laboratory, Didcot, United Kingdom
[3]ALBA Synchrotron, Cerdanyola del Vallès, Barcelona, Spain

To be submitted

ABSTRACT

The lipids located in the outermost layer of the skin, known as the stratum corneum (SC), play a crucial role in maintaining the barrier function of the skin. The primary components of the SC lipid matrix are ceramides (CERs), cholesterol (CHOL) and free fatty acids (FFAs). They form two crystalline lamellar phases, the long periodicity phase and short periodicity phase, referred to as the LPP and SPP, respectively. In inflammatory skin conditions like atopic dermatitis and psoriasis, there are alterations in the SC CER composition, such as an increased concentration of a sphingosine-based CER (CER NS), while the concentration of a phytosphingosine-based CER (CER NP) is decreased. In this study, a lipid model was created exclusively forming the SPP, to investigate whether alterations in the CER NS:CER NP molar ratio would affect the lipid organization and whether the arrangement of the lipids is similar as observed in the LPP. Lipid models were prepared using CER NS: CER NP at ratios of 1:2 (mimicking a healthy SC ratio) and 2:1 (ratio observed in inflammatory skin diseases). The CERs were combined with CHOL and FFA C24. The findings indicate that the acyl chains of CER NS and CER NP and FFAs are in close proximity within the SPP unit cell, similarly as observed for the LPP. This also implies that CER NS and CER NP adopt an extended CER conformation in the SPP unit, resembling the arrangement in the inner layer of LPP models. The two compositions showed slightly different hydrogen bonding networks, which might be attributed to intermolecular hydrogen bonding interactions among the CER NP head groups.

INTRODUCTION

Ceramides (CERs) represent one of the main lipid classes of the intercellular regions of the outermost layer of the skin, the stratum corneum (SC). CERs belong to the group of sphingolipids, an important component of biological membranes, which are involved in different biological processes like cell proliferation, differentiation and apoptosis (1, 2). CERs, along with cholesterol (CHOL) and free fatty acids (FFAs), form the highly organized lipid matrix of the SC, which restricts water loss and preventing the permeation of pathogens and other hazardous materials into the body (3-6). The SC lipid matrix does not include phospholipids, in contrast with other biological membranes (7).

The organization of SC lipids is different from other membranes with high CHOL content. In those membranes often a liquid ordered phase is present (8). Lipids in human SC are organized into two coexisting crystalline lamellar phases with repeat distances of ~13 nm and ~6 nm called the long and short periodicity phases (LPP and SPP), respectively (9-11). Previous studies have shown that the esterified ω-hydroxy sphingosine ceramide (CER EOS) plays an important role in the formation of the LPP (12, 13). When CER EOS is not present in the lipid model systems, only the SPP is formed. A gradual increase in CER EOS concentration enhances the formation of the LPP in SC lipid model systems and in SC at the expense of the SPP (14).

Within the LPP and SPP phases, the lipid chains can have different packing densities within the lamellae, referred to as the lateral organization: orthorhombic (ordered phase, very dense packing of lipids), hexagonal (ordered phase, but less dense packing) or liquid phase (disordered lipid packing) (15-17). The human SC lipids mainly adopt an orthorhombic packing, with a smaller fraction of lipids forming a hexagonal packing. Even small liquid domains have been reported in human SC (18).

The SC lipids play a crucial role in the skin barrier function (5, 19). Changes in the SC lipid composition have been reported in inflammatory skin diseases, like psoriasis, atopic dermatitis or seborrheic dermatitis (19-25). Among the different lipid compositional changes, the altered ratio of the CERs containing non-hydroxy acyl chains linked to a sphingosine chain (CER NS) and a phytosphingosine chain (CER NP) is often encountered in diseased SC, and it was reported to correlate with an impaired skin barrier (23, 25, 26). The effect of the CER NS:CER NP molar ratio on the lipid organization and barrier function was recently studied using a lipid model that formed exclusively the LPP (27). The aim of this study was to investigate the effect of a variation of this ratio in a lipid model of which the lipids form only the SPP (in the absence of CER EOS).

The study was performed using lipid models that mimic important aspects of the SC lipid organization. Previously, it was shown that lipid models consisting of isolated CERs (extracted from porcine or human SC) mixed with CHOL and FFAs can mimic the unique lamellar organization of the SC lipids (28-30). Moreover, replacing the isolated porcine or human CERs with their synthetic counterparts did not affect the lamellar phase behavior

of the lipid models, which still mimicked the native SC lipid organization (31-35). The CER composition of lipid models forming only the SPP varied in different studies from a mix of CER subclasses alongside CHOL and FFAs, to systems which only included a single CER subclass, with most of the studies focusing on CER NS (36-41). A similar lamellar and lateral organization of the lipids was reported for the models prepared with five different CER subclasses and models with only CER NS, mixed with CHOL and FFAs. Using lipid models with a limited number of components offers the possibility of a more detailed analysis due to the possibility to use deuterated lipids.

In this study we used the CER NS: CER NP molar ratio of 1:2 (mimicking the ratio observed in healthy SC) and 2:1 (an approximate ratio corresponding to severe inflammatory skin diseases) (23), mixed with CHOL and FFA C24. The lamellar organization, the lipid packing and lipid chain interactions were examined, as well as the hydrogen network formed in the systems.

MATERIALS AND METHODS

Materials

The CERs used in this study were *N*-(tetracosanoyl)-sphingosine (CER NS C24), *N*-(tetracosanoyl)-phytosphingosine (CER NP C24) and these two CERs with perdeuterated acyl chain (CER NSd47 and CER NPd47), kindly donated by Evonik (Essen, Germany) (Figure S1). CER NS with the sphingosine chain terminally deuterated (CER NSd7) was acquired from Avanti Polar Lipids (Alabama, USA). CHOL, lignoceric acid (FFA C24), D_2O and the acetate buffer salts were obtained from Sigma-Aldrich-Chemie GmbH (Schnelldorf, Germany). The perdeuterated FFA C24 (DFFA C24) was purchased from Arc Laboratories B.V. (Apeldoorn, The Netherlands). All organic solvents were of analytical grade, acquired from Biosolve B.V. (Valkenswaard, The Netherlands). The Nuclepore track-etched membranes were purchased from Whatman (Kent, UK). The milli-Q water was of Millipore quality.

Lipid model compositions and preparation

The lipid models were prepared in equimolar ratio of CERs, CHOL and FFA C24 (1:1:1). Two ratios of CER NS: CER NP were included in this study: 1:2 and 2:1 (Table 1). For the Fourier-transform infrared spectroscopy (FTIR) studies, similar models were prepared with DFFA C24, CER NSd47 and/or CER NPd47. For Neutron diffraction studies, a model with CER NSd7 was prepared (SPP NS:NP 2:1). All of the models studied are presented in Table 1.

Table 1. Sample compositions and abbreviations of the lipid models studied

Lipid model	Composition	Molar ratios
SPP NS:NP 1:2	CER NS C24: CER NP C24: CHOL: FFA C24	0.33:0.66:1:1
SPP NS:NP 2:1	CER NS C24: CER NP C24: CHOL: FFA C24	0.66:0.33:1:1
SPP NSd47:NPd47:DFFA 1:2	CER NSd47: CER NPd47: CHOL: DFFA C24	0.33:0.66:1:1
SPP NSd47:NPd47:DFFA 2:1	CER NSd47: CER NPd47: CHOL: DFFA C24	0.66:0.33:1:1
SPP NS:NPd47:DFFA 1:2	CER NS: CER NPd47: CHOL: DFFA C24	0.33:0.66:1:1
SPP NS:NPd47:DFFA 2:1	CER NS: CER NPd47: CHOL: DFFA C24	0.66:0.33:1:1
SPP NSd47:NP:DFFA 1:2	CER NSd47: CER NP: CHOL: DFFA C24	0.33:0.66:1:1
SPP NSd47:NP:DFFA 2:1	CER NSd47: CER NP: CHOL: DFFA C24	0.66:0.33:1:1
SPP NSd7:NP 2:1	CER NSd7: CER NP: CHOL: FFA C24	0.66:0.33:1:1

First, to prepare the samples, the required amount of each individual lipid was dissolved in chloroform: methanol (2:1, v/v), at a concentration of 5 mg/mL. For the samples used for FTIR studies, 1 mg of the lipid composition was sprayed on an AgBr window over a 10 x 10 mm area. The samples for X-ray studies were dissolved in hexane: ethanol (2:1, v/v) and then sprayed on a Nuclepore polycarbonate membrane, over an area of 2 x 3 mm. During spraying, a Camag Linomat IV sprayer (Muttenz, Switzerland) was used with a spraying rate of 14 s/µL. For the neutron diffraction measurements, 10 mg of lipids dissolved in chloroform: methanol (2:1, v/v) were sprayed on a silicon substrate over an area of 1.2 x 3.8 cm^2, using the same spraying conditions. All samples were equilibrated at 95 °C for 65 min, then slowly cooled to room temperature over 50 min. Lastly, the samples were hydrated with either deuterated acetate buffer (pH 5.0, for FTIR studies) or D_2O/H_2O buffer (at three ratios, 8%, 50% and 100% D_2O) for neutron studies. This hydration occurred at 37 °C for at least 12 hours. Prior to the X-ray measurements, the lipid samples were maintained at 80% relative humidity for at least 24 h.

FTIR measurements

The FTIR data were collected on a PerkinElmer Frontier FTIR (PerkinElmer, Waltham, USA), with a nitrogen cooled mercury cadmium telluride detector. The sample compartment was purged with a continuous flow of dry air to remove moisture. Each spectrum consists of 77 interferograms with a resolution of 1 cm^{-1} (wavenumber). The samples were measured in the wavenumber range of 500-4000 cm^{-1}, between 10 and 90 °C at a heating rate of 4 min/°C. The spectra were extracted using TimeBase (PerkinElmer, Waltham, USA) and processed using Spectrum (Perkin Elmer, Waltham, USA). The data was deconvoluted using γ = 2.2 and a smoothing factor of 76.7. For all lipid compositions measurements were carried out in triplicate.

By analyzing the CH_2 symmetric stretching vibrations (ν_sCH_2), information about the lateral packing and the phase transition of the lipid chains was acquired. The ν_sCH_2 vibrations are observed at ~2849 cm^{-1} and the CD_2 symmetric stretching vibrations at

~2090 cm^{-1} ($\nu_s CD_2$). The mid-phase transition temperature is defined as the temperature at which the lipids are transitioning from orthorhombic to hexagonal packing (T_mO-H) or from hexagonal to liquid (T_mH-L) packing. It was calculated by using the linear regression curve fitting method described elsewhere (39). The lipid chain packing is determined by examining the CH_2 and CD_2 scissoring vibrations (δCH_2, wavenumber range: 1462-1473 cm^{-1}; δCD_2, wavenumber range: 1085-1095 cm^{-1}). Python scripts were used for determination of the δCH_2 and δCD_2 peak positions (fitting Lorentzian peaks) and peak heights. A peak height ratio (OR/MID) was then calculated as the ratio of the average peak height of the two orthorhombic peaks and the height of the central peak. Statistical analyses were performed using Graphpad Prism (v.8) to determine the statistical significance of the mid-phase transition temperatures and scissoring peak splitting of the different compositions (unpaired t-test, significance level set at $P<0.05$). For the amide vibrations (amide I ~1650 cm^{-1} and amide II ~1550 cm^{-1}) the peak positions were determined by peak fitting using the Fityk software (42).

X-ray diffraction measurements

Small-angle X-ray diffraction (SAXD) measurements were performed at the NCD-SWEET beamline (ALBA Synchrotron, Barcelona, Spain), using a Pilatus 1M detector with a pixel array of 981 × 1043, each pixel: 172 × 172 μm^2. The sample to detector distance was 2.148 m, beam wavelength was 0.999 Å. The temperature for the measurements was 23 °C and the samples were scanned for 20 s. Silver behenate was used for calibration of the setup. The one-dimensional SAXD profiles of the scattering intensity as a function of the scattering vector (q) were obtained after the integration of the two-dimensional scattering plot, over a 90° segment from the beam center. The scattering vector (q) is calculated using the formula: $q = (4\pi \sin\theta)/\lambda$, where θ represents the scattering angle and λ is the wavelength. The positions of the n^{th} order diffraction peak (q_n) were determined by peak fitting with the Fityk software, using the Pearson VII function (42). Least squares fitting was used to calculate the repeat distance of the lamellar phase (d), as $d = 2n\pi/q_n$. For peaks that correspond to unknown phases (i.e., not part of a lamellar phase), the spacing at the peak position q was calculated as $spacing = 2\pi/q$.

Neutron diffraction measurements

The small-angle neutron diffraction measurements were performed on the LARMOR instrument at ISIS Neutron and Muon Source (Rutherford Appleton Laboratory, UK). The wavelength range of the neutron beam (with a size 1 x 30 mm) was 1 – 12.5 Å. The distance between the detector and the sample was 4.4 m. The detector was set at 2θ angle of 5° to the direct beam (area covered 664 × 600 mm; pixel size 4 × 8 mm). The angle of the sample to the beam was 2.5°. An aluminum chamber was used for the sample environment, which allowed a constant temperature of the windows of the chamber at

42°C to prevent condensation. An empty chamber was used for a background measurement, which was subtracted from each sample. The samples were measured for 4 h each (40 μA/h accelerator proton charge) at 25 °C for each of the three hydration buffer ratios. A direct beam measurement was used for the normalization to the incident flux shape and the detector efficiency.

To monitor the normalized intensity as a function of the scattering vector (*q*), the neutron data was reduced using the Mantid software framework (43). The resulting *q*-range was 0.032 – 0.991 nm^{-1}. The Bragg equation was used to convert the scattering angle (2θ) to *q* as $q = 4\pi\ sin\theta\ /\ \lambda$. Based on the positions of the equidistant Bragg peaks, the repeat distance (*d*) of the lamellar phase was calculated as $d = 2\pi n/q_n$, with *n* representing the diffraction order number of the peak at the position q_n.

The intensity of each diffraction order was obtained by fitting the Bragg peaks (Fityk software, with a Pearson VII function) (42). Next, the structure factor amplitude for each diffraction order ($|F_n|$) was determined using the formula $\left|F_n\right| = A_n\sqrt{LI_n}$, where L is the Lorentz correction factor, that can be assumed equal to *q*, due to the high degree of lipid lamellae orientation (44). A_n, the correction factor for the sample absorption, was calculated with the formula below, where *l* is the thickness of the lipid sample and μ is the linear attenuation coefficient (45):

$$A_n = \frac{1}{\sqrt{\frac{sin\theta}{2\mu l}\left(1-e^{\frac{-2\mu l}{sin\theta}}\right)}}$$

The contrast variation method with D_2O/H_2O buffer levels (100%, 50%, and 8%) was used to determine the phase signs of the water profile, which are obtained from the positive or negative signs of the slopes of the linear correlation of the absolute structure factors of the samples hydrated at 100% and 8% D_2O/H_2O (46). Assuming water is associated with the hydrophilic head groups located at the boundary of the unit cell, we used the following phase signs combination: - + - + for the four diffraction orders detected in the samples. Next, the F_n with the corresponding phase signs are plotted as a function of the D_2O/H_2O buffer ratio (Figure S2), resulting in a linear fitting for each diffraction order.

The scattering length density profile (SLD) of the SPP unit was obtained by Fourier reconstructions using the structure factor values and the phase signs with the following equation:

$$\rho(x) = F_0 + 2\sum_{n=1}^{n_{max}} F_h\ cos\left(\frac{2\pi nx}{d}\right)$$

where *x* is the distance in the unit cell and *x* = 0 represents the center of the unit cell. F_0 represents the scattering density per unit volume. This was calculated using the lipid sample density and its chemical composition (one water molecule per lipid was included) (47). The SLD profile of the deuterated moiety is determined from the difference between the SLD profile of the deuterated sample and the SLD profile of the protiated sample (both

hydrated at 8% D_2O/H_2O) and this net SLD profile indicates the location of the deuterated part of the lipid chain.

The SLD data was placed on a "relative absolute" scale using a scaling factor, as described previously (44, 48, 49). For the SPP NSd7:NP 2:1 sample, in the SLD profile of the NSd7 chain, the peak area (SLD_a) and peak height (SLD_h) were fitted. The peak area obtained from the subtraction of the SLD profiles of the SPP NS:NP 2:1 sample from the SPP NSd7:NP 2:1 sample, represents the scattering of the deuterium atoms from the CER NS sphingosine chain (SLD_{dif}). The relative absolute SLD profile ($SLD_{correct}$) was calculated as:

$$SLD_{correct} = \frac{SLD_h * SLD_{dif}}{SLD_a}$$

The scaling factor that was then applied to the structure factor values (F_n) was calculated as the ratio between $SLD_{correct}$ and SLD_h values.

RESULTS AND DISCUSSION

Lamellar organization of the two models

The lamellar organization of the two lipid models with CER NS:CER NP ratio 1:2 and 2:1 was examined with SAXD. Figure 1 shows the diffraction profiles of the two systems. The SPP NS:NP 2:1 system is characterized by a series of equidistant peaks, indicating a lamellar phase with a repeat distance of 5.4 nm, the SPP. The only peak that is not assigned to the SPP is phase-separated crystalline CHOL (positioned at q = 1.8 nm^{-1}). The diffraction profile of the SPP NS:NP 1:2 model also shows a series of three equidistant peaks with the repeat distance of 5.4 nm, indicating the formation of the SPP. However, the SAXD profile of this model also shows two other phases indicated in Figure 1. The hash symbols designate a lamellar phase with a d-spacing twice that of the SPP (d = 10.8 nm, first diffraction peak at q = 0.58 nm^{-1}), which has its other diffraction orders overlapping the first, second and third SPP peaks. There are previous reports about a lamellar phase with ~10.6 nm repeat distance in compositions that included CER NH C24 (50, 51), CER NS C24 (52) (Shamaprasad et al. unpublished) and a mixture of CER NS C24/CER NH C24 (53). This phase with a suggested double-bilayer structure was first reported in 1993, but was not considered representative for SC and it was suggested to be an artifact of the sample preparation technique used (54).

The plus symbol in Figure 1 identifies an unknown phase with a peak at a q = 1.4 nm^{-1} (spacing 4.4 nm), which has been observed previously in other compositions and it was suggested that this is a crystalline phase containing CER NP C24 (55). Dahlen et al. reported that pure CER NP C24 needs to be orthorhombically packed and it would adopt a V-shape conformation with a tilt angle of ~ 41°. A spacing of 4.4 nm was also reported in an equimolar model with CER NP C24, CHOL and FFA C24, and the 4.4 nm phase was suggested to represent the V-shape arrangement of CER NP (56).

Unlike the denoted phase separation for the SPP NS:NP 1:2 model, lipid models forming the LPP (the same ratio between the lipid, but with the addition of CER EOS) did not form multi-phase systems even when the CER NS:CER NP molar ratio was 1:2 (27). This suggests that the addition of CER EOS improves the miscibility of the lipids in the model (36, 57).

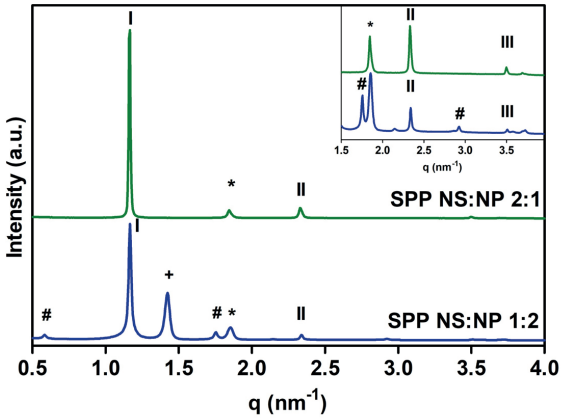


Figure 1. SAXD profiles of the SPP NS:NP 1:2 (blue, lower) and SPP NS:NP 2:1 (green, upper) models. The SPP diffraction orders are indicated with Roman numbers, the asterisk (*) indicates phase-separated CHOL peaks, the hash (#) indicates the peaks corresponding to a lamellar phase with a d-spacing of 10.8 nm and the plus (+) indicates an unknown peak. The top-right panel shows an expanded view of the profile for the *q* range 1.5 – 3.6 nm^{-1}. Data represents an average of 2 measurements.

Lateral organization of the models

Next, the lateral lipid organization was examined using FTIR. The δCH_2 vibrations for the protiated SPP NS:NP 1:2 and SPP NS:NP 2:1 models show two clear peaks at approximately 1462 cm^{-1} and 1473 cm^{-1} (characteristic for orthorhombic packing) and a smaller central peak at 1467 cm^{-1} (attributed to the hexagonal packing of the lipids) (Figure 2A). Peak fitting with Python scripts was used to determine the accurate δCH_2 peak position, the δCH_2 peak splitting (distance between the two peaks caused by an orthorhombic packing), and then the peak height ratio of the average of the two orthorhombic peaks and the hexagonal middle peak (OR/MID). While the δCH_2 peak splitting distance was the same for both models (10.3 ± 0.08 cm^{-1}, Table 2), the SPP NS:NP 1:2 model had a significantly higher central peak relative to the two orthorhombic peaks, and thus a lower OR/MID ratio (1.9 ± 0.1), than the SPP NS:NP 2:1 model (OR/MID ratio 2.3 ± 0.1). The δCH_2 vibrations suggest that both models adopt primarily an orthorhombic packing, however, a small fraction of lipids forms a hexagonal packing, which is higher in the SPP NS:NP 1:2 model. In Figure S3, the δCH_2 vibrations are provided in the 10-50°C temperature range. These vibrations indicate an orthorhombic to hexagonal phase transition.

The thermotropic curves of the $\nu_s CH_2$ vibrations are shown in Figure 2B. At 10°C the $\nu_s CH_2$ wavenumber is <2849 cm^{-1} indicating a high conformational order, while at 32°C there is a transition to a less ordered system, indicated by the increase of the $\nu_s CH_2$ wavenumber. Correlating the $\nu_s CH_2$ vibrations with the observations from the δCH_2 vibrations (Figure S3), this corresponds to the transition from the orthorhombic to hexagonal lipid packing. The mid-phase transition temperatures were similar for the two models, as indicated in Table 2. When the temperature is further increased, another transition can be observed at ~70°C as depicted in Figure 2B, from hexagonal lipid packing to a liquid phase. The difference between the mid-phase transition temperatures (T_m H-L) of the two models is statistically significant ($P<0.05$), as the SPP NS:NP 2:1 model showed a sharper transition with T_m H-L = 70.8 ± 1.8°C, than the transition observed for the SPP NS:NP 1:2 model with T_m H-L = 74.6 ± 0.4 °C (Table 2).

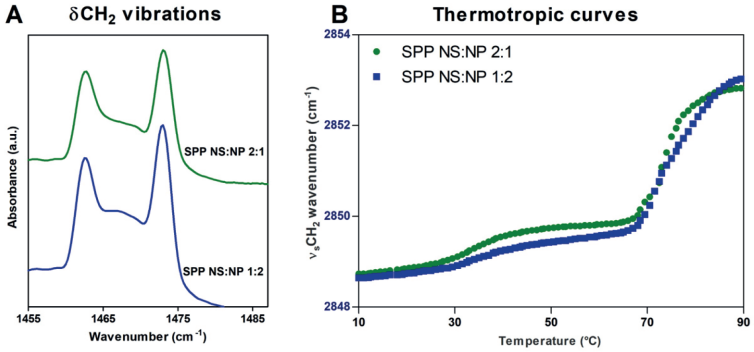


Figure 2. (A) δCH_2 vibrations of the two protiated models, measured at 10°C. (B) Thermotropic curves of the SPP NS:NP 1:2 and 2:1 models, showing the $\nu_s CH_2$ wavenumbers as a function of temperature in the range 10-90°C.

Table 2. δCH_2 peak splitting distance, δCH_2 peak height ratio (OR/MID) of the two SPP models, at 10°C, and the mid-phase transition temperatures (T_m O-H and T_m H-L). Data is shown as an average of 3 measurements for each composition ± SD.

Lipid model	δCH_2 peak splitting ± SD	OR/MID peak height ratio ± SD	T_m O-H ± SD (°C)	T_m H-L ± SD (°C)
SPP NS:NP 1:2	10.3 ± 0.1	1.9 ± 0.1	32.4 ± 0.7	74.6 ± 0.4
SPP NS:NP 2:1	10.3 ± 0.1	2.3 ± 0.1	32.6 ± 1.6	70.8 ± 1.8

Increased hydrogen bonding in the SPP NS:NP 1:2 model

The presence of the hydroxyl and the amide group in the CER structure allows them to act as both a hydrogen bond donor and acceptor. The amide I (~1650 cm^{-1}) and amide II (~1550 cm^{-1}) vibrations measured with FTIR were used to examine hydrogen bonding in the CER head group regions. The amide I band results mainly from the C=O stretching vibration and the amide II reflects primarily the N-H bending vibration and C-N stretching

vibration. Stronger hydrogen bonding can be concluded when there is a lower frequency of the amide I and a higher frequency of amide II vibrations (i.e., the positions of the two amide vibrations are closer) (58, 59). The amide I vibrations are split into two components in the SPP NS:NP 1:2 model, with a peak positioned at 1612.8 ± 0.8 cm^{-1} and another peak at 1640.7 ± 0.5 cm^{-1} (Figure 3). In the spectrum of the SPP NS:NP 2:1 model, the amide I frequency is characterized by a broad peak, centered at 1634.7 ± 2.5 cm^{-1}. The peak corresponding to the amide II band has the same position in both models (1547.9 ±0.3 cm^{-1} for SPP NS:NP 1:2 and 1548.1 ± 0.6 cm^{-1} for SPP NS:NP 2:1 model).

Comparing the two systems from Figure 3, the SPP NS:NP 1:2 system displayed a lower wavenumber of the amide I vibration and a shorter distance to the amide II peak, indicating stronger hydrogen bonding compared to the SPP NS:NP 2:1 model. The intermolecular hydrogen bonding between two CER NP headgroups might contribute to the shift in position and the doublet of the amide I frequency, as it was reported to occur for pure CER NP (60). This difference in the hydrogen bonding of the two models is in agreement with other studies, as a stronger hydrogen bonding determined by CER NP compared to CER NS was previously reported for single component systems, as well as in SPP and LPP models (59-61).

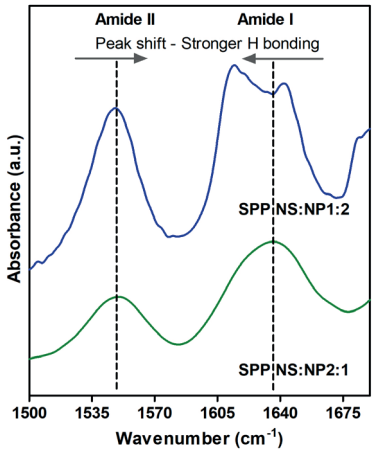


Figure 3. FTIR spectrum of the region 1500 – 1680 cm^{-1} at 10°C, showing the amide I and II frequencies in the SPP NS:NP 2:1 (green, bottom) and SPP NS:NP 1:2 model (blue, top). The shift of the two amide peaks indicates a difference in the hydrogen bond network in the system.

Thermotropic behavior indicates phase separation in SPP NS:NP 1:2 model

To further investigate the lipid mixing of the models, some of the lipids were replaced with their deuterated counterparts: perdeuterated acyl chain of CER NP and/or CER NS and perdeuterated FFA C24. The thermotropic curves of these models (Figure 4) show different behavior of the two SPP models (1:2 and 2:1 ratios). The SPP NS:NP 2:1 models are characterized by sharp transitions from hexagonal to liquid phase, similar to the

protiated sample discussed previously (Figure 2B). Moreover, a similar thermotropic response of the $\nu_s CH_2$ and $\nu_s CD_2$ vibrations is detected for the SPP NS:NP 2:1 models. This indicates that the hexagonal to liquid phase transitions of the protiated and deuterated lipids occur in the same temperature range when the temperature is increased; thus, the lipid chains are well mixed in the model.

Figure 4 shows that the SPP NS:NP 1:2 models have a larger hexagonal to liquid phase-transition temperature range than the SPP NS:NP 2:1 model. On average, this phase transition of the SPP NS:NP 1:2 models occurs over a 20°C temperature range, while for the SPP NS:NP 2:1 models, this is 12°C. However, the protiated and deuterated chains of both SPP NSd47:NPd47:DFFA 1:2 and SPP NS:NPd47:DFFA 1:2 models melt in the same temperature range (Figure 4A and B), indicating that the protiated and deuterated lipids have a similar thermotropic behavior. The SPP NSd47:NP:DFFA 1:2 model (Figure 4C) shows different ranges in transition temperature for the deuterated and protiated lipids, indicating that lipid domains of different composition are formed in this model.

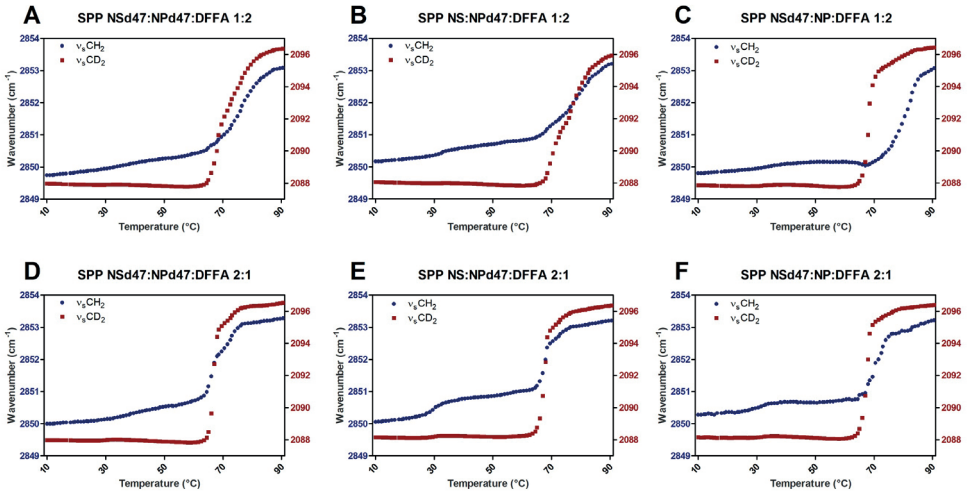


Figure 4. Thermotropic curves of the $\nu_s CH_2$ and $\nu_s CD_2$ vibrations for the SPP NS: NP 1:2 (A-C) and 2:1 (D-F) ratio models with different deuterated chains. The wavenumbers of the $\nu_s CH_2$ and $\nu_s CD_2$ peak positions (left and right y-axis, respectively) are plotted in the 10-90°C temperature range. Data shown as an average of 3 measurements for each composition.

The mid-transition temperature of the deuterated and protiated chains in the SPP NSd47:NP DFFA 1:2 deuterated models is significantly different, as shown in Table 3. This suggests that the lipids in this mixture do not mix homogenously. The SAXD data of the SPP NS:NP 1:2 model showed an unidentified phase with a spacing at 4.4 nm, which as discussed above, might contain primarily CER NP. The differences in the mid-transition temperatures between the protiated and deuterated lipids could be caused by this crystalline CER NP rich phase. Due to the presence of a high concentration of CER NP, it is expected to have a delayed onset of the melting process of the protiated chains. This is in

agreement with the observation that in the SPP NSd47:NPd47:DFFA 1:2 model the protiated chains do not show a delay in the hexagonal - liquid transition (Figure 4D).

There is only a weak phase transition from orthorhombic to hexagonal packing of the protiated lipid chains in most compositions shown in Figure 4, as in most compositions the $\nu_s CH_2$ wavenumber shows a slight and steady increase up to 50°C. This is an indication that the protiated lipids (CHOL, sphingosine and phytosphingosine chains) adopt primarily a hexagonal organization (except in the SPP NS:NPd47:DFFA 2:1 model). Unlike these SPP systems, in the LPP models studied recently, clear transitions from orthorhombic to hexagonal phases were noticed in the thermotropic plots of the deuterated samples (27). It has been previously reported that CER EOS may enhance the formation of the orthorhombic phase, as the long acyl chains of CER EOS might increase the van der Waals interactions (36, 62). Thus, the presence of CER EOS acyl chains could be a possible explanation for the aforementioned differences between these SPP systems and the LPP models.

Table 3. The mid-phase transition temperature of the hexagonal – liquid phase (T_m H-L), the δCD_2 peak splitting and the OR/MID δCD_2 peak height ratio of the deuterated SPP models. The scissoring peak data is calculated at 10°C. Data represents an average of 3 measurements for each composition with the standard deviations.

Lipid model	T_m H-L ± SD (°C)	δCD_2 peak splitting ± SD (cm^{-1})	OR/MID peak height ratio ± SD
SPP NSd47:NPd47:DFFA 1:2	75.3 ± 0.6	7.2 ± 0.1	5.3 ± 0.3
SPP NSd47:NPd47:DFFA 2:1	68.6 ± 0.6	7.2 ± 0.1	5.3 ± 0.4
SPP NS:NPd47:DFFA 1:2	76.8 ± 0.4	5.9 ± 0.1	3.3 ± 0.2
SPP NS:NPd47:DFFA 2:1	68.1 ± 0.9	5.0 ± 0.1	2.9 ± 0.2
SPP NSd47:NP:DFFA 1:2	80.7 ± 1.4	6.4 ± 0.1	2.7 ± 0.2
SPP NSd47:NP:DFFA 2:1	74.5 ± 0.9	6.2 ± 0.1	3.4 ± 0.2

At 32°C (skin temperature), the wavenumbers of the $\nu_s CH_2$ vibration in the SPP NSd47:NPd47:DFFA 1:2 and 2:1 systems are 2850.1 ± 0.2 cm^{-1} and 2850.2 ± 0.1 cm^{-1}, respectively. The stretching wavenumber at this temperature indicates that the protiated sphingosine and phytosphingosine chains and CHOL have less conformational ordering than at 10°C. The conformational disordering of the sphingosine chain of CER NS was previously reported by Engberg et al., who labeled this phase as a fluid, highly mobile phase, based on the ^2H NMR results (40). However, a clear distinction should be made regarding the packing of the sphingosine chain of CER NS, as in FTIR terminology a fluid disordered phase is characterized by a $\nu_s CH_2$ wavenumber >2853 cm^{-1} and a $\nu_s CD_2$ wavenumber >2096 cm^{-1}. In the Engberg et al. study, the $\nu_s CH_2$ wavenumber of the deuterated sphingosine CER NS chain is ~2089.5 cm^{-1} (40), which indicates some conformational disordering, but not a fluid phase as detected by FTIR.

The linear conformation of CER NS and CER NP is similar to LPP models

The mixing of the lipid chains is further examined using the scissoring vibrations. The results are provided in Figure 5, which shows the splitting of the δCD_2 and δCH_2 vibrations in the FTIR spectra of the various compositions. In an orthorhombic packing, the hydrocarbon lipid chains are packed tightly, allowing short-range coupling of the CH_2-CH_2 groups, interaction of neighboring CH_2 groups, resulting in a peak splitting of the δCH_2 vibrations. The size of the orthorhombic domains determines the δCH_2 peak splitting distance, with a maximum peak splitting distance of 7.3 ± 0.1 cm^{-1} obtained when the lipid domains are around 100 chains (63, 64). Similarly, when deuterated lipid chains are included in the models, the CD_2-CD_2 chains interact if they are neighboring, resulting in two separated δCD_2 peaks at ~1085 and ~1092 cm^{-1}. However, if the deuterated chains are neighboring protiated chains that participate in the same lattice, CD_2-CH_2 interactions occur, resulting in the loss of the CD_2-CD_2 chain frequency coupling. A central peak is formed in both the δCD_2 vibrations (~1088 cm^{-1}) and δCH_2 vibration (~1468 cm^{-1}), resulting in a shallower depth between the two orthorhombic peaks.

Large deuterated domains are formed in the SPP NSd47:NPd47:DFFA models (1:2 and 2:1 ratios; Figure 4 A,D), as the distance of the δCD_2 peak splitting is 7.2 ± 0.1 cm^{-1} in both compositions (Table 3). These values are close to the maximum δCD_2 peak splitting value obtained for pure DFFA C24 (7.3 ± 0.1 cm^{-1}), which suggests that the acyl chains of CER NS and CER NP are neighboring the DFFA chains. An indication of the number of CH_2-CD_2 interactions is the peak ratio of the two orthorhombic peaks and the central peak (OR/MID ratio). This ratio was calculated by peak fitting. The OR/MID ratio values obtained for this model are very high, indicating that the CD_2-CD_2 chain interactions are predominant in the system (Table 3).

To further investigate the deuterated lipid domains in the SPP models, CER NSd47 was replaced by the protiated CER NS in the SPP NS:NPd47:DFFA (1:2 and 2:1) models. Both models indicate that smaller deuterated lipid domains are present (Table 3). The OR/MID peak height ratios of these models are significantly decreased compared to the SPP NSd47:NPd47:DFFA models, indicating that in the SPP NS:NPd47:DFFA models there are significantly less CD_2-CD_2 chain interactions and more CH_2-CD_2 interactions. This confirms that the deuterated acyl chain of CER NS is part of the deuterated domains formed in the SPP NSd47:NPd47:DFFA models. Neighboring of these chains is only possible when CER NS and CER NP are present in a linear arrangement in the SPP models, with the acyl chain and (phyto)sphingosine chain on either side of the headgroup. The difference in the δCD_2 peak splitting values between the SPP NS:NPd47:DFFA 1:2 and SPP NS:NPd47:DFFA 2:1 models (Table 3) are probably only caused by the different concentrations of the deuterated CER NP in the models. Next, CER NPd47 was replaced by its protiated counterpart resulting in the SPP NSd47:NP:DFFA 1:2 and 2:1 models. The conclusions of the SPP NS:NPd47:DFFA models also apply to the SPP NSd47:NP:DFFA

models: smaller deuterated lipid domains than the SPP NSd47:NPd47:DFFA models and a linear arrangement of CER NS and CER NP.

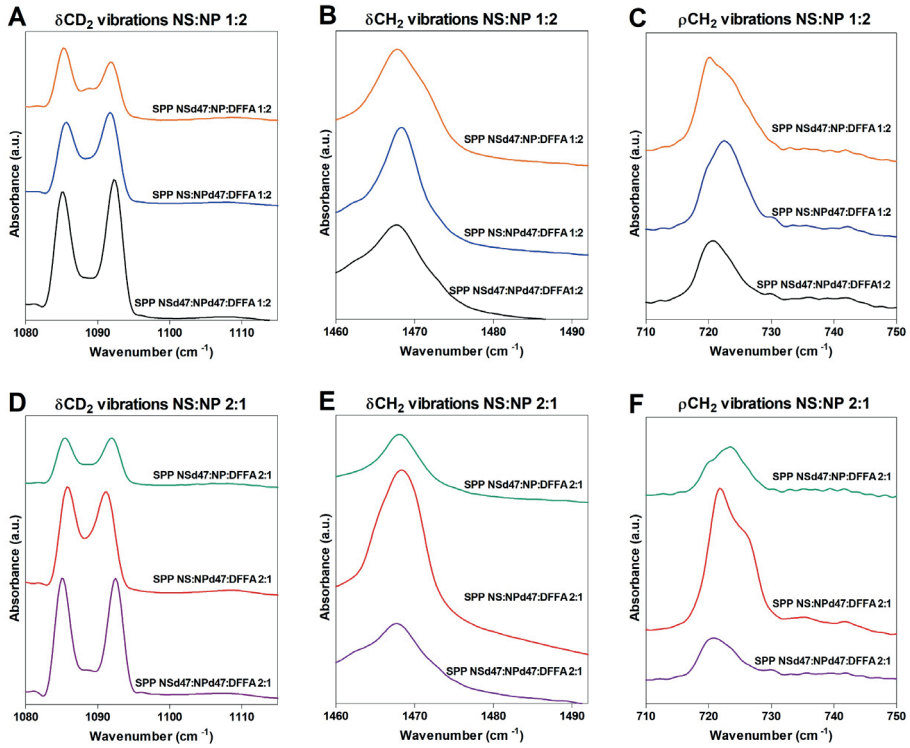


Figure 5. δCD_2 vibrations (A,D), δCH_2 vibrations (B,E) and ρCH_2 vibrations (C,F) for the partially deuterated models SPP NSd47:NP:DFFA, SPP NS:NPd47:DFFA and SPP NSd47:NPd47:DFFA with the CER NS:CER NP ratio 1:2 (top row of panels) and 2:1 (bottom row), measured at 10°C.

The linear arrangements of CER NS and CER NP are also observed in LPP models with the same composition (CER EOS: CER NS: CER NP: CHOL: FFAC24) (27, 46). Studies of the LPP models using neutron diffraction and the peak splitting observed in FTIR measurements both indicate that the acyl chains of CER NS and CER NP are neighboring FFA C24, regardless of the CER NS:CER NP molar ratio, similar to the results observed in the SPP model in the present study. The linear conformation of CER NS was reported in previous studies using LPP models with different compositions (65, 66) and SPP models (38, 40) (Shamaprasad et al. unpublished), however, the conformation of CER NP in SPP models was often debated, with different possible arrangements suggested, such as V-shape (55, 56) or hairpin conformation (67). The V-shape configuration was detected in a phase with a repeat distance of 4.3 nm, likely representing phase-separated CER NP. In the

SPP with 5.4 nm repeat distance, CER NP is suggested to be arranged in either hairpin or extended conformations.

When CER NS and CER NP are in a linear conformation, the acyl chains of CER NS and CER NP are neighboring the FFAs, as discussed above, consequently the sphingosine and phytosphingosine chains of the CERs and CHOL are also neighboring in another part of the repeating unit of the SPP. The δCH_2 vibrations of the deuterated SPP models (SPP NSd47:NPd47:DFFA, SPP NSd47:NP:DFFA, SPP NS:NPd47:DFFA 1:2 and 2:1 ratios) are characterized by the presence of a singlet at 1468 cm^{-1} (Figure 5B,E). As the sphingosine chains and CHOL are neighboring, an absence of the doublet in the δCH_2 vibrations indicates that there is almost no orthorhombic packing of the these protiated lipid chains. To investigate this further, the rocking vibrations are also examined to provide more information about the chain packing (Figure 5C,F). A broad single peak is observed at ~720 cm^{-1} for the SPP NSd47:NPd47:DFFA models (1:2 and 2:1 ratios), as well. The singlet in these two models suggest that the (phyto)sphingosine chains and the CHOL are mainly hexagonally packed. The sphingosine chain of CER NS and CHOL were previously reported to form a dynamic phase with a high mobility in SPP models (40) (Shamaprasad et al. unpublished).

Neutron diffraction shows the symmetric structure of the SPP

For the neutron diffraction measurements, the SPP NS:NP 2:1 model was selected to avoid the overlap of the diffraction peaks with peaks from the unknown phases observed in the SPP NS:NP 1:2 model. The SLD profiles of the protiated SPP NS:NP 2:1 sample, hydrated at 8% and 100% D_2O, are shown in Figure 6A. The profile of the protiated sample is characterized by a high SLD value at the borders of the unit cells, indicating that the lipid head groups are located at the boundary of the unit cell.

The SLD profile of the CER NSd7 chain (in the SPP NSd7:NP 2:1 sample) displays two peaks at the position of ~0.7 nm from the unit cell center (~2 nm from the unit cell border) (Figure 6B). A linearly extended sphingosine chain of C18 chain length corresponds to a length of ~ 1.9 nm, assuming a C-C bond length of 0.125 nm and 15 C-C bonds (66). Thus, the SLD profile intensity shows the location of the NSd7 terminally deuterated chain with the CER head group at the unit cell border. The proposed arrangement is schematically shown in Figure S4.

The neutron diffraction data indicates a symmetric structure of the SPP unit, also for CER NSd7 chain, which is located at both head group regions. This contrasts with the FTIR results that suggest an asymmetric arrangement, also of CER NS. The FTIR results of the SPP NS:NP 2:1 system indicate that the acyl chains of CER NS, CER NP and FFA C24 are neighboring, as shown by the large lipid domains indicated by the scissoring vibration measurements. This suggests an asymmetric arrangement in the SPP profile: on one side the CHOL neighboring the (phyto)sphingosine chains, while FFAs are positioned next to the acyl chains of the CERs. However, while the FTIR scissoring vibrations provide

information about the domain sized formed, neutron diffraction shows the overall mean orientation of the lipids in the system. If the asymmetric arrangement is present in a mirrored orientation with lipids domains larger than 100 chains, FTIR will detect an asymmetric arrangement (based on the interactions between neighboring lipid chains), while neutron diffraction will detect this as a symmetric arrangement, as this technique provides information based on the sum of the two mirror arrangements (Figure S4).

This study shows for the first time in the same SPP composition that the neutron diffraction data indicate a symmetric arrangement, while the FTIR data can only be explained by an asymmetric arrangement. Engberg et al. already proposed an asymmetric arrangement solely based on FTIR data for model containing a single CER (40).

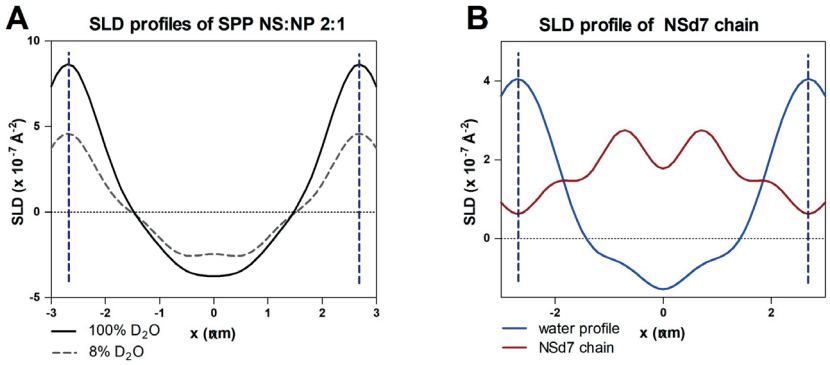


Figure 6. (A) SLD profile of the SPP NS:NP 2:1 sample hydrated at 100% and 8% D_2O/H_2O buffer and (B) SLD water profile (in blue) of the sample and the SLD profile of the CER NSd7 chain (in red). The vertical dashed lines indicate the borders of the repeating unit of the SPP.

CONCLUSION

In this study, the impact of altering the molar ratio of CER NS and CER NP, one of the lipid compositional changes in inflammatory skin diseases, was examined in lipid models that formed exclusively the SPP. The results were compared to previously studied LPP models with the same composition and CER NS:CER NP ratio. In the SPP models, CER NS and CER NP adopt an extended conformation, with the acyl chains of the two CERs in proximity to the FFA C24 chain in the SPP unit, similar to the arrangement described in the LPP unit cell. The different thermotropic behavior reported in the SPP NS:NP 1:2 model and the X-ray diffraction profile indicates that there are lipid domains formed in this system, possibly this is a CER NP-rich phase. Unlike these observations, in LPP models no phase separation is observed, suggesting that the addition of CER EOS improves not only the lipid barrier (33, 35), but also enhances the miscibility of the lipid chains. Moreover, the SPP systems investigated in this study and the corresponding LPP models previously studied showed a different conformational ordering of the lipids. In SPP models with deuterated acyl chain

of CER NS and CER NP and DFFA, the protiated lipids show a higher conformational disordering of the chains compared to the LPP models (at 10°C). This could be due to the acyl chain of CER EOS probably located in the outer layers with the sphingosine and phytosphingosine chains and the CHOL, which improves the lipid ordering in the outer layers of the LPP (44). While some aspects are similar in the SPP and LPP models with different ratios of CER NS:CER NP, the absence of CER EOS affects the mixing of the lipid chains and allows domain formation in models with a high concentration of CER NP. This determines a larger effect when changing the CER NS:CER NP ratio on the lipid organization in SPP models, compared to LPP systems.

ACKNOWLEDGEMENTS

We thank the ALBA Synchrotron (Cerdanyola del Vallès, Spain) and ISIS Neutron and Muon Source (Didcot, United Kingdom) for the experimental beam time to perform the X-ray scattering and neutron diffraction measurements. ISIS data DOI: 10.5286/ISIS.E.RB2069000-1 (68). We are grateful to Evonik (Essen, Germany) for providing the CERs for this study. This study was financially supported by the National Institutes of Health (National Institute of Arthritis and Muscoskeletal and Skin Diseases), grant number R01AR072679.

REFERENCES

1. Hannun, Y. A. (1996). Functions of Ceramide in Coordinating Cellular Responses to Stress. *Science*. 274, 1855-9.
2. Taha, T. A., Mullen, T. D., Obeid, L. M. (2006). A house divided: ceramide, sphingosine, and sphingosine-1-phosphate in programmed cell death. *Biochim Biophys Acta*. 1758(12), 2027-36.
3. Wertz, P. W., Miethke, M. C., Long, S. A., Strauss, J. S., Downing, D. T. (1985). The composition of the ceramides from human stratum corneum and from comedones. *J Invest Dermatol*. 84(5), 410-2.
4. Weerheim, A., Ponec, M. (2001). Determination of stratum corneum lipid profile by tape stripping in combination with high-performance thin-layer chromatography. *Arch Dermatol Res*. 293, 191-9.
5. Madison, K. C. (2003). Barrier function of the skin: "la raison d'etre" of the epidermis. *J Invest Dermatol*. 121(2), 231-41.
6. Proksch, E., Brandner, J. M., Jensen, J.-M. (2008). The skin: an indispensable barrier. *Experimental Dermatology*. 17(12), 1063-72.
7. Ponec, M., Weerheim, A., Lankhorst, P., Wertz, P. (2003). New Acylceramide in Native and Reconstructed Epidermis. *J Invest Dermatol*. 120(4), 581-8.
8. Demel, R. A., de Kruyff, B. (1976). The Function of Sterols in Membranes. *Biochim Biophys Acta*. 457, 109-32.
9. White, S. H., Mirejovsky, D., King, G. I. (1988). Structure of Lamellar Lipid Domains and Corneocyte Envelopes of Murine Stratum Corneum. An X-ray Diffraction Study. *Biochemistry*. 27, 3725-32.
10. Bouwstra, J. A., Gooris, G. S., van der Spek, J. A., Bras, W. (1991). Structural investigations of human stratum corneum by small-angle X-ray scattering. *J Invest Dermatol*. 97(6), 1005-12.
11. Hill, J. R., Wertz, P. W. (2003). Molecular models of the intercellular lipid lamellae from epidermal stratum corneum. *Biochimica et Biophysica Acta (BBA) - Biomembranes*. 1616(2), 121-6.
12. Bouwstra, J. A., Gooris, G. S., Dubbelaar, F. E., Weerheim, A., IJzerman, A. P., Ponec, M. (1998). Role of ceramide 1 in the molecular organization of the stratum corneum lipids. *J Lipid Res*. 39, 186-96.
13. Uche, L. E., Gooris, G. S., Bouwstra, J. A., Beddoes, C. M. (2021). High concentration of the ester-linked omega-hydroxy ceramide increases the permeability in skin lipid model membranes. *Biochim Biophys Acta Biomembr*. 1863(1), 183487.
14. Bouwstra, J. A., Nadaban, A., Bras, W., McCabe, C., Bunge, A., Gooris, G. S. (2023). The skin barrier: An extraordinary interface with an exceptional lipid organization. *Prog Lipid Res*. 101252.
15. Mendelsohn, R., Rerek, M. E., Moore, D. J. (2000). Infrared spectroscopy and microscopic imaging of stratum corneum models and skin. *Physical Chemistry Chemical Physics*. 2(20), 4651-7.
16. Boncheva, M., Damien, F., Normand, V. (2008). Molecular organization of the lipid matrix in intact Stratum corneum using ATR-FTIR spectroscopy. *Biochim Biophys Acta*. 1778(5), 1344-55.
17. Damien, F., Boncheva, M. (2010). The extent of orthorhombic lipid phases in the stratum corneum determines the barrier efficiency of human skin in vivo. *J Invest Dermatol*. 130(2), 611-4.
18. Björklund, S., Nowacka, A., Bouwstra, J. A., Sparr, E., Topgaard, D. (2013). Characterization of Stratum Corneum Molecular Dynamics by Natural-Abundance 13C Solid-State NMR. *PLoS One*. 8(4), e61889.
19. van Smeden, J., Janssens, M., Gooris, G. S., Bouwstra, J. A. (2014). The important role of stratum corneum lipids for the cutaneous barrier function. *Biochim Biophys Acta*. 1841(3), 295-313.
20. Motta, S., Monti, M., Sesana, S., Caputo, R., Carelli, S., Ghidoni, R. (1993). Ceramide composition of the psoriatic scale. *Biochim Biophys Acta*. 1182, 147-51.
21. Janssens, M., van Smeden, J., Gooris, G. S., Bras, W., Portale, G., Caspers, P. J., et al. (2011). Lamellar lipid organization and ceramide composition in the stratum corneum of patients with atopic eczema. *J Invest Dermatol*. 131(10), 2136-8.
22. Sahle, F. F., Gebre-Mariam, T., Dobner, B., Wohlrab, J., Neubert, R. H. (2015). Skin diseases associated with the depletion of stratum corneum lipids and stratum corneum lipid substitution therapy. *Skin Pharmacol Physiol*. 28(1), 42-55.
23. Yokose, U., Ishikawa, J., Morokuma, Y., Naoe, A., Inoue, Y., Yasuda, Y., et al. (2020). The ceramide [NP]/[NS] ratio in the stratum corneum is a potential marker for skin properties and epidermal differentiation. *BMC Dermatology*. 20(1).

24. Uchino, T., Kamiya, D., Yagi, H., Fujino-Shimaya, H., Hatta, I., Fujimori, S., et al. (2023). Comparative analysis of intercellular lipid organization and composition between psoriatic and healthy stratum corneum. *Chem Phys Lipids*. 254, 105305.
25. Rousel, J., Nădăban, A., Saghari, M., Pagan, L., Zhuparris, A., Theelen, B., et al. (2024) Lesional skin of seborrheic dermatitis patients is characterized by skin barrier dysfunction and correlating alterations in the stratum corneum ceramide composition. *Exp. Dermatol.* 33(1), e14952.
26. van Smeden, J., Al-Khakany, H., Wang, Y., Visscher, D., Stephens, N., Absalah, S., et al. (2020). Skin barrier lipid enzyme activity in Netherton patients is associated with protease activity and ceramide abnormalities. *J Lipid Res*. 61(6), 859-69.
27. Nădăban, A., Rousel, J., El Yachioui, D., Gooris, G. S., Beddoes, C. M., Dalgliesh, R. M., et al. (2023). Effect of sphingosine and phytosphingosine ceramide ratio on lipid arrangement and barrier function in skin lipid models. *J Lipid Res*. 64(8), 100400.
28. McIntosh, T. J., Stewart, M. E., Downing, D. T. (1996). X-ray Diffraction Analysis of Isolated Skin Lipids: Reconstitution of Intercellular Lipid Domains. *Biochemistry*. 35(12), 3649-53.
29. Bouwstra, J., Gooris, G., Cheng, K., A., W., Bras, W., Ponec, M. (1996). Phase behavior of isolated skin lipids. *J Lipid Res*. 37, 999 - 1011.
30. Bouwstra, J. A., Gooris, G. S., Dubbelaar, F. E. R., Ponec, M. (2001). Phase behavior of lipid mixtures based on human ceramides: coexistence of crystalline and liquid phases. *J Lipid Res*.42(11), 1759-70.
31. de Jager, M. W., Gooris, G. S., Ponec, M., Bouwstra, J. A. (2005). Lipid mixtures prepared with well-defined synthetic ceramides closely mimic the unique stratum corneum lipid phase behavior. *J Lipid Res*. 46(12), 2649-56.
32. Janssens, M., Gooris, G. S., Bouwstra, J. A. (2009). Infrared spectroscopy studies of mixtures prepared with synthetic ceramides varying in head group architecture: coexistence of liquid and crystalline phases. *Biochim Biophys Acta*. 1788(3), 732-42.
33. Opalka, L., Kovacik, A., Maixner, J., Vavrova, K. (2016). Omega-O-Acylceramides in Skin Lipid Membranes: Effects of Concentration, Sphingoid Base, and Model Complexity on Microstructure and Permeability. *Langmuir*. 32(48), 12894-904.
34. Uche, L. E., Gooris, G. S., Bouwstra, J. A., Beddoes, C. M. (2019). Barrier Capability of Skin Lipid Models: Effect of Ceramides and Free Fatty Acid Composition. *Langmuir*. 35(47), 15376-88.
35. Opálka, L., Kováčik, A., Pullmannová, P., Maixner, J., Vávrová, K. (2020). Effects of omega-O-acylceramide structures and concentrations in healthy and diseased skin barrier lipid membrane models. *J Lipid Res*. 61(2), 219-28.
36. Mojumdar, E. H., Gooris, G. S., Bouwstra, J. A. (2015). Phase behavior of skin lipid mixtures: the effect of cholesterol on lipid organization. *Soft Matter*. 11, 4326-36.
37. Skolova, B., Janusova, B., Zbytovska, J., Gooris, G., Bouwstra, J., Slepicka, P., et al. (2013). Ceramides in the skin lipid membranes: length matters. *Langmuir*. 29(50), 15624-33.
38. Skolova, B., Hudska, K., Pullmannova, P., Kovacik, A., Palat, K., Roh, J., et al. (2014). Different phase behavior and packing of ceramides with long (C16) and very long (C24) acyls in model membranes: infrared spectroscopy using deuterated lipids. *J Phys Chem B*. 118(35), 10460-70.
39. Oguri, M., Gooris, G. S., Bito, K., Bouwstra, J. A. (2014). The effect of the chain length distribution of free fatty acids on the mixing properties of stratum corneum model membranes. *Biochim Biophys Acta*. 1838(7), 1851-61.
40. Engberg, O., Kovacik, A., Pullmannova, P., Juhascik, M., Opalka, L., Huster, D., et al. (2020). The Sphingosine and Acyl Chains of Ceramide [NS] Show Very Different Structure and Dynamics That Challenge Our Understanding of the Skin Barrier. *Angew Chem Int Ed*. 59, 17383 - 7.
41. Gooris, G. S., Kamran, M., Kros, A., Moore, D. J., Bouwstra, J. A. (2018). Interactions of dipalmitoylphosphatidylcholine with ceramide-based mixtures. *Biochim Biophys Acta Biomembr*. 1860(6), 1272-81.
42. Wojdyr, M. (2010). Fityk: a general-purpose peak fitting program. *Journal of Applied Crystallography*. 43(5), 1126-8.
43. Arnold, O., Bilheux, J. C., Borreguero, J. M., Buts, A., Campbell, S. I., Chapon, L., et al. (2014). Mantid—Data analysis and visualization package for neutron scattering andμSR experiments. *Nuclear Instruments and Methods in Physics Research Section A: Accelerators, Spectrometers, Detectors and Associated Equipment*. 764, 156-66.

44. Mojumdar, E. H., Gooris, G. S., Groen, D., Barlow, D. J., Lawrence, M. J., Deme, B., et al. (2016). Stratum corneum lipid matrix: Location of acyl ceramide and cholesterol in the unit cell of the long periodicity phase. *Biochim Biophys Acta*. 1858(8), 1926-34.
45. Franks, N. P., Lieb, W.R. (1979). The Structure of Lipid Bilayers and the Effects of General Anaesthetics: An X-ray and Neutron Diffraction Study. *J Mol Biol*. 133, 469-500.
46. Nădăban, A., Gooris, G. S., Beddoes, C. M., Dalgliesh, R. M., Bouwstra, J. A. (2022). Phytosphingosine ceramide mainly localizes in the central layer of the unique lamellar phase of skin lipid model systems. *J Lipid Res*. 63(9), 100258.
47. NIST Center of Neutron Research, https://www.ncnr.nist.gov/resources/activation/ (Accessed: 2021).
48. Wiener, M. K., G.; White, S. (1991). Structure of a fluid dioleoylphosphatidylcholine bilayer determined by joint refinement of x-ray and neutron diffraction data 1. Scaling of neutron data and the distributions of double bonds and water. *Biophys J*. 60, 568-76.
49. Mojumdar, E. H., Gooris, G. S., Barlow, D. J., Lawrence, M. J., Deme, B., Bouwstra, J. A. (2015). Skin lipids: localization of ceramide and fatty acid in the unit cell of the long periodicity phase. *Biophys J*. 108(11), 2670-9.
50. Kovacik, A., Vogel, A., Adler, J., Pullmannova, P., Vavrova, K., Huster, D. (2018). Probing the role of ceramide hydroxylation in skin barrier lipid models by (2)H solid-state NMR spectroscopy and X-ray powder diffraction. *Biochim Biophys Acta Biomembr*. 1860(5), 1162-70.
51. Kovacik, A., Silarova, M., Pullmannova, P., Maixner, J., Vavrova, K. (2017). Effects of 6-Hydroxyceramides on the Thermotropic Phase Behavior and Permeability of Model Skin Lipid Membranes. *Langmuir*. 33(11), 2890-9.
52. Pullmannova, P., Ermakova, E., Kovacik, A., Opalka, L., Maixner, J., Zbytovska, J., et al. (2019). Long and very long lamellar phases in model stratum corneum lipid membranes. *J Lipid Res*. 60(5), 963-71.
53. Pullmannova, P., Curikova-Kindlova, B. A., Ondrejcekova, V., Kovacik, A., Dvorakova, K., Dulanska, L., et al. (2023). Polymorphism, Nanostructures, and Barrier Properties of Ceramide-Based Lipid Films. *ACS Omega*. 8(1), 422-35.
54. Parrott, D. T., Turner, J. E. (1993). Mesophase formation by ceramides and cholesterol: a model for stratum corneum lipid packing? *Biochim Biophys Acta*. 1147, 273 - 6.
55. Dahlen, B., Pascher, I. (1979). Molecular arrangements in sphingolipids. Thermotropic phase behaviour of tetracosanoylphytosphingosine. *Chem Phys Lipids*. 24, 119 - 33.
56. Schroeter, A., Stahlberg, S., Skolova, B., Sonnenberger, S., Eichner, A., Huster, D., et al. (2017). Phase separation in ceramide[NP] containing lipid model membranes: neutron diffraction and solid-state NMR. *Soft Matter*. 13(10), 2107-19.
57. de Jager, M., Gooris, G., Ponec, M., Bouwstra, J. (2004). Acylceramide head group architecture affects lipid organization in synthetic ceramide mixtures. *J Invest Dermatol*. 123(5), 911-6.
58. Moore, D. J., Rerek, M. E., Mendelsohn, R. (1997). FTIR Spectroscopy Studies of the Conformational Order and Phase Behavior of Ceramides. *J Phys Chem B*. 101, 8933-40.
59. Moore, D. J., Rerek, M. E., Mendelsohn, R. (1999). Role of ceramides 2 and 5 in the structure of the stratum corneum lipid barrier. *Int J Cosmet Sci*. 21(5), 353-68.
60. Rerek, M. E., Chen, H., Markovic, B., Van Wyck, D., Garidel, P., Mendelsohn, R., et al. (2001). Phytosphingosine and Sphingosine Ceramide Headgroup Hydrogen Bonding: Structural Insights through Thermotropic Hydrogen/Deuterium Exchange. *J Phys Chem B*. 105, 9355 - 62.
61. Uche, L. E., Gooris, G. S., Beddoes, C. M., Bouwstra, J. A. (2019). New insight into phase behavior and permeability of skin lipid models based on sphingosine and phytosphingosine ceramides. *Biochim Biophys Acta Biomembr*. 1861(7), 1317-28.
62. de Sousa Neto, D., Gooris, G., Bouwstra, J. (2011). Effect of the omega-acylceramides on the lipid organization of stratum corneum model membranes evaluated by X-ray diffraction and FTIR studies (Part I). *Chem Phys Lipids*. 164(3), 184-95.
63. Moore, D. J., Rerek, M. E., Mendelsohn, R. (1997). Lipid Domains and Orthorhombic Phases in Model Stratum Corneum: Evidence from Fourier Transform Infrared Spectroscopy Studies. *Biochemical and Biophysical Research Communications*. 231, 797 - 801.

64. Mendelsohn, R., Moore, D. J. (1998). Vibrational spectroscopic studies of lipid domains in biomembranes and model systems. *Chem Phys Lipids*. 96, 141-57.
65. Beddoes, C. M., Gooris, G. S., Bouwstra, J. A. (2018). Preferential arrangement of lipids in the long-periodicity phase of a stratum corneum matrix model. *J Lipid Res*. 59(12), 2329-38.
66. Beddoes, C. M., Gooris, G. S., Foglia, F., Ahmadi, D., Barlow, D. J., Lawrence, M. J., et al. (2020). Arrangement of Ceramides in the Skin: Sphingosine Chains Localize at a Single Position in Stratum Corneum Lipid Matrix Models. *Langmuir*. 36(34), 10270-8.
67. Schmitt, T., Lange, S., Dobner, B., Sonnenberger, S., Hauss, T., Neubert, R. H. H. (2018). Investigation of a CER[NP]- and [AP]-Based Stratum Corneum Modeling Membrane System: Using Specifically Deuterated CER Together with a Neutron Diffraction Approach. *Langmuir*. 34(4), 1742-9.
68. Bouwstra, J. A., Beddoes, C. M., Nădăban, A., Dalgliesh, R. M., Gooris, G. S. (2020) The effect of ceramide head group on the lipid organization in the long periodicity phase of stratum corneum substitutes. STFC ISIS Neutron and Muon Source. DOI: https://doi.org/ 10.5286/ISIS.E.RB2069000.

SUPPLEMENTAL INFORMATION

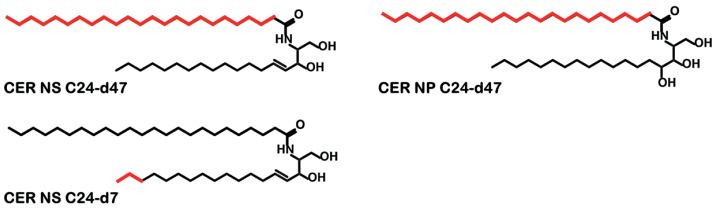


Figure S1. The molecular structure of the CERs used in this study. The deuterated moieties are depicted in red (the acyl chains of CER NS and CER NP and the terminally deuterated sphingosine chain of CER NS).

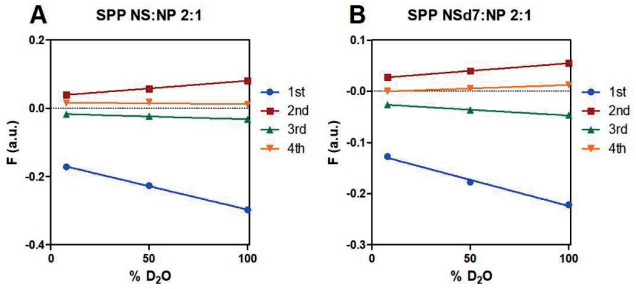


Figure S2. Linear fitting of the structure factors as a function of the percentage of D_2O in the D_2O/H_2O buffer for the SPP NS:NP 2:1 model and SPP NSd7:NP 2:1 models. The four diffraction orders are indicated by different symbols and colors: first (dot, blue), second (square, red), third (triangle, green), fourth (triangle, orange).

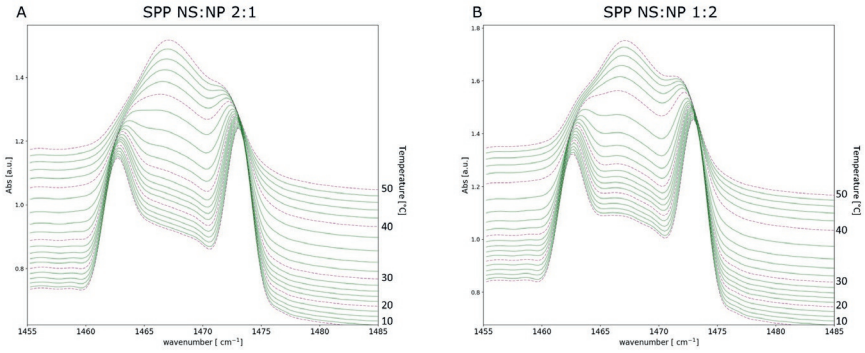


Figure S3. The δCH_2 vibrations of the SPP NS:NP 2:1 (A) and SPP NS:NP 1:2 (B) models, measured in the temperature range 10 – 50 °C.

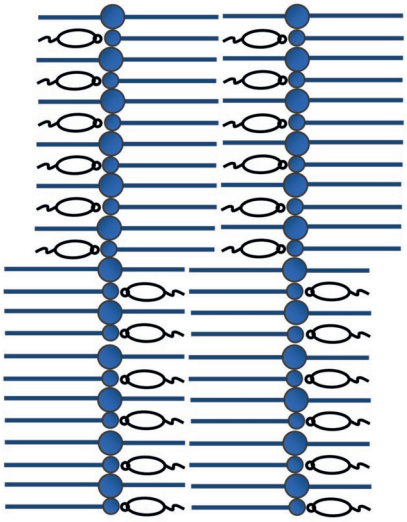
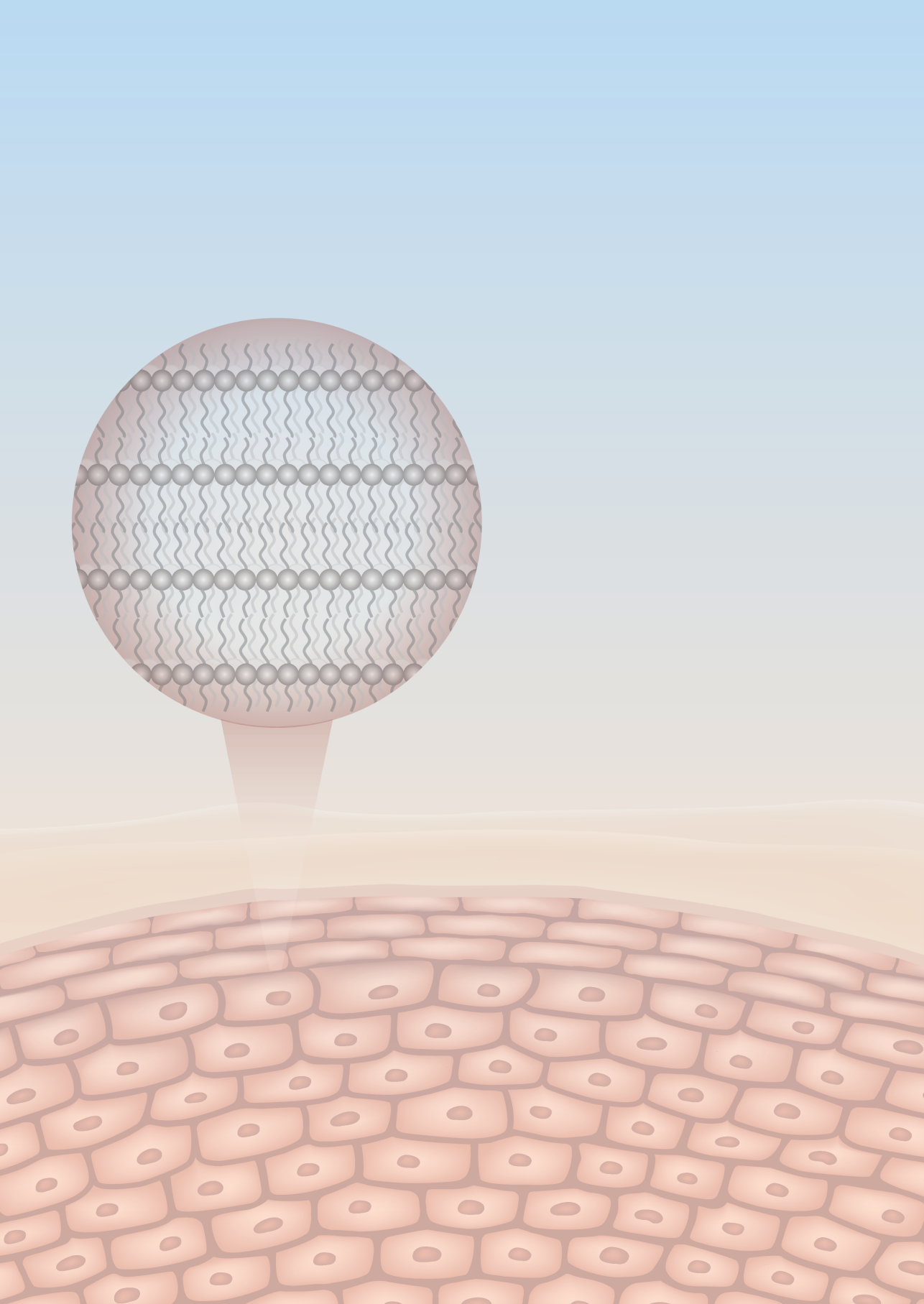


Figure S4. Proposed schematic model for the arrangement of the SPP unit cell. CHOL is shown in black, FFA is indicated as a single acyl chain in blue and the CER is depicted in blue, in an extended conformation (the acyl chain and sphingoid base on each side of the head group). The asymmetric structure mirrors itself within the lamellar structure, resulting in a symmetric structure of the SPP unit.



CHAPTER 6

The molecular arrangement of ceramides in the unit cell of the long periodicity phase of stratum corneum models shows a high adaptability to different ceramide head group structures

Authors and affiliations:
Andreea Nădăban[1], Gerrit S. Gooris[1], Charlotte M. Beddoes[1], Robert M. Dalgliesh[2], Marc Malfois[3], Bruno Demé[4], Joke A. Bouwstra[1*]

[1]Division of BioTherapeutics, Leiden Academic Centre for Drug Research, Leiden University, Leiden, The Netherlands
[2]ISIS Neutron and Muon Source, Science and Technology Facilities Council, Rutherford Appleton Laboratory, Didcot, United Kingdom
[3]ALBA Synchrotron, Cerdanyola del Vallès, Barcelona, Spain
[4]Institut Laue-Langevin, Grenoble, France

Submitted to BBA – Biomembranes (November 2023)

ABSTRACT

The stratum corneum (SC) lipid matrix, composed primarily of ceramides (CERs), cholesterol and free fatty acids (FFA), has an important role for the skin barrier function. The presence of the long periodicity phase (LPP), a unique lamellar phase, is characteristic for the SC. Insight into the lipid molecular arrangement within the LPP unit cell is imperative for understanding the relationship between the lipid subclasses and the skin barrier function. In this study, the impact of the CER head group structure on the lipid arrangement and barrier functionality was investigated using lipid models forming the LPP. The results demonstrate that the positions of CER *N*-(tetracosanoyl)-sphingosine (CER NS) and CER *N*-(tetracosanoyl)-phytosphingosine (CER NP), two essentials CER subclasses, are not influenced by the addition of another CER subclass (*N*-(tetracosanoyl)-dihydrosphingosine (CER NdS), *N*-(2R-hydroxy-tetracosanoyl)-sphingosine (CER AS) or D-(2R-hydroxy-tetracosanoyl)-phytosphingosine (CER AP)). However, differences are observed in the lipid organization and the hydrogen bonding network of the three different models. A similar localization of CER NP and CER NS is also observed in a more complex lipid model, with the CER subclass composition mimicking that of human SC. These studies show the adaptability and insensitivity of the LPP unit cell structure to changes in the lipid head group structures of the CER subclasses.

INTRODUCTION

The barrier function of the skin is mainly provided by the stratum corneum (SC), the uppermost layer of the skin (1). The SC consists of corneocytes embedded in a lipid matrix, with the latter representing the continuous pathway for permeation of compounds through the skin. Thus, the SC lipid matrix plays an important role to prevent undesired environmental compounds from entering the skin and to reduce excess water loss from the body (2). Ceramides (CER), free fatty acids (FFA) and cholesterol (CHOL) are the main SC lipid classes, present in an approximately equimolar ratio (3, 4). Phospholipids are not present in the SC, whereas they are prominently present in biological membranes of living cells (5). CERs are part of the sphingolipid family and play an important role in the regulation of cellular processes (6). Currently, 25 CER subclasses have been identified, with most of them having an acyl chain linked to a sphingoid base by an amide bond (7). All CER subclasses and FFAs have a wide chain length distribution.

The SC lipids are organized in two crystalline lamellar phases, a long periodicity phase (LPP) with a repeat distance of 13 nm and a short periodicity phase (SPP) with a repeat distance of 6 nm (8, 9). Previous studies have shown that the esterified ω-hydroxy ceramides (CER EO subclass) (Figure S1) are unique to the SC and are required for the formation of the LPP (10-12). In the absence of the CER EO subclass, primarily the SPP is formed (13). In some publications another lamellar phase has been reported in lipid model systems (14-17). However, there are no indications that this phase has been detected in SC. Within the lamellar phases in the SC, the lipid chains can adopt different packing densities, referred to as the lateral organization: orthorhombic (ordered phase, very dense packing), hexagonal (an ordered phase, but the lipid chains are less densely packed) or liquid phase (highly disordered phase) (18-20). The lipids in the SC lipid matrix are predominantly organized in an orthorhombic phase, with a fraction of the lipids adopting a hexagonal packing. The formation of liquid phase domains has also been reported for lipids in the SC (21).

Lipid model systems that resemble the lipid organization in the native SC provide detailed insight about the interactions between the different lipid subclasses. Previous studies used isolated human or porcine CERs mixed with synthetic FFAs and CHOL to prepare lipid models, which had a similar lipid organization to native SC (22-24). In subsequent studies, fully synthetic focused on lipid models were prepared with a synthetic CER composition mimicking the porcine or human CER subclasses. These models formed the LPP and SPP, similar to the lipid systems with isolated CERs and the native SC (11, 25-27). The next step was incorporating a limited number of CER subclasses mixed with FFAs and CHOL, aiming to keep the same phase behavior. This is of importance as simple lipid models are an excellent tool to gain detailed insight about the molecular arrangement of the lipids in the system, as deuterated lipids can be included in the mixture. If the

appropriate CER subclasses are chosen for the composition, even with a few numbers of CER subclasses, these lipid models still resemble the lipid phase behavior of SC (26-30).

Due to the co-existing lamellar phases (LPP and SPP), the lipid arrangement in these models is difficult to investigate using neutron diffraction, because of the partial overlap of the diffraction peaks of the two lamellar phases in the neutron scattering profile. To exclusively form the LPP, the unique lamellar phase in SC, the concentration of the esterified ω-hydroxy sphingosine ceramide (CER EOS) has to be increased to 30 or 40 mol% of the CER composition (10, 11). When forming only this lamellar phase, much more detail can also be obtained using other methods, such as Fourier transform infrared spectroscopy (FTIR) and neutron diffraction. Increasing the CER EOS level does not change the molecular arrangement of the repeating unit of the LPP, it only increases the fraction of lipids forming the LPP (10, 31). The molecular arrangement of the SPP in lipid models with different compositions was previously modelled using molecular dynamics simulations (32-35).

Understanding the role of the lipid subclasses for the lipid organization is crucial for explaining the changes in lipid composition and organization in diseased skin. For this reason, the lipid arrangement of the LPP unit cell has been investigated. Small-angle neutron diffraction (SANS) can provide the localization of water molecules and deuterated lipids in the LPP unit cell, using contrast variation of D_2O/H_2O hydration buffers and deuterated compounds, while FTIR provides information about lipid domain forming and the neighboring lipid chains. Previous studies identified the location of CER EOS, CHOL, FFAs, CER *N*-(tetracosanoyl)-sphingosine (CER NS) and CER *N*-(tetracosanoyl)-phytosphingosine (CER NP) (Figure S1) in lipid models with different compositional complexity (30, 36-38). According to these studies the lipids are arranged in a trilayer in the LPP unit cell. The outer layers of the LPP consist of the acyl chain of CER EOS and the CHOL, while the FFAs and acyl chains of CER NP and CER NS are predominantly localized in the central layer of the LPP. CER NS and CER NP have been reported to mainly adopt a linear conformation, as depicted schematically in Figure S2.

In the present study the influence of *N*-(2R-hydroxy-tetracosanoyl)-sphingosine (CER AS C24), D-(2R-hydroxy-tetracosanoyl)-phytosphingosine (CER AP C24) and CER N-(tetracosanoyl)-dihydrosphingosine (CER NdS C24) (Figure S1) on the lipid organization and barrier function of lipids assembled in the LPP was investigated. First, a model with only CER EOS, CER NP, CER NS and one of these additional CER subclasses (CER AS, CER AP or CER NdS) together with CHOL and FFA was used. It was observed that the additional CER subclasses did not affect the positions of the acyl chain of CER NP and CER NS in the trilayer unit cell. Additional studies show that the two acyl chains are similarly positioned even in a complex model representing the human SC CER subclass composition, suggesting an insensitivity of the LPP to the CER subclass composition.

MATERIALS AND METHODS

Materials

The following synthetic CERs used in the study: *N*-(30-Linoleoyloxy-triacontanoyl)-sphingosine (CER EOS C30), *N*-(tetracosanoyl)-sphingosine (CER NS C24), *N*-(tetracosanoyl)-phytosphingosine (CER NP C24), *N*-(2R-hydroxy-tetracosanoyl)-sphingosine (CER AS C24), D-(2R-hydroxy-tetracosanoyl)-phytosphingosine (CER AP C24) and CER NS and CER NP with perdeuterated acyl chains (NSd47, NPd47) were kindly donated by Evonik (Essen, Germany). CER N-(tetracosanoyl)-dihydrosphingosine (CER NdS C24) was purchased from Avanti Polar Lipids (Alabama, USA). CHOL, palmitic acid (FFA C16), stearic acid (FFA C18), arachidic acid (FFA C20), behenic acid (FFA C22), lignoceric acid (FFA C24), D_2O and the acetate buffer salts were obtained from Sigma-Aldrich-Chemie GmbH (Schnelldorf, Germany). Deuterated FFA C24 (DFFA24) was acquired from Arc Laboratories B.V. (Apeldoorn, The Netherlands). Analytical grade organic solvents were purchased from Biosolve B.V. (Valkenswaard, The Netherlands). The nucleopore polycarbonate membranes were purchased from Whatman (Kent, UK).

Lipid compositions preparation

An equimolar ratio of CERs:CHOL:FFAs was used for all lipid compositions. The CER fraction contained CER EOS (40% of CER fraction), CER NS, CER NP and either CER AS, CER AP or CER NdS for the simple models (CERs structures presented in Figure S1). The composition of the models mimicking human CER model is indicated in Table 1 by Human. This is based on the human model investigated by Uche et al. (21), but the concentration of CER EOS was increased to 40 mol% of total CERs in this study, to avoid the simultaneous formation of the LPP and SPP. The FFA composition of the Human model is denoted by FFA5 and consists of FFAs with chain lengths of C16, C18, C20, C22 and C24 (at molar percentages of 1.8, 4.0, 7.6, 47.8, 38.8%). Deuterated models were prepared by replacing CER NS, CER NP and FFA C24 (or FFA5) with their deuterated counterparts (indicated in the model names and in bold).

The details for the sample preparation used for each biophysical technique are provided in Table 2. The lipids were dissolved in the appropriate solvent at a concentration of 5 mg/ml, then a Camag Linomat IV device (Muttenz, Switzerland) was used to spray the lipids under a gentle stream of nitrogen (spraying rate 14 s/µl) around 1 mm from the support. An automatic equilibrator was then used at a heating rate of 4°C/min until a temperature of 95°C was reached (for the models with CER AS, CER AP or CER NdS). The sample was maintained at this temperature for 65 min, then slowly cooled to 25°C. For the Human models, the equilibration temperature was 85°C, maintained for 30 min, which was high enough to ensure the melting of the lipids.

Table 1. Lipid models used in this study, with deuterated lipids indicated in bold

Sample name	Composition	Molar ratio
LPP NS:NP:AS	EOS C30: NS C24: NP C24: AS C24: CHOL: FFA C24	0.4: 0.15:0.15:0.3: 1: 1
LPP NS:NP:AP	EOS C30: NS C24: NP C24: AP C24: CHOL: FFA C24	0.4: 0.15:0.15:0.3: 1: 1
LPP NS:NP:NdS	EOS C30: NS C24: NP C24: NdS C24: CHOL: FFA C24	0.4: 0.15:0.15:0.3: 1: 1
LPP NSd47:NP:AS	EOS C30: **NS C24-d47:** NP C24: AS C24: CHOL: FFA C24	0.4: 0.15:0.15:0.3: 1: 1
LPP NS:NPd47:AS	EOS C30: NS C24: **NP C24-d47:** AS C24: CHOL: FFA C24	0.4: 0.15:0.15:0.3: 1: 1
LPP NSd47:NP:AP	EOS C30: **NS C24-d47**: NP C24: AP C24: CHOL: FFA C24	0.4: 0.15:0.15:0.3: 1: 1
LPP NS:NPd47:AP	EOS C30: NS C24**: NP C24-d47**: AP C24: CHOL: FFA C24	0.4: 0.15:0.15:0.3: 1: 1
LPP NSd47:NP:NdS	EOS C30: **NS C24-d47**: NP C24: NdS C24: CHOL: FFA C24	0.4: 0.15:0.15:0.3: 1: 1
LPP NS:NPd47:NdS	EOS C30: NS C24: **NP C24-d47:** NdS C24: CHOL: FFA C24	0.4: 0.15:0.15:0.3: 1: 1
LPP NSd47:NPd47:AS:DFFA	EOS C30: **NS C24-d47: NP C24-d47**: AS C24: CHOL: **DFFA C24**	0.4: 0.15:0.15:0.3: 1: 1
LPP NSd47:NPd47:AP:DFFA	EOS C30: **NS C24-d47: NP C24-d47**: AP C24: CHOL: **DFFA C24**	0.4: 0.15:0.15:0.3: 1: 1
LPP NSd47:NPd47:NdS:DFFA	EOS C30: **NS C24-d47: NP C24-d47**: NdS C24: CHOL: **DFFA C24**	0.4: 0.15:0.15:0.3: 1: 1
Human	EOS C30: NS C24: NP C24: AS C24: NdS C24: AP C24: CHOL: FFA5	0.4: 0.09: 0.22: 0.09: 0.09: 0.11 : 1: 1
Human-NSd47	EOS C30: **NS C24-d47**: NP C24: AS C24: NdS C24: AP C24: CHOL: FFA5	0.4: 0.09: 0.22: 0.09: 0.09: 0.11 : 1: 1
Human-NPd47	EOS C30: NS C24: **NP C24-d47**: AS C24: NdS C24: AP C24: CHOL: FFA5	0.4: 0.09: 0.22: 0.09: 0.09: 0.11 : 1: 1

Table 2. Sample preparation information for each analytical technique

Technique	Lipid amount	Solvent	Support	Spraying area	Hydration
SAXD	1 mg	hexane/ ethanol (2:1, v/v)	nucleopore polycarbonate membrane	2 x 3 mm^2	24 h, 80% relative humidity, 25°C
FTIR	1 mg	chloroform/ methanol (2:1, v/v)	silver bromide window	1 x 1 cm^2	≥12 h, acetate buffer in D_2O (pH 5), 37°C
SANS	10 mg	chloroform/ methanol (2:1, v/v)	silicon substrate	1.2 x 3.8 cm^2	≥12 h, D_2O/H_2O buffer (100%, 50%, 8%), 37°C
TEWL	1 mg	hexane/ ethanol (2:1, v/v)	nucleopore polycarbonate membrane	1 x 1 cm^2	30 min, 25°C

The samples were hydrated before the measurements. The different techniques required individual hydration methods; however, the phase behavior was not affected by the difference in hydration method.

Small-angle X-ray diffraction (SAXD)

SAXD measurements were performed at the ALBA Synchrotron (Barcelona, Spain), using the NCD-SWEET beamline, with a Pilatus 1M detector with a pixel array 981 × 1043 (pixel size 172 × 172 μm^2). The wavelength of the X-ray beam was 0.999 Å and the sample to detector distance was 2.148 m. Silver behenate was used as a calibration of the set-up. Two samples were measured for each composition, with each sample scanned for 20 s, at 23°C. The one-dimensional SAXD profiles of the scattering intensity as a function of the scattering vector (q) were obtained after the integration of the two-dimensional scattering plot, over a 90° segment from the beam center. The scattering vector (q) was calculated using the formula: $q = (4\pi \sin\theta)/\lambda$, where θ represents the scattering angle and λ is the wavelength. The peak positions (q_n) were determined by peak fitting in Fityk (Pearson VII function) (39). Least square fitting was used to calculate the repeat distance of the lamellar phase (d), as follows: $d = 2n\pi/q_n$, where n is the diffraction peak order number.

FTIR

A PerkinElmer Frontier FTIR (PerkinElmer, Waltham, USA), with a nitrogen cooled mercury cadmium telluride detector, was used for FTIR data collection. The sample compartment was continuously purged with a dry air flow to remove moisture from the environment. Each spectrum represents 77 interferograms collected with a resolution of 1 cm^{-1}, in the wavenumber range 500 - 4000 cm^{-1}. The samples were measured between 10 and 90 °C, at a heating rate of 4 min/°C. The extraction of the spectra was performed in TimeBase (Perkin Elmer, Waltham, USA) and the processing in Spectrum (Perkin Elmer, Waltham, USA). Data processing included deconvolution (γ = 2.2) and smoothing of the spectra (factor 76.7%). Three measurements were performed for each lipid model.

The CH_2 symmetric stretching vibrations (ν_sCH_2, ~2849 cm^{-1}) provide information about the conformational ordering. The deuterated CD_2 stretching vibration occurs at ~2090 cm^{-1} (ν_sCD_2). The ν_sCH_2 and ν_sCD_2 vibrations are measured in the temperature range 10-90°C. The midpoint transition temperature represents the average temperature the lipids are transitioning from orthorhombic to hexagonal packing (T_MO-H) or from hexagonal to liquid (T_MH-L) packing, calculated as previously described (40). The CH_2 and CD_2 scissoring vibrations (δCH_2, 1462-1473 cm^{-1}; δCD_2, 1085-1095 cm^{-1}) provide information about the lipid chain packing. The peak positions of the δCH_2 and δCD_2 vibrations at 10°C and the peak heights were determined using Python scripts. A peak height ratio (OR/MID) was calculated as the ratio of the average peak height of the two orthorhombic peaks and the height of the central peak. The exact positions of the amide I

vibration (~1650 cm^{-1}) and amide II vibration (~1550 cm^{-1}) were also determined by peak fitting.

Neutron diffraction at ISIS Neutron and Muon Source

Neutron diffraction measurements of the LPP NS:NP:AS, LPP NS:NP:AP and LPP NS:NP:NdS models were performed on the LARMOR instrument at ISIS Neutron and Muon Source (Rutherford Appleton Laboratory, UK). The neutron beam wavelength range was 1 – 12.5 Å and the sample – detector distance was 4.4 m. The angle of the sample to the beam was 2.5° and the detector was set at a 2θ angle of 5° to the direct beam (area covered 664 × 600 mm; pixel size 4 × 8 mm). The sample environment was an aluminum chamber and an empty chamber was used for background measurement (subtracted from the scattering profile of each sample). The samples were measured at each hydration buffer (100%, 50% and 8% D_2O/H_2O) for 4 h (40 μA/h accelerator proton charge) at 25°C. A direct beam measurement was used for the normalization to the incident flux shape and the detector efficiency.

The Mantid software was used for reducing the data and normalizing the intensity as a function of the scattering vector (q) (41). The resulting q-range was 0.032 – 0.991 nm^{-1}. The Bragg equation was used to convert the scattering angle (2θ) to q: $q = 4\pi sin\theta \,/\, \lambda$. Based on the positions of the equidistant Bragg peaks, the repeat distance (d) of the lamellar phase was calculated: $d = 2\pi n/q_n$; with n representing the diffraction order number of the peak at the position q_n.

Next, the scattering length density profiles (SLD) were determined for each sample, using the data analysis procedure previously described (36, 37). The intensity of each diffraction order was obtained by fitting the Bragg peaks (Fityk software, with a Pearson VII function) (39). Next, the structure factor amplitude for each diffraction order ($|F_n|$) was determined using the formula: $\left|F_n\right| = A_n\sqrt{LI_n}$, where L represents the Lorentz correction factor, which can be assumed equal to q, due to the high degree of lipid lamellae orientation. A_n, the correction factor for the sample absorption, was calculated with the formula below, where l is the thickness of the lipid sample and μ is the linear attenuation coefficient (42):

$$A_n = \frac{1}{\sqrt{\frac{sin\theta}{2\mu l}\left(1-e^{\frac{-2\mu l}{sin\theta}}\right)}}$$

The D_2O/H_2O contrast variation method was used for the determination of the water profile phase signs. These phase signs are obtained from the positive or negative signs of the slope of the difference between the absolute structure factors $|F_n|$ of the sample hydrated at 100% and 8% D_2O/H_2O, as previously described (38). Assuming that the lipid head groups are located at the unit cell boundary, the water molecules are located close to the hydrophilic lipid head groups at the cell boundary as well. This assumption results in the phase signs for the water profile of the LPP NS:NP:AS, LPP NS:NP:AP and LPP

NS:NP:NdS protiated samples - + - + - +. Then, the F_n with the corresponding phase signs are plotted as a function of the D_2O/H_2O buffer ratio (Figure S3). The centrosymmetric structure of the LPP is indicated by the linear fitting obtained from plotting the F_n values as a function of D_2O/H_2O buffer for all samples (36, 37).

The phase signs of the protiated and deuterated lipid samples were individually determined based on the positive or negative sign of the F_n at 8% D_2O/H_2O buffer (Figure S3). We chose to use the data obtained using 8% D_2O/H_2O as at this composition the total scattering contribution of the water molecules is zero. As can be observed in Figure S3, for all protiated and deuterated samples the resulting phase signs combination was - + - + - +.

The scattering length density profile (SLD) of the LPP unit cell was obtained by Fourier reconstruction using the structure factor values and the phase signs with the following equation (x is the distance in the unit cell, x=0 represents the center of the unit cell):

$$\rho(x) = F_0 + 2\sum_{n=1}^{n_{max}} F_h \cos\left(\frac{2\pi n x}{d}\right)$$

The scattering density per unit volume (F_0) was determined using the density of the lipid sample and its chemical composition and it included one water molecule per lipid (43). By subtracting the SLD profile of the protiated sample from the SLD profile of the deuterated sample (both hydrated at 8% D_2O/H_2O, as the contribution of the buffer to the SLD is 0 at this ratio), the SLD profile of the deuterated moiety is obtain. This resulting SLD profile indicates the location of the deuterated lipid chain in the LPP unit cell.

The "relative absolute" SLD data were calculated following the steps previously described (36, 37, 44). Based on previous measurements using the same LARMOR instrument settings and composition with CER NS with a sphingosine deuterated (CER NSd7), a scaling factor (S_f) was introduced, calculated as the ratio between the peak areas of the NSd7 and NPd47 chains of the CER EOS/CER NS/CER NP model (38). The peak area of the SLD profile of NPd47 chain (fitted for the LPP NS:NPd47:NdS model from this study) was then multiplied by S_f to obtain the corrected NPd47 peak area, scaled to previous measurements (SLD_{area}). The factor for calculating the "relative absolute" SLD values ($SLD_{correct}$) is the ratio between the scattering of the deuterium atoms in the NPd47 chain (SLD_{dif}) and the corrected peak area of the NPd47 SLD (SLD_{area}). SLD_{dif} is the difference between the scattering of a deuterated CER acyl chain ($C_{23}D_{47}$) and the protiated CER acyl chain ($C_{23}H_{47}$). The $SLD_{correct}$ factor was applied to the scattering factor F_n values, transforming the data to the "relative absolute" scale.

Neutron diffraction at the Institut Laue-Langevin

The molecular arrangement in a lipid model with a composition mimicking the human SC was examined as well. Neutron diffraction measurements were performed on the protiated model and the models with either the deuterated acyl chain of CER NS or CER NP, to examine the location of these two chains in the LPP unit cell. These membrane diffraction measurements were performed at the D16 small-angle neutron diffractometer,

at Institut Laue-Langevin (ILL, Grenoble, France), as previously described (30, 36, 37, 45). In short, the incoming slit-collimated beam, with a wavelength of 4.45 Å, was set at 30 mm vertically and 3 mm horizontally, to ensure the proper illumination of the sample during data collection of all the diffraction orders. The diffraction patterns were measured in reflection mode, using MILAND, a ^{3}He detector (320 x 320 mm; special resolution of 1 x 1 mm), with a sample to detector distance of 0.95 m.

Each sample was mounted in an aluminum humidity chamber (46), maintained at 25°C and 99% RH and measured for 4 h (for the 100% and 50% D_2O/H_2O hydration buffers) and 9 h (for the 8% D_2O/H_2O buffer), depending on the signal to noise ratio. The samples were rotated (Ω axis) between 0.05 and 10.2° (in steps of 0.05°) at a detector angle (γ) of 11.2° (in the Ω range 0.05 - 2.25°), to separate the first and second order from the direct beam, and 12° (Ω range 1.8 - 10.2°), to cover the second to ninth diffraction orders of the LPP. For each diffraction order, the scans were measured at the specular angle ± 0.1° (total of 5 scans), which were then averaged and fitted. The scattering data were reduced, the background (empty aluminum chamber) was subtracted and the peaks were fitted using the processing software LAMP (47). The data were converted from the scattering angle 2θ to q-values using the Bragg equation: $q = 4\pi sin\theta \,/\, \lambda$. The SLD calculation was further performed as described above. The linear fitting of the structure factor F_n values as a function of the D_2O/H_2O ratio is illustrated in Figure S4.

Trans-epidermal water loss (TEWL)

To measure TEWL values, the lipid samples were mounted in Permegear in-line diffusion cells (Bethlehem, USA), with a diffusion area of 0.28 cm^2. The acceptor compartment was filled with MiliQ water and the donor compartment was empty. TEWL was monitored using the AquaFlux AF200 device (Biox Systems Ltd., London, UK), which was connected to the diffusion cells using a measurement cap. The TEWL flux was measured each 10 s for 30 mins. The steady-state TEWL was calculated as an average of the values obtained during the last 10 min of the 30 mins measurement period. At least six samples were measured for each composition. GraphPad Prism 8 was used for statistical analysis (one-way ANOVA test with Bonferroni correction; $P < 0.05$ and t test for comparisons of two groups; $P < 0.05$).

RESULTS AND DISCUSSION

Lamellar and lateral organization

The lamellar organization of the LPP simple models was investigated with SAXD. The X-ray diffraction profiles of the LPP NS:NP:NdS, LPP NS:NP:AS and LPP NS:NP:AP models display seven equidistant peaks corresponding to a lamellar phase with the repeat distance of 12.6, 12.7 and 12.9 nm, respectively (Figure 1). The diffraction peak intensity distribution

(second order with the highest intensity, followed by the first and then the third order) is characteristic for the LPP (31). The increase in repeat distance is in agreement with the findings of Uche et al. (48). They reported repeat distances of models with CER EOS (40m/m%) and either CER NS, CER NP, CER AS or CER AP (60m/m%) mixed with CHOL and FFAs; an increase in the LPP repeat distance was observed when comparing the EOS/AS (12.6 nm) and EOS/AP (13.4 nm) models. A peak at q= 1.8 nm^{-1} is detected in all samples and it corresponds to phase-separated crystalline CHOL. The peaks of the LPP NS:NP:NdS and LPP NS:NP:AS models are generally sharp, however, for the LPP NS:NP:AP model the peaks corresponding to the third, fourth and sixth diffraction orders are slightly asymmetric, indicating that an additional phase might be present.

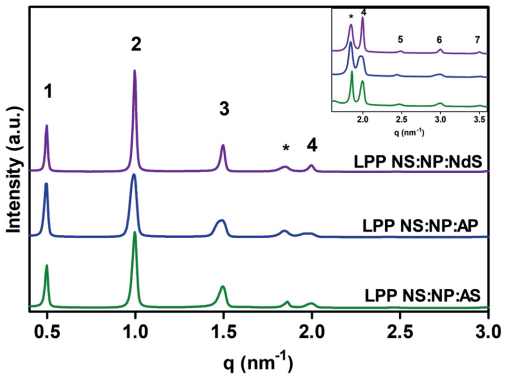


Figure 1. The SAXD profiles of the three lipid models (LPP NS:NP:NdS in purple, LPP NS:NP:AP in blue and LPP NS:NP:AS in green). The insert displays the zoomed in q-range 1.6 – 3.6 nm^{-1}. The LPP diffraction orders are depicted with Arabic numbers and phase separated (crystalline) CHOL is denoted with the asterisk (*).

Next, the lateral organization was examined using FTIR. Figure 2A displays the δCH_2 vibrations of the LPP NS:NP:NdS, LPP NS:NP:AS and LPP NS:NP:AP models and Figure 2B the thermotropic behavior of the $\nu_s CH_2$ vibrations. The peak splitting indicates the presence of an orthorhombic packing in all three compositions. The position of the δCH_2 vibration peaks was determined by peak fitting. From the positions the δCH_2 peaks, the splitting distance (distance between the two δCH_2 peaks) was determined and this distance was around 10.6 cm^{-1}. In comparison, pure FFA C24 has maximum δCH_2 peak splitting of 10.7 cm^{-1} (unpublished), thus this denotes that the size of the orthorhombic domains in the three models is close to maximum splitting indicating large domain sizes of at least 100 lipid molecules (49, 50). In addition, a δCH_2 peak height ratio was calculated (OR/MID) as the ratio of the two orthorhombic peaks heights and the central (middle) peak height (Table 4). This is of interest as a higher fraction of hexagonal packing (peak position at around 1467 cm^{-1} thus attributing to the MID peak) will result in a shallower dip and thus a lower height ratio of OR/MID peaks. The OR/MID height ratio of the LPP

NS:NP:AP model is 2.5, smaller than the other models (2.9 and 3.3), suggesting that a larger fraction of the lipids in this AP model is hexagonally packed in comparison to the other two models, but the size of the orthorhombic domains is very similar in the three models. Uche et al. reported an increased hexagonal phase in a model with CER EOS/CER AP (40/60 mol%) in comparison with a similar model with either CER AS, CER NS or CER NP (48). This showed a similar tendency as the models examined in this study.

The thermotropic curves of the $\nu_s CH_2$ vibrations of the LPP NS:NP:NdS, LPP NS:NP:AS and LPP NS:NP:AP models are plotted in Figure 2B. At 10°C, the $\nu_s CH_2$ wavenumbers of all models are <2849 cm^{-1}, which demonstrates a high conformational ordering of the lipids corresponding to an orthorhombic lipid packing, as shown by the δCH_2 vibrations shown in Figure 2A at 10°C. This remains stable up to ~32°C when a transition is indicated by the increase of the $\nu_s CH_2$ wavenumber to ~2850 cm^{-1}. This represents the phase transition from orthorhombic to a less ordered phase, probably a hexagonal packing.

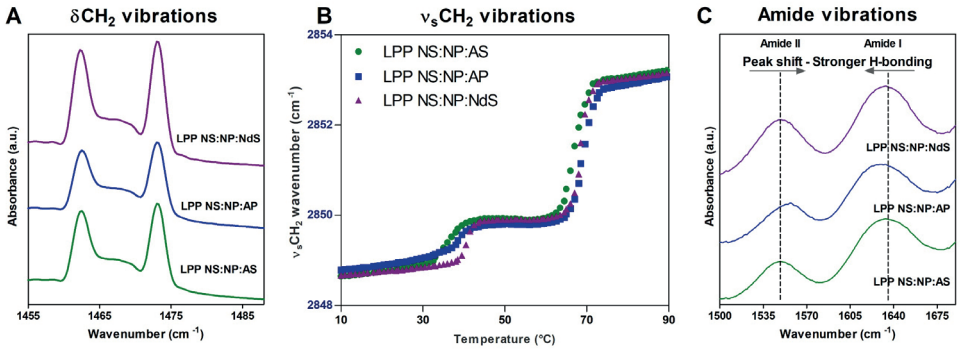


Figure 2. (A) δCH_2 vibrations of the LPP NS:NP:NdS, LPP NS:NP:AP and LPP NS:NP:AS, measured by FTIR at 10°C. (B) Thermotropic plots of the three samples with the wavenumbers of the $\nu_s CH_2$ frequencies displayed in the temperature range 10-90°C. (C) FTIR spectrum of the region 1500 – 1680 cm^{-1}, displaying the two amide vibrations at 10°C. The data for each lipid model represents an average of three separate measurements.

Figure S5 shows the δCH_2 vibrations at 25°C (temperature used for the other methods: SANS, TEWL) and at 40°C. At 25°C the two δCH_2 peaks are still fairly well separated, with the distance between the peaks of 10.2 cm^{-1} for the LPP NS:NP:NdS model, while for the LPP NS:NP:AS and LPP NS:NP:AP models, it was 9.9 and 9.7 cm^{-1} respectively. The peak splitting distance at 25°C is lower in comparison with the 10°C measurements (Table 3), and the same trend is observed for the OR/MID peak height ratio at 25°C (OR/MID ratio values are 1.6 ± 0.1, 1.9 ± 0.1 and 2.9 ± 0.1 for the LPP NS:NP:AS, LPP NS:NP:AP and LPP NS:NP:NdS respectively). As it can be seen from Figure S5B, at 40°C the δCH_2 vibrations show a broader peak with a shoulder, indicating the ongoing transition to the hexagonal packing of the lipids.

The mid-phase transition temperatures (Table 3) reveal small differences between the three models, especially for the orthorhombic to hexagonal phase transition (T_MO-H). This transition in the LPP NS:NP:NdS model occurs at a higher temperature (40.8 ± 0.3 °C) compared to the other two models, which have similar mid-transition temperatures (36.2 ± 1.4 °C and 38.7 ± 0.6 °C for LPP NS:NP:AS and LPP NS:NP:AP models respectively). The differences in the mid-phase transition temperatures explain the OR/MID δCH_2 peak height ratios observed at 25°C. The LPP NS:NP:NdS model shows the least differences in comparison to the values obtained at 10°C, due to the higher phase transition temperature to a hexagonal phase in this model.

The hexagonal to liquid phase transitions occur in comparable temperature ranges and the T_MH-L shows no significant differences between the three models (Table 3). The lipid mixing is followed using partially deuterated samples and this is described below.

Table 3. Midpoint transition temperatures for the three models, the δCH_2 scissoring peak distances and the peak positions of the amide I and II vibrations. Data are shown as averages with standard deviations for 3 repeat measurements.

Lipid sample	δCH_2 peak distance (cm^{-1})	δCH_2 OR/MID peak height ratio	T_MO-H (°C)	T_MH-L (°C)	Amide peak position (cm^{-1})
LPP NS:NP:AS	10.7 ± 0.1	2.9 ± 0.1	36.2 ± 1.4	67.3 ± 0.7	1547.0 ± 0.9 1635.8 ± 0.1
LPP NS:NP:AP	10.6 ± 0.1	2.5 ± 0.3	38.7 ± 0.6	69.1 ± 0.9	1548.1 ± 0.3 1627.5 ± 0.1
LPP NS:NP:NdS	10.8 ± 0.1	3.3 ± 0.1	40.8 ± 0.3	68.6 ± 0.3	1547.3 ± 0.2 1632.6 ± 0.4

Hydrogen bonding network in the models

The head group structure of the various CER subclasses investigated is different among the models, as CER NdS, CER AS and CER AP have a different number of hydroxyl groups. These CERs can act as both hydrogen bond donor and/or acceptor, thus FTIR studies focusing on amide vibrations can provide information about hydrogen bonding network in the systems. The amide I vibration (~1650 cm^{-1}) results from the C=O stretching vibration and the amide II (~1550 cm^{-1}) vibration is determined by both the N-H bending and C-N stretching vibrations. If the position of the two amide vibrations is closer (when the amide I has a lower frequency and amide II a higher frequency), this indicates a stronger hydrogen bonding (51, 52). In the simple LPP models the amide I and II vibrations are characterized by broad peaks (Figure 2C). The exact peak positions have been determined by peak fitting (Table 3). The LPP NS:NP:NdS and LPP NS:NP:AS models have a similar distance between the amide I and II vibrations, indicating a similar hydrogen bonding network (Figure 2C). However, the LPP NS:NP:AP model shows a higher frequency for the amide II peak and lower amide I frequency, resulting in a smaller distance between the two peaks. This indicates that the inclusion of CER AP in the lipid model results in a

stronger hydrogen bonding, in comparison with the other two models, but this is not surprising as the head group of CER AP contains four hydroxyl groups.

The difference in hydrogen bonding is in agreement with previous studies, which reported stronger hydrogen bonding for phytosphingosine-based CERs than for the sphingosine-based CERs, in single component systems, in three components systems, as well as in model systems forming the LPP (48, 52, 53). It is likely that both the concentration of CER AS, CER AP or CER NdS in this study (30 mol% of total CERs) and the composition of the models, leads to a weaker hydrogen bond network than in single component CER systems.

Lipid barrier measured by trans-epidermal water loss (TEWL)

TEWL measurements were performed to examine the lipid barrier changes after adding an extra CER subclass to the mixture, with the TEWL of the three models with either CER AS, CER NdS or CER AP being compared with the model with the composition CER EOS, CER NS, CER NP, CHOL, FFA C24 (LPP NS:NP 1:1). (Figure 3). The lipid organization of this LPP NS:NP 1:1 model was reported in a previous study and it can be considered a control sample (38). The TEWL of the LPP NS:NP:AS and LPP NS:NP:AP models is significantly increased compared to the LPP NS:NP 1:1 model, while there is no significant difference for the TEWL flux of LPP NS:NP:NdS model compared to the control model (one-way ANOVA test). The LPP NS:NP:AS model showed a poorer barrier function compared to the LPP NS:NP:AP model as well, as shown by the significant differences in the TEWL (t test of the two groups).

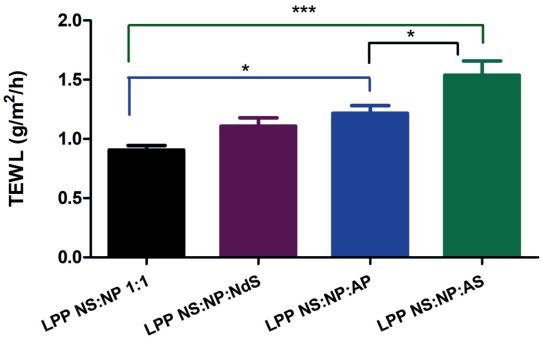


Figure 3. Trans-epidermal water loss of the models, calculated as an average of the steady flux in the last 10 min of the measurements. Data are shown as averages with standard deviations of n≥6 measurements of different lipid membranes per group (* P<0.05; *** P<0.005)

There are at least two factors that play a role in the permeability of the lipid barrier in comparing these systems: hydrogen bonding and the fraction of lipids organized in hexagonal packing. The hydrogen bond network might have an important role for the barrier function, as a dense hydrogen network might reduce the permeation of water

molecules through the lipid layers and this would lead to a lower TEWL. However, the presence of a larger fraction of lipids adopting a hexagonal packing might enhance the permeation of molecules though the lipid layer, causing a reduced lipid barrier (54). As shown in Figure S5A (Supplemental Material), at 25°C the LPP NS:NP:NdS model has a higher fraction of orthorhombically packed lipids compared to the LPP NS:NP:AS and LPP NS:NP:AP models. Thus, this small packing difference between the models, as well as the stronger hydrogen bond network of CER AP in comparison with the other two models, explains the trend observed for the TEWL, with the highest permeability to water measured for the LPP NS:NP:AS model.

Differences in the permeability of LPP models with different CER head group structure were also observed by Uche et al. in a previous study, where phytosphingosine-based CER models (with CER AP or CER NP) showed a lower permeability than the sphingosine-based CER models (CER AS or CER NS) (48). In models forming only the SPP, a study by Kováčik et al. indicates a higher water loss of the CER NP model compared to the CER NS model, with no differences between the models involving CER AP, CER AS or CER NdS (55). The different results compared to our finding are probably due to extensive phase separation in these models that also affect the packing of the lipids.

Molecular arrangement of the LPP unit cell

Neutron diffraction measurements were carried out for the protiated models (LPP NS:NP:AS, LPP NS:NP:AP and LPP NS:NP:NdS) and the models that included either the deuterated acyl chain of CER NS (NSd47) or CER NP (NPd47) to identify the effect of the CER AS, AP and NdS on the position of the deuterated acyl chains in the LPP unit cell. The one-dimensional scattering intensity plots (Figure S6, Supplemental information) showed a sequence of six equidistant peaks identified as the LPP diffraction orders. Apart from there, there is a peak at 1.8 nm^{-1}, corresponding to crystalline CHOL (phase separated) but there was no overlap with the peak corresponding to the fourth LPP diffraction order. As noted in the SAXD plots, the diffraction peaks of the LPP NS:NP:AP model are broader, but no co-existing phases were detected.

After the structure factors and corresponding phase signs were determined for each sample, the SLD profiles were obtained. The SLD profiles of the water were determined by subtraction of the SLD intensity of the protiated sample equilibrated and measured at 100% D_2O/H_2O and at 8% D_2O/H_2O hydration. Figure 4A, D, G display the water SLD profiles of the three models. Two regions of high intensity are present at the border of the LPP unit cell (at approximately 6.3 nm from the center of the unit cell). Besides these, there are also two inner water regions located at 2.2 ± 0.1 nm from the unit cell center. The position of the water molecules is near the lipid head group regions (and not next to the hydrophobic lipid tails), therefore the water SLD profile demonstrates that the trilayer structure of the LPP is centrosymmetric, as previously reported (36, 37).

Next, we determined the acyl chain locations of CER NS and CER NP in the unit cell. The SLD profiles of the deuterated NSd47 and NPd47 chains were calculated by subtracting the SLD profile of the protiated sample from the deuterated samples, hydrated with the 8% D_2O/H_2O buffer. The resulting SLD profiles represent the localization of the acyl chains of CER NS or CER NP in the LPP unit cell (Figure 4 B,C,E,F,H and I). The LPP NS:NPd47:NdS model is characterized by an increased intensity of the SLD in the middle of the unit cell, as well as an elevation at the outer layers (Figure 4B). Thus, the deuterated acyl chains of CER NP are positioned mainly in the central layer of the LPP, while a small part of the lipid chains are located at the unit cell boundaries. The LPP NSd47:NP:NdS model shows the same intensity distribution in the SLD profile, suggesting the same position for the acyl chains of CER NS and CER NP in the unit cell of the LPP (Figure 4C).

Examining the SLD profiles of the LPP NS:NPd47:AP and LPP NSd47:NP:AP lipid models (Figure 4E,F), as well as LPP NS:NPd47:AS and LPP NSd47:NP:AS systems (Figure 4H,I), the same SLD distribution is present as for the LPP NS:NP:AP samples, indicating the same location of the deuterated acyl chains of CER NP and CER NS in these unit cells (primarily in the inner layer of the unit cell of the LPP, with a small part of the chains at boundary of the unit cell). The percentage of deuterated CERs in each model is the same (15 mol% of CER content, which represents ~5 mol% of total lipids) and the relative absolute intensities of the six SLD profiles are similar between the lipid models, suggesting the same distribution of the deuterated chains is present in all the systems.

These results indicate that the addition of another CER in a simpler LPP NS:NP model does not influence the arrangement of CER NS and CER NP in the unit cell of the LPP. The location of these two CERs is the same as reported in previous studies of lipid models that form the LPP (30, 36, 38, 56). These studies used both simple lipid models comprising of only two or three CERs (CER EOS, CER NS and CER NP) and a more complex model with a CER composition mimicking the pig SC composition.

The CER AS, CER NdS and CER AP that were included in this study have the same chain length as CER NS and CER NP (24 carbon atoms). As the molecular arrangement of CER NS or CER NP is not affected by including one of these three CERs, this demonstrates that the LPP arrangement is insensitive to changes in CER subclass. Previous studies showed that replacing 75 mol% of long chain CER NS (C24) with short chain CER NS (C16) in a LPP model influences the lipid organization (57). Thus, it is likely that this would influence the molecular arrangement in the LPP as well. Furthermore, Beddoes et al. concluded that the CER headgroup structure has an important role for the molecular lipid arrangement in the LPP unit: when a proportion of the CERs is replaced with FFAs (with the same chain length as the CER), a redistribution of the CERs can occur (45). Therefore, the presence of the CER head group is important but changing the nature of the CER head group has no effect on the lipid molecular arrangement in the LPP unit cell.

The position of CER AS, CER AP or CER NdS could not be identified in this study due to the unavailability of these deuterated acyl chains of the CER subclasses commercially. However, important information about their location can be obtained when examining the lipid chain interactions, by performing FTIR studies as described in the next section.

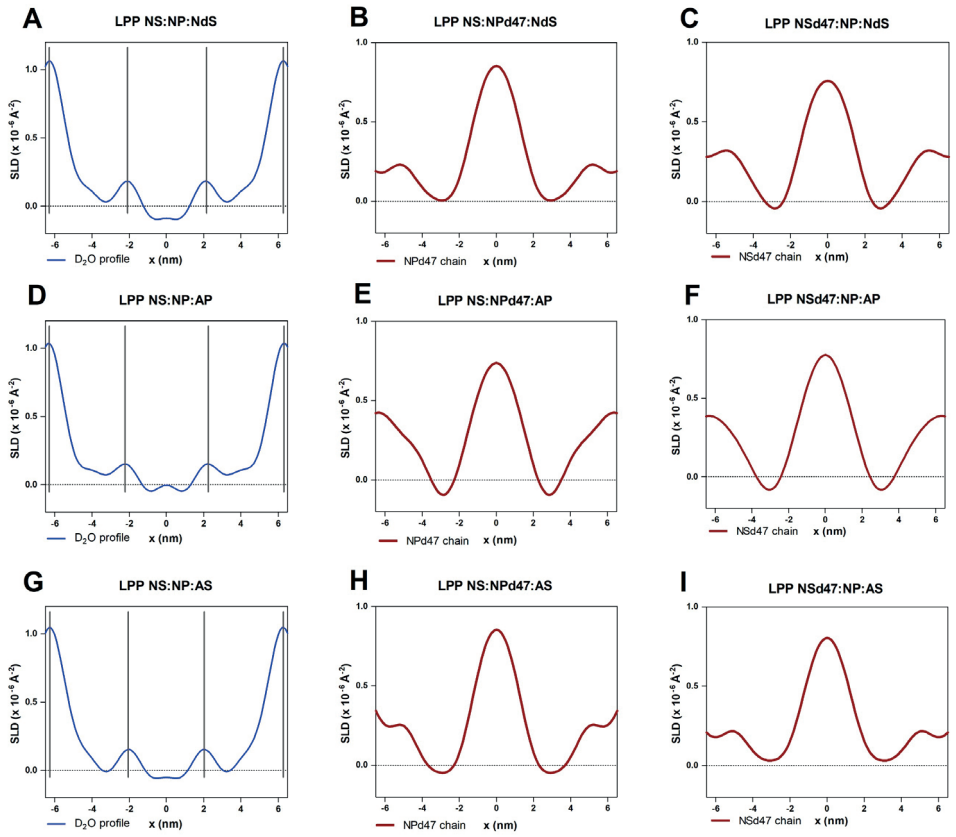


Figure 4. The neutron SLD profiles of the water (A, D, G), acyl chain of CER NP and acyl chain of CER NS in the LPP NS:NP:NdS (B,C), LPP NS:NP:AP (E,F) and LPP NS:NP:AS (H,I) models. The SLD water profiles are determined from the subtraction of the SLD profiles of the protiated sample measured at 8% D_2O/H_2O buffer hydration from the 100% D_2O/H_2O buffer. The vertical black lines (A, D, G) denote the localization of the water molecules in the LPP unit, thus also the lipid head groups position.

Lipid chain interactions

The lipid chain interactions were examined using the peak splitting of the δCD_2 and δCH_2 vibrations from the FTIR spectra (Figure 5). When the lipids form an orthorhombic packing, the CH_2 chains are densely packed, resulting in CH_2-CH_2 (or CD_2-CD_2) short-range coupling due to the proximity of the CH_2 (CD_2) groups. As a consequence, the scissoring

vibrations split into two peaks. The distance between two scissoring peaks is dependent on the size of the orthorhombic domains.

The δCH_2 and δCD_2 frequencies have a considerable vibrational energy variation (δCH_2 vibrations are between 1460 – 1480 cm^{-1} and the δCD_2 vibrations between 1080 – 1095 cm^{-1}). When the lipid domain size is around 100 chains, the maximum peak splitting is achieved (50, 51). If deuterated and protiated chains are in close proximity, CD_2-CH_2 interactions occur and because of the vibrational energy difference the CD_2-CD_2 chain interactions are lost. Such interactions result in a single peak at 1088 cm^{-1}. In combination with CD_2-CD_2 peak splitting, a larger peak at 1088 cm^{-1} leads to poorer peak separation of the two orthorhombic peaks and a smaller depth between the peaks.

In the LPP NS:NP 1:1 model previously investigated (CER EOS, CER NP, CER NS, CHOL and FFA C24), it was concluded that the acyl chains of CER NS and CER NP together with FFA C24 are all primarily located in the inner layer of the LPP trilayer unit (38). This is based on the localization of the CER NP and CER NS acyl chains from neutron diffraction measurements and FTIR (δCD_2 peak splitting distance of 6.4 ± 0.1 cm^{-1} for the lipid model with NSd47, NPd47 and DFFA – Table 4). Moreover, CER NS and CER NP adopted the linear conformation (with the acyl and sphingosine chain oriented on both sides of the CER headgroup). The neutron diffraction results presented above for the three models investigated in this study indicate a primary location of the acyl chains of CER NP and CER NS in the inner layer of the LPP unit cell as well. No information is available about the position of the acyl chains belonging to CER AP, CER AS or CER NdS as these deuterated CERs are not commercially available.

However, if CER AS, CER AP or CER NdS chains are partly located in the inner layer of the LPP, the δCD_2 peak splitting should be reduced, as protiated chains (sphingosine chains, acyl chains or both) will interfere with the CD_2-CD_2 chain interactions and consequently will reduce the deuterated domain size. The δCD_2 vibrations of the three models with deuterated NS and deuterated NP show a δCD_2 peak splitting distance between 5.3 – 5.5 cm^{-1} (Table 4). As a significant reduction in the δCD_2 peak splitting is observed compared to the LPP NS:NP 1:1 model (6.4 ± 0.1 cm^{-1}), these results suggest that there are more protiated lipid chains neighboring the deuterated chains of CER NP, CER NS and FFA in the LPP NSd47:NPd47:AS:DFFA, LPP NSd47:NPd47:AP:DFFA and LPP NSd47:NPd47:NdS:DFFA models compared to the LPP-NSd47-NPd47-DFFA model. As previous studies reported that CER NP and CER NS are arranged in a linear conformation in LPP lipid models, with the acyl chains and sphingoid bases placed on either side of the CER head group (in lipid models with different compositions, both simple and complex models) (29, 30, 38, 56), it is likely that this is the case for the models used in this study. Therefore, it is expected that the reduction in splitting is caused by the acyl or sphingosine chains of CER AS, CER AP and CER NdS located in the central layer. A clear conclusion cannot be drawn only based on these FTIR results, as other complementary techniques are needed to confirm which lipid chains are neighboring the CER NS and CER NP acyl chains and FFAs.

δCH_2 vibrations show a broad peak at ~1467 cm^{-1} for all three models, while in the LPP NSd47:NPd47:NdS:DFFA system there is also a small shoulder on the left side of the peak (Figure 5B). This suggests that a portion of the protiated lipid chains might be hexagonally packed. The chains forming the hexagonal packing are located in the boundary layers of the LPP.

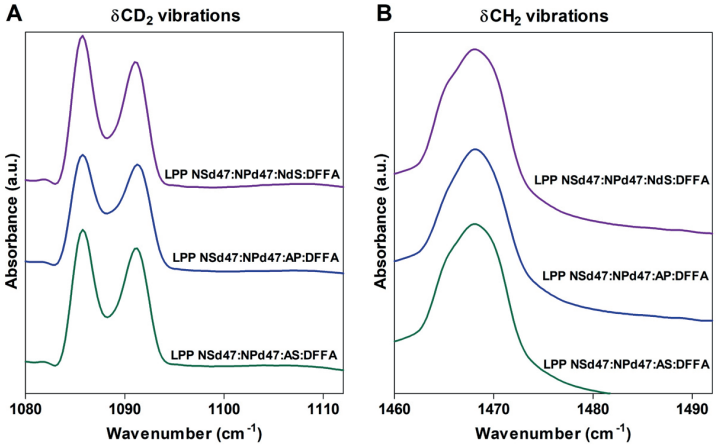


Figure 5. The δCD_2 vibrations (A) and δCH_2 vibrations (B) of the three partially deuterated models (10°C measurements). Deuterated FFA C24 and CER NS and CER NP with the deuterated acyl chain are included in these samples.

From the thermotropic curves of these three partially deuterated models (Figure S7) it can be observed that the protiated lipid chains undergo an orthorhombic – hexagonal phase transition, with the mid-transition temperatures shown in Table 5. The temperature ranges at which the transition takes place for the NdS and AS samples are smaller and sharper transitions can be observed, in contrast to the AP sample. The mid-transition temperatures are similar for the three models, both for the orthorhombic - hexagonal and hexagonal – liquid transitions (Table 4) and no significant differences were noted between the models. When comparing the thermotropic curve of the deuterated and protiated lipid chains, Figure S7 shows that the phase transitions occur in the same temperature ranges, for each model. This suggests that all lipids are well-mixed in the systems, part of the same lattice, as they are able to undergo phase transitions simultaneously.

Table 4. The splitting distance of the δCD_2 peak calculated at 10°C and the midpoint phase transition temperatures for the deuterated models. Data are presented as mean ± standard deviation of three measurements for each lipid composition.

Lipid sample	δCD_2 peak splitting distance (cm^{-1})	T_MO-H (°C)	T_MH-L (°C)
LPP NSd47:NPd47:AS:DFFA	5.4 ± 0.04	36.1 ± 0.8	63.9 ± 1.2
LPP NSd47:NPd47:AP:DFFA	5.5 ± 0.01	37.9 ± 1.5	66.7 ± 1.4
LPP NSd47:NPd47:NdS:DFFA	5.3 ± 0.01	39.8 ± 0.8	67.1 ± 1.2
LPP NS:NP 1:1 *	6.4 ± 0.1	-	-

* obtained from a previous study (38)

Lipid arrangement in a human ceramide model

The molecular arrangement in a lipid model with a composition mimicking the human SC was investigated as well. This model contains seven CER subclasses and a mix of FFAs with different chain lengths (Table 1) and it has the same lipid composition as used by Uche et al. (27). The SLD profiles corresponding to CER NP and CER NS with a deuterated acyl chain of were calculated as described above for the other lipid models. The two SLD profiles show high intensities in the inner part of the unit cell of the LPP (Figure S8 A,B). These results indicate that the acyl chains of CER NP and CER NS are predominantly located in the inner layer of the LPP, as was identified for the simple LPP models discussed above, as well as in previous studies (29, 30, 36, 38). The similar location of CER NS and CER NP in lipid models with various CER subclass composition complexity demonstrates the adaptability of the LPP structure to different CER head group compositions, indicating that the LPP lipid arrangement is insensitive to the CER composition.

Different models for the lipid arrangement in the LPP unit cell

Using neutron, X-ray diffraction and FTIR data, a model of the arrangement of the lipids in the LPP has been previously proposed, in which the acyl chains of the CERs and FFAs are predominantly located in the central layer, except the acyl chain of CER EOS, which is positioned in the two outer layers of the trilayer model together with the sphingoid chains and cholesterol, as represented in Figure S2 (29, 30, 36, 37, 58). As shown in this study and in previous papers, this model is consistent irrespective of whether a simpler lipid model (only containing CER EOS and CER NS subclasses) or a more complex lipid model (porcine CER and human CER model) is used (30, 37, 38). Using ruthenium tetroxide staining the SC lamellar organization was for the first time reported by Madison et al. (59). These studies showed broad-narrow-broad sequence of lucent bands in one repeating unit. Ruthenium tetroxide is a strong oxidizer that reacts with the double bonds of the lipid chains and the hydroxyl groups of the CERs (60). Thus, both the head groups and the linoleate position will turn into dark regions in the electron micrographs. Our proposed molecular arrangement is in agreement with the broad-narrow-broad lucent bands pattern reported.

The group of Norlen has studied the SC lamellar organization using cryo-electron microscopy. In their most recent paper two lamellar phases were reported, one with a repeat distance of 11-12 nm and a second one with a repeat distance of ~6 nm, which might represent the LPP and SPP (61). However, for the 11-12 nm phase, a two-layer asymmetric pattern was reported, which is not in agreement with the trilayer symmetric arrangement obtained using SAXD and Neutron diffraction (9, 30, 36, 37, 62).

Very recently another lipid arrangement has been proposed by Fandrei et al. for the simple LPP model with CER EOS and CER NS subclasses, based on NMR and neutron diffraction data (63). In that study, the assumption that the head groups of the lipids are located at the LPP unit cell boundary was disregarded and other phase signs were chosen for the structure factors during neutron data analysis. The newly proposed arrangement was mainly suggested based on the NMR findings of the isotropic linoleate tails of CER EOS. One of the essential differences between the model proposed previously in our papers and this new model by Fandrei et al. is the location of the acyl chain of CER EOS, which is positioned in the same layer as the acyl chains of CER NS and FFAs, with its isotropic linoleate forming the layer in the central part of the unit cell (63). Although this model is in accordance with respect to the NMR data, it raises the question whether such an isotropic fluid layer is in agreement with the high order displayed by X-ray diffraction patterns reported in their publication, but also in other studies, in which the various diffraction orders are very sharp indicating very ordered lamellar phases (9, 31, 63). It is important to mention that in the lipid models described by Fandrei et al. both the LPP and SPP are formed. However, the fraction of lipid classes in each of these phases cannot be quantified. As a result, the actual molar ratio between the lipids forming the LPP is not known. Another point of discussion is the permeability of the lipid model. In the model proposed by Fandrei et al. at a percentage of 30 m/m% CER EOS, the isotropic linoleate chains of CER EOS form a separate layer in the LPP. This would be expected to increase substantially the permeability of the lipid model compared to a model with a much lower concentration of CER EOS. However, it has been reported that a percentage of 10 mol% CER EOS (formation of both LPP and SPP) and 30% mol% CER EOS (formation of LPP exclusively) results in similar flux of ethyl-PABA across the membrane (10). It is important to note that in our lipid models the width of the δCD_2 splitting distance varies between 6.4 and 6.6 cm^{-1} and although the splitting distance is large, it is less than the maximum splitting distance of 7.4 cm^{-1} (29, 57). Whether this slight difference is due to a limited intercalation of protiated chains in the deuterated domains or the presence of disordered linoleate domains needs to be studied in future.

Further investigations are required to fully establish which model describes most accurately the lipid molecular arrangement in the LPP. Both models have in common the isotropic linoleate domains and the linear arrangement of the CERs. Calculating the neutron diffraction data obtained in this study with the phase signs used by Fandrei et al. (63) shows that in that model the acyl chains of both CER NS and CER NP still have the

same position in the LPP unit cell (Figure S9). This indicates that the conclusions of the present study regarding the adaptability of the lamellar structure to variations in the CER head groups are also translatable to this recently proposed lipid arrangement.

CONCLUSION

This study demonstrates that the lipid molecular arrangement in the unit cell of the LPP is insensitive to differences in the head group structure of the CERs and the complexity of the lipid model. Addition of either CER AS, CER NdS or CER AS in an LPP model along CER EOS, CER NP, CER NS, CHOL and FFA C24 did not change the acyl chain position of CER NP and CER NS or the lipid organization, however, it affected the TEWL, the hydrogen bond network of the models and the lateral packing, due to the different CER head group architecture. The lipid chain interactions investigated with FTIR suggest that CER AS, CER AP and CER NdS are located in the central layer of the LPP. The position of the acyl chains of CER NP and CER NS in the LPP unit cell is also similar in a complex lipid model that mimics the CER subclass composition of human SC and it is in agreement with previous reports.

ACKNOWLEDGEMENTS

We thank Prof. Dr. David Barlow and Prof. Dr. M. Jayne Lawrence (University of Manchester, U.K.) for the collaboration and critically reading the manuscript. We are thankful to Evonik (Essen, Germany) for donating the CERs utilized in this study. We would like to thank ISIS Neutron and Muon Source (Didcot, United Kingdom), Institut Laue-Langevin (Grenoble, France) and ALBA Synchrotron (Cerdanyola del Vallès, Spain) for the experimental beam time to perform the neutron and X-ray scattering measurements. ISIS neutron diffraction data DOI: 10.5286/ISIS.E.RB1969003-1 (53) and DOI: 10.5286/ISIS.E.RB2069000-1 (54). ILL neutron diffraction data DOI: 10.5291/ILL-DATA.9-13-939 (55). This study was financially supported by the National Institutes of Health (National Institute of Arthritis and Muscoskeletal and Skin Diseases), grant number R01AR072679.

REFERENCES

1. Menon, G. K., Cleary, G. W., Lane, M. E. (2012). The structure and function of the stratum corneum. *Int J Pharm*. 435(1), 3-9.
2. Proksch, E., Brandner, J. M., Jensen, J.-M. (2008). The skin: an indispensable barrier. *Experimental Dermatology*. 17(12), 1063-72.
3. Wertz, P. W., Miethke, M. C., Long, S. A., Strauss, J. S., Downing, D. T. (1985). The composition of the ceramides from human stratum corneum and from comedones. *J Invest Dermatol*. 84(5), 410-2.
4. Weerheim, A., Ponec, M. (2001). Determination of stratum corneum lipid profile by tape stripping in combination with high-performance thin-layer chromatography. *Arch Dermatol Res*. 293, 191-9.
5. Ponec, M., Weerheim, A., Lankhorst, P., Wertz, P. (2003). New Acylceramide in Native and Reconstructed Epidermis. *J Invest Dermatol*. 120(4), 581-8.
6. Hannun, Y. A., Obeid, L. M. (2008). Principles of bioactive lipid signalling: lessons from sphingolipids. *Nat Rev Mol Cell Biol*. 9(2), 139-50.
7. Kawana, M., Miyamoto, M., Ohno, Y., Kihara, A. (2020). Comparative profiling and comprehensive quantification of stratum corneum ceramides in humans and mice by LC/MS/MS. *J Lipid Res*. 61(6), 884-95.
8. White, S. H., Mirejovsky, D., King, G. I. (1988). Structure of Lamellar Lipid Domains and Corneocyte Envelopes of Murine Stratum Corneum. An X-ray Diffraction Study. *Biochemistry*. 27, 3725-32.
9. Bouwstra, J. A., Gooris, G. S., van der Spek, J. A., Bras, W. (1991). Structural investigations of human stratum corneum by small-angle X-ray scattering. *J Invest Dermatol*. 97(6), 1005-12.
10. Uche, L. E., Gooris, G. S., Bouwstra, J. A., Beddoes, C. M. (2021). High concentration of the ester-linked omega-hydroxy ceramide increases the permeability in skin lipid model membranes. *Biochim Biophys Acta Biomembr*. 1863(1), 183487.
11. Opalka, L., Kovacik, A., Pullmannova, P., Maixner, J., Vavrova, K. (2020). Effects of omega-O-acylceramide structures and concentrations in healthy and diseased skin barrier lipid membrane models. *Journal of lipid research*. 61(2), 219-28.
12. Opálka, L., Meyer, J. M., Ondrejčeková, V., Svatošová, L., Radner, F. P. W., Vávrová, K. (2022). ω-O-Acylceramides but not ω-hydroxy ceramides are required for healthy lamellar phase architecture of skin barrier lipids. *J Lipid Res*. 63(6), 100226.
13. Bouwstra, J. A., Gooris, G. S., Dubbelaar, F. E., Weerheim, A., IJzerman, A. P., Ponec, M. (1998). Role of ceramide 1 in the molecular organization of the stratum corneum lipids. *J Lipid Res*. 39, 186-96.
14. Kovacik, A., Silarova, M., Pullmannova, P., Maixner, J., Vavrova, K. (2017). Effects of 6-Hydroxyceramides on the Thermotropic Phase Behavior and Permeability of Model Skin Lipid Membranes. *Langmuir*. 33(11), 2890-9.
15. Kovacik, A., Vogel, A., Adler, J., Pullmannova, P., Vavrova, K., Huster, D. (2018). Probing the role of ceramide hydroxylation in skin barrier lipid models by (2)H solid-state NMR spectroscopy and X-ray powder diffraction. *Biochim Biophys Acta Biomembr*. 1860(5), 1162-70.
16. Pullmannova, P., Ermakova, E., Kovacik, A., Opalka, L., Maixner, J., Zbytovska, J., et al. (2019). Long and very long lamellar phases in model stratum corneum lipid membranes. *J Lipid Res*. 60(5), 963-71.
17. Pullmannova, P., Curikova-Kindlova, B. A., Ondrejcekova, V., Kovacik, A., Dvorakova, K., Dulanska, L., et al. (2023). Polymorphism, Nanostructures, and Barrier Properties of Ceramide-Based Lipid Films. *ACS Omega*. 8(1), 422-35.
18. Mendelsohn, R., Rerek, M. E., Moore, D. J. (2000). Infrared spectroscopy and microscopic imaging of stratum corneum models and skin. *Physical Chemistry Chemical Physics*. 2(20), 4651-7.
19. Boncheva, M., Damien, F., Normand, V. (2008). Molecular organization of the lipid matrix in intact Stratum corneum using ATR-FTIR spectroscopy. *Biochim Biophys Acta*. 1778(5), 1344-55.
20. Damien, F., Boncheva, M. (2010). The extent of orthorhombic lipid phases in the stratum corneum determines the barrier efficiency of human skin in vivo. *J Invest Dermatol*. 130(2), 611-4.
21. Björklund, S., Nowacka, A., Bouwstra, J. A., Sparr, E., Topgaard, D. (2013). Characterization of Stratum Corneum Molecular Dynamics by Natural-Abundance 13C Solid-State NMR. *PLoS One*. 8(4), e61889.
22. Bouwstra, J., Gooris, G., Cheng, K., A., W., Bras, W., Ponec, M. (1996). Phase behavior of isolated skin lipids. *J Lipid Res*. 37, 999 - 1011.
23. McIntosh, T. J., Stewart, M. E., Downing, D. T. (1996). X-ray Diffraction Analysis of Isolated Skin Lipids: Reconstitution of Intercellular Lipid Domains. *Biochemistry*. 35(12), 3649-53.
24. Bouwstra, J. A., Gooris, G. S., Dubbelaar, F. E. R., Ponec, M. (2001). Phase behavior of lipid mixtures based on human ceramides: coexistence of crystalline and liquid phases. *J Lipid Res*. 42(11), 1759-70.

25. de Jager, M. W., Gooris, G. S., Ponec, M., Bouwstra, J. A. (2005). Lipid mixtures prepared with well-defined synthetic ceramides closely mimic the unique stratum corneum lipid phase behavior. *J Lipid Res*. 46(12), 2649-56.
26. Opalka, L., Kovacik, A., Maixner, J., Vavrova, K. (2016). Omega-O-Acylceramides in Skin Lipid Membranes: Effects of Concentration, Sphingoid Base, and Model Complexity on Microstructure and Permeability. *Langmuir*. 32(48), 12894-904.
27. Uche, L. E., Gooris, G. S., Bouwstra, J. A., Beddoes, C. M. (2019). Barrier Capability of Skin Lipid Models: Effect of Ceramides and Free Fatty Acid Composition. *Langmuir*. 35(47), 15376-88.
28. Janssens, M., Gooris, G. S., Bouwstra, J. A. (2009). Infrared spectroscopy studies of mixtures prepared with synthetic ceramides varying in head group architecture: coexistence of liquid and crystalline phases. *Biochim Biophys Acta*. 1788(3), 732-42.
29. Beddoes, C. M., Gooris, G. S., Bouwstra, J. A. (2018). Preferential arrangement of lipids in the long-periodicity phase of a stratum corneum matrix model. *J Lipid Res*. 59(12), 2329-38.
30. Beddoes, C. M., Gooris, G. S., Foglia, F., Ahmadi, D., Barlow, D. J., Lawrence, M. J., et al. (2020). Arrangement of Ceramides in the Skin: Sphingosine Chains Localize at a Single Position in Stratum Corneum Lipid Matrix Models. *Langmuir*. 36(34), 10270-8.
31. Gooris, G. S., Kamran, M., Kros, A., Moore, D. J., Bouwstra, J. A. (2018). Interactions of dipalmitoylphosphatidylcholine with ceramide-based mixtures. *Biochim Biophys Acta Biomembr*. 1860(6), 1272-81.
32. Badhe, Y., Schmitt, T., Gupta, R., Rai, B., Neubert, R. H. H. (2022). Investigating the nanostructure of a CER[NP]/CER[AP]-based stratum corneum lipid matrix model: A combined neutron diffraction & molecular dynamics simulations approach. *Biochim Biophys Acta Biomembr*. 1864(10), 184007.
33. Moore, T. C., Iacovella, C. R., Leonhard, A. C., Bunge, A. L., McCabe, C. (2018). Molecular dynamics simulations of stratum corneum lipid mixtures: A multiscale perspective. *Biochemical and Biophysical Research Communications*. 498(2), 313-8.
34. Moore, T. C., Hartkamp, R., Iacovella, C. R., Bunge, A. L., McCabe, C. (2018). Effect of Ceramide Tail Length on the Structure of Model Stratum Corneum Lipid Bilayers. *Biophys J*. 114(1), 113-25.
35. Shamaprasad, P., Moore, T. C., Xia, D., Iacovella, C. R., Bunge, A. L., McAbe, C. (2022). Multiscale Simulation of Ternary Stratum Corneum Lipid Mixtures: Effects of Cholesterol Composition. *Langmuir*. 38(24), 7496-511.
36. Mojumdar, E. H., Gooris, G. S., Barlow, D. J., Lawrence, M. J., Deme, B., Bouwstra, J. A. (2015). Skin lipids: localization of ceramide and fatty acid in the unit cell of the long periodicity phase. *Biophys J*. 108(11), 2670-9.
37. Mojumdar, E. H., Gooris, G. S., Groen, D., Barlow, D. J., Lawrence, M. J., Deme, B., et al. (2016). Stratum corneum lipid matrix: Location of acyl ceramide and cholesterol in the unit cell of the long periodicity phase. *Biochim Biophys Acta*. 1858(8), 1926-34.
38. Nădăban, A., Gooris, G. S., Beddoes, C. M., Dalgliesh, R. M., Bouwstra, J. A. (2022). Phytosphingosine ceramide mainly localizes in the central layer of the unique lamellar phase of skin lipid model systems. *J Lipid Res*. 63(9), 100258.
39. Wojdyr, M. (2010). Fityk: a general-purpose peak fitting program. *Journal of Applied Crystallography*. 43(5), 1126-8.
40. Oguri, M., Gooris, G. S., Bito, K., Bouwstra, J. A. (2014). The effect of the chain length distribution of free fatty acids on the mixing properties of stratum corneum model membranes. *Biochim Biophys Acta*. 1838(7), 1851-61.
41. Arnold, O., Bilheux, J. C., Borreguero, J. M., Buts, A., Campbell, S. I., Chapon, L., et al. (2014). Mantid—Data analysis and visualization package for neutron scattering andμSR experiments. *Nuclear Instruments and Methods in Physics Research Section A: Accelerators, Spectrometers, Detectors and Associated Equipment*. 764, 156-66.
42. Franks, N. P., Lieb, W.R. (1979). The Structure of Lipid Bilayers and the Effects of General Anaesthetics: An X-ray and Neutron Diffraction Study. *J Mol Biol*. 133, 469-500.
43. NIST Center of Neutron Research. https://www.ncnr.nist.gov/resources/activation/, 2022 (accessed 1 February 2022).
44. Wiener, M. K., G.; White, S. (1991). Structure of a fluid dioleoylphosphatidylcholine bilayer determined by joint refinement of x-ray and neutron diffraction data 1. Scaling of neutron data and the distributions of double bonds and water. *Biophys J*. 60, 568-76.
45. Beddoes, C. M., Gooris, G. S., Barlow, D. J., Lawrence, M. J., Dalgliesh, R. M., Malfois, M., et al. (2022). The importance of ceramide headgroup for lipid localisation in skin lipid models. *Biochim Biophys Acta Biomembr*. 1864(6), 183886.

46. Gonthier, J., Barrett, M. A., Aguettaz, O., Baudoin, S., Bourgeat-Lami, E., Demé, B., et al. (2019). BerILL: The ultimate humidity chamber for neutron scattering. *Journal of Neutron Research*. 21, 65-76.
47. Richard, D., Ferrand, M., Kearley, G. J. (1996). Analysis and Visualisation of Neutron Scattering Data. *Journal of Neutron Research*. 4, 33-9.
48. Uche, L. E., Gooris, G. S., Beddoes, C. M., Bouwstra, J. A. (2019). New insight into phase behavior and permeability of skin lipid models based on sphingosine and phytosphingosine ceramides. *Biochim Biophys Acta Biomembr*. 1861(7), 1317-28.
49. Moore, D. J., Rerek, M. E., Mendelsohn, R. (1997). Lipid Domains and Orthorhombic Phases in Model Stratum Corneum: Evidence from Fourier Transform Infrared Spectroscopy Studies. *Biochemical and Biophysical Research Communications*. 231, 797 - 801.
50. Mendelsohn, R., Moore, D. J. (1998). Vibrational spectroscopic studies of lipid domains in biomembranes and model systems. *Chem Phys Lipids*. 96, 141-57.
51. Moore, D. J., Rerek, M. E., Mendelsohn, R. (1997). FTIR Spectroscopy Studies of the Conformational Order and Phase Behavior of Ceramides. *J Phys Chem B*. 101, 8933-40.
52. Moore, D. J., Rerek, M. E., Mendelsohn, R. (1999). Role of ceramides 2 and 5 in the structure of the stratum corneum lipid barrier. *Int J Cosmet Sci*. 21(5), 353-68.
53. Rerek, M. E., Chen, H., Markovic, B., Van Wyck, D., Garidel, P., Mendelsohn, R., et al. (2001). Phytosphingosine and Sphingosine Ceramide Headgroup Hydrogen Bonding: Structural Insights through Thermotropic Hydrogen/Deuterium Exchange. *J Phys Chem B*. 105, 9355 - 62.
54. Mojumdar, E. H., Kariman, Z., van Kerckhove, L., Gooris, G. S., Bouwstra, J. A. (2014). The role of ceramide chain length distribution on the barrier properties of the skin lipid membranes. *Biochim Biophys Acta*. 1838(10), 2473-83.
55. Kovacik, A., Pullmannova, P., Opalka, L., Silarova, M., Maixner, J., Vavrova, K. (2021). Effects of (R)- and (S)-alpha-Hydroxylation of Acyl Chains in Sphingosine, Dihydrosphingosine, and Phytosphingosine Ceramides on Phase Behavior and Permeability of Skin Lipid Models. *Int J Mol Sci*. 22(14).
56. Nădăban, A., Rousel, J., El Yachioui, D., Gooris, G. S., Beddoes, C. M., Dalgliesh, R. M., et al. (2023). Effect of sphingosine and phytosphingosine ceramide ratio on lipid arrangement and barrier function in skin lipid models. *J Lipid Res*. 64(8), 100400.
57. Uche, L. E., Gooris, G. S., Bouwstra, J. A., Beddoes, C. M. (2021). Increased Levels of Short-Chain Ceramides Modify the Lipid Organization and Reduce the Lipid Barrier of Skin Model Membranes. *Langmuir*. 37(31), 9478-89.
58. Groen, D., Gooris, G. S., Barlow, D. J., Lawrence, M. J., van Mechelen, J. B., Deme, B., et al. (2011). Disposition of ceramide in model lipid membranes determined by neutron diffraction. *Biophys J*. 100(6), 1481-9.
59. Madison, K. C., Swartzendruber, D. C., Wertz, P. W., Downing, D. T. (1987). Presence of intact intercellular lipid lamellae in the upper layers of the stratum corneum. *J Invest Dermatol*. 88(6), 714-8.
60. Hill, J. R., Wertz, P. W. (2003). Molecular models of the intercellular lipid lamellae from epidermal stratum corneum. *Biochimica et Biophysica Acta (BBA) - Biomembranes*. 1616(2), 121-6.
61. Narangifard, A., Wennberg, C. L., den Hollander, L., Iwai, I., Han, H., Lundborg, M., et al. (2021). Molecular Reorganization during the Formation of the Human Skin Barrier Studied In Situ. *J Invest Dermatol*. 141(5), 1243-53 e6.
62. Groen, D., Gooris, G. S., Bouwstra, J. A. (2009). New insights into the stratum corneum lipid organization by X-ray diffraction analysis. *Biophys J*. 97(8), 2242-9.
63. Fandrei, F., Havrisak, T., Opalka, L., Engberg, O., Smith, A. A., Pullmannova, P., et al. (2023). The intriguing molecular dynamics of Cer[EOS] in rigid skin barrier lipid layers requires improvement of the model. *J Lipid Res*. 64(5), 100356.
64. Bouwstra, J., Gooris, G., Dalgliesh, R. M., Beddoes, C. M., Nădăban, A. (2020) Understanding the effect of Ceramide NP concentration on the skin's long periodicity phase - relevant for atopic eczema studies. DOI: https://doi.org/10.5286/ISIS.E.RB1969003.
65. Bouwstra, J. A., Beddoes, C. M., Nădăban, A., Dalgliesh, R. M., Gooris, G. S. (2020) The effect of ceramide head group on the lipid organization in the long periodicity phase of stratum corneum substitutes. STFC ISIS Neutron and Muon Source. DOI: https://doi.org/10.5286/ISIS.E.RB2069000.
66. Lawrence, M. J., Barlow, D. J., Beddoes, C. M., Deme, B., Gooris, G. S., Nădăban, A. (2021) Investigating the molecular basis of inflammatory skin conditions. Institut Laue-Langevin (ILL). DOI: https://doi.org/10.5291/ILL-DATA.9-13-939.

SUPPLEMENTAL INFORMATION

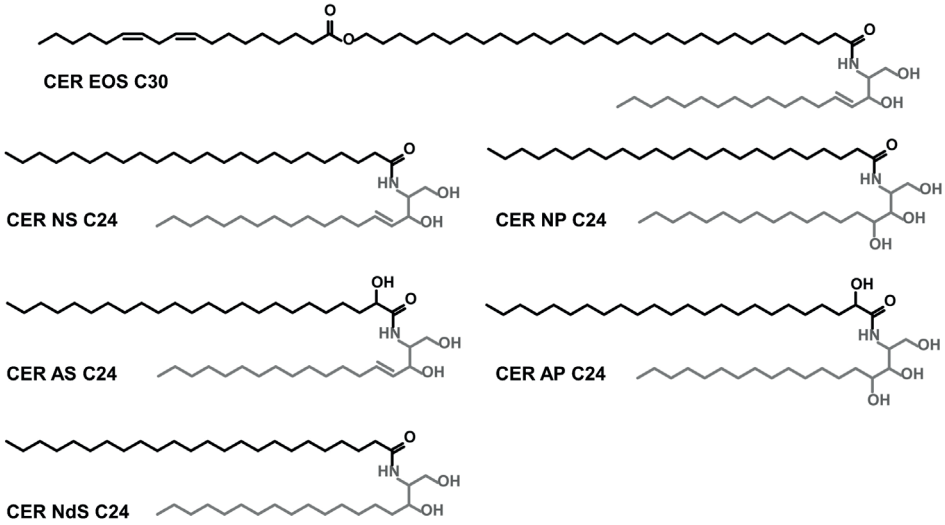


Figure S1. The CERs included in the lipid compositions and their structures.

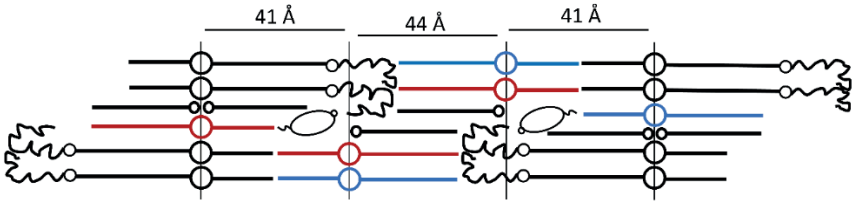


Figure S2. The molecular arrangement of lipids in the LPP unit cell trilayer, in a model with the composition CER EOS C30: CER NS C24: CER NP C24: CHOL: FFA C24 (molar ratio 0.4:0.3:0.3:1:1). Reprinted from Nădăban et al. (1). CER NS is highlighted in red and CER NP in blue, whereas CER EOS, FFA C24 and CHOL are in black.

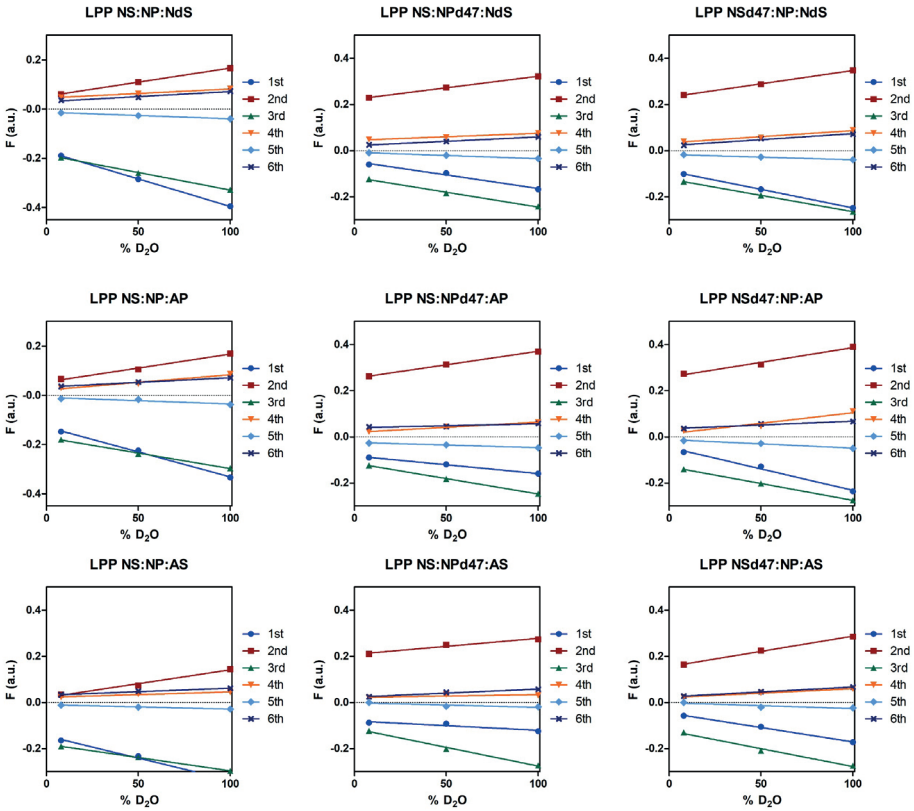


Figure S3. Linear correlation of the structure factors with the D_2O percentage (in the D_2O/H_2O buffer) of the six diffraction orders of the LPP models LPP NS:NP:NdS, LPP NS:NP:AP and LPP NS:NP:AS. Each diffraction order is indicated by different colors and symbols: first (square, dark blue), second (triangle, red), third (diamond, green), fourth (dot, orange), fifth (triangle, light blue), sixth (cross, grey).

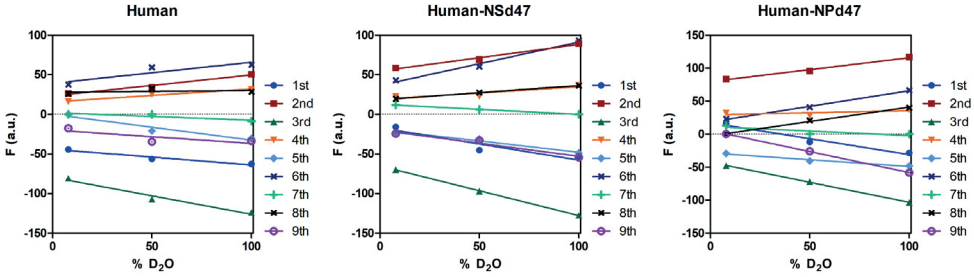


Figure S4. Linear correlation of the structure factors with the D_2O/H_2O hydration level for the protiated Human model, Human-NSd47 (with the deuterated CER NS acyl chain) and Human-NPd47 model (with the deuterated CER NP acyl chain). Each diffraction order is indicated by different colors and symbols: first (square, dark blue), second (triangle, red), third (diamond, green), fourth (dot, orange), fifth (triangle, light blue), sixth (cross, grey), seventh (plus, light green), eighth (cross, black) and ninth (circle, magenta).

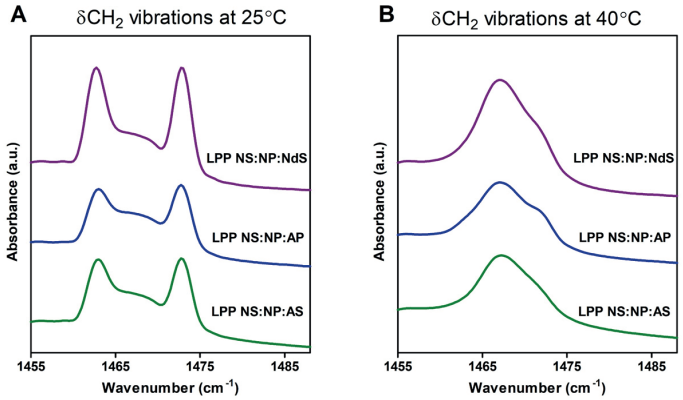


Figure S5. The CH_2 scissoring vibrations of the LPP NS:NP:NdS, LPP NS:NP:AP and LPP NS:NP:AS, measured by FTIR at 25°C and 40°C. The lipid model name is indicated on each curve.

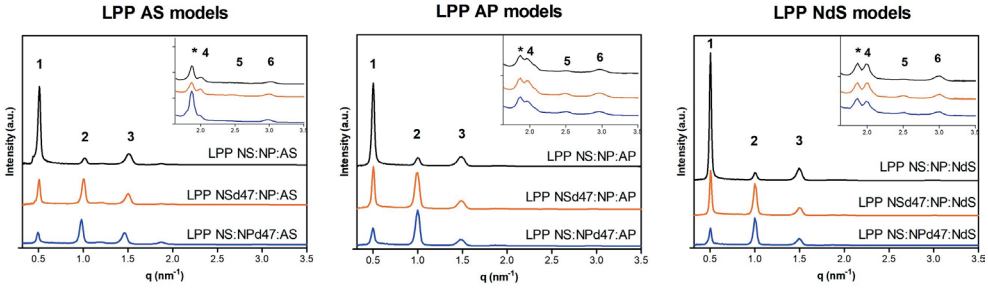


Figure S6. One-dimensional neutron scattering plots for the three models (LPP NS:NP:AS, LPP NS:NP:AP and LPP NS:NP:NdS), protiated and deuterated, at 100% D_2O/H_2O buffer ratio. The inserted cassette displays a zoom-in of the scattering vector (q) region 1.7 - 3.5 nm^{-1}. The six diffraction orders corresponding to the LPP are denoted with numbers and the phase-separated CHOL diffraction peak is marked with an asterisk.

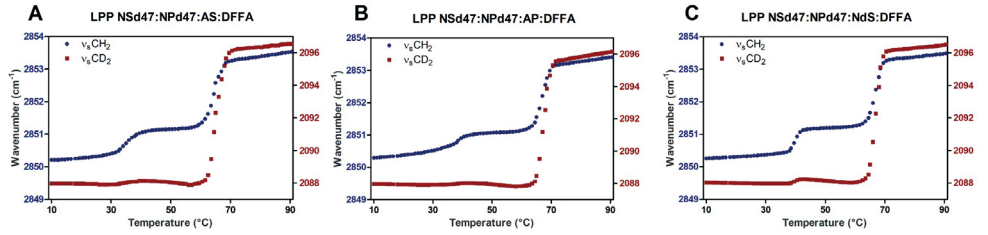


Figure S7. The ν_sCH_2 and ν_sCD_2 thermotropic curves of the three lipid systems that include the deuterated CER NS and CER NP acyl chains and DFFA (LPP NSd47:NPd47:AS:DFFA, LPP NSd47:NPd47:AP:DFFA and LPP NSd47:NPd47:NdS:DFFA). The wavenumbers of the ν_sCH_2 and ν_sCD_2 peak positions (left and right y-axis) are plotted in the 10-90°C temperature range. An average of three separate measurements per lipid sample is plotted in the graphs.

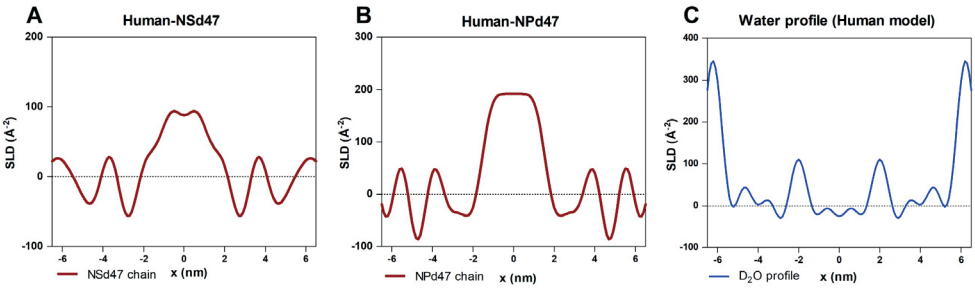


Figure S8. The net neutron SLD profile of the of the deuterated CER NS47 acyl chain (A) and CER NPd47 acyl chain (B) in the human complex model and the water profile of the human model (C). The net SLD profiles of the NSd47 and NPd47 chains display high intensities in the inner part of the LPP unit cell (B,C). The profiles also show other elevations in intensity at ~4.1 nm from the unit cell center, however these can be attributed to the truncation of the data due to data processing.

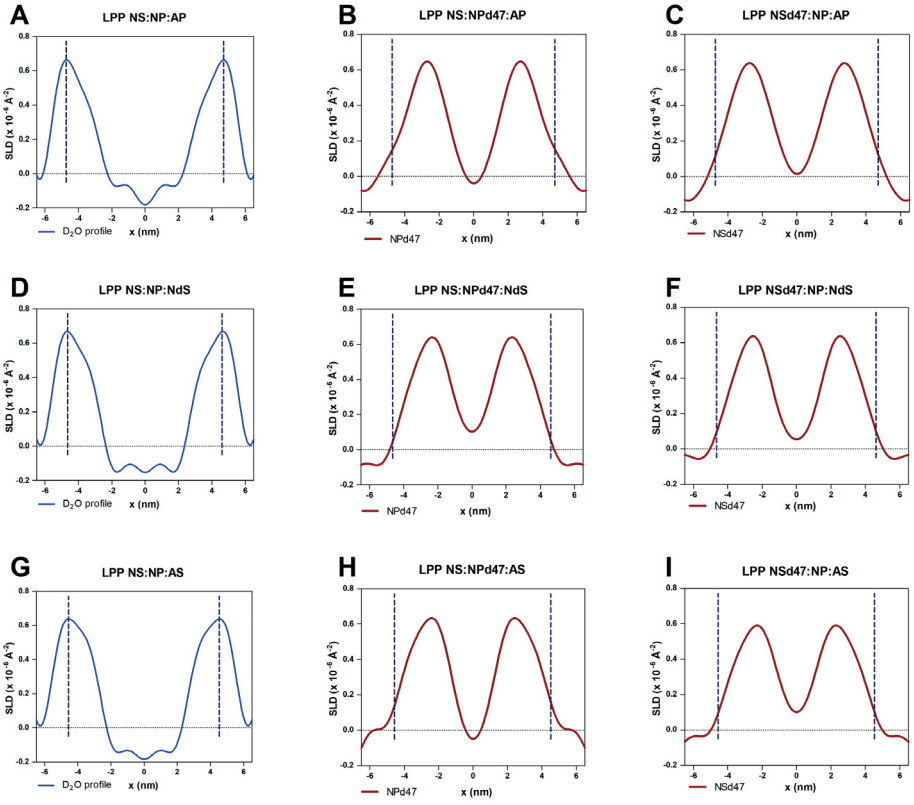
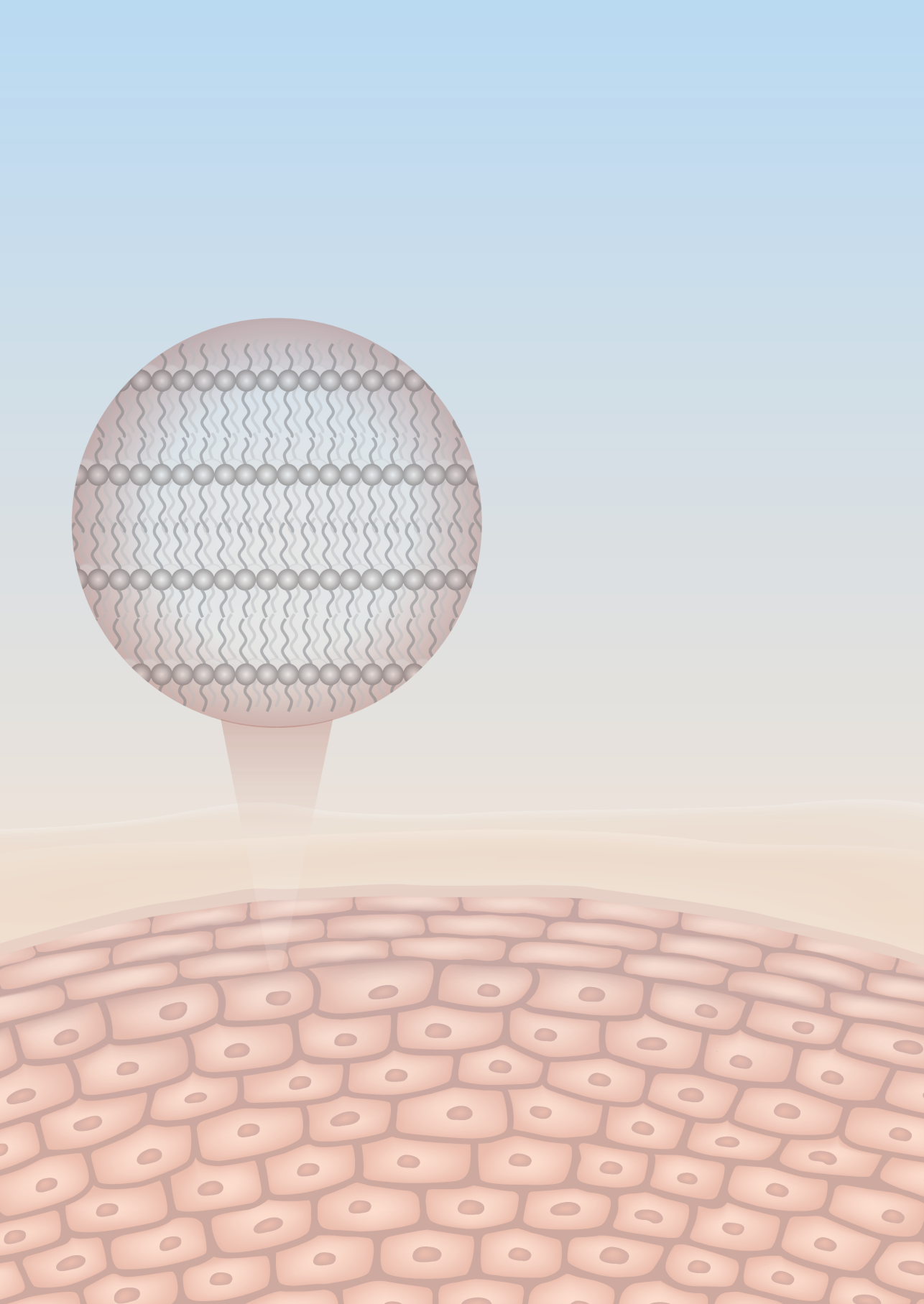


Figure S9. The neutron SLD profiles of the water (A, D, G), acyl chain of CER NP and acyl chain of CER NS in the LPP NS:NP:AP (B,C), LPP NS:NP:NdS (E,F) and LPP NS:NP:AS (H,I) models. These SLD profiles are calculated according to the method suggested by Fandrei et al. (2), with the most suitable phase sign combination for the six diffraction orders (- - + - + -). The SLD profile of the water shows the peak position at ~4.4 nm from unit cell center, indicating the lipid headgroup location. The position of the headgroup region in each sample is indicated by the black dotted line.

SUPPLEMENTARY REFERENCES:

1. Nădăban, A., Gooris, G. S., Beddoes, C. M., Dalgliesh, R. M., Bouwstra, J. A. (2022). Phytosphingosine ceramide mainly localizes in the central layer of the unique lamellar phase of skin lipid model systems. J Lipid Res. 63(9), 100258.
2. Fandrei, F., Havrisak, T., Opalka, L., Engberg, O., Smith, A. A., Pullmannova, P., et al. (2023). The intriguing molecular dynamics of Cer[EOS] in rigid skin barrier lipid layers requires improvement of the model. J Lipid Res. 64(5), 100356.



CHAPTER 7

Summary and perspectives

SUMMARY

The barrier function of the skin is attributed to the outer-most layer, the stratum corneum (SC), that protects the body from pathogens from the external environment and prevents water loss from the body (1, 2). The SC comprises of corneocytes (keratin-rich dead cells), embedded in a lipid matrix. The latter represents an important pathway for compounds permeating through the skin. The main SC lipid classes are ceramides (CERs), cholesterol (CHOL) and free fatty acids (FFAs), present in the SC in an approximately equimolar ratio (3).

X-ray diffraction investigations revealed that the SC lipids form two distinct crystalline lamellar phases, identified as the short periodicity phase (SPP) and long periodicity phase (LPP), each characterized by a repeat distance of approximately 6 and 13 nm, respectively (4, 5). The LPP has a trilayer structure (one central layer and two outer layers), is exclusively found in SC and is reported as crucial for maintaining the skin barrier function (6). Within the lamellar structure, most of the SC lipids are organized in a dense orthorhombic lateral packing (at skin temperature, ~32°C), while a fraction of the lipids adopts a less dense hexagonal organization (7, 8).

In inflammatory skin diseases, such as atopic dermatitis, psoriasis or Netherton syndrome, the SC lipid composition is different compared to healthy SC and the barrier function of the skin is impaired (9-18). Some of the lipid changes commonly reported for these three skin diseases are: an increased fraction of unsaturated CERs and FFAs, shorter carbon chain length of the CERs and FFAs and altered CER subclass ratios. In clinical studies these alterations were previously correlated with the barrier function, measured by trans-epidermal water loss (TEWL). However, as these lipid compositional changes occur simultaneously in diseased SC, the primary factor responsible for the increased TEWL cannot be identified in clinical studies. Lipid models represent an excellent alternative for studying systematically the role of lipid characteristics on the skin barrier function. This is explained in **Chapter 1** of this thesis.

The studies described in this thesis focused on understanding the effect of the CER subclass composition on the lipid organization and barrier function. Firstly, the CER composition of the inflammatory skin disease seborrheic dermatitis (SD) was examined in a clinical study. Subsequent studies using lipid model systems aimed to investigate the influence of changes in the CER subclass composition as observed in SD on the lipid organization, the lipid barrier function and the conformation of CER NS and CER NP.

In **Chapter 2**, skin barrier impairment, changes in the microbiome, and CER compositional changes in the skin of seborrheic dermatitis (SD) patients are described. The main characteristics for this inflammatory skin disease are an imbalanced immune system resulting in inflammation, cutaneous microbial dysbiosis and an impaired skin barrier function. The aim of the study was to characterize the CER composition of lesional and non-lesional SC of 37 patients and relate that to the impaired barrier function. The results

showed a significantly impacted barrier in lesional SC as measured by TEWL and a significant correlation between TEWL values and several CER compositional changes: i) increased molar ratio of CER NS:CER NP, ii) elevated fraction of CER NS with a short chain length (C34), iii) increased degree of unsaturated CER NS and iv) decreased average total chain length of CERs (acyl chain + sphingosine base) in lesional SC. This indicates the interdependence of the impaired barrier function and the CER compositional changes in SD. The influence of the CER chain length, degree of unsaturation and increased level of CER NS with a short chain length have already been studied and these factors affect the lipid barrier in model systems. However, no information was reported so far about the effect of an altered CER NS:CER NP molar ratio.

Chapter 3 aimed to examine the location of CER *N*-(tetracosanoyl)-phytosphingosine (CER NP C24) in the unit cell of the LPP using neutron diffraction and compare its location with CER *N*-(tetracosanoyl)-sphingosine (CER NS C24). CER NP was selected as this CER subclass is the most abundant in the human SC and its location in the LPP unit cell was not determined yet. As deuterated lipids are required and interpretations in simple systems can be very detailed, the lipid model consists of only CER EOS, CER NS, CER NP, CHOL and FFA C24 (CER NS: CER NP ratio 1:1). The detailed analysis was performed by using Fourier transform infrared (FTIR) spectroscopy and neutron diffraction. The study showed that this lipid composition formed the LPP trilayer structure, with the repeating unit cell consisting of an inner layer and two outer layers. Within the LPP unit cell, CER NP adopts a similar location as CER NS, with the acyl chains of CER NP being localized predominantly in the inner layer of the LPP unit. FTIR studies showed that the acyl chains of CER NP and CER NS and the FFA C24 chains are neighboring and are all located primarily in the inner layer of the LPP unit cell. This also suggests that CER NP adopts a linear conformation, similar to that of CER NS. The results of this study were a starting point for understanding the importance of the CER NS:CER NP lipid ratio, which is further described in the next chapter.

The effect of an altered CER NS:CER NP ratio on lipid organization and lipid barrier was the focus of the research described in **Chapter 4**. This ratio is changed not only in SD, but also in other inflammatory skin diseases such as atopic dermatitis and psoriasis. The lipid models were prepared with the CER NS:CER NP ratio of 1:2 (mimicking the ratio in healthy SC) and 2:1 (mimicking the ratio in SC of inflammatory skin). Subsequently, the lipid organization and barrier function were examined. The lipids in both compositions formed the LPP. A combined approach using neutron diffraction and FTIR showed that within the LPP unit cell the position of CER NS and CER NP is very similar to that of the CER NS:CER NP 1:1 ratio. Both of these acyl chains were mainly positioned in the inner layer, but with a minor part located in the outer layers of the LPP. TEWL, a measure of barrier functionality, was significantly elevated in the CER NS:CER NP 2:1 model (mimicking the ratio in inflammatory skin diseases) compared to the CER NS:CER NP 1:2 ratio (representing healthy skin), while the flux of the model drug ethyl-p-aminobenzoic acid (E-

PABA) was not different in the two models. These findings offer a more in-depth understanding of lipid organization in both healthy and diseased skin, implying that in clinical studies, the molar ratio between CER NS:CER NP entailing the same chain length, contributes to barrier impairment, but it might not be the primary factor.

In the studies described in **Chapter 5** a lipid model forming exclusively the SPP was prepared to examine whether the change in CER NS: CER NP molar ratio has a similar effect on the lipid organization as that observed in the LPP. Simple lipid models were prepared with CER NS and CER NP (ratio 1:2 mimicking healthy SC ratio and 2:1 mimicking inflammatory skin diseases), mixed with CHOL and FFA C24. The results suggest that the acyl chains of CER NS, CER NP and FFAs are neighboring in the SPP unit cell and that the CER NS and CER NP adopt an extended CER conformation in the SPP unit, similar to the arrangement in the inner layer of the LPP models described in the previous chapter. The SPP NS:NP 1:2 model is characterized by the presence of a lipid domain containing phase-separated CER NP. Unlike the SPP model, phase separation is not observed in the LPP models and this suggests that the addition of CER EOS improves the miscibility of the lipids in the model. The two SPP compositions displayed a different hydrogen bonding network, as the CER NS:CER NP 1:2 model showed a stronger hydrogen bonding than the CER NS:CER NP 2:1 model, which might be determined by the intermolecular hydrogen bonding between the CER NP head groups.

In the previous chapters simple systems were used with only two or three CER subclasses. In **Chapter 6** studies are described in which the number of CER subclasses is expanded, to examine whether more complex mixtures affect the lipid organization, barrier function and the location of the acyl chains of CER NS and CER NP in the unit cell. First, CER compositions were examined with four CER subclasses, where either *N*-(2R-hydroxy-tetracosanoyl)-sphingosine (CER AS C24), *D*-(2R-hydroxy-tetracosanoyl)-phytosphingosine (CER AP C24) or CER *N*-(tetracosanoyl)-dihydrosphingosine (CER NdS C24) were used as an additional CER subclass. The lipid organization, lipid molecular arrangement and permeability of the LPP models were examined. The results show that the inclusion of an additional CER subclass did not impact the locations of the acyl chains of CER NS and CER NP in the LPP trilayer unit cell. Then finally, a complex lipid model mimicking the composition of the human SC CER subclass was examined. Again, the two acyl chains of CER NS and CER NP maintained their positions in the inner layer of the unit cell. This suggests a remarkable insensitivity of the location of the acyl chains of CER NS and CER NP in the LPP unit cell with respect to variations in CER subclass composition. However, the different head group structures of CER AS, CER AP and CER NdS had an effect on the hydrogen bonding network in the lipid models, as the addition of CER AP (with the most hydroxyl groups in the structure) resulted in a stronger hydrogen bonding in comparison with the other two models.

In summary, seborrheic dermatitis lesions are characterized by skin barrier dysfunction and an altered lipid composition and organization of the SC. The observed

changes in lipid composition and barrier perturbation are similar to other inflammatory skin diseases including atopic dermatitis, psoriasis and Netherton syndrome. Previously, the effect of some lipid compositional changes, such as the reduction of the level of CER EO subclass, lower chain length of the FFAs and CERs and the degree of unsaturation of the FFAs, were investigated using lipid models.

Reducing the concentration of the CER EO subclass (either CER EOS alone or a combination of CER EOS, CER EOH, CER EOP, and CER EOdS) in lipid models corresponds to a lower lipid fraction forming the LPP (6, 19, 20). This had an effect on the flux of model drugs such as indomethacin and E-PABA, which was increased by ~2-fold when the CER EO concentration was reduced. Another CER compositional change, the increased fraction of short chain CERs, also affected the barrier function, as the addition of CER NS C34 and CER AS C34 resulted in a higher E-PABA flux in a model mimicking the human CER composition (~2-fold increase compared to control) (20).

Changes in the FFA composition have a considerable impact on the barrier function. When FFA C24 was replaced by a mix of FFA with different chain lengths (FFA_{mix}, including the short chains of FFA C16 and C18), the fluxes of the model drugs indomethacin, theophylline and E-PABA were increased 3, 4 and 7-fold, respectively (21, 22). Increasing the fraction of short chain FFAs in the FFA_{mix}, determined a 3-fold higher flux of E-PABA in a model mimicking the human CER composition (20). An elevation of the level of mono-unsaturated free fatty acids (muFFAs) in the lipid composition, affected the lateral lipid organization by increasing the disordering in lipid chain conformations and it influenced the barrier function, as the flux of hydrocortisone was 5-fold higher, while the TEWL had approximately a 3-fold increase (23). However, these models contained a larger degree of unsaturation than detected in skin diseases, like atopic dermatitis.

In this thesis, translational studies are described focusing on the importance of the CER subclass composition on the barrier function. As presented in **Chapter 4** in the LPP models, there was a 1.5-fold increase of the TEWL values for the CER NS:CER NP 2:1 ratio (diseased SC) compared to the CER NS:CER NP 1:2 ratio (healthy SC), while no significant differences were observed for the diffusion of the model drug E-PABA. The studies described in **Chapter 4 and 5,** the effect of the CER NS:CER NP ratio in LPP and SPP models, and in **Chapter 6,** focusing on the CER subclass composition, result in a better understanding of the influence of this CER ratio on the lipid organization and barrier function. These studies show that the lamellar organization does not change when the CER head group composition is different (with the exception of CER EOS) and only minor changes are detected in the lateral packing.

Concluding, the results of this thesis show that a change in CER subclass composition contributes to the skin barrier disfunction and that the lamellar organization is very flexible when the CER subclass composition is altered. The results also suggest that CER NS:CER NP ratio might not be a major factor in the barrier impairment. Previous studies

show that the chain length reduction (primarily of FFA, but also of CERs) has more impact on the barrier function, compared to the CER subclass compositional changes.

The studies outlined in this thesis additionally demonstrate that simplified lipid model systems, when prepared with selected CER subclasses, can resemble key aspects of the human SC lipid organization. Simple models prove to be effective for conducting a more thorough investigation and gaining a deeper understanding of the lipid-related alterations observed in inflammatory skin diseases.

PERSPECTIVES

Perspectives for repairing the skin barrier

Restoring the skin barrier function through the application of topical formulations including emollients designed to enhance the compromised barrier has been a focal point in the treatment of patients with atopic dermatitis (24, 25). Future studies should aim to develop formulations including lipid subclasses that can restore the barrier in diseased SC. Regarding the CERs, these formulations should contain especially phytosphingosine-based CERs (CER NP and CER AP with a total chain length of at least 42 carbon atoms) and CER EO-subclasses (CER EOS, CER EOP), the latter having a total chain length of at least 66 carbon atoms. These total CER chain lengths of at least 42 and 66 carbon atoms are close to the most abundant chain lengths in normal SC. However, applying a topical cream with these long-chain CERs will not immediately repair the lipid compositional disbalance in the SC of inflammatory skin. First, the CERs need to partition in the SC lipid matrix and secondly, if successful, the short chain lengths of CERs (especially CER NS C34), high levels of CER NS subclass and the disbalance between in CER/FFA ratio are not yet corrected. However, during long-term topical treatment, the inflammation might be reduced, thereby maybe normalizing lipid synthesis in the viable epidermis. Therefore, in the long-term, topical treatment might improve lipid composition, lipid organization and the skin barrier function.

It is vital to comprehend the mechanism of the topical application, its interaction with SC lipids, and its impact on permeability when developing an effective topical formulation. In literature there are hardly any reports on the interactions of the formulations with the skin. A recent study showed that a topical cream, containing CER NP, CER AP, CER EOP and CHOL improved the lipid organization (measured using FTIR) after a 4-week application on eczema-prone skin, in comparison with a ceramide-free reference cream (26). Although the authors reported an improved lipid organization after the treatment, the conclusions were only based on the stretching vibrations. Moreover, there is no information on the partitioning of the lipids into the lipid matrix and no information about the altered lipid profile (CERs or FFAs) that might be caused by the treatment. Therefore, future studies should also include a thorough lipidomic analysis to elucidate the uptake of the topically

applied lipids into the lipid matrix of the SC. This can be investigated by including deuterated CERs in the formulation, which would allow a more detailed lipid analysis and lipid organization.

Previous studies mainly focused on the CER composition in the SC of inflammatory skin diseases, whereas there are only limited reports on the FFAs composition in (diseased) SC (16, 18). In future, more focus should be put on both the ratio between the CER:FFA and the FFA chain length distribution in diseased skin compared to controls. FFAs are crucial for the formation of the orthorhombic packing of the lipids (21, 27), while CERs usually have a less important effect on this packing. In atopic dermatitis, the hexagonal packing is increased at the expense of an orthorhombic packing, and the FFA/CER ratio seems to be lower (16). Especially longer chain length of FFAs (typically FFA C24) will be more effective in enhancing an orthorhombic packing compared to shorter-chain FFAs. Furthermore, it was previously shown that FFAs topically applied on skin can be intercalated in the lipid lamellae in the lipid matrix in SC (28). Therefore, including the FFAs with long chain lengths in a formulation could enhance barrier repair.

Some recent approaches are shifting from symptom control to using biologics to target individual inflammatory pathways. It was reported that, among others, interleukin (IL)-4 and IL-13 are the major cytokines involved in atopic dermatitis, as they interfere with the lipid synthesis in the skin by inhibiting the expression of elongases (29). Dupilumab, an antibody to the IL-4 receptor, has been approved as a treatment of atopic dermatitis and showed significant improvement in the severity of the disease (30). The effect of dupilumab on the SC lipid composition has not been thoroughly investigated, but an important first step has been reported by Berdyshev et al. (31). They reported an increase in the amount of CER EOS and a decrease in the fraction of CER NS in lesional and non-lesional skin already after 2 weeks treatment. The change in the amount of CER NS correlated with an improved skin barrier function as monitored by TEWL. A more detailed lipid analysis should be performed to further examine the entire CERs subclass composition, as well as the CER chain length distribution, and the CER:CHOL:FFA molar ratio, in comparison with control SC. As FFAs play an important role in the lateral packing, in future studies it would also be of interest to examine the FFA chain length distribution in lesional and non-lesional skin. Apart from the lipid composition, the lipid organization should also be examined after the treatment, to investigate whether the lamellar organization and the lateral packing are improved in the SC. This will result in a better understanding of the barrier repair mechanism.

Future studies using lipid model membranes

The studies performed in this thesis showed that when selecting the proper CER subclasses, the complexity of the CER subclass composition of a lipid model does not influence the lamellar phases and only minor changes are noticed in the lateral packing of the lipids. This was shown when comparing the LPP NS:NP models (with different CER

NS:CER NP molar ratio) to a complex model resembling the human CER subclass composition (Chapters 4 and 6). In all these compositions, a certain level of CER NS is present. These results are also in agreement with a very simple LPP model composed of only CER EOS and CER NS (mixed with FFAs and CHOL) (32). This CER composition (CER EOS/CER NS) could be used to further study the impact of the CER chain length changes on the barrier function in diseased skin. As CER NS with a large variety of chain lengths is commercially available (Avanti Polar Lipids, U.S.A.), this allows a systematic study to examine the chain length reduction of CER NS.

Previous studies revealed the important role of FFAs on the lipid organization and barrier function using lipid models. However, until now the molar ratio between CER:FFA was not the focus of lipid model studies. When performing clinical studies to determine the CER:FFA ratio in the different inflammatory skin diseases as suggested in the previous section, the effect of the altered CER:FFA molar ratio can be investigated using lipid models to examine its role in skin barrier impairment.

Lipid model systems can also be used to understand the mechanism of action of topical formulations. As discussed above, lipids that are lacking in the diseased SC lipid composition (CERs, FFAs) can be incorporated in various formulations aimed at repairing the barrier. A further investigation of their efficacy and mechanism of action could be performed using lipid model systems. Deuterated lipids of interest should be included in the formulation, which can be applied on the surface of lipid model systems. The uptake of the lipids can be examined by investigating the lateral and lamellar lipid organization and molecular arrangement of the lipid models. This will provide information about the mechanism of action of these formulations. For example, when measuring the scissoring frequencies using FTIR it can be examined whether deuterated lipids (could also be moisturizers) form mixed crystalline lattices with the SC lipids, or that they form separate domains. The barrier improvement could also be examined using TEWL measurements and permeability studies of these lipid models.

In addition to lipid compounds employed in topical formulations, the incorporation of moisturizers is a common practice to enhance the skin barrier. Lipid models can be used to examine the effect of lipophilic moisturizers on the skin barrier. X-ray diffraction and FTIR can offer insights into the influence of moisturizers on lamellar phases and lateral organization of lipid models after exposure to these compounds, while neutron diffraction can be employed to unravel the molecular interactions of the lipids with these molecules. The observations from these studies could potentially influence the development of methods aimed at repairing the skin barrier.

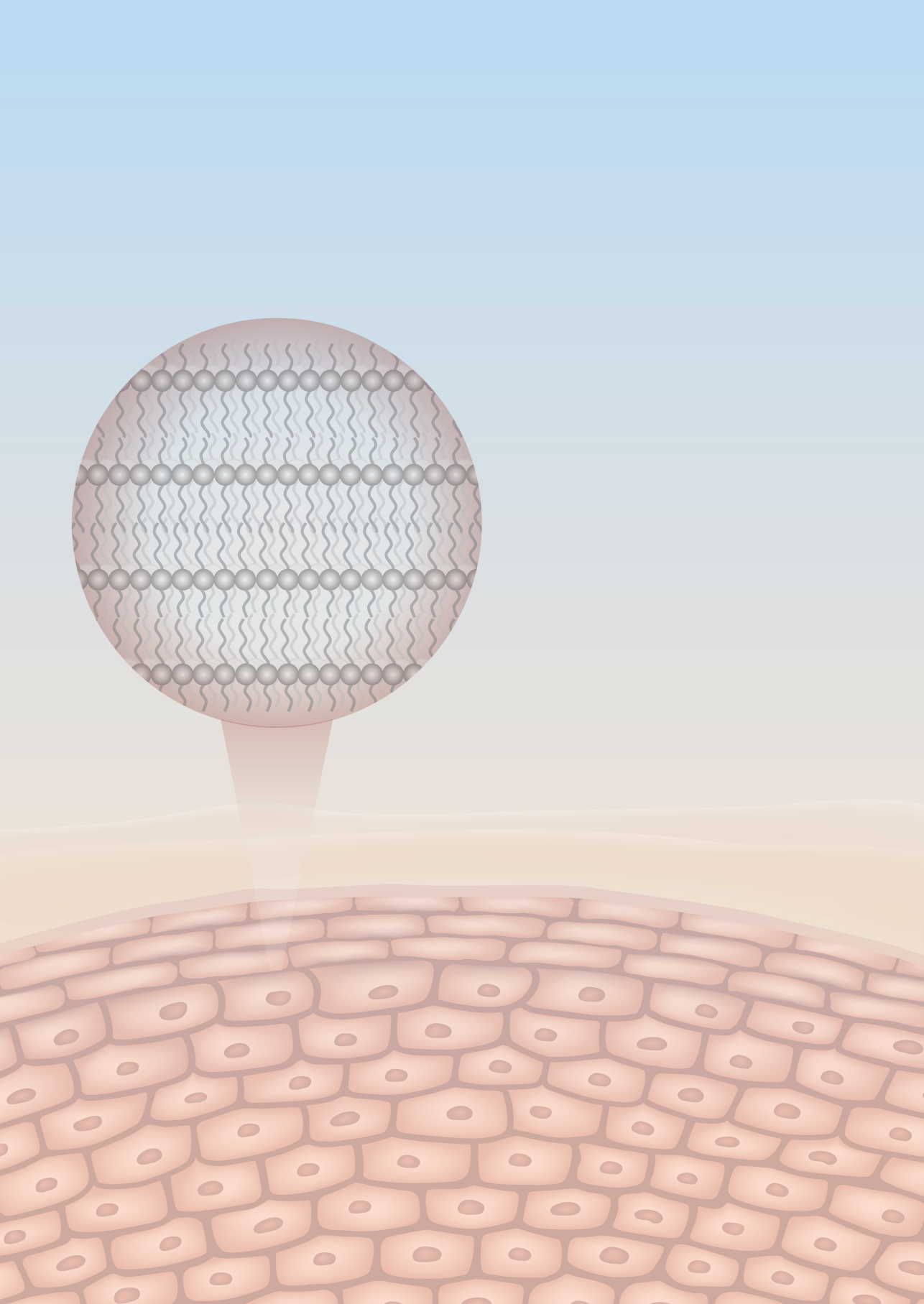
Molecular simulations of lipid models represent a valuable tool for validating experimental hypothesis and exploring structural features that are inaccessible to experimental methods. These simulations provide atom-level information that can contribute to a better understanding of lipid organization and barrier function. Further research should first aim to solve some of the current issues associated with the long-time

scale required for the simulation of large lipid systems and high computational cost (33). Future studies should focus on developing methods for the simulation of diffusion and permeability of compounds through the lipid systems. To predict the flux of chemical compounds though the skin, it is essential to integrate multiscale simulations with multiphasic diffusion models resembling a brick-and-mortar structure (the structure of the native SC), which account for the microscopic heterogeneity within the lipid matrix. Combining both experimental and simulation techniques would offer a comprehensive description of the lipid membrane structure and behavior.

REFERENCES

1. Madison, K. C. (2003). Barrier function of the skin: "la raison d'etre" of the epidermis. *J Invest Dermatol*. 121(2), 231-41.
2. Proksch, E., Brandner, J. M., Jensen, J.-M. (2008). The skin: an indispensable barrier. *Experimental Dermatology*. 17(12), 1063-72.
3. Weerheim, A., Ponec, M. (2001). Determination of stratum corneum lipid profile by tape stripping in combination with high-performance thin-layer chromatography. *Arch Dermatol Res*. 293, 191-9.
4. Bouwstra, J. A., Gooris, G. S., van der Spek, J. A., Bras, W. (1991). Structural investigations of human stratum corneum by small-angle X-ray scattering. *J Invest Dermatol*. 97(6), 1005-12.
5. Garson, J. C., Doucet, J., Leveque, J. L., Tsoucaris, G. (1991). Oriented structure in human stratum corneum revealed by X-ray diffraction. *J Invest Dermatol*. 96(1), 43-9.
6. de Jager, M., Groenink, W., Bielsa i Guivernau, R., Andersson, E., Angelova, N., Ponec, M., et al. (2006). A novel in vitro percutaneous penetration model: evaluation of barrier properties with p-aminobenzoic acid and two of its derivatives. *Pharm Res*. 23(5), 951-60.
7. Bouwstra, J., Gooris, G., Ponec, M. (2002). The Lipid Organisation of the Skin Barrier: Liquid and Crystalline Domains Coexist in Lamellar Phases. *Journal of Biological Physics*. 28, 211-23.
8. Boncheva, M., Damien, F., Normand, V. (2008). Molecular organization of the lipid matrix in intact Stratum corneum using ATR-FTIR spectroscopy. *Biochim Biophys Acta*. 1778(5), 1344-55.
9. Motta, S., Monti, M., Sesana, S., Caputo, R., Carelli, S., Ghidoni, R. (1993). Ceramide composition of the psoriatic scale. *Biochim Biophys Acta*. 1182, 147-51.
10. Di Nardo, A., Wertz, P. W., Giannetti, A., Seidenari, S. (1998). Ceramide and Cholesterol Composition of the Skin of Patients with Atopic Dermatitis. *Acta Derm Venereol* 78, 27-30.
11. Ishikawa, J., Narita, H., Kondo, N., Hotta, M., Takagi, Y., Masukawa, Y., et al. (2010). Changes in the Ceramide Profile of Atopic Dermatitis Patients. *J Invest Dermatol*. 130(10), 2511-4.
12. Janssens, M., van Smeden, J., Gooris, G. S., Bras, W., Portale, G., Caspers, P. J., et al. (2011). Lamellar lipid organization and ceramide composition in the stratum corneum of patients with atopic eczema. *J Invest Dermatol*. 131(10), 2136-8.
13. Janssens, M., van Smeden, J., Gooris, G. S., Bras, W., Portale, G., Caspers, P. J., et al. (2012). Increase in short-chain ceramides correlates with an altered lipid organization and decreased barrier function in atopic eczema patients. *J Lipid Res*. 53(12), 2755-66.
14. van Smeden, J., Janssens, M., Boiten, W. A., van Drongelen, V., Furio, L., Vreeken, R. J., et al. (2014). Intercellular skin barrier lipid composition and organization in Netherton syndrome patients. *J Invest Dermatol*. 134(5), 1238-45.
15. van Smeden, J., Al-Khakany, H., Wang, Y., Visscher, D., Stephens, N., Absalah, S., et al. (2020). Skin barrier lipid enzyme activity in Netherton patients is associated with protease activity and ceramide abnormalities. *J Lipid Res*. 61(6), 859-69.
16. Boer, D. E. C., van Smeden, J., Al-Khakany, H., Melnik, E., van Dijk, R., Absalah, S., et al. (2020). Skin of atopic dermatitis patients shows disturbed beta-glucocerebrosidase and acid sphingomyelinase activity that relates to changes in stratum corneum lipid composition. *Biochim Biophys Acta Mol Cell Biol Lipids*. 1865(6), 158673.
17. Yokose, U., Ishikawa, J., Morokuma, Y., Naoe, A., Inoue, Y., Yasuda, Y., et al. (2020). The ceramide [NP]/[NS] ratio in the stratum corneum is a potential marker for skin properties and epidermal differentiation. *BMC Dermatology*. 20(1).
18. Uchino, T., Kamiya, D., Yagi, H., Fujino-Shimaya, H., Hatta, I., Fujimori, S., et al. (2023). Comparative analysis of intercellular lipid organization and composition between psoriatic and healthy stratum corneum. *Chem Phys Lipids*. 254, 105305.
19. Opalka, L., Kovacik, A., Maixner, J., Vavrova, K. (2016). Omega-O-Acylceramides in Skin Lipid Membranes: Effects of Concentration, Sphingoid Base, and Model Complexity on Microstructure and Permeability. *Langmuir*. 32(48), 12894-904.
20. Uche, L. E., Gooris, G. S., Bouwstra, J. A., Beddoes, C. M. (2019). Barrier Capability of Skin Lipid Models: Effect of Ceramides and Free Fatty Acid Composition. *Langmuir*. 35(47), 15376-88.

21. Uchiyama, M., Oguri, M., Mojumdar, E. H., Gooris, G. S., Bouwstra, J. A. (2016). Free fatty acids chain length distribution affects the permeability of skin lipid model membranes. *Biochim Biophys Acta*. 1858(9), 2050-9.
22. Pullmannova, P., Pavlikova, L., Kovacik, A., Sochorova, M., Skolova, B., Slepicka, P., et al. (2017). Permeability and microstructure of model stratum corneum lipid membranes containing ceramides with long (C16) and very long (C24) acyl chains. *Biophys Chem*. 224, 20-31.
23. Mojumdar, E. H., Helder, R. W., Gooris, G. S., Bouwstra, J. A. (2014). Monounsaturated fatty acids reduce the barrier of stratum corneum lipid membranes by enhancing the formation of a hexagonal lateral packing. *Langmuir*. 30(22), 6534-43.
24. Boiten, W. A., Berkers, T., Absalah, S., van Smeden, J., Lavrijsen, A. P. M., Bouwstra, J. A. (2018). Applying a vernix caseosa based formulation accelerates skin barrier repair by modulating lipid biosynthesis. *J Lipid Res*. 59(2), 250-60.
25. Hon, K. L., Leung, A. K., Barankin, B. (2013). Barrier repair therapy in atopic dermatitis: an overview. *Am J Clin Dermatol*. 14(5), 389-99.
26. Danby, S. G., Andrew, P. V., Kay, L. J., Pinnock, A., Chittock, J., Brown, K., et al. (2022). Enhancement of stratum corneum lipid structure improves skin barrier function and protects against irritation in adults with dry, eczema-prone skin. *Br J Dermatol*. 186(5), 875-86.
27. Beddoes, C. M., Rensen, D. E., Gooris, G. S., Malfois, M., Bouwstra, J. A. (2021). The Importance of Free Fatty Chain Length on the Lipid Organization in the Long Periodicity Phase. *Int J Mol Sci*. 22(7).
28. Berkers, T., van Dijk, L., Absalah, S., van Smeden, J., Bouwstra, J. A. (2017). Topically applied fatty acids are elongated before incorporation in the stratum corneum lipid matrix in compromised skin. *Experimental Dermatology*. 26(1), 36-43.
29. Berdyshev, E., Goleva, E., Bronova, I., Dyjack, N., Rios, C., Jung, J., et al. (2019). Lipid abnormalities in atopic skin are driven by type 2 cytokines. *JCI Insight*. 3(4), 1-15.
30. Hamilton, J. D., Suarez-Farinas, M., Dhingra, N., Cardinale, I., Li, X., Kostic, A., et al. (2014). Dupilumab improves the molecular signature in skin of patients with moderate-to-severe atopic dermatitis. *J Allergy Clin Immunol*. 134(6), 1293-300.
31. Berdyshev, E., Goleva, E., Bissonnette, R., Bronova, I., Bronoff, A. S., Richers, B. N., et al. (2022). Dupilumab significantly improves skin barrier function in patients with moderate-to-severe atopic dermatitis. *Allergy*. 77(11), 3388-97.
32. Beddoes, C. M., Gooris, G. S., Foglia, F., Ahmadi, D., Barlow, D. J., Lawrence, M. J., et al. (2020). Arrangement of Ceramides in the Skin: Sphingosine Chains Localize at a Single Position in Stratum Corneum Lipid Matrix Models. *Langmuir*. 36(34), 10270-8.
33. Shamaprasad, P., Frame, C. O., Moore, T. C., Yang, A., Iacovella, C. R., Bouwstra, J. A., et al. (2022). Using molecular simulation to understand the skin barrier. *Prog Lipid Res*. 88, 101184.



APPENDICES

NEDERLANDSE SAMENVATTING

Introductie

De huid is het grootste orgaan van het lichaam en vormt de belangrijkste barrière tegen factoren van buitenaf. Andere essentiële biologische functies van de huid zijn thermoregulatie, het waarnemen van externe omgevingsprikkels zoals pijn en warmte, de synthese van vitamine D en de uitscheiding van ureum en zouten (1). De menselijke huid bestaat uit de epidermis (opperhuid), de dermis (lederhuid) en de hypodermis (het onderhuids bindweefsel) (2). De epidermis is de buitenste laag van de huid en vernieuwt zich continu. De epidermis bestaat uit vier verschillende lagen: het stratum basale, stratum spinosum, stratum granulosum en stratum corneum (SC). De barrièrefunctie van de huid wordt voornamelijk gevormd door het SC, de bovenste laag van de epidermis (3). De enige continue transportroute door de huid wordt gevormd door de lipidenmatrix in het SC. Hierdoor spelen de SC lipiden een belangrijke rol bij het voorkomen van overmatig vochtverlies vanuit het lichaam en het tegenhouden van ongewenste stoffen uit het externe milieu.

De lipiden in de SC lipidenmatrix zijn onder te verdelen in drie groepen, namelijk ceramiden (CERs), cholesterol (CHOL) en vrije vetzuren (FFAs). Deze zijn ongeveer in een equimolaire verhouding aanwezig in het menselijk SC (4). CERs maken deel uit van de sfingolipidenfamilie en zijn naast hun belangrijke functie bij de vorming van de huidbarrière ook betrokken bij cellulaire processen, zoals apoptose, proliferatie en de differentiatie van huidcellen (5, 6). CERs bestaan uit een sfingoïde base die via een amidebinding gekoppeld is aan een acylketen. Tot nu toe zijn er 25 verschillende CER subklassen geïdentificeerd in menselijk SC (7). Een aantal CER subklassen belangrijk in het onderzoek beschreven in dit proefschrift bestaan uit een sfingoïde base (sfingosine, fytosfingosine) gekoppeld aan een non-hydroxy acylketen via een amidebinding, genoemd CER NS and CER NP. Een andere CER subklasse, CER EOS, heeft een ultralange ω-hydroxy-acylketen, die via een ester groep verbonden aan een onverzadigd vetzuur en via een amide gekoppeld aan een sfingosine base. CER EOS is cruciaal voor de vorming van de LPP.

De CERs variëren ook in de lengte van hun vetzuur en sfingoide keten. Elke subklasse heeft een grote verscheidenheid aan aantal koolstofatomen in zowel de acylketen als de keten van de sfingoïde base. De totale ketenlengte (acyl + sfingoïde base) ligt meestal tussen 32 en 72 koolstofatomen, waarbij de variatie in de lengte van de acylketen groter is dan de variatie in de lengte van de sfingoïde base (7-9).

De SC lipiden vormen opeen gestapelde laagjes, de zogenaamde lamellaire fasen, waarbij de lamellen bij benadering parallel aan het oppervlak van de SC georiënteerd zijn (10). Uit röntgendiffractie studies van menselijk SC bleek dat er twee lamellaire fasen met repeterende eenheden van ongeveer 13 nm en 6 nm aanwezig zijn. Deze lamellaire fasen worden aangeduid als de lange periodiciteitsfase (LPP) en korte periodiciteitsfase (SPP) (11, 12). Binnen de lamellaire fasen in het SC kunnen de lipiden in verschillende

dichtheden gerangschikt worden, aangeduid als de laterale pakking: een orthorombische (een kristallijne fase met een zeer dichte pakking), hexagonale (een geordende fase, maar de lipidenketens bevinden zich verder van elkaar) of een vloeibare fase (een zeer ongeordende fase) (13-15). De lipiden in menselijk SC zijn voornamelijk georganiseerd in een dichte kristallijne orthorombische pakking, maar een klein deel van de lipiden vormt een hexagonale pakking of zelfs een vloeibare fase (16, 17).

Bij inflammatoire huidziekten, zoals constitutioneel eczeem, psoriasis of Netherton-syndroom, verschilt de SC lipidensamenstelling van die in gezond SC en is de barrièrefunctie van de huid aangetast (18-24). Veranderingen in de SC lipidensamenstelling zijn, onder andere, een verhoogd percentage onverzadigde CERs en FFAs, een kortere koolstofketenlengte van de CERs en FFAs, en een afwijkende samenstelling van CER subklassen. In klinische studies konden deze veranderingen worden gecorreleerd met een verminderde barrièrefunctie. Dit is bepaald door de verdamping van water door de huid te meten, het zogenaamde trans-epidermaal waterverlies (TEWL). Aangezien verschillende veranderingen in de lipidensamenstelling gelijktijdig optreden in inflammatoire huid, kan er geen causaal verband gelegd worden tussen de verhoogde TEWL en de lipidensamenstelling in klinische studies. Lipidenmodellen vormen een alternatief om systematisch de rol van specifieke lipiden op de barrièrefunctie van de huid te onderzoeken. Dit wordt beschreven in **Hoofdstuk 1** van dit proefschrift.

Het verband tussen lipidensamenstelling, lipidenorganisatie en barrièrefunctie

De studies beschreven in dit proefschrift richten zich op het effect van de verandering in CER subklasse samenstelling op de lipidenorganisatie en de barrièrefunctie. Allereerst werd de CER samenstelling van een inflammatoire huidziekte, seborroïsch eczeem (SE), onderzocht in een klinische studie. In de vervolgonderzoeken werden lipidenmodelsystemen gebruikt om het effect van veranderingen in de samenstelling van de CER subklassen op de lipidenorganisatie en de barrièrefunctie (gevormd door de lipiden) te onderzoeken.

In **Hoofdstuk 2** worden huidbarrière verstoring, veranderingen in het microbioom en de veranderingen in CER samenstelling in de huid van patiënten met SE beschreven. De belangrijkste kenmerken van deze inflammatoire huidaandoening zijn een ontregeld immuunsysteem resulterend in inflammatie, cutane microbiële dysbiose en een aangetaste huidbarrièrefunctie. Het doel van de studie was om de CER samenstelling van aangedaan en niet-aangedaan SC van 37 SE patiënten te karakteriseren en deze te relateren aan de barrièrefunctie. Uit de resultaten blijkt dat de aangedane huid een significant slechtere huidbarrière heeft. Dit was gebaseerd op TEWL metingen. Tevens was er een significante correlatie tussen de TEWL-waarden en veranderingen in de CER samenstelling. Er was een i) een positieve correlatie met de molaire verhouding tussen CER NS en CER NP, ii) een positieve correlatie met de mate van aanwezigheid van CER NS met een totale ketenlengte van 34 koolstofatomen (C34), iii) een positieve correlatie met

de mate van onverzadiging in CER NS en iv) een negatieve correlatie met de gemiddelde totale ketenlengte van CERs. Uit deze resultaten blijkt dat de aangetaste barrièrefunctie afhankelijk is van de CER samenstelling in SE. De invloed van de CER ketenlengte, de mate van onverzadiging en de grotere fractie CER NS C34 op de barrièrefunctie zijn al onderzocht met behulp van de lipidenmodelsystemen. Het bleek dat al deze veranderingen de lipidenbarrière verminderen. Echter, het effect van veranderingen in de molaire verhouding van CER NS:CER NP op de barrièrefunctie was nog niet onderzocht.

Om de rol van CER NS en CER NP in de barrièrefunctie beter te begrijpen was het doel van het onderzoek beschreven in **hoofdstuk 3** om de positie van CER *N*-(tetracosanoyl)-phytosphingosine (CER NP C24) in de repeterende eenheid (de zogenaamde eenheidscel) van de LPP te onderzoeken. Deze positie werd vervolgens vergeleken met de positie van CER *N*-(tetracosanoyl)-sphingosine (CER NS C24). We kozen voor CER NP omdat deze CER subklasse het meest voorkomt in het menselijk SC en zijn locatie in de LPP-eenheidscel nog niet was bepaald. De gedetailleerde analyse werd uitgevoerd met Fourier-transform infraroodspectroscopie (FTIR) en neutronendiffractie. Voor dit onderzoek zijn gedeutereerde lipiden nodig, dus werd een eenvoudig lipidensysteem gebruikt met slechts 3 CER, subklassen namelijk CER NS C24 en CER NP C24 en CER EOS. CER EOS zorgt er voor dat alleen de LPP gevormd wordt. Deze CER subklassen werden gecombineerd met CHOL en een FFA met ketenlengte van 24 koolstofatomen (FFA C24). De verhouding van CER NS: CER NP was 1:1. Uit de neutronendiffractie studies bleek dat deze lipidensamenstelling een repeterende eenheidscel vormt die uit drielagen bestaat: een centrale laag met aan weerzijden een buitenlaag. Uit het onderzoek blijkt dat de positie van CER NP C24 vergelijkbaar is met de positie van CER NS in deze LPP eenheidscel, waarbij de acylketens van CER NP zich voornamelijk in de centrale laag bevinden. Uit de daarop volgende FTIR-studies bleek dat de acylketens van CER NP en CER NS en de FFA C24 ketens naast elkaar liggen in de centrale laag van de eenheidscel. Dit kan alleen als CER NP een lineaire conformatie aanneemt, met de acylketen en sfingoïde basis aan weerszijden van de hydrofiele kopgroep, vergelijkbaar met conformatie van CER NS. De resultaten van deze studie vormden het uitgangspunt om het effect van een verandering in de verhouding tussen CER NS en CER NP in detail te onderzoeken, zoals beschreven in het volgende hoofdstuk.

Het effect van een veranderde CER NS: CER NP ratio op de lipidenorganisatie en lipidenbarrière stond centraal in **hoofdstuk 4**. Deze verhouding verandert niet alleen in aangedane huid van SE, maar ook bij andere inflammatoire huidziekten zoals constitutioneel eczeem en psoriasis. De lipidenmodellen werden bereid met een CER NS:CER NP verhouding van 1:2 (vergelijkbaar met de verhouding in gezonde SC) en 2:1 (vergelijkbaar met de verhouding in SC van inflammatoire huidziekten). De lipidenorganisatie en barrièrefunctie van de modellen werden onderzocht. De lipiden in beide samenstellingen vormden de LPP. Er werd gebruik gemaakt van neutronendiffractie en FTIR. Uit de metingen bleek dat binnen de eenheidscel van de LPP de positie van CER

NS en CER NP sterk overeenkomt met de posities gevonden wanneer de verhouding CER NS:CER NP 1:1 was gebruikt. Beide acylketens waren voornamelijk gelokaliseerd in de centrale laag van de eenheidscel. Ook nu werd weer TEWL gebruikt om de barrièrefunctie te onderzoeken, maar nu de barrière van de lipidenmodellen. De TEWL waarden waren significant hoger in het CER NS:CER NP 2:1 model dan in het CER NS:CER NP 1:2 model, maar de veranderingen waren beperkt. Deze bevindingen geven een gedetailleerder inzicht in de lipidenorganisatie in zowel gezonde als zieke huid. Hieruit kunnen we concluderen dat in klinische studies de molaire verhouding tussen CER NS:CER NP wel bijdraagt aan een barrièreverstoring, maar waarschijnlijk niet de primaire factor is.

In **hoofdstuk 5** werd een lipidenmodel gebruikt dat uitsluitend de SPP vormt om te onderzoeken of het effect van een gewijzigde molaire verhouding CER NS:CER NP op de lipidenorganisatie vergelijkbaar is met het effect dat in de eenheidscel van de LPP werd waargenomen. Er werd gebruik gemaakt van eenvoudige lipidenmodellen bestaande uit CHOL, FFA C24 en CER NS en CER NP (molaire verhouding 1:2 vergelijkbaar met gezond SC en 2:1 vergelijkbaar met inflammatoire huidziekten), maar nu zonder CER EOS. Uit de resultaten blijkt dat de acylketens van CER NS, CER NP en FFA C24 naast elkaar liggen in de SPP eenheidscel, waarbij CER NS en CER NP een lineaire conformatie aannemen, vergelijkbaar met de ordening in de binnenste laag van de LPP-modellen beschreven in het vorige hoofdstuk. Het SPP NS:NP 1:2 model wordt gekenmerkt door de aanwezigheid van een andere fase dat CER NP bevat. In tegenstelling tot het SPP-model wordt fasescheiding niet waargenomen in de LPP-modellen en dit suggereert dat de toevoeging van CER EOS de menging van de lipiden in het model verbetert. Uit FTIR metingen blijkt dat de twee SPP-samenstellingen verschillende waterstofbrug bindingen hebben: het CER NS:CER NP 1:2-model vertoonde een sterkere waterstofbrug binding dichtheid dan het CER NS:CER NP 2:1-model. Dit wordt veroorzaakt door de intermoleculaire waterstofbruggen tussen de CER NP-kopgroepen.

In de eerdere studies werden eenvoudige systemen gebruikt met slechts twee of drie CER-subklassen. In **hoofdstuk 6** worden studies beschreven waarin het aantal CER-subklassen is uitgebreid om te onderzoeken of complexe lipidenmodellen de lipidenorganisatie en barrièrefunctie beïnvloeden. Eerst werden lipidenmengsels onderzocht met vier CER-subklassen, waarbij ofwel *N*-(2R-hydroxy-tetracosanoyl)-sfingosine (CER AS C24), *D*-(2R-hydroxy-tetracosanoyl)-fytosfingosine (CER AP C24) of CER *N*-(tetracosanoyl)-dihydrosfingosine (CER NdS C24) werden gebruikt als extra CER-subklasse. Ook werd weer CER EOS toegevoegd om voornamelijk de LPP te vormen. De lipidenorganisatie, moleculaire rangschikking en permeabiliteit van de LPP-modellen werden onderzocht. Uit de resultaten blijkt dat het toevoegen van een extra CER-subklasse de positie van de acylketens van CER NS en CER NP in de LPP drielagen eenheidscel niet verandert. Naast de eenvoudige modellen werd ook een complex lipidenmodel onderzocht met een CER samenstelling die lijkt op de samenstelling in menselijke SC. De twee acylketens van CER NS en CER NP behielden nog steeds hun positie

in de binnenste laag van de eenheidscel. Hieruit blijkt een opmerkelijke ongevoeligheid voor de positie van de acylketens van CER NS en CER NP in de LPP-eenheidscel wanneer de samenstelling van de CER subklassen verandert. De verschillende kopgroepstructuren van CER AS, CER AP en CER NdS hadden een effect op de waterstofbrug vorming in de lipidenmodellen: de toevoeging van CER AP (met de meeste hydroxy groepen in het molekuul) resulteerde in een sterkere waterstofbrug binding in vergelijking met de andere twee modellen.

Conclusie

Uit de in **Hoofdstuk 2** beschreven studies blijkt dat SE worden gekenmerkt door een verminderde huidbarrière en een veranderde CER samenstelling in het SC. Deze veranderingen in lipidensamenstelling en barrièreverstoring zijn vergelijkbaar met veranderingen gevonden in andere inflammatoire huidziekten, waaronder constitutioneel eczeem, psoriasis en het Netherton syndroom. Eerder werd het effect van een aantal veranderingen in de lipidensamenstelling, zoals de kortere ketenlengte van de FFAs en CERs en de onverzadigingsgraad van FFAs, onderzocht met behulp van lipidenmodellen. Het effect van de verhouding CER NS:CER NP, een van de belangrijkste veranderingen in zieke huid, werd echter niet onderzocht. Zoals beschreven in **hoofdstuk 4** werd er een significante toename van de TEWL-waarden waargenomen voor de CER NS:CER NP 2:1 ratio (zieke SC) in vergelijking met de CER NS:CER NP 1:2 ratio (gezonde SC). Dit is een indicatie dat een hogere CER NS:CER NP ratio bijdraagt aan een verminderde barrièrefunctie.

De onderzoeken beschreven in de **hoofdstukken 4, 5 en 6** leiden tot een beter begrip van de invloed van de samenstelling van de CER subklassen op de lipidenorganisatie en de barrièrefunctie. Uit deze studies blijkt dat de lamellaire organisatie niet verandert wanneer de samenstelling van de CER kopgroep verandert (met uitzondering van CER EOS) en dat er alleen kleine veranderingen worden waargenomen in de laterale pakking.

Uit de beschreven studies blijkt dat het onderzoeken van eenvoudige lipidenmodelsystemen bijdraagt tot een beter inzicht in de veranderingen in lipidensamenstelling zoals waargenomen in inflammatoire huidziekten.

REFERENCES

1. Chuong, C. M., Nickoloff, B. J., Elias, P. M., Goldsmith, L. A., Macher, E., Maderson, P. A., et al. (2002). What is the 'true' function of skin? *Experimental Dermatology*. 11(2), 159-87.
2. Proksch, E., Brandner, J. M., Jensen, J.-M. (2008). The skin: an indispensable barrier. *Experimental Dermatology*. 17(12), 1063-72.
3. Menon, G. K., Cleary, G. W., Lane, M. E. (2012). The structure and function of the stratum corneum. *Int J Pharm*. 435(1), 3-9.
4. Weerheim, A., Ponec, M. (2001). Determination of stratum corneum lipid profile by tape stripping in combination with high-performance thin-layer chromatography. *Arch Dermatol Res*. 293, 191-9.
5. Hannun, Y. A., Obeid, L. M. (2008). Principles of bioactive lipid signalling: lessons from sphingolipids. *Nat Rev Mol Cell Biol*. 9(2), 139-50.
6. Cha, H. J., He, C., Zhao, H., Dong, Y., An, I. S., An, S. (2016). Intercellular and intracellular functions of ceramides and their metabolites in skin (Review). *Int J Mol Med*. 38(1), 16-22.
7. Kawana, M., Miyamoto, M., Ohno, Y., Kihara, A. (2020). Comparative profiling and comprehensive quantification of stratum corneum ceramides in humans and mice by LC/MS/MS. *J Lipid Res*. 61(6), 884-95.
8. Ohnari, H., Naru, E., Sakata, O., Obata, Y. (2023). Distribution of Domains Formed by Lateral Packing of Intercellular Lipid in the Stratum Corneum. *Chem Pharm Bull*. 71, 31-40.
9. Masukawa, Y., Narita, H., Sato, H., Naoe, A., Kondo, N., Sugai, Y., et al. (2009). Comprehensive quantification of ceramide species in human stratum corneum. *J Lipid Res*. 50(8), 1708-19.
10. Madison, K. C., Swartzendruber, D. C., Wertz, P. W., Downing, D. T. (1987). Presence of intact intercellular lipid lamellae in the upper layers of the stratum corneum. *J Invest Dermatol*. 88(6), 714-8.
11. Bouwstra, J. A., Gooris, G. S., van der Spek, J. A., Bras, W. (1991). Structural investigations of human stratum corneum by small-angle X-ray scattering. *J Invest Dermatol*. 97(6), 1005-12.
12. Garson, J. C., Doucet, J., Leveque, J. L., Tsoucaris, G. (1991). Oriented structure in human stratum corneum revealed by X-ray diffraction. *J Invest Dermatol*. 96(1), 43-9.
13. Mendelsohn, R., Rerek, M. E., Moore, D. J. (2000). Infrared spectroscopy and microscopic imaging of stratum corneum models and skin. *Physical Chemistry Chemical Physics*. 2(20), 4651-7.
14. Boncheva, M., Damien, F., Normand, V. (2008). Molecular organization of the lipid matrix in intact Stratum corneum using ATR-FTIR spectroscopy. *Biochim Biophys Acta*. 1778(5), 1344-55.
15. Damien, F., Boncheva, M. (2010). The extent of orthorhombic lipid phases in the stratum corneum determines the barrier efficiency of human skin in vivo. *J Invest Dermatol*. 130(2), 611-4.
16. Bouwstra, J. A., Gooris, G. S., Salomons-de Vries, M. A., van der Spek, J. A., Bras, W. (1992). Structure of human stratum corneum as a function of temperature and hydration: A wide-angle X-ray diffraction study. *Int J Pharm*. 84, 205-16.
17. Björklund, S., Nowacka, A., Bouwstra, J. A., Sparr, E., Topgaard, D. (2013). Characterization of Stratum Corneum Molecular Dynamics by Natural-Abundance 13C Solid-State NMR. *PLoS One*. 8(4), e61889.
18. Motta, S., Monti, M., Sesana, S., Caputo, R., Carelli, S., Ghidoni, R. (1993). Ceramide composition of the psoriatic scale. *Biochim Biophys Acta*. 1182, 147-51.
19. Di Nardo, A., Wertz, P. W., Giannetti, A., Seidenari, S. (1998). Ceramide and Cholesterol Composition of the Skin of Patients with Atopic Dermatitis. *Acta Derm Venereol* 78, 27-30.
20. Ishikawa, J., Narita, H., Kondo, N., Hotta, M., Takagi, Y., Masukawa, Y., et al. (2010). Changes in the Ceramide Profile of Atopic Dermatitis Patients. *J Invest Dermatol*. 130(10), 2511-4.
21. Janssens, M., van Smeden, J., Gooris, G. S., Bras, W., Portale, G., Caspers, P. J., et al. (2012). Increase in short-chain ceramides correlates with an altered lipid organization and decreased barrier function in atopic eczema patients. *J Lipid Res*. 53(12), 2755-66.
22. van Smeden, J., Janssens, M., Boiten, W. A., van Drongelen, V., Furio, L., Vreeken, R. J., et al. (2014). Intercellular skin barrier lipid composition and organization in Netherton syndrome patients. *J Invest Dermatol*. 134(5), 1238-45.
23. Yokose, U., Ishikawa, J., Morokuma, Y., Naoe, A., Inoue, Y., Yasuda, Y., et al. (2020). The ceramide [NP]/[NS] ratio in the stratum corneum is a potential marker for skin properties and epidermal differentiation. *BMC Dermatology*. 20(1).
24. Uchino, T., Kamiya, D., Yagi, H., Fujino-Shimaya, H., Hatta, I., Fujimori, S., et al. (2023). Comparative analysis of intercellular lipid organization and composition between psoriatic and healthy stratum corneum. *Chem Phys Lipids*. 254, 105305.

CURRICULUM VITAE

Andreea Nădăban was born on the 19th of November 1993 in Arad, Romania. After graduating from the National College Elena Ghiba Birta Arad in 2012, she started her Chemistry BSc degree at the West University of Timişoara. She moved to The Netherlands in September 2015 to follow the Analytical Sciences MSc degree at the Vrije Universiteit Amsterdam and the University of Amsterdam (joint degree). During her study, she performed a 10 months internship at the Clinical Chemistry laboratory of VUmc Amsterdam. In September 2017 she started working as a LC-MS technician at the division of BioTherapeutics of the Leiden Academic Centre for Drug Research (LACDR), Leiden University. In April 2019 she started her PhD project at the LACDR under the supervision of Prof. dr. Joke Bouwstra and Prof. dr. Robert Rissmann, which resulted in this thesis.

LIST OF PUBLICATIONS

From this thesis:

- Nădăban, A., Frame, C.O., El Yachioui, D., Gooris, G.S., Dalgliesh, R.M., Malfois, M., Iacovella, C.R., Bunge, A.L., M^{c}Cabe, C.M., Bouwstra, J.A. (2024). The sphingosine and phytosphingosine ceramide ratio in lipid models forming the short periodicity phase: an experimental and molecular simulation study, *Langmuir*, submitted.
- Nădăban, A., Gooris, G. S., Beddoes, C. M., Dalgliesh, R. M., Malfois, M., Deme, B., Bouwstra, J. A. (2023). The molecular arrangement of ceramides in the unit cell of the long periodicity phase of stratum corneum models shows a high adaptability to different ceramide head group structures. *Biochim. Biophys. Acta Biomembr.*, submitted.
- Rousel, J., Nădăban, A., Saghari, M., Pagan, L., Zhuparris, A. et al. (2023), Lesional skin of seborrheic dermatitis patients is characterized by skin barrier dysfunction and correlating alterations in the stratum corneum ceramide composition, *Exp. Dermatol.* 33(1): 14952.
- Nădăban, A., Rousel, J., El Yachioui, D., Gooris, G. S., Beddoes, C. M., Dalgliesh, R. M., Malfois, M., Rissmann, R., Bouwstra, J.A. (2023). Effect of sphingosine and phytosphingosine ceramide ratio on lipid arrangement and barrier function in skin lipid models. *J. Lipid Res*. 64(8), 100400.
- Nădăban, A., Gooris, G. S., Beddoes, C. M., Dalgliesh, R. M., Bouwstra, J. A. (2022). Phytosphingosine ceramide mainly localizes in the central layer of the unique lamellar phase of skin lipid model systems. *J Lipid Res*. 63(9), 100258.

Author:

- Shamaprasad, P., Nădăban, A., Iacovella, C.R., Gooris, G.S., Bunge, A.L. et al. (2024), The phase behavior of skin-barrier lipids: a combined approach of experiments and simulations, *Biophys. J.*, submitted.
- Bouwstra, J.A., Nădăban, A., Bras, W., McCabe, C., Bunge, A. et al. (2023), The skin barrier: an extraordinary interface with an exceptional lipid organization, *Prog. Lipid Res.* 92: 101252.
- Rousel, J., Saghari, M., Pagan, L., Nădăban, A., Gambrah, T. et al. (2023), Treatment with the Topical Antimicrobial Peptide Omiganan in Mild-to-Moderate Facial Seborrheic Dermatitis versus Ketoconazole and Placebo: Results of a Randomized Controlled Proof-of-Concept Trial, *Int. J. Mol. Sci.* 24(18): 14315.
- Helder, R.W.J., Rousel, J., Boiten, W.A., Gooris, G.S., Nădăban, A. et al. (2023), The effect of PPAR isoform (de)activation on the lipid composition in full-thickness skin models, *Exp. Dermatol.* 32(4): 469-478.
- Petracca, B., Nădăban, A., Eeman, M., Gooris, G.S., Bouwstra, J.A. (2021), Effects of ozone on stratum corneum lipid integrity and assembly, *Chem. Phys. Lipids.* 240: 105121.
- Mieremet, A., Helder, R.W.J., Nădăban, A., Boiten, W.A., Gooris, G.S. et al. (2021), Multitargeted approach for the optimization of morphogenesis and barrier formation in human skin equivalents*, Int. J. Mol. Sci.* 22(11): 5790.
- Helder, R.W.J., Rousel, J., Boiten, W.A., Gooris, G.S., Nădăban, A. et al. (2021), Improved organotypic skin model with reduced quantity of monounsaturated ceramides by inhibiting stearoyl-CoA desaturase-1*, Biochim. Biophys. Acta Mol. Cell Biol. Lipids* 1866(4): 158885.
- Mieremet, A., Helder, R.W.J., Nădăban, A., Gooris, G.S., Boiten, W.A. et al. (2019), Contribution of Palmitic Acid to Epidermal Morphogenesis and Lipid Barrier Formation in Human Skin Equivalents, *Int. J. Mol. Sci.* 20(23): 6069.